

Comparability of Microphone Array Measurements in Open and Closed Wind Tunnels

vorgelegt von
Dipl.-Ing.
Stefan Kröber
aus Berlin

von der Fakultät V - Verkehrs- und Maschinensysteme
der Technischen Universität Berlin
zur Erlangung des akademischen Grades

Doktor der Ingenieurwissenschaften
- Dr.-Ing -

genehmigte Dissertation

Promotionsausschuss:

Vorsitzender: Prof. Dr.-Ing. D. Peitsch
Gutachter: Prof. Dr.-Ing. W. Nitsche
Gutachter: Prof. Dr. rer. nat. Dr.-Ing. habil. A. Dillmann

Tag der wissenschaftlichen Aussprache: 27. November 2013

Berlin 2013
D 83

"The genuine rationalist does not think that he or anyone else is in possession of the truth; nor does he think that mere criticism as such helps us achieve new ideas. But he does think that, in the sphere of ideas, only critical discussion can help us sort the wheat from the chaff. He is well aware that acceptance or rejection of an idea is never a purely rational matter; but he thinks that only critical discussion can give us the maturity to see an idea from more and more sides and to make a correct judgement of it."

Karl Popper ("All Life is Problem Solving" (1999))



The described research in this thesis was supported by the German Aerospace Center.

Abstract

The phased microphone array has become a widely used tool in aeroacoustic testing for the localization and quantification of sound sources. Measurements are often carried out in wind tunnels with open or closed test sections. The underlying thesis investigates the performance and comparability of microphone array measurements conducted in wind tunnels with open and closed test sections and carries out a systematic comparison. The various effects influencing the aeroacoustic results of testing in different wind tunnels can be summarized in three main groups. Deviations can result from influences which can affect the aeroacoustic sound generation. The second group concerns differences in the experimental setup. Finally, the third group consists of the varying test section boundary conditions and propagation effects. In the framework of the assessment of the comparability of microphone array measurements in open and closed wind tunnels, this thesis focuses on the third group - the influence of test section boundary conditions and propagation effects on microphone array results. Nonetheless, the first two points are also of concern and discussed in this thesis.

The present study focuses on the beamforming accuracy and reliability in both wind tunnel types with respect to source position, source topology, relative and absolute levels of beamforming results, signal-to-noise ratio and integrated spectra. Therefore, three different wind tunnel model concepts with varying complexity are used in this thesis in order to examine on the one hand the propagation and boundary effects and on the other hand, the influence of the aerodynamic properties on the aeroacoustic sound generation in open and closed test sections. The aim is to keep the experimental setup and conditions as identical as possible in both test facilities, because it enables the examination of these test section-dependent effects and a distinction between them.

All three used models have fulfilled the primary defined requirements on such sources so that a wide range of flow and boundary effects influencing the aeroacoustic sound generation and propagation have been identified, investigated and quantified in the conducted experiments. In general, being independent from the installed model, the open test section exhibits a higher signal-to-noise ratio than the closed test section, especially for lower frequencies where wind tunnel background noise (generated by the fan, channel modes, aeroacoustic noise from mountings, etc.) and the turbulent boundary layer are predominating in the closed test section. In contrast to this, the signal-to-noise ratio of the open test section is typically decreased by the coherence loss induced by the turbulent shear layer at higher frequencies.

In principle, the 1/3 octave band source maps for all three different models, derived from measurements in both wind tunnels, show a similar and comparable source topology as long as the flow conditions were similar in both test facilities, whereby frequency-dependent differences in the source

maps appear due to the different test section dependent boundary conditions and propagation effects. On the one hand the reflections caused by the reverberant walls of the closed test section can significantly alter the measured absolute sound pressure levels compared with the open anechoic test section results where almost no reflections are present. The reflections affect strongly the results in the low frequency domain if 1/3 octave bands are evaluated. Besides that, the retrieved source positions can also be influenced, even at high frequencies, but then, the impact is confined to a small number of narrow-band source maps. On the other hand the scattering of sound waves off turbulent flow structures in the shear layer of the open test section degrades the quality and quantity of the beamforming results caused by coherence loss of the measured signals. This effect becomes more dominant in the high-frequency regime. The maximum deviation in the underlying experiments between the absolute levels of the integrated spectra between both test sections is similar for all three models and does not exceed 4.6 dB.

Zusammenfassung

Die Mikrofon-Arraymesstechnik ist eine etablierte und weitverbreitete Messtechnik für die Lokalisierung und Quantifizierung von Schallquellen in aeroakustischen Experimenten. Derartige Messungen werden oft im Windkanal mit offener oder geschlossener Messstrecke durchgeführt. Die vorliegende Arbeit untersucht die Leistungsfähigkeit und Vergleichbarkeit von Mikrofon-Arraymessungen in offenen und geschlossenen Messstrecken und führt einen systematischen Vergleich durch.

Die verschiedenen Effekte, welche die Ergebnisse aeroakustischer Messungen in unterschiedlichen Messstrecken beeinflussen, können in drei übergeordneten Gruppen zusammengefasst werden. Abweichungen können von Unterschieden in der aeroakustischen Schallgenerierung herrühren. Die zweite Gruppe von Einflüssen betrifft Unterschiede in der Versuchsanordnung. Die dritte und letzte Gruppe besteht aus Einflüssen infolge unterschiedlicher Randbedingungen in den verschiedenen Messstrecken sowie den messstreckenbedingten Effekten, welche die Schallausbreitung beeinflussen. Im Rahmen der Beurteilung der Vergleichbarkeit von Mikrofon-Arraymessungen in offenen und geschlossenen Windkanälen konzentriert sich diese Dissertation auf die dritte Gruppe – den Einfluss der Messstreckenrandbedingungen und die Auswirkung von Ausbreitungseffekten auf die Mikrofon-Arrayergebnisse. Nichtsdestotrotz werden die ersten beiden genannten Punkte auch im Rahmen dieser Arbeit ebenso diskutiert.

Die vorliegende Studie konzentriert sich auf die Genauigkeit und Zuverlässigkeit der Mikrofon-Arraymesstechnik in beiden Windkanaltypen bezüglich Quellposition, Quelltopologie, relativen und absoluten Pegeln, Signal-Rausch-Verhältnis sowie integrierter Spektren. Aus diesem Grund werden drei verschiedene Schallquellenkonzepte mit unterschiedlicher Komplexität verwendet, um einerseits Schallausbreitungs- und Randeffekte und andererseits den Einfluss der aerodynamischen Eigenschaften der unterschiedlichen Windkanaltypen auf die aeroakustische Schallgenerierung zu untersuchen. Das Ziel ist es, den Versuchsaufbau und die Versuchsbedingungen so identisch wie möglich in beiden Testeinrichtungen zu halten, weil so die Möglichkeit gegeben ist, die messstreckenabhängigen Effekte zu untersuchen und im Einzelnen zu quantifizieren.

Alle drei verwendeten Modelle wurden den an sie gestellten primären Anforderungen an solche Vergleichsquellen gerecht, so dass eine Vielzahl von Effekten, welche aeroakustische Messungen beeinflussen, in den durchgeführten Experimenten identifiziert, untersucht und quantifiziert werden konnten. Zum einen gehören hierzu schallausbreitungsbeeinflussende Phänomene und Randbedingungen aufgrund der Messstreckenbegrenzungen und zum anderen sind strömungsinduzierte Einflüsse auf die aeroakustische Schallgenerierung in diesem Zusammenhang zu nennen.

Im Allgemeinen, unabhängig vom installierten Modell, weist die offene

Messstrecke ein höheres Signal-Rausch-Verhältnis auf als die geschlossene Messstrecke. Das gilt insbesondere für tiefe Frequenzen in der geschlossenen Messstrecke, wo das Windkanalhintergrundrauschen (erzeugt durch das Gebläse, Kanalmoden, aeroakustische Schallquellen generiert von Halterungen, usw.) und die turbulente Grenzschicht die Messungen stark beeinflussen. Im Gegensatz dazu wird typischerweise das Signal-Rausch-Verhältnis der offenen Messstrecke bei hohen Frequenzen durch den von der turbulenten Scherschicht induzierten Kohärenzverlust der gemessenen Signale verringert.

So lange die Strömungsverhältnisse in beiden Windkanälen vergleichbar sind weisen die Terzbandquellkarten für die drei verwendeten Modelle, gemessen in beiden Windkanaltypen, prinzipiell eine ähnliche und vergleichbare Quelltopologie auf. Nichtsdestotrotz treten frequenzabhängige Unterschiede und Störungen in den Quellkarten auf, hervorgerufen durch die unterschiedlichen messstreckenabhängigen Randbedingungen und Ausbreitungseffekte sowie die windkanalspezifischen Strömungsverhältnisse.

Auf der einen Seite verursachen die schallharten Kanalwände der geschlossenen Messstrecke Reflexionen, welche die gemessenen Schalldruckpegel erheblich verändern können im Vergleich zur offenen, reflexionsarmen Messstrecke, wo der Einfluss von Reflexionen vernachlässigbar ist. Die Reflexionen beeinflussen insbesondere die Ergebnisse im tieffrequenten Terzbandbereich. Abgesehen davon kann die lokalisierte Quellposition auch bei hohen Frequenzen von Reflexionen beeinflusst werden, aber dann beschränkt sich der Einfluss auf eine kleine Anzahl von schmalbandigen Quellkarten. Auf der anderen Seite verursacht die Streuung von Schallwellen an turbulenten Strukturen in der Scherschicht der offenen Messstrecke einen Kohärenzverlust der gemessenen Signale, was zu einer Verschlechterung der Qualität und Quantität der Mikrofon-Arrayergebnisse führt. Dieser Effekt wird speziell im hochfrequenten Bereich dominanter. Die maximal auftretende Pegeldifferenz zwischen den integrierten Spektren der Quellkarten ermittelt aus den Experimenten in beiden Messstreckentypen ist für alle drei Modelle ähnlich und beträgt nicht mehr als 4,6 dB.

Contents

List of symbols	xiii
Abbreviations	xvii
1 Introduction	1
1.1 Motivation and classification of the problem of comparability	1
1.2 Aerodynamic and aeroacoustic properties of closed and open wind tunnels	4
1.2.1 Aerodynamic properties	4
1.2.2 Acoustic properties	6
1.3 Literature review	9
1.3.1 Comparison of trailing edge noise	10
1.3.2 Comparison of noise from a high-lift system	11
1.3.3 Comparison of noise from landing gear	13
1.3.4 Brief summary of the studies	14
1.4 Objective and outline of this thesis	15
2 Localization and quantification of sound sources with phased microphone arrays	17
2.1 A brief historical overview	17
2.2 The Delay-and-Sum Beamformer	19
2.2.1 Mathematical formulation of the Delay-and-Sum Beamformer	20
2.2.2 Properties of the Delay-and-Sum Beamformer	22
2.2.3 Improvements of the SNR	24
2.2.4 Quantification of results	26
2.2.5 Deconvolution	28
2.3 Beamforming with flow	29
2.3.1 Closed test section	29
2.3.2 Open test section	35
2.3.3 Turbulent scattering and spectral broadening	48
2.3.4 Absorption	55
2.4 Source type and directivity effects	56

3	Overview of the employed sound sources	59
3.1	General sound source requirements	59
3.2	Reference sound source	60
3.3	Plate with cavities	63
3.3.1	Cavity noise mechanisms	64
3.3.2	Design of the plate with cavities	70
3.4	Unswept wing with high-lift-system	73
3.4.1	Slat noise sources and physical mechanisms of sound generation	74
4	Experimental setup, instruments and methods	79
4.1	The wind tunnels	79
4.1.1	AWB	79
4.1.2	GroWiKa	80
4.2	Measurement techniques and equipment	80
4.3	Installation of the models and measurement equipment	83
4.3.1	Reference sound source	84
4.3.2	Plate with cavities	84
4.3.3	Wing with high-lift system	84
4.3.4	Geometrical setup in the wind tunnels	86
4.3.5	Far-field measurement setup	88
4.4	Aeroacoustic comparability	89
4.5	Estimation of installation and wind tunnel effects	91
4.5.1	Array resolution	91
4.5.2	Emission angle and directivity effects	92
4.5.3	Transmission coefficient	95
4.5.4	Reflections in the closed test section	96
4.6	Data acquisition and test program	96
4.6.1	Reference sound source	97
4.6.2	Plate with cavities	99
4.6.3	Wing with high-lift system	99
4.7	Comments to the presentation of the results	100
4.7.1	Single microphone spectra	100
4.7.2	Source maps	101
4.7.3	Microphone signal coherence	101
4.7.4	Far-field microphone spectra	101
5	Experimental results of the reference sound source	103
5.1	Single microphone spectra measured in both wind tunnels	103
5.1.1	Broadband signals	103
5.1.2	Tonal signals	104
5.1.3	Brief summary of the single microphone measurements	107
5.2	Microphone array results from the open test section	107
5.2.1	Source maps	108

5.2.2	Microphone signal coherence	113
5.3	Microphone array results from the closed test section	116
5.3.1	Source maps	116
5.3.2	Microphone signal coherence	121
5.4	Comparison of the results of the open and closed test section	124
5.4.1	Source maps and microphone signal coherence	124
5.4.2	SNR, integrated and far-field spectra	125
5.4.3	Source position	130
5.5	Summary of the results of the reference sound source	134
6	Experimental results of the plate with cavities	137
6.1	Cavity microphone results	137
6.1.1	Noise spectra of the cavity microphones	137
6.1.2	Microphone signal coherence	139
6.1.3	Flow velocity influence on cavity microphone spectra .	140
6.1.4	Test section type influence on cavity microphone spectra	143
6.2	Beamforming results of the plate model	145
6.2.1	Open test section	145
6.2.2	Closed test section	147
6.3	Comparison of the results of the open and closed test section	150
6.3.1	Source maps	150
6.3.2	SNR, integrated and far-field spectra	151
6.4	Summary of the results with the plate model	153
7	Experimental results on a wing with high-lift system	155
7.1	Aerodynamic results	155
7.2	Beamforming results of the wing with high-lift system	158
7.2.1	Open test section	158
7.2.2	Closed test section	160
7.3	Comparison of the results of the open and closed test sections	162
7.3.1	Source maps	163
7.3.2	Integrated spectra	166
7.4	Summary of the results of the wing with high-lift system	168
8	Comparison of the experimental results	171
9	Summary and outlook	175
A	Results from microphone array measurements	191
A.1	Microphone signal coherence obtained from measurements in the closed test section	191

B	Aerodynamic measurements	195
B.1	Characteristics of the shear layer in the open test section of the AWB	195
B.2	Static pressure measurements	196
C	Turbulent scattering	199
C.1	Measurements from Brooks and Humphreys (1999)	199
D	Estimation of various effects influencing the cavity microphone spectra of the plate model	201
D.1	Adjustment of the parameters of the Rossiter model to the measurements in the open test sections	201
D.2	Estimation of the temperature influence on the cavity microphone spectra	202
D.3	Estimation of the influence of solid blockage on the cavity microphone spectra	203
	List of figures	214
	List of tables	215

List of symbols

Variables

A	pressure amplitude
A_ϕ	amplitude of velocity potential
B	arbitrary point coordinates
B_c	bicoherence coefficient
C_s	spatial coherence coefficient
D_c	cavity depth
$E\{.\}$	expectation value
F_L	lift force
F_p	pressure force
He	Helmholtz number
K_r	empirical constant accounting for vortex convection velocity
I	identity matrix
L	output power of the beamformer
L_b	number of signal blocks
L_c	cavity length
L_p	sound pressure level (ref. $2 \cdot 10^{-5} Pa$)
M	Mach number
N	number of microphones
P	complex-valued pressure amplitude
Q	complex-valued source strength
\mathbf{R}	cross-spectral matrix
$\hat{\mathbf{R}}$	noisy cross-spectral matrix
$\tilde{\mathbf{R}}$	estimated cross-spectral matrix
\mathbf{R}_I	real-valued diagonal matrix
\mathbf{R}_{off}	complex-valued off-diagonal matrix
R	specific gas constant
S	cross-sectional area
S_z	particle displacement amplitude
St	Strouhal number
T	temperature
T_p	transmission factor associated with the pressure

T_u	free stream turbulence level
T_ϕ	transmission factor associated with the velocity potential
\mathbf{U}	three-dimensional flow velocity vector
U	flow velocity in x-direction
U_c	vortex convection velocity
\mathbf{V}	three-dimensional surface velocity vector
W_c	cavity width
X	complex-valued spectrum
$\mathcal{F}\{.\}$	Fourier-Transformation
\mathcal{G}	scan plane
\mathcal{M}_n^x	n-th order moment spectrum
\mathcal{N}	order of power series
\mathcal{P}	point spread function
S	surface function
\mathcal{T}	phase function
\mathbb{T}	Lighthill stress tensor
a	block number index
a_{max}	maximum number of blocks
\mathbf{b}	measured signal vector
c	speed of sound
c_p	pressure coefficient
\mathbf{d}	distance vector
f	frequency
f_c	cut-off frequency
f_s	sampling frequency
f_u	anti-aliasing filter cut-off frequency
i	complex argument
\mathbf{k}	wavenumber vector
k	index
k_x	wavenumber component in x -direction
k_y	wavenumber component in y -direction
k_z	wavenumber component in z -direction
l	length
l_w	length of the wing
\mathbf{n}	normal vector
n_x	normal vector component in x -direction
n_y	normal vector component in y -direction
n_z	normal vector component in z -direction
m	index of microphone number
m_r	Rossiter mode number
p	pressure
p_{ref}	reference pressure
q	source strength
\mathbf{r}	distance vector

r	distance between source and observer
\mathbf{s}	steering vector
s_m	steering function of the m-th microphone
s_z	particle displacement in z-direction
t	time
v_z	acoustic velocity in z-direction
\mathbf{x}	position vector
\mathbf{x}_f	focussed source position vector
x	coordinate
y	coordinate
z	coordinate
Γ	microphone signal coherence
α	angle-of-attack
β	Doppler factor
γ	empirical constant accounting for time lag
δ	delta function
δ_b	boundary layer thickness
δ_s	shear layer thickness
η_x	mode number in x-direction
η_y	mode number in y-direction
η_z	mode number in z-direction
θ	geometrical angle between source and observer
ϑ	observation angle
κ	heat capacity ratio
λ	wavelength
μ	dynamic viscosity
ν	kinematic viscosity
ρ	density
σ	beamformer output in time domain
σ_χ^2	noise variance
ς	beamformer output in frequency domain
τ	time (integration variable)
ϕ	velocity potential
χ	noise signal
ω	angular frequency
ω_{tone}	angular frequency of the test tone
∇	Nabla operator
\cdot	scalar product

Subscripts

cs	closed test section
------	---------------------

<i>di</i>	dipole
<i>exp</i>	experimental
<i>i</i>	index
<i>j</i>	index
<i>l</i>	index
<i>m</i>	index
<i>mono</i>	monopole
<i>n</i>	index
<i>os</i>	open test section
<i>rms</i>	root mean square value
<i>s</i>	shear layer
<i>sim</i>	simulated
<i>o</i>	source
\int	integrated
1/3	1/3 octave band
∞	reference value

Superscripts

*	complex conjugate
'	transmitted wave
"	reflected wave
~	Doppler transformed variables
^	dimensionless variable
\mathcal{H}	Hermite form
T	transposed vector
I	domain with flow
II	domain without flow

Abbreviations

CPV	Coherent Particle Velocity method
DLR	German Aerospace Center
DNW	German-Dutch Wind Tunnels
DR	diagonal removal
DSB	Delay-and-Sum Beamformer
LLF	Large Low-Speed Facility
MEMS	Microelectromechanical System
SNR	signal-to-noise ratio
cs	closed test section
os	open test section

Chapter 1

Introduction

The phased microphone array has become a widely used tool in aeroacoustic testing for the localization and quantification of sound sources. In aviation, this measurement technique is often employed on models of aircrafts and aircraft components in various wind tunnels having open or closed test sections. In spite of the widely-used application of microphone arrays there is still the need of examining the test-section dependent influences and uncertainties on the aeroacoustic results arising from the differing properties of open and closed wind tunnels. The present thesis focuses on the comparability and the performance of microphone array measurements conducted in open and closed test wind tunnels and performs a systematic comparison.

In the following, this chapter provides the introduction into the topic underlying this thesis. In the context of this framework, the motivation and the classification of the problem into the concept of providing input data for new aircraft design and its components (1.1) is outlined. After that, a review is given concerning the few relevant published studies addressing this question of comparability (section 1.3). At the end of this chapter, the objective and the outline of this thesis are presented (section 1.4).

1.1 Motivation and classification of the problem of comparability

Increased restrictions worldwide on community noise and the need to reduce interior noise have led to increased interest in predicting and localizing sound sources and in quantifying their levels with existing aircraft, with the ultimate goal with future aircraft of addressing the question of noise at each design stage as early as possible. Nowadays, for this purpose, a wide variety of information coming from various methods finds use in order to assess the noise characteristics as depicted in figure 1.1. Amongst others, measurement campaigns performing flight or flyover testing on the actual aircraft under free-flight conditions provide valuable information not only for the design of

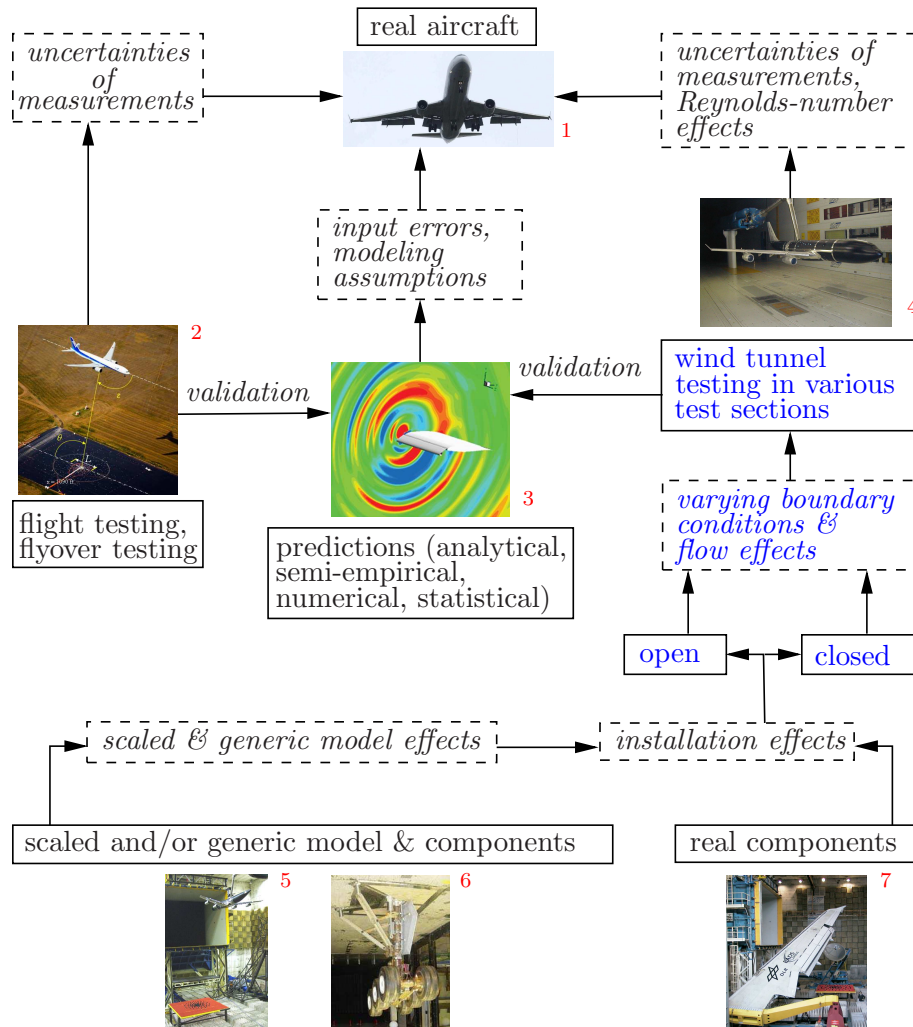


Figure 1.1: Overview showing the various sources providing input data for designing new aircraft and general improvements of the aeroacoustic performance. Uncertainties and effects influencing the selected method or the testing are framed by the boxes with dashed lines. The red numbers are footnote links to the bibliographical references.

¹Siller et al. (2006)
²Brusniak (2008)
³Dobrzynski (2010)
⁴Oerlemans and Sijstma (2004)
⁵Oerlemans et al. (2007)
⁶Ravetta et al. (2004)
⁷Dobrzynski (2010)

1.1. MOTIVATION AND CLASSIFICATION OF THE PROBLEM OF COMPARABILITY

new aircraft but also for improvements of existing ones. Nonetheless, such tests are very expensive, not all measurement techniques can be applied and the possibility of modifications to existing aircrafts is limited. There is also the fact that the uncertainties regarding the employed measurement techniques and the actual measurement conditions can influence the results. Therefore one makes use of other methods which are capable of providing beneficial and important information for the design of new aircrafts.

Simulations constitute the second important column which comprises analytical, semi-empirical, numerical and statistical predictions. Results derived from simulations are typically sensitive to input errors and modeling assumptions, making validation with experimental data essential.

The last and widely used source of information is wind tunnel tests in open or closed test sections. Both test section types have different aerodynamic and aeroacoustic properties which will influence the extrapolation of the measured data to the real aircraft under free-flight conditions. The selection of the test section type depends on the investigated problem. Two groups of configuration are usually examined: on the one hand, real components (on 1:1 scale), while on the other hand, scaled and/or generic models or components. In both cases the measurement results are influenced by effects arising from the way the model is installed in the test section. In addition to these installation effects, one has to expect influences arising from the use of scaled and generic models or components. In fact, scaling-induced influences often arise from non-accurately scaled models or components due to limitations in the manufacturing process or to difficulties in model handling and placement. Common examples are the thickness of trailing edges of airfoils and high-lift devices and the design of model tracks ([Dobrzynski \(2010\)](#)). As a consequence of the simplification, generic models and components can sometimes not properly simulate the physical mechanisms lying behind the aeroacoustic sound generation processes; this can be due to the poor design, and would subsequently lead to false results. Apart from the model and installation issues the varying boundary conditions and flow effects in the test section influence differently the measurement results in open and closed test sections. Independent of the type of wind tunnel used, uncertainties in the measurement Reynolds-number will further influence the results of the performed experiments in wind tunnels ([Ahlefeldt et al. \(2010\)](#)). In the majority of the conducted wind tunnel experiments, most tests on aircraft are conducted at too low Reynolds-numbers, as compared with the corresponding free-flight conditions, due to the lack of sufficiently large test facilities, especially when measuring the noise characteristics using phased microphone arrays. Finally, all uncertainties and influences are most likely additive, depending on what kind of prediction models or testing are used and which path in figure 1.1 is taken.

As mentioned at the beginning of this chapter, this thesis focuses on the comparability and the performance of microphone array measurements

conducted in open and closed test section wind tunnels, as shown in blue text in the overview in figure 1.1. The current work deals with the extent to which the comparability is given or not, based on the specific boundary conditions of open and closed test sections and their individual flow effects. In this context, the issue of installation and model effects are not disregarded. Accordingly, the underlying topic of this thesis contributes to the greater group of themes concerning the important question about the comparability and transferability of aeroacoustic results derived from wind tunnel measurements to the free-flight of a real aircraft.

1.2 Aerodynamic and aeroacoustic properties of closed and open wind tunnels

The following sections describe existing aerodynamic and acoustic features of open and closed wind tunnels. In this context, all important facts with respect to the comparability of microphone array results will be considered in the form of a brief overview, followed by an in-depth description of these phenomena. All following considerations assume low speed wind tunnel testing with Mach number $M < 0.3$, hence indicating incompressible flow. The finite size and the wind tunnel boundaries are the main factor influencing the aerodynamic and aeroacoustic properties in the test section, and lead to differences to free-flight conditions in unbounded flow.

1.2.1 Aerodynamic properties

The subsequent section outlines the aerodynamic properties of closed and open wind tunnels as specified by Barlow et al. (1999). The explanations are focussed on two-dimensional cases, since throughout this thesis the main focus is on the application of two-dimensional models in the wind tunnel experiments (see chapter 3).

Closed wind tunnel The flow in wind tunnels with closed test sections is typically bounded by hard walls, as depicted in figure 1.2. A boundary layer develops along the wind tunnel surface with increasing thickness in stream wise direction. The flow outside of the boundary layers and the model wake can be practically considered as potential flow. For wind tunnels with non-varying cross-section of the test section the thickening of the boundary layer as it progresses toward the diffuser results in a static pressure gradient along the axis of the test section when no model is present due to the resultant effective cross-section diminution of the jet area. This static pressure variation produces a force oriented in drag direction (i.e. downstream) and is denoted by *horizontal buoyancy*. An installed model in the closed wind tunnel reduces the effective cross-sectional area for the flow, which leads to an

1.2. AERODYNAMIC AND AEROACOUSTIC PROPERTIES OF CLOSED AND OPEN WIND TUNNELS

additional contraction of the streamlines. The so-called *solid blockage* produces an effective change in oncoming flow speed and subsequently raises the dynamic pressure resulting in an increase of the forces and moments for a given angle-of-attack. Somewhat similar to the *solid blockage* is the *wake blockage*. This refers to the additional contraction of the streamlines as a consequence of the finite size of the model wake which increases the measured drag. Furthermore, in a closed test section the *streamline curvature* of the flow is altered as compared to the corresponding curvature in an infinite (unbounded) stream. For a wing it results in an increased moment coefficient, a lift increase and an increased angle-of-attack. In general, the *horizontal buoyancy* is normally very small and insignificant in closed wind tunnels as compared with *solid* and *wake blockage* and the *streamline curvature*. For the sake of completeness, the so-called *downwash* is a fundamental three-dimensional effect and refers to the induced downward component of the flow velocity. At a given geometric angle-of-attack the *downwash* is too small in the closed test section compared with the test object being under free-flight conditions.

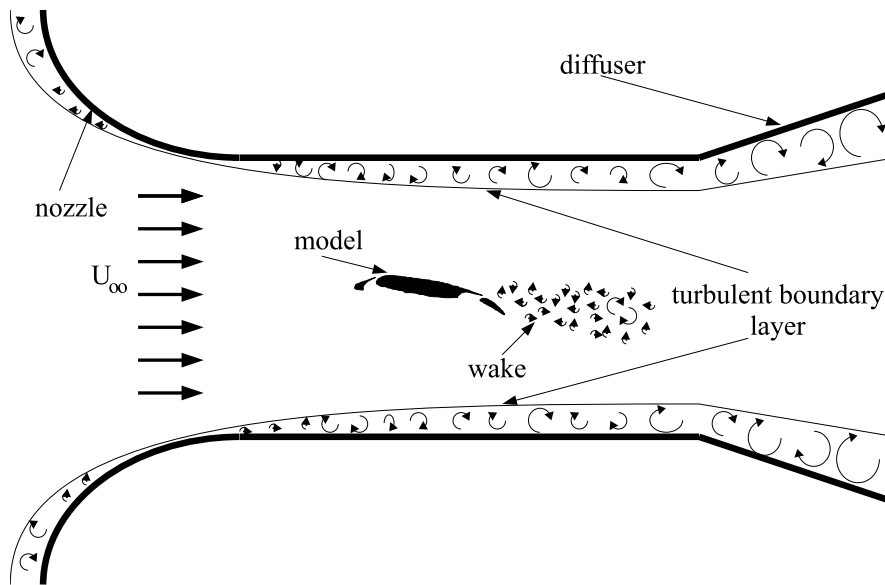


Figure 1.2: Schematic setup of the aerodynamic testing in the closed test section of a wind tunnel.

Open wind tunnels The open jet wind tunnel is characterized by an unbounded test section as shown in figure 1.3. At the boundary of the test section there is a shear layer instead of a wall boundary layer as in the closed test section case. This generally results in a higher level of unsteadiness of

the flow. The *horizontal buoyancy* is normally considered as negligible in this kind of wind tunnels. In an open wind tunnel, the jet is usually free to expand and subsequently, the *solid* and *wake blockage* are smaller than in the closed wind tunnel, but nevertheless still not zero. The *streamline curvature* of the flow differs again from that for free-flight condition so that the moment coefficient, lift and angle-of-attack are decreased. The three-dimensional *downwash* effect is too large at a given geometric angle-of-attack in the open test section compared with the corresponding free-flight conditions.

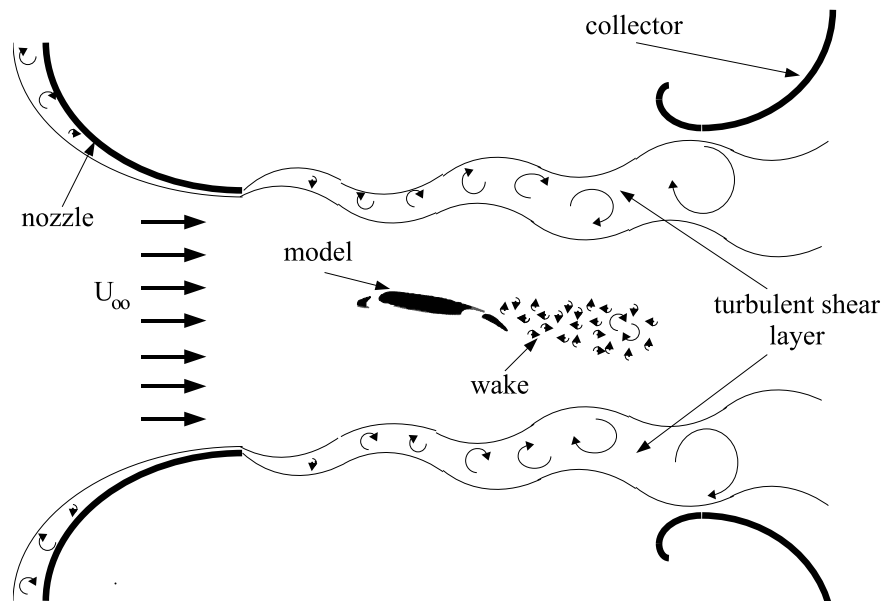


Figure 1.3: Schematic setup of the aerodynamic testing in the open test section of a wind tunnel.

Finally, these different aerodynamic wind tunnel properties can be summarized as follows: by performing aerodynamic measurements with the same flow velocity in a closed and open wind tunnel using the same model with an identical geometrical angle-of-attack there will be differences in the static pressure gradient along the model and variations in the velocity distribution.

1.2.2 Acoustic properties

The following consideration comprises the acoustic properties of open and closed wind tunnel test sections which will be briefly outlined here. A more detailed explanation of the acoustic properties and their influence on aeroacoustic testing is given in chapter 2.

1.2. AERODYNAMIC AND AEROACOUSTIC PROPERTIES OF CLOSED AND OPEN WIND TUNNELS

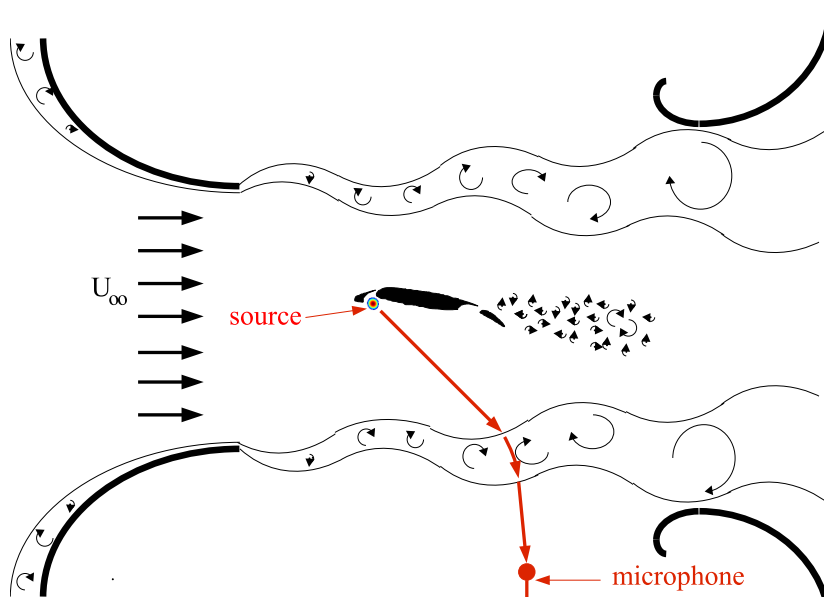


Figure 1.4: Schematic setup of aeroacoustic testing in the open test section of a wind tunnel.

Open wind tunnels Aeroacoustic testing in open jet wind tunnels is depicted schematically in figure 1.4. Typically, the model is positioned inside the potential core of the jet, while the microphone locations are outside this core flow. Hence, the sound waves emitted from aeroacoustic sources in the vicinity of the model have to pass through the potential flow in the jet core and the turbulent wind tunnel shear layer before reaching the microphone. This sound propagation through the flow is accompanied by several effects which may influence the accuracy of aeroacoustic measurements and make it more difficult to interpret these results correctly: *convection*, *refraction*, *transmission*, *scattering*, *absorption* and *spectral broadening* of the incident sound waves. The source, located in the potential core of the jet, emits a sound wave and the convection of the wave takes place through the parallel flow until the turbulent shear layer is reached. While propagating through the shear layer the incoming sound waves are refracted as a result of the mean velocity gradient. The propagation direction and the travel path of the wave from the source to the receiver are changed when compared with the case without flow. In addition, only a part of the incident acoustic wave energy is transmitted to the microphone while the rest is reflected, which is also a consequence of the mean velocity gradient across the shear layer. In the limiting case the transmission coefficient takes a value of zero being equivalent to total reflection, so that in this case no incident acoustic energy is transmitted through the shear layer to the observer located outside and

thus sound waves are trapped inside the jet. The constitution of such a so-called "zone of silence" depends on the flow Mach number and the angle of incidence of the sound wave on the shear layer, as reported, for example, by Ribner (1956) and Amiet (1975). Due to the reflection of the incident sound at the shear layer the sound waves can reach the observer via different multiple paths, so that when a reflected wave is finally transmitted through the shear layer, an ambiguity of the measured sound regarding its source can occur.

The interaction of sound with turbulence is related to the phenomenon of scattering and spectral broadening (also termed as haystacking in literature (McAlpine et al. (2009))). Scattering at turbulent eddies in the shear layer leads to redistribution of the energy of the incoming wave in other directions than that of the incident wave, so that an initially coherent signal becomes distorted. In addition, a redistribution of acoustic energy in other frequency bands, different from the original, takes place. Apart from the scattering and spectral broadening effects caused by the interaction of sound with turbulence, the absorption of sound by turbulent structures in the shear layer reduces the measured amplitude outside the flow. Furthermore, superimposed on the source signal is noise from the wind tunnel and from aerodynamic sound generated by the shear layer and other installations and mountings within the flow. All these disturbances would lead to a performance loss of the acoustic measurement if they are not taken into account by applying appropriate corrections which influence proper quantitative and spatial measurement of the sound source characteristics in aeroacoustic experiments.

Closed wind tunnel By performing aeroacoustic measurements in closed test sections the model is normally placed in the center of the test section - outside the wind tunnel wall boundary layers - and the microphones are typically mounted in the wind tunnel wall (flush or recessed) or an in-flow microphone with nose cone finds use as shown in Figure 1.5. Hence, the sound waves emitted from aeroacoustic sources on the model are convected along the potential flow and have to pass through the typically turbulent boundary layer before reaching the microphones. In general, the sound propagation through the boundary layer has no significant effect on the measured signal in terms of transmission, reflection, refraction, scattering and absorption as long the boundary layer thickness is not too large compared with the wavelength of the examined acoustic signal. Since they are flush mounted, the microphones in both installation cases are subjected to strong hydrodynamic pressure fluctuations induced by the turbulent boundary layer. This so-called *pseudo sound* is associated with the convection of turbulent eddy structures in the boundary layer. These pressure fluctuations do not satisfy the wave equation and do not propagate with the speed of sound. The

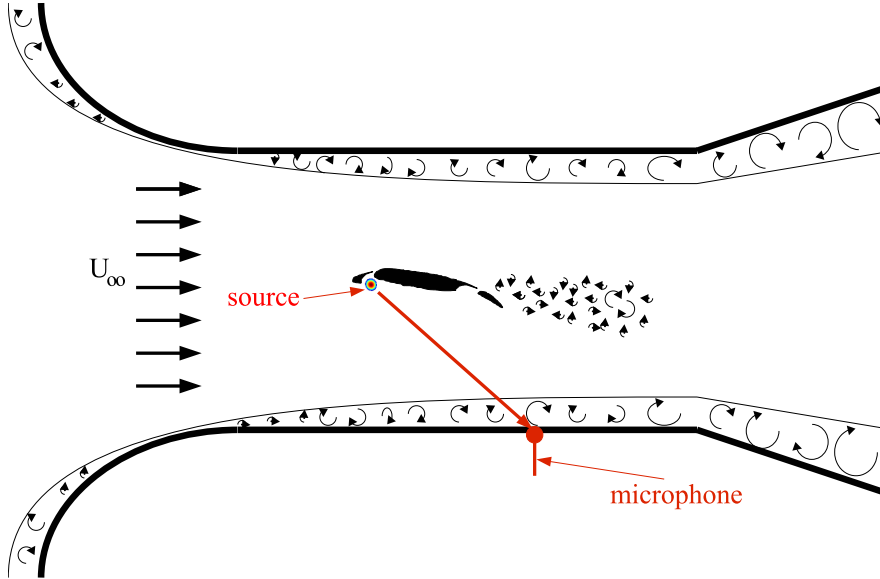


Figure 1.5: Schematic setup of the aeroacoustic testing in the closed test section of a wind tunnel.

presence of *pseudo sound* can result in a dramatic decrease of the signal-to-noise ratio (SNR) of the measured microphone signal, since for a single microphone it is impossible to distinguish between sound and *pseudo sound*. A further decrease of the SNR, especially in the low frequency range, is caused by the wind tunnel background noise generated from, for example, the fan, turning vanes and channel modes. The reverberant walls of the closed test section are also of concern, since they cause reflections and the measured signal accuracy may be affected by interferences and multipath arrivals. In contrast to the open test section, far-field measurements cannot be performed in this type of test section.

1.3 Literature review

Due to the different aerodynamic and aeroacoustic characteristics of the two test section types as described above, there is still some uncertainty as to how far it is possible to compare results from aeroacoustic measurements, particularly with regard to beamforming results, obtained from different wind tunnels with different test sections. Up until now there are only a few studies concerning different aerodynamic problems addressing this question in particular. The following considerations focus on the literature review of these few publications.

1.3.1 Comparison of trailing edge noise

One topic of great interest for the present thesis is the study performed by [Herrig et al. \(2005\)](#), who conducted a study examining trailing edge noise. They carried out aerodynamic and aeroacoustic measurements of two-dimensional airfoils for wind turbines in open and closed wind tunnels and performed a comparison. In the closed test section the aerodynamic performance of the airfoil was assessed by measuring the pressure distribution. The resulting lift was estimated by integration of the measured surface pressures. Subsequently, the aerodynamic results were corrected accounting for solid blockage and streamline curvature so that the results correspond to infinite flow conditions. Due to the strong wind tunnel background noise and the low source strength trailing edge noise measurements were not possible using microphone arrays in the closed test section. Therefore, they employed the Coherent Particle Velocity method (CPV) using two hotwire probes placed on both sides of the airfoil in order to assess the trailing edge noise source. In the open wind tunnel a balance provided the lift generated by the same airfoil used in the closed wind tunnel. This time the trailing edge source localization and quantification was performed via beamforming using a microphone array and they did not apply CPV.

Of particular significance in this study was the choice of the corresponding cases in both test sections for conducting the comparison. In order to perform a comparison between two wind tunnels, the pressure distributions should match as closely as possible, because the aerodynamic and subsequently the aeroacoustic characteristics can be strongly influenced by small changes in the flow field. The evaluation of the aerodynamic measurements revealed that a higher angle-of-attack is necessary in the open wind tunnel in order to achieve the same lift coefficient compared with the closed test section; this is caused by the different wind tunnel boundary conditions, as discussed before. However, based on the aerodynamic results from the measurements and additional simulations it became apparent that an identical pressure distribution could not be achieved employing the same airfoil contour in both wind tunnels. Furthermore, the transition location was determined and shown, for an equal lift coefficient, to lie further upstream in the open than in the closed facility. Finally, when comparing the acoustic results from both wind tunnels they used the cases where the lift coefficient was 17% lower in the open wind tunnel than in the closed wind tunnel. The gradient of the pressure distributions was then nearly the same and the transition locations were also similar in both facilities, which led to boundary layer states at the trailing edge which resemble each other reasonably well.

As a consequence of the different measurement methods only trailing edge noise spectra could be compared in the two wind tunnels, since no information about the source location and distribution are provided by CPV.

Nonetheless, in order to convert the particle velocity information of the sound waves from CPV into pressure fluctuations several source assumptions have to be made. They modeled the trailing edge noise source by incoherent monopole sources in order to perform the conversion into sound pressure. This model would most likely introduce uncertainties regarding the obtained sound pressure levels due to the anisotropic directivity of the trailing edge noise sources. Further corrections were required because of the slightly varying flow velocities (60 m/s and 58 m/s in the closed and open wind tunnels, respectively) during the different test campaigns. Due to the low SNR of the CPV measurements in the closed wind tunnel it was possible to measure the sound associated with the trailing edge in the range from 0.6 to 3 kHz. In the open test section the SNR from the microphone measurements is much higher, leading to reasonable results in the wider range of 0.5 to 5 kHz. For the 1/3 octave bands in the range between 1 and 2 kHz the spectra collapse quite well, but outside of this domain larger deviations occur. Finally, it is not clear whether these deviations are a result of the different applied measurement techniques or whether they arise from the varying acoustic properties of both test sections or whether there are still differences in the aeroacoustic sound generation due to differences in the two flow fields.

1.3.2 Comparison of noise from a high-lift system

The objective of the study from [Oerlemans et al. \(2007\)](#) was to assess the reliability of absolute and relative array level measurements for open and closed wind tunnel test sections using test results from different measurement campaigns ([Oerlemans and Sijstma \(2004\)](#)). They performed phased microphone array measurements in the DNW-LLF open and closed wind tunnel test sections on wing noise generated from a 1:10.6 scaled Airbus A340 model. The first wind tunnel test was conducted in the DNW-LLF open test section to optimize and validate several noise reduction concepts employing far-field microphones and an out-of-flow microphone array. A second test campaign was performed in the DNW-LLF closed test section with the aim of assessing the aerodynamic properties of the most promising sound reduction devices. In addition, microphone array measurements were also carried out in order to examine the acoustic performance of these noise reduction devices. As a side effect, the measurement results of both test campaigns could then be used by [Oerlemans et al. \(2007\)](#) for performing a comparison between microphone array results obtained from open and closed test section measurements using the same model configuration in both cases. The only model difference between the two test campaigns was the different tripping used on the slats, but it was found that there was no influence on the aerodynamic performance of the wing or the broadband wing noise levels. The model was tested in take-off, landing, and approach configurations,

and, as a background noise reference, also in the clean ("cruise") configuration. Measurements were performed at various wind speeds and various angles-of-attack. As discussed before, the geometrical angle-of-attack had to be lower in the closed than in the open test section in order to compensate for the open jet effect and to obtain the same total lift (measured by a balance).

The acoustic measurements were conducted using a 4 m diameter out-of-flow microphone array in the open test section and a 1 m diameter wall array in the closed test section. The out-of-flow array consisted of 140 microphones mounted in an acoustically open metal grid, while in the closed test section the array consisted of 128 microphones flush-mounted in a rigid plate. Not only were the two arrays different, but also the array-model arrangement differed. In the open and closed test section the distance between model and array was 7.6 m and 3 m, respectively. Due to the different array diameters and distances, the (maximum) opening angle was 29° for the out-of-flow array and 19° for the closed test section array resulting in different array resolutions and point spread functions. Moreover, the microphones of the out-of-flow array were simultaneously used as far-field microphones enabling comparisons with the spectra derived from the integration of the source maps. The authors compared the noise data obtained from both types of wind tunnels for the cases of equal lift of the model.

In the closed test section the main diagonal elements of the cross-spectral matrix were contaminated by the turbulent boundary layer fluctuations of the tunnel wall and in the open test section the SNR was reduced by the sound transmission through the turbulent shear layer. Both effects lead to source maps with a high noise floor. Therefore, in both test sections diagonal removal (see e.g. chapter 2.2.3) was applied and it drastically improved the SNR and thus, the quality of the source maps and the possibility to identify sources. The comparison between the closed and open test section source maps revealed basically a consistent source distribution although the array resolutions were different. In terms of source resolution the open jet array performs better than the closed section array at low frequencies, but worse at high frequencies. Test-section specific blurring effects occurred due to background noise in the closed and coherence loss caused by the turbulent shear layer in the open test section. However, in some source maps there are sources present in one test section which do not appear in the other. It was assumed that this is an indication that the local flow conditions differed in both test sections, even though the produced lift was identical. As well as the source maps, integrated spectra were also obtained in order to compare absolute levels. When diagonal removal (see chapter 2.2.3) is applied, the integrated levels in the open test section are close to the far-field microphone levels at low frequencies, but significantly lower for increasing frequency (partially more than 10 dB) which is a result of the coherence loss due to the turbulent shear layer. The spectrum for the closed test section is

relatively close to the far-field microphone levels over the whole frequency range leading to deviations smaller than 3 dB. [Oerlemans et al. \(2007\)](#) again hazarded a guess that the deviations between the integrated levels in the closed test section and the open jet far-field microphones could be due to a difference in the flow parameters. Reflections in the reverberant closed test section were not specifically quoted as possible reasons for the observed deviations. Besides the absolute levels relative spectra were also examined using the averaged auto-powers of the far-field microphones of the open test section as a reference. The relative array levels in the closed test section agree with the open jet to within 1 dB, provided that the flow conditions - and therefore the noise source characteristics - are similar; however, no examination of the flow fields of both test sections was presented by the authors.

1.3.3 Comparison of noise from landing gear

Another interesting study addresses the noise from landing gears. [Li et al. \(2011\)](#) have investigated noise generated by aircraft landing gear employing a 1/4 scale A340 main landing gear model that has been tested using a range of different measurement methods and test facilities. Experiments were first conducted in a conventional closed-section wind tunnel (at the University of Southampton) using two phased microphone arrays mounted on the ceiling and sidewall of the tunnel, in order to assess and evaluate the noise-reduction potential of modified fairings. Noise tests were then performed in an open-jet aeroacoustic facility (Noise Test Facility (NTF) at QuinetiQ) using only far-field microphones to verify the wind-tunnel test results. The aeroacoustic facility test results were finally projected to full scale and compared with the full-scale model tests in the open test section of the DNW-LLF ([Dobrzynski and Buchholz \(1997\)](#)). The conducted comparison was based on integrated spectra derived from the source maps computed via beamforming and far-field microphone spectra whereas only relative spectra of the modified fairings were compared using the non-modified landing gear configuration as reference. Besides the differing measurement techniques used, there were also differences in the experimental setup between the individual test campaigns in the various wind tunnels. In the closed test section the scaled model tests were performed at the wind speed of 40 m/s, which is about half of the actual aircraft approaching speed. In contrast to that, in the open jet facility (NTF) the measurements of the landing gear noise were made at 78 m/s which is approximately the aircraft landing speed. In addition, the full scale landing gear tests in the DNW-LLF were performed at flow velocities at 62 and 75 m/s. In order to enable a comparison between these different measurements the results were scaled to the same Strouhal number.

Although a comparison of the relative landing gear spectra between the

closed test section (integrated source maps) and the open jet facility (far-field microphone data) shows mainly similar trends, one nevertheless still observes deviations of up to 3 dB. The interpretation of this difference was that the installed modified fairings increase the flow blockage of the gear in the closed wind tunnel (the wind tunnel blockage was originally 10 %), leading to an increased flow speed around the large components and thus strengthening the sources.

Projecting the NTF far-field data to full scale using Strouhal number scaling and comparing with far-field data measured in the DNW on a real landing gear showed quite good agreement in both the absolute levels and the shape of the noise spectrum, although the absence of some small geometrical details in the model-scale tests affected agreement at high frequencies. The variations are typically less than 3 dB. At high frequencies the NTF model generated less noise, which may be an indication of a slightly simplified geometry (e.g. lack of brake dressings).

1.3.4 Brief summary of the studies

Based on the studies outlined briefly above, it becomes apparent that the deviations between aeroacoustic measurements in different wind tunnel types can have various reasons which can be classified into three different main groups. The first group is associated with the employed models which were the source of aeroacoustic sound generation:

1. All examined models were highly complex with respect to the flow field around the models and the generated aeroacoustic sound field so that detailed noise characteristics are unknown a priori.
2. The results presented in these publications further reveal that it is difficult, and sometimes impossible, to maintain the same flow conditions in the two types of test sections, which in turn could lead to these deviations in the aeroacoustic measurements.
3. In some experiments the employed models possess geometrical differences. On the one hand the scaling was different which resulted in different Reynolds and Helmholtz numbers when performing a comparison of the measurement results. On the other hand the absence of some geometrical details between the used models might lead to changes in the aeroacoustic sound generation and subsequently might result in deviations between the different measurement campaigns.

A second type of effects being responsible for possible deviations is linked to the experimental setup and test parameters:

4. At least partly, different measurement techniques were used, introducing uncertainties when comparing these results.

5. Furthermore, different geometrical arrangements and test parameter settings were employed. On the one hand the different arrangements in conjunction with the aeroacoustic sources directivity can result in deviations between the test results. On the other hand, for example, the tests were performed employing different flow velocities, which leads to differences in the Reynolds and Mach numbers and will affect the aeroacoustic sound generation. These differences require assumptions about the sources in order to convert the measured data enabling a comparison and thus constitute a source for possible deviations.

The third group comprises effects which arise from the different test section-dependent boundary conditions and subsequently affect the sound propagation and the resulting sound field:

6. In the open test section the shear layer will influence the sound propagation.
7. In the closed test section the acoustic measurements will be affected by the wall boundary layer and the reverberant walls of the test section.
8. The wind tunnel background noise will be vary in different test sections and will influence the measurement results in a variety of ways.

Due to the chosen models, test setups and parameters in the experiments from [Herrig et al. \(2005\)](#), [Oerlemans et al. \(2007\)](#) and [Li et al. \(2011\)](#), it was not clearly possible to distinguish between these three groups of possible sources of deviation, much less to quantify their contributions.

1.4 Objective and outline of this thesis

In the present thesis a systematic comparison is presented between microphone array measurements in a closed and an open test section. This means that the conducted experiments were specifically designed in order to carry out the intended comparison. Being mindful of the issues arising from the publications in the literature review, these possible sources of deviation are to be kept in mind in this thesis in formulating the method for the experimental comparison. The aim is to keep the experimental setup and test conditions as identical as possible in both cases and select appropriate models in order to avoid or at least to reduce the influences of the points 1. to 5. enumerated above. This will enable an examination of the test section-dependent effects (see the above enumerated items 6. to 8.) and to distinguish between them. The study focuses on the beamforming accuracy and reliability in both wind tunnel types with respect to source position, relative and absolute levels of beamforming results, signal-to-noise ratio (SNR) and integrated spectra using three different wind tunnel models which permit

a discrimination between the individual effects. A further aim is to illustrate ways and provide decision guidance with respect to the feasibility of aeroacoustic measurements and the selection of the appropriate wind tunnel test section for the examination of aeroacoustic problems by means of the microphone array technique.

Chapter 2 addresses a wide variety of aspects associated with the localization and quantification of sound sources with phased microphone arrays. As an introduction, a brief historical review on aeroacoustic source localization is given. This follows an extensive discussion of the Delay-and-Sum Beamformer and its properties. In preparation for the comparison of beamforming results obtained in open and closed wind tunnels, the influence of flow, test section properties and aeroacoustic source characteristics on the beamforming process is examined in detail and - provided that appropriate correction procedures are available - these correction procedures are presented. Within the framework of the comparison, the required model characteristics and the three different employed models themselves are given in chapter 3. After a presentation of the experimental setup, which include the wind tunnels, instruments, methods and the conducted test program (chapter 4), the experimental results derived in both wind tunnels of the first model are presented and discussed in chapter 5. In the two subsequent chapters 6 and 7 the experimental results obtained from the other two models are presented and evaluated in detail. The comparison of the obtained experimental results from all three models is presented in chapter 8. Finally, the performed work is summarized in chapter 9 which also includes the comparison between the experimental results from all three models and the observations made from other relevant publications. In addition, open issues and possible future directions and developments are also proposed and discussed.

Chapter 2

Localization and quantification of sound sources with phased microphone arrays

This chapter addresses a wide variety of aspects associated with the localization and quantification of sound sources with phased microphone arrays. As introduction, a brief historical review about aeroacoustic source localization is given. Subsequently, an extensive discussion of the Delay-and-Sum Beamformer and its properties is given (section 2.2). In preparation for the comparison of beamforming results obtained in open and closed wind tunnel test sections the influence of flow, test section properties and aeroacoustic source characteristics on the beamforming process is examined in detail (section 2.3 and 2.4).

2.1 A brief historical overview

Since decades, phase arrays have been used for the localization of sources, what kind so ever, in the fields of astronomy, sonar, radar and seismology. In the field of aeroacoustic testing the developing and application started in the 1970's. Grosche (1973) examined aeroacoustic sound sources of subsonic and supersonic jets by using an acoustic mirror. Figure 2.1 illustrates the principle of the acoustic mirror. The concave mirror shown on the left side is a part of the ellipsoid of revolution indicated by the dashed line. It has two focal points which are marked by small circles. A microphone is positioned in that focal point close to the mirror. Sound waves emanating from a source in the other focal point are focused upon the microphone by reflection at the elliptical mirror surface. The sound waves travel from the

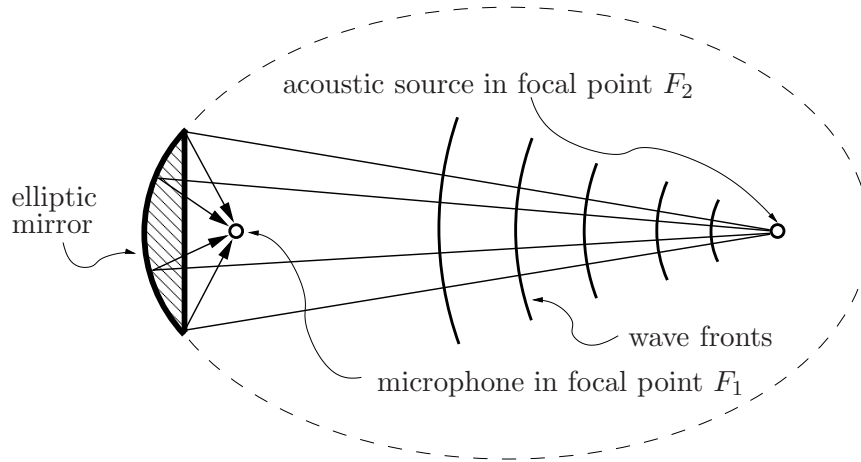


Figure 2.1: Schematic sketch of an elliptic mirror microphone.

source along different paths to the mirror surface, are then reflected and reach in phase the mirror microphone due to the same travel path length of the sound waves. Consequently, the mirror acts as amplifier for the mirror microphone for sound generated at the focal point F_2 as compared to its free field value. Sound waves radiated from other locations are concentrated by the mirror upon other image points. The main disadvantage of the elliptic mirror is that it needs to be traversed or rotated for examining arbitrary source location what could be a very time consuming process. In contrast to that, the phased microphone array technique requires only short time measurements, since the focusing on many different potential source positions is performed by the signal processing algorithms. One of the first application of a phased microphone array for mapping of aeroacoustic jet noise sources was conducted by [Billingsley and Kinns \(1976\)](#) using a line array with 14 microphones. In the later course of the 70's and 80's microphone arrays were employed for detecting noises in various fields, for example at high-speed trains ([King III and Bechert \(1979\)](#); [Barsikow et al. \(1987\)](#)). Since the 90's, in consequence of the fast development of powerful computers and continuously improving data acquisition, microphone arrays are increasingly used and well established in aeroacoustic testing. The applications comprise model-scale and full-model investigations in wind tunnels ([Underbrink and Dougherty \(1996\)](#); [Piet and Elias \(1997\)](#); [Sijstma and Holthusen \(1999\)](#); [Dobrzynski et al. \(2001\)](#)) and flyover measurement ([Michel et al. \(1998\)](#)), for instance. In scale-model testing the frequency range of interest is much higher compared to full-scale object resulting in frequencies of interest up to 100 kHz and more ([Mosher \(1996\)](#)).

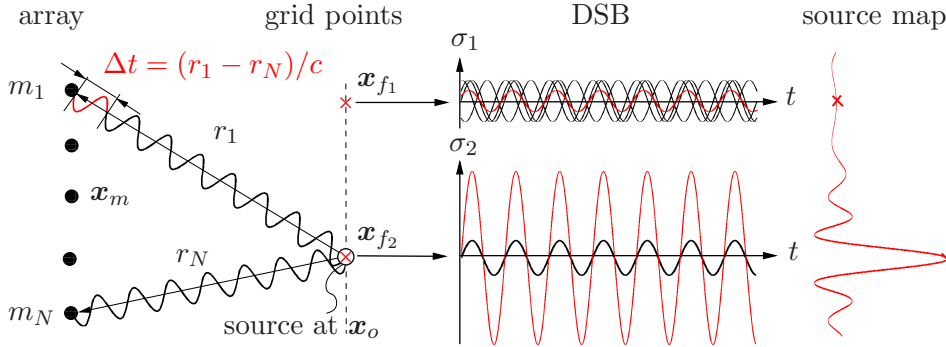


Figure 2.2: Illustration of the Delay-and-Sum Beamformer (extended illustration based on a sketch from [Oerlemans \(2009\)](#)).

2.2 The Delay-and-Sum Beamformer

The Delay-and-Sum Beamformer (DSB) is a classical and robust beamforming algorithm for the localization of signal sources as described among others by [Johnson and Dudgeon \(1993\)](#). In the following the explanation of the DSB is given for an array consisting of N microphones. Figure 2.2 depicts schematically the source-receiver situation. The monopole sound source is located at \mathbf{x}_o in a homogeneous stagnant medium and the sound wave travels directly with the sound speed c to the microphones m_1 to m_N . Due to the different distances r_m between source and observers the recorded time signals differ from each other with respect to the signal travel time and the measured amplitudes exhibit variations being proportional to $1/r_m$. The basic idea behind the DSB is to use the different signal travel times for the localization of sound sources. This wave propagation from the source to the two microphones m_1 and m_N is exemplarily illustrated in figure 2.2. The travel distance difference of the wave between both microphones is marked red in the signal sequence and the wave travel time difference is given by Δt . At first, one defines a grid within the area of assumed source locations. For convenience, the defined grid in the illustration comprises only the two grid points \mathbf{x}_{f_1} and \mathbf{x}_{f_2} . For each grid point the microphone signals are shifted in time in order to take into account the differing travel times. These time delays of the signals correspond to a virtual shift of the microphone positions along the line between the focused source location and the microphone position so that finally, all microphones lie virtually on the surface of a spherical sector whereas the focused grid point and the sphere center point are identical. Consequently, all delayed microphone signals are in phase. In addition, the signal amplitudes are corrected for a decrease in amplitude which is inversely proportional to the distances between source and receiver and ultimately, a summation of all microphone signals is conducted. In the case that the focused grid point and the real source position comply with

each other the DSB results in a signal amplified by factor N . In relation to the illustration in figure 2.2 this is the case for the focussing on the grid point \mathbf{x}_{f_2} which leads to an amplified DSB-signal σ_2 (marked red) compared with the single microphone signals (marked black). If there is no source at the focused location (see grid point \mathbf{x}_{f_1}), it yields a small amplitude sum, since the microphone signals are out of phase. Briefly summarized, the DSB delays and sums up the microphone signals. Basically, by amplifying the signal of the focus point the DSB and the previously described elliptic mirror technique follow the same fundamental idea. In contrast to the DSB, the elliptic mirror performs the focusing on the potential source location by means of hardware (mirror) and in the case of the DSB by means of the signal processing algorithm (spatial filter).

2.2.1 Mathematical formulation of the Delay-and-Sum Beamformer

Figure 2.2 illustrates schematically the waves emitted from a monopole sound source at location \mathbf{x}_o and the microphones arranged on a line at the positions \mathbf{x}_m . Assuming that the density ρ and the speed of sound c are constant in a medium at rest, the pressure field p of a single monopole sound source with the source strength $q(t)$ can be specified by the classic inhomogeneous wave equation

$$\left(\frac{1}{c^2} \frac{\partial^2}{\partial t^2} - \nabla^2\right) p = q(t) \delta(\mathbf{x} - \mathbf{x}_o) \quad (2.2.1)$$

with its well-known free-field solution (see e.g. Pierce (1981))

$$p(\mathbf{x}_o, \mathbf{x}_m, t) = \frac{1}{4\pi} \frac{q(\mathbf{x}_o, t - \frac{|\mathbf{x}_m - \mathbf{x}_o|}{c})}{|\mathbf{x}_m - \mathbf{x}_o|} \quad (2.2.2)$$

for the pressure field of a monopole where the variable t denotes the time. It is obviously that the received signal observed by the microphones depends on the distance $|\mathbf{x}_m - \mathbf{x}_o|$ between observer and source. The signal travel times

$$t_{m,o} = \frac{|\mathbf{x}_m - \mathbf{x}_o|}{c} \quad (2.2.3)$$

are proportional to the distance between the receiver location and source position. The DSB compensates the travel time differences of the various microphones by focussing on the believed source position \mathbf{x}_f and delays accordingly the travel time

$$t_{m,f} = \frac{|\mathbf{x}_m - \mathbf{x}_f|}{c}. \quad (2.2.4)$$

2.2. THE DELAY-AND-SUM BEAMFORMER

Consequently, one obtains for the beamformer output $\sigma(\mathbf{x}_f, t)$ in the form of the time-delayed and summed up individual microphone signals

$$\sigma(\mathbf{x}_f, t) = \frac{4\pi}{N} \sum_{m=1}^N r_m p(\mathbf{x}_o, \mathbf{x}_m, t + t_{m,f}). \quad (2.2.5)$$

The term $r_m = |\mathbf{x}_m - \mathbf{x}_f|$ ensures the compensation of the spherical amplitude decay and the output is divided by the number of microphones. It is often convenient to perform the calculation of the DSB in the frequency domain. The monopole solution 2.2.2 of the inhomogeneous wave equation can be easily transformed in the frequency domain by means of the Fourier-transformation yielding the complex pressure field

$$P(\mathbf{x}_m, \omega) = \mathcal{F}\{p(\mathbf{x}_m, t)\} = \int_{-\infty}^{\infty} p(\mathbf{x}_m, t) e^{-i\omega t} dt = \frac{Q(\omega) e^{-i\omega t_{m,o}}}{4\pi r_m}, \quad (2.2.6)$$

with ω denoting the annular frequency. Now, the time shift corresponds to a phase shift which is represented by the term $e^{-i\omega t_{m,o}}$. As before, the DSB performs an amplitude and phase compensation carried out in the frequency domain resulting in

$$\varsigma(\mathbf{x}_f, \omega) = \frac{4\pi}{N} \sum_{m=1}^N r_m P(\mathbf{x}_m, \omega) e^{i\omega t_{m,f}} = \frac{1}{N} \sum_{m=1}^N s_m(\mathbf{x}_f, \omega) P(\mathbf{x}_m, \omega). \quad (2.2.7)$$

$s_m(\mathbf{x}_f, \omega)$ is the so-called steering function which is responsible for the focussing on the believed source location and can be formulated as

$$s_m(\mathbf{x}_f, \omega) = 4\pi |\mathbf{x}_m - \mathbf{x}_f| e^{i\omega t_{m,f}}. \quad (2.2.8)$$

The steering functions of all microphones can be summarized in the so-called steering vector

$$\mathbf{s}(\mathbf{x}_f, \omega) = \begin{pmatrix} 4\pi |\mathbf{x}_1 - \mathbf{x}_f| e^{i\omega t_{1,f}} \\ 4\pi |\mathbf{x}_2 - \mathbf{x}_f| e^{i\omega t_{2,f}} \\ \vdots \\ 4\pi |\mathbf{x}_N - \mathbf{x}_f| e^{i\omega t_{N,f}} \end{pmatrix}. \quad (2.2.9)$$

In a uniform manner, the complex microphone signals can also be arranged in a vector

$$\mathbf{b}(\omega) = \begin{pmatrix} P(\mathbf{x}_1, \omega) \\ P(\mathbf{x}_2, \omega) \\ \vdots \\ P(\mathbf{x}_N, \omega) \end{pmatrix}. \quad (2.2.10)$$

This enables the compact formulation of the beamformer output:

$$\varsigma(\mathbf{x}_f, \omega) = \frac{\mathbf{s}^H \mathbf{b}}{N}. \quad (2.2.11)$$

Typically, one is interested in the output power L of the beamformer. This can be easily taken into account by using

$$L = |\varsigma(\mathbf{x}_f, \omega)|^2 = \frac{|\mathbf{s}^H \mathbf{b}|^2}{N^2} = \frac{\mathbf{s}^H \mathbf{b} \mathbf{b}^H \mathbf{s}}{N^2} = \frac{\mathbf{s}^H \mathbf{R} \mathbf{s}}{N^2}, \quad (2.2.12)$$

whereas the cross-spectral matrix

$$\mathbf{R} = \mathbf{b} \mathbf{b}^H \quad (2.2.13)$$

is determined by the outer product of the microphone signal's Fourier transform. The notation $(.)^H$ labels the Hermite form of a vector. Finally, with equation 2.2.12 one has the ability to compute the beamformer output for many possible source positions in order to localize the sources. The DSB has turned out in a multitude of applications as a robust and reliable beamforming algorithm. Besides the DSB many other beamforming algorithms have been developed for various fields of application (e.g. conventional beamformer, Capon beamformer, Yule-Walker beamformer, MUSIC, ESPRIT, etc. (Johnson and Dudgeon (1993), Stoica and Moses (2005))). Due to various reasons, only the DSB and the conventional beamformer (Sijtsma (2004)) are widely used for aeroacoustic measurements. The difference of the conventional beamformer and the DSB consists of a varying steering vector formulation.

2.2.2 Properties of the Delay-and-Sum Beamformer

In the following only these fundamental properties of the DSB will be briefly summarized which are thought to be important within the framework of this thesis. A much more comprehensive insight into the general principles of array signal processing was given among others by Johnson and Dudgeon (1993). In the book of Mueller (2002) the focus was settled on beamforming in aeroacoustics providing an excellent overview about this topic.

A microphone array consists of individual sensors having a certain spatial distribution. These discrete receivers sample spatially the wave field generated by a source. Subsequently, a microphone array can be considered as spatial filter bank. The properties of such a filter are essential for the array performance in terms of the localization and quantification of sources. The so-called *array impulse response* or *point spread function*¹ provides general information about the array performance by calculating the output of the beamformer using a single monopole source as input.

¹The term point spread function has its origin from optics and describes the response of an imaging system to a point source.

The main features of the frequency-dependent point spread function are schematically illustrated in figure 2.3. Due to the finite array size a monopole point source cannot be resolved as point source. Instead, one obtains a broadened peak - the main lobe exhibiting a certain beamwidth. The beamwidth depends primarily on the aperture of the array, the distance between array and source and the sound wave frequency. A sufficiently small beamwidth is required for the resolution capabilities of the array in order to discriminate closely spaced

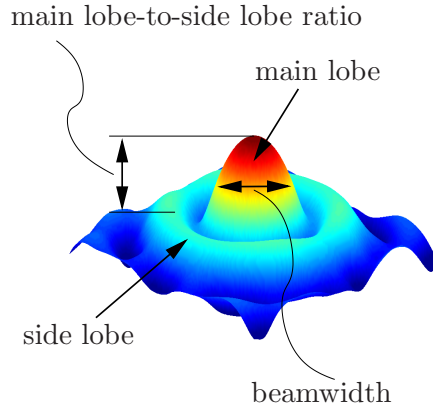


Figure 2.3: schematic example of the point-spread-function

sources. In addition, as a consequence of the spatial filtering side lobes will occur. The height of the side lobe relative to the main lobe establishes the effective dynamic range of the microphone array which can be characterized by the so-called main lobe-to-side lobe ratio (MSR). In general, the strongest side lobes in the source map are controlled by the loudest source. Therefore, the MSR is a helpful measure of the dynamic range below the loudest source where it is possible to detect sources and distinguish them clearly from side lobes. Another occurring, and in fact undesirable, phenomenon is *spatial aliasing*. This effect results from spatially undersampling of the sound waves by the array leading to an inability to distinguish between multiple source locations. In order to avoid spatial undersampling [Underbrink \(2002\)](#) suggests a minimum microphone spacing which does not exceed one-half wavelength.

On closer examination it becomes apparent that the individual elements of the cross-spectral matrix \mathbf{R} contribute in a variety of ways to the source maps generated via the DSB. Before going into detail it is helpful to look at the properties of the cross-spectral matrix. This matrix is always at least positive semi-definite and of Hermitian form designating the following interesting features (see e.g. [Sijtsma \(2004\)](#)). \mathbf{R} is a quadratic and symmetric matrix with real main diagonal elements (signal auto powers) and complex-valued off-diagonal elements (signal cross powers). The real-valued main diagonal elements do not contain phase information which are essential for the source location by means of beamforming. This property can be illustrated by, firstly, splitting the cross-spectral matrix into two quadratic matrices:

$$\mathbf{R} = \mathbf{R}_{off} + \mathbf{R}_I. \quad (2.2.14)$$

\mathbf{R}_{off} contains the complex-valued off-diagonal elements and has zeros on

the main diagonal. The other matrix \mathbf{R}_I is a diagonal matrix containing the real-valued elements of the original cross-spectral matrix on its main diagonal. Then, in a second step, beamforming is performed using a simulated monopole. The total source map which results from beamforming applying the complete cross-spectral matrix \mathbf{R} is depicted in figure 2.4. It is a superposition of the source maps derived from the real- and complex-valued parts of the cross-spectral matrix demonstrating the underlying significance of the off-diagonal elements for the source localization with beamforming. The main diagonal part of the cross-spectral matrix acts basically as spatially dependent offset (due to the spherical divergence of the monopole sound field). The main contribution to the source localization will be accomplished by the off-diagonal elements of the cross-spectral matrix.

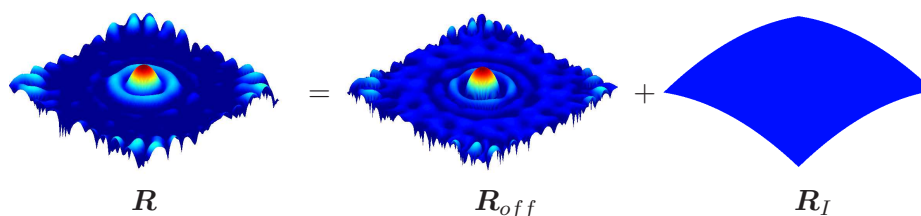


Figure 2.4: Source map of a single monopole source as a superposition of source maps which are related to matrices \mathbf{R}_I and \mathbf{R}_{off} . The matrix \mathbf{R}_I is a diagonal matrix containing the real-valued elements of the original cross-spectral matrix \mathbf{R} on its main diagonal. The other matrix \mathbf{R}_{off} contains the complex-valued off-diagonal elements and has zeros on the main diagonal.

Additional information can be extracted from the source maps using the spatial coherence introduced by [Horne et al. \(2000\)](#):

$$C_s(\mathbf{x}_{f_1}, \mathbf{x}_{f_2}, \omega) = \frac{[\mathbf{s}^H(\mathbf{x}_{f_1}, \omega) \mathbf{R} \mathbf{s}(\mathbf{x}_{f_2}, \omega)][\mathbf{s}^H(\mathbf{x}_{f_1}, \omega) \mathbf{R} \mathbf{s}(\mathbf{x}_{f_2}, \omega)]^H}{[\mathbf{s}^H(\mathbf{x}_{f_1}, \omega) \mathbf{R} \mathbf{s}(\mathbf{x}_{f_1}, \omega)][\mathbf{s}^H(\mathbf{x}_{f_2}, \omega) \mathbf{R} \mathbf{s}(\mathbf{x}_{f_2}, \omega)]}. \quad (2.2.15)$$

With this expression it is possible to compute the spatial coherence between the two focussed points \mathbf{x}_{f_1} and \mathbf{x}_{f_2} in the source map. [Oerlemans and Sijtsma \(2002\)](#) has applied the spatial coherence for the identification of mirror sources, since the real source and the mirror source are correlated. They also estimated the spatial coherence length of trailing edge noise sources. Moreover the spatial coherence can be used to remove side lobes from the source maps as shown by [Sijtsma \(2007\)](#), because side lobes are coherent to the corresponding main lobe.

2.2.3 Improvements of the SNR

The following highlights some practical aspects of the DSB affecting the beamforming process and its results. On the one hand unwanted noise will

influence the measured signal and its signal-to-noise ratio (SNR) (see e.g. [Dougherty \(2002\)](#), [Sijstma and Holthusen \(1999\)](#), [Oerlemans et al. \(2007\)](#)). On the other hand the signals are typically available in the form of discrete and finite time series in practical applications. Both facts have to take into account in the application of beamforming. Beginning with the latter fact, the original continuous microphone signals are sampled using an analog digital converter giving discrete values in order to enable digital processing. The time series are partitioned into a number of L_b blocks. Each block typically consists of 2^n samples allowing the use of the Fast Fourier Transformation (FFT). Before applying such an algorithm in order to obtain the complex signal vector \mathbf{b}_l for each signal block each time series block is multiplied by a window function (e.g. von-Hann, Hamming, Bartlett, Kaiser, rectangular window, etc.) in order to minimize leakage effects. Finally, the estimation of the cross-spectral matrix

$$\tilde{\mathbf{R}} = E\{\mathbf{b}_l \mathbf{b}_l^H\} \quad (2.2.16)$$

is given by the computation of the expectation value $E\{\cdot\}$. Let us assume the stochastic process is ergodic the ensemble average in equation 2.2.16 can be replaced by the time average ([Khinchin and Gamov \(1949\)](#)). The time average in turn can be estimated by

$$\tilde{\mathbf{R}} = \frac{1}{L_b} \sum_{l=1}^{L_b} \mathbf{b}_l \mathbf{b}_l^H. \quad (2.2.17)$$

In measurements the signals of interest are typically superimposed by additional disturbances, so that the measured signal consists of the desired signals and the noise signals χ . One obtains for the cross-spectral matrix

$$\bar{\mathbf{R}} = E\{(\mathbf{b}_l + \chi_l)(\mathbf{b}_l + \chi_l)^H\}. \quad (2.2.18)$$

The disturbances are assumed to be spatially white with components having zero mean and the identical variance σ_χ^2 . Furthermore, let us suppose that the signals and the noise are statistically independent, then, the equation (2.2.18) simplifies to

$$\bar{\mathbf{R}} = E\{\mathbf{b}_l \mathbf{b}_l^H\} + E\{\chi_l \chi_l^H\} = \tilde{\mathbf{R}} + \sigma_\chi^2 \mathbf{I}. \quad (2.2.19)$$

The evaluation of the expectation value $E\{\chi_l \chi_l^H\}$ yields the diagonal matrix $\sigma_\chi^2 \mathbf{I}$ with the noise variance on the diagonal elements and with zeros on the off-diagonal elements because the noise of each sensor is uncorrelated with that of the others giving zero expectation values. Under these conditions it becomes apparent that averaging the cross-spectral matrix over many realizations is helpful with respect to improvement the SNR because after a sufficient number of averages the off-diagonal of the cross-spectral matrix can be considered as noise-free. Another and very powerful approach,

focussing also on the improvement of the SNR, is the so-called diagonal removal technique (DR) (see e.g. [Dougherty \(2002\)](#)). It has been shown in the previous section [2.2.2](#) that the auto powers on the main diagonal of the cross-spectral matrix does not really contribute to the source localization in the beamforming process. In addition, in the case of the made assumption regarding the noise characteristics, only the main diagonal of the estimated cross-spectral matrix is corrupted by the additional disturbances. Consequently, if these values are set to zero and only the averaged (and subsequently noise-free) off-diagonal elements are taken into account one can achieve a dramatic increase of the SNR in the beamforming results. Unfortunately, this technique comes along with a drawback. The removal of the main diagonal of the cross-spectral matrix can change its properties. Now, one cannot necessarily assume that the cross-spectral matrix is still positive semi-definite so that the matrix may possess negative eigenvalues. This can lead to negative values at the beamformer output. Of course, this is not a physically meaningful result, since the source power is a positive value or it is zero if no source is present.

A further possibility to improve the SNR is an increase of the number of sensors. ([Johnson and Dudgeon \(1993\)](#)) have demonstrated that the SNR of the beamforming process is related to the number of microphones. Each doubling of the number of sensors results in a SNR increase of about 3 dB. However, this is the most cost-intensive method for improving the SNR.

2.2.4 Quantification of results

In general, one is not only interested in the source location, because absolute levels from the entire model or model subcomponents are also of concern and provide valuable information for the evaluation of noise reduction concepts and for the noise predictions of the real object. The source map $L(\mathbf{x})$, computed with a beamforming algorithm, can directly provide absolute source levels only in special cases. The reason for that are the finite beamwidth and the side lobe characteristics of the beamformer which are expressed by the point spread function $\mathcal{P}(\mathbf{x}, \mathbf{x}_o)$, introduced in section [2.2.2](#). The point spread function represents the source map as a function of \mathbf{x} that would result from a monopole point source at the location \mathbf{x}_o . Assuming that the source distribution $q(\mathbf{x}_o)$ consists of an aggregation of incoherent sources the beamformer output can be written as ([Dougherty \(2005\)](#)):

$$L(\mathbf{x}) = \int_{\mathbf{x} \in \mathcal{G}} q(\mathbf{x}_o) \mathcal{P}(\mathbf{x}, \mathbf{x}_o) d\mathbf{x}, \quad (2.2.20)$$

whereas \mathcal{G} denotes the scan plane of the beamformer output. The convolution integral in equation [2.2.20](#) is a so-called Fredholm integral equation of the first kind for $q(\mathbf{x}_o)$. Due to the convolution of the true source distribution with the point spread function of the beamformer the source map is also

denoted as dirty map. According to [Sijtsma \(2004\)](#) absolute source pressure levels can be extracted from the dirty map if the following constraints are fulfilled. The sources have to be incoherent point sources and possess, at least in the direction of the array, a uniform directivity. Beyond that the spatial resolution of the beamformer has to be high enough in order to separate different sources and the distance between the sources must sufficiently large so that the main lobes of the sources are not contaminated by side lobes from the other sources. Finally, there must be no coherence loss of the measured source signals and no reflections (free space assumption). If these constraints can be fulfilled, then the source strength can be found as the (local) peak value in the dirty map. However, this is practically never the case in aeroacoustic wind tunnel testing. Subsequently, source power integration methods have been developed to overcome this issue, among others by [Brooks and Humphreys \(1999\)](#). This procedure for the determination of quantitative source spectra consists of two basic steps. At first, the source map is integrated and secondly, this integral is normalized in order to take into account the width of the point spread function of the beamformer:

$$L_f = \left(\int_{\mathbf{x} \in \mathcal{G}} L_{exp}(\mathbf{x}) d\mathbf{x} \right) \left(\frac{P_{sim}}{\int_{\mathbf{x} \in \mathcal{G}} L_{sim}(\mathbf{x}) d\mathbf{x}} \right). \quad (2.2.21)$$

$L_{exp}(\mathbf{x})$ denotes the source map which is computed from the measured data in the experiment. This dirty map is then integrated over all scan points \mathbf{x} which belong to the scan plane grid \mathcal{G} . The subsequent normalization is obtained by performing a simulation for a monopole source at the center of the integration region. $L_{sim}(\mathbf{x})$ is the simulated beamforming source map which would result from the simulated point monopole source having a mean-squared pressure amplitude of P_{sim} . This integration approach was verified using single microphone measurements of a loudspeaker without flow by various authors ([Burnside et al. \(2002\)](#), [Oerlemans et al. \(2007\)](#)). [Brooks and Humphreys \(1999\)](#) have also evaluated this procedure in open jet wind tunnel tests and the integrated levels agreed within 1.5 dB provided that the complete cross-spectral matrix is used. The application of the diagonal removal technique is accompanied by an unpleasant side effect. On the one hand it can improve the SNR of the source maps as explained in the previous section [2.2.3](#), but on the other hand the integration technique becomes less reliable. Now, the cross-spectral matrix is not positive semi-definite anymore which can result in negative values of the beamformer output $L_{exp}(\mathbf{x})$. This can corrupt the integrated values L_f . A possible alternative is to ignore the not physical negative values and replace them by zero. A more reasonable method was proposed by [Dougherty \(2002\)](#). The introduction of a threshold into the integration scheme can eliminate this problem. One only considers those values being larger than the threshold which is defined by the source

maximum minus a certain value. Some care is required for the choice of the threshold. Setting the threshold to be smaller than the MSR of the beamformer a contamination of the integral by side lobes can be excluded, since the side lobes are controlled by the loudest source in the wind tunnel. If the highest source is missed, then the threshold will be too low and side lobes will contribute to the integral. In the contrary case, defining the threshold too high, some real noise sources will be excluded from the integral. Nevertheless, with a careful determination of the threshold one can retrieve accurate sound pressure levels.

The described integration method implicitly assumes a shift invariant point spread function in the area of the scan plane. If this is not fulfilled one can use multiple subdomains for the integration and normalization or in the limiting case, performing the procedure for every scan point as described by [Brooks and Humphreys \(1999\)](#). Of course, this approach requires a much higher computing time. Another integration method taking into account coherent sources has been proposed by [Oerlemans and Sijtsma \(2002\)](#) using the spatial coherence as suggested by [Horne et al. \(2000\)](#).

2.2.5 Deconvolution

As indicated above the beamforming results of processed phased microphone array data, the so-called dirty map, represent sound sources that are convolved with the point spread function of the beamformer, which depends on array geometry, array aperture and frequency. That means that the array output is contaminated with side lobes and the finite width of the main lobe makes it sometimes difficult to interpret the array results and to establish reliable quantitative results. In order to remedy these difficulties deconvolution approaches have been introduced and adapted for aeroacoustic measurements. These methods aim at removing side lobes and resolution effects from the beamforming results in order to improve the spatial resolution of source maps. From a dirty source map generated by the beamformer, an uncorrelated source distribution $q(\mathbf{x})$ is determined by inverting iteratively equation [2.2.20](#). This requires a modeling of the point spread function $\mathcal{P}(\mathbf{x}, \mathbf{x}_o)$ which is typically assumed as the monopole response of the beamformer. The algorithms of [Brooks and Humphreys \(2004\)](#) (DAMAS), [Dougherty \(2005\)](#) (DAMAS2), [Ravetta et al. \(2006\)](#) (LORE) and [Ehrenfried and Koop \(2006\)](#) (NNLS) work in that way. Further deconvolution techniques have been proposed treating also coherent sources by [Brooks and Humphreys \(2006\)](#) (DAMAS-C) and [Suzuki \(2008\)](#). The CLEAN-SC algorithm, introduced by [Sijtsma \(2007\)](#), is an exception within the various deconvolution algorithms. In contrast to the other methods this one models the point spread function by means of the spatial coherence of the sources maps, generated from the measured data.

In general, the deconvolution algorithm may have the ability to im-

prove the standard beamforming results, but they require high computational costs. Another issue arises from the mathematical properties of equation 2.2.20. Fredholm integral equations of the first kind are known to be ill-posed problems (Dougherty (2005)) and in addition, the data obtained from aeroacoustic measurements are typically very noisy. The deconvolution schemes can introduce artificial noise which affects the reconstructed source distribution and the convergence of the iterative solution remains an issue (Ehrenfried and Koop (2006)). In this thesis the experiments were designed in that way that the acoustic sources could have been separated very well with the microphone array technique in order to avoid the possible uncertainties introduced by deconvolution schemes.

2.3 Beamforming with flow

Up to now the influence of the wind tunnel flow on the sound propagation has not taken into account in the beamforming process. In the following subsections this will be addressed and all applied test section dependent corrections are introduced and explained in detail.

2.3.1 Closed test section

Travel time

Figure 2.5 depicts the geometrical situation in the closed test section. The monopole sound source is located in the flow at the position \mathbf{x}_o and the microphone is at the position \mathbf{x}_m . In this scenario the sound wave propagation is superimposed by the motion of the fluid having the flow velocity U . In order to take into account the influence of the flow the classic wave equation 2.2.1 needs to be extended. This results in the *convective wave equation* (see e.g. Pierce (1981))

$$\left(\frac{1}{c^2} \left(\frac{\partial}{\partial t} + \mathbf{U} \cdot \nabla \right)^2 - \nabla^2 \right) p = q(t) \delta(\mathbf{x} - \mathbf{x}_o). \quad (2.3.1)$$

Assuming an uniform flow profile in positive x -direction with the velocity U it simplifies to:

$$\frac{1}{c^2} \left(\frac{\partial^2 p}{\partial t^2} + 2U \frac{\partial^2 p}{\partial t \partial x} + U^2 \frac{\partial^2 p}{\partial x^2} \right) - \Delta p = q(t) \delta(\mathbf{x} - \mathbf{x}_o). \quad (2.3.2)$$

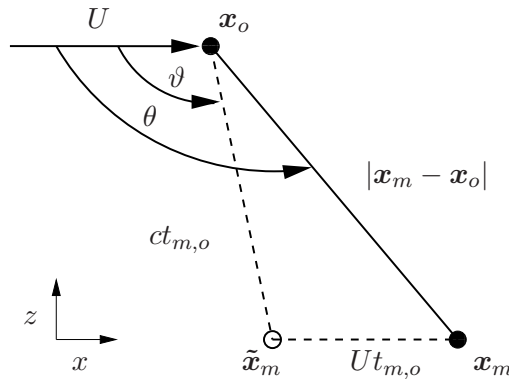


Figure 2.5: Source-observer scenario in the closed test section.

CHAPTER 2. LOCALIZATION AND QUANTIFICATION OF SOUND SOURCES WITH PHASED MICROPHONE ARRAYS

One method of deriving a solution for equation (2.3.12) is to apply a Lorentz transformation to the classic wave equation (2.2.1) as described by Chapman (2000). Provided that the flow is subsonic the free-space solution of equation (2.3.2) can then be expressed in terms of the Doppler factor $\beta = \sqrt{1 - M^2}$, whereas $M = U/c$ denotes the Mach number, and the Doppler transformed coordinates

$$\begin{aligned}\tilde{\mathbf{x}}_m &= (\tilde{x}_m, \tilde{y}_m, \tilde{z}_m) = (x_m/\beta^2, y_m/\beta, z_m/\beta) \\ \tilde{\mathbf{x}}_o &= (\tilde{x}_o, \tilde{y}_o, \tilde{z}_o) = (x_o/\beta^2, y_o/\beta, z_o/\beta)\end{aligned}\quad (2.3.3)$$

as

$$p(\mathbf{x}_o, \mathbf{x}_m, t) = \frac{1}{4\pi\beta^2} \frac{q(\mathbf{x}_o, t + \frac{M(\tilde{x}_m - \tilde{x}_o)}{c} - \frac{|\tilde{\mathbf{x}}_m - \tilde{\mathbf{x}}_o|}{c})}{|\tilde{\mathbf{x}}_m - \tilde{\mathbf{x}}_o|}.\quad (2.3.4)$$

As a consequence of the flow motion in x -direction the travel time from the source to the receiver changes to:

$$t_{m,o} = \frac{M(\tilde{x}_m - \tilde{x}_o)}{c} - \frac{|\tilde{\mathbf{x}}_m - \tilde{\mathbf{x}}_o|}{c}.\quad (2.3.5)$$

This solution in the back-transformed coordinates reads as

$$t_{m,o} = \frac{1}{c\beta^2} \left[M(x_m - x_o) - \sqrt{(x_m - x_o)^2 + \beta^2\{(y_m - y_o)^2 + (z_m - z_o)^2\}} \right].\quad (2.3.6)$$

The flow influence is illustrated in figure 2.5. Without flow the emitted sound waves with the emission angle ϑ would impinge at the position $\tilde{\mathbf{x}}_m$ after the travel time $t_{m,o}$, but due to the superposition with the flow motion the waves are shifted downstream by the distance $Ut_{m,o}$ and finally, they reach the m -th microphone at the position \mathbf{x}_m . Subsequently, the flow changes the wave propagation path and the emission angle of the received signals by the m -th microphone compared with the still air. The flow impact is not only confined to the travel time the amplitude is also altered compared with case when the medium is at rest leading to the denominator of equation 2.3.4

$$4\pi\beta^2|\tilde{\mathbf{x}}_m - \tilde{\mathbf{x}}_o| = 4\pi\sqrt{(x_m - x_o)^2 + \beta^2\{(y_m - y_o)^2 + (z_m - z_o)^2\}}.\quad (2.3.7)$$

This result is a combination of two different effects influencing the sound radiation pattern (see e.g. Mueller (2002)). Due to the moving flow the sound waves undergo a convective amplification. Sound waves radiated upstream will be amplified and sound radiated downstream will be attenuated relative to case without flow. The convective amplification is proportional to the factor $1/(1 - M \cos \vartheta)^n$. In the current expression the exponent is $n = 1$ due to the assumption of a purely mathematical monopole point source. This approach does not address the question how such a source could be physically realized. For example, if the fluid is at rest the sound field of a point monopole sound source can be generated by a physical process involving the unsteady creation of mass at the position of the point source (see

e.g. [Dowling and Ffowcs Williams \(1983\)](#)). Now positioning this point mass source in a moving fluid and applying the above described method it yields a convective amplification factor with an exponent $n = 2$ emphasizing the dependence of the physical source mechanism on the convective amplification factor. Following [Morse and Ingard \(1968\)](#), in contrast to mathematical monopole point source the exponent n needs to be raised depending on the aeroacoustic source type (monopole and dipole $n = 2$, quadrupole $n = 3$). For the experiments conducted in the present work, the observation angle ϑ is typically close to $\pi/2$ and the Mach number is $M \approx 0.1$, so that consequently the influence on the aeroacoustic measurements of the convective amplification factor with its exponent uncertainty will be negligible. Even though convective amplification occurs, there is no Doppler frequency shift since the observer does not move with respect to the source.

The second effect is associated with the influence of the flow on the propagation path which differs with the propagation path of the no flow case and consequently, the amplitude decay changes. The wave fronts are convected by the superimposed flow velocity and this leads to a propagation velocity $c \pm U$ depending on whether the waves propagate downstream or upstream. The change in the wave propagation velocity causes a change in wavelength because of the constant frequency. Thereby an upstream traveling wave covers a larger distance towards the flow compared with the motion in flow direction even though both observer positions have the same distance to the source. Both effects interfere with each other and result in the expression for the amplitude decay of equation [\(2.3.7\)](#). In this context, for small Mach numbers the flow induced amplitude difference, compared with the case of a still medium, is very small. For example, for $M = 0.1$ it yields $\beta^2 = 0.99$ instead of $\beta^2 = 1$ as one would obtain for the fluid at rest. Another interesting fact becomes apparent when supposing that the source and the observer are located on the x -axis having $y_m = z_m = y_o = z_o = 0$. Then, the above described effects of the convective amplification and flow induced amplitude decay compensate each other, so that for this scenario the measured amplitudes by the observer are identical for the cases with and without flow. Note, this holds only for an exponent of the convective amplification factor of $n = 1$. For higher exponents there will be no exact compensation. In general, setting M to zero, then the expressions for the travel time and the amplitude decay correspond to the solution of equation [2.2.2](#) where the fluid is at rest.

In order to take into account the flow effects on the sound propagation in the beamforming process it is essential to modify the steering vector formulation of equation [2.2.8](#) with respect to the here derived expressions for the travel time (equation [\(2.3.6\)](#)) and amplitude decay compensation (equation [\(2.3.7\)](#)).

Reflections

In the closed test section reflections are of major concern, since the reverberant walls reflect most of the incident acoustic energy and the reflections are coherent with the original source signal so that direct and reflected waves will add constructively and destructively depending on the relative phase. The reflections can influence beamforming results in a qualitative and quantitative manner. Among other things deviations from the source strength and source position, as one would obtain under anechoic conditions, can occur as reported by [Oerlemans and Sijstma \(2000\)](#) and [Sijstma and Holthusen \(2003\)](#), for instance. In addition, a decrease of resolution and SNR have been observed ([Guidati et al. \(2002\)](#)). These effects become more distinct with decreasing distance between the source and the reflecting surface. Of course, various considerations have been made concerning this matter in order to overcome these drawbacks. On the one hand a wide variety of adopted source-receiver models have been proposed and on the other hand some approaches make use of the temporal coherence of the time series of the pressure signal generated by aeroacoustic sources. Beginning with the latter idea [Mosher \(1996\)](#) suggests to apply a time window for the processing of the time series in beamforming which is shorter than the travel time differences between the source signals and its reflected waves. In this special case the reflections appear as incoherent at the array for broadband sources. However, the possibility of shortening the time window length is limited due to the required minimum frequency resolution so that this time constraint cannot often be fulfilled, since the frequency resolution has typically a higher priority. Furthermore in the presence of periodic sources this procedure yields no improvements. No matter what time window length is chosen the reflections will always be coherent.

A second class of approaches incorporates the reflections in the source-receiver model. The reflections are modeled by mirror sources and are taken into account in the computation of the steering vectors. Due to multiple reflections, there are theoretically an infinite number of mirror sources or in other words an infinite number of source-boundary interactions. In practical applications the order of interactions can be confined because of the damping effects on the reflecting surfaces and the distance proportional amplitude decay of the sound waves. The so-called "reflection canceller", proposed by [Guidati et al. \(2002\)](#) for wind tunnels with rectangular cross-section, can provide improvements of the low-frequency results, but this method can also introduce distinct errors for higher frequencies in consequence of a lack of robustness, as pointed out by [Sijstma and Holthusen \(2003\)](#). The "reflections canceller" requires a very accurate knowledge of the mirror source position, the wall impedance and the source directivity otherwise the deviations will result in phase errors, especially for higher frequencies, lowering the robustness and accuracy of the approach. Moreover the original beam

pattern of the microphone array is altered by the application of the mirror sources. This method implicitly introduces mirror arrays by modeling the reverberant walls and the effective array can have a disadvantageous beam pattern with a decreased resolution. In order to overcome these drawbacks [Sijstma and Holthusen \(2003\)](#) have proposed a mirror source minimization technique which leaves the steering vector unchanged and introduces an additional constraint of low output from the direction of the mirror source. In fact, this algorithm provides better results than the "reflection canceller" and exhibits a higher degree of robustness. Nonetheless, for low frequencies there are still occurring deviations between the true and reconstructed source position. Besides that, the performance of the minimization approach suffers from the computing time which can reach up to 20 times more than the computing time for the standard beamformer.

These analytical mirror or image source models can be easily applied to simple wind tunnel geometries (e.g. empty duct with rectangular or round cross-section). For more complex geometries and taking into account the reverberant surfaces of the model and mountings and the complex wall impedance it requires a much more complex reflection model which is accompanied by an increased effort in the realization process. In theory, measured Green's functions in the reverberant environment, which model the transfer function between array microphones and the beamformer focus point, should give the most accurate results. Such an approach can capture all essential characteristics of the wind tunnel with an installed model with respect to reflections without making simplifications and uncertainties concerning the complex wall impedance. Then, the measured Green's functions are incorporated in the beamforming process. [Fenech and Takeda \(2007, 2008\)](#) has applied and evaluated this approach. They performed corresponding measurements in a wind tunnel with closed test section, but they only obtained disappointing results. The main problem is associated with the accurate measurement of the Green's function which requires a point source having an omni-directional sound field. This is extremely difficult to generate. Furthermore, such a method is very time-consuming, since measurements have to be conducted for each microphone grid-point combination.

In spite of great efforts no practical and reliable method has been developed so far for the corrections of reflections in the beamforming process. Subsequently, in the great majority of the applications the influence of reflections is typically ignored and thus, potential deviations are accepted.

Boundary layer and background noise Phased microphone array inflow measurements in closed test sections using flush mounted microphones in the wind tunnel wall are normally subject to strong hydrodynamic pressure fluctuations induced by the turbulent boundary layer. This can result in a dramatic decrease of the sensor SNR which causes artifacts in beam-

forming source maps. In the last decade many concepts have been developed and validated, mainly for reducing the influence of turbulent boundary layer noise on the measured microphone signals in the closed test section, on the one hand by improving the experimental setup and on the other by using advanced signal processing techniques. One of them is the diagonal removal technique which was outlined in section 2.2.3.

Sijstma and Holthusen (1999) and Horne and James (1999) have evaluated the effect of first, recessing the microphones in order to separate them from the unsteady boundary layer flow, and secondly, covering the microphones with acoustically transparent materials such as foam, perforated plates and metal screens in order to suppress microphone self-noise. This latter approach was found to be effective in reducing the self-noise for low frequencies, but it also introduces some reverberations and directivity distortions due to directional transmissivity through the screen. Jaeger et al. (2000) have enhanced the previous concept by introducing a thin Kevlar® cloth for covering the recessed microphones and achieved an improved SNR in the low frequency range. At higher frequencies, a slight noise increase was observed. Another concept involves the modification of a closed wind tunnel (Remillieux et al. (2008), Smith et al. (2005)) and Ito et al. (2010). The wind tunnel walls of the test section are replaced by tensioned Kevlar® cloth which separates the wind tunnel test section from a surrounding anechoic chamber where the microphone array is placed. With such kind of installation it is possible to combine the aerodynamic properties of a closed test section without having the drawback of hydrodynamic pressure fluctuations influencing the microphones. Nevertheless, the acoustic transparency and the influence of the Kevlar® cloth on the aerodynamic properties are still subject of examinations in the current two existing wind tunnels with such a test section worldwide.

Besides the boundary layer noise, wind tunnel background noise is also of major concern. This results in a further decrease of the SNR, especially in the low frequency range. It is connected among others things with the wind tunnel background noise generated from the fan, turning vanes and channel modes, for example. Addressing this matter various signal processing techniques have been proposed to cope with this particular situation. The Principal Component Analysis (PCA) belongs to this class of advanced signal processing techniques that can separate the signal from the noise sources subspace under certain conditions and assumptions. For phased microphone array measurements the cross spectral matrix is decomposed in eigenvalues and eigenvectors as shown by Dougherty (1997) and Long (2003). For aeroacoustic applications it is normally difficult to distinguish the signal subspace from the noise subspace. However, the number of sources is restricted by the number of used microphones and the SNR has to be high enough to adapt this approach. The BiCLEAN-algorithm, proposed by Ehrenfried et al. (2006) separates the noise from the source signal by means of the wavenum-

ber spectrum. For example, disturbances propagating in upstream direction, e.g. generated by the fan, have a distinct wavenumber spectrum which can be removed from the cross spectral matrix in order to improve the quality of source maps. With respect to practical applications it is disadvantageous that this procedure requires a very high computational effort.

Due to the various drawbacks, none of the previously described methods could be established as a standard procedure for reducing the influence of turbulent boundary layer noise or separating it from the signals. Solely, the diagonal removal technique, described in section 2.2.3, finds wide and successful use to suppress the influence of the turbulent boundary layer pressure fluctuations. The turbulent pressure fluctuations only partially fulfill the assumed noise model (spatial white noise) which was applied in section 2.2.3. Theoretically, the hydrodynamic pressure fluctuations have a certain and frequency-dependent coherence length. This means that the complex off-diagonal elements of the averaged cross-spectral matrix are still affected by the turbulent boundary layer pressure fluctuations. In practice, the effect becomes important only for small distances between the sensors in low-speed wind tunnel testing as shown by Shin et al. (2007). They figured out that the boundary layer contributions to the cross-spectra will only be significant for streamwise-separated microphone pairs with spacing less than about 5 cm for the flow velocity of 60 m/s. Hence, in many cases the cross-spectra of the majority of the microphones are not influenced by the hydrodynamic pressure fluctuations induced by the turbulent boundary layer.

2.3.2 Open test section

In the open test section of a wind tunnel the model is typically placed inside the potential core of the jet and the microphone locations are outside the flow. Hence, the sound waves emitted from aeroacoustic sources of the model have to pass through the wind tunnel shear layer before reaching the microphone. This sound propagation through a turbulent shear layer is accompanied by several effects as already mentioned in chapter 1.2.2. If these effects are not properly taken into account they may influence the beamforming accuracy. In order to address this matter, many analytical and numerical methods have been developed and subsequently published by various authors, mainly focused on the effects accompanied by the refraction caused by the mean velocity gradient in the shear layer. Many concepts are based on a simplified flow model for the two limiting cases of sound propagation. At low frequencies the properties of the medium change abruptly on the wavelength scale, so that the finite thickness of the shear layer appears as interface with zero thickness which is also termed vortex-sheet model. In contrast to that, at high frequencies the wavelengths are much smaller than the relevant length scales of the medium allowing the application of

geometrical acoustics and subsequently, the sound propagation can be calculated along rays. Furthermore these simplified models typically restrict the appearance of the shear layer to simple geometries with plane or cylindrical shapes as done by Amiet (1975) and Amiet (1978), respectively. The computational effort is normally easily to manage, but the validity is limited, for instance the source positions are limited to on-axis positions of the jet centerline in the case of a cylindrical shear layer in the analytical model of Amiet (1978). This restriction was abandoned in the extended model of Morfey and Joseph (2001). Candel (1977) has solved numerically the ray equations so that an arbitrary three-dimensional flow can be treated, but again the validity is confined to high frequency sound propagation. Finally, one succeeded in overcoming the frequency limitations of the previous shear layer correction methods allowing arbitrary frequencies with more complex approaches as proposed by Tester and Morfey (1976); Morfey and Tester (1977) and Ehrenfried et al. (2005). They solved numerically the Lilley equation (Lilley (1973)) and the linearized Euler equations, respectively. However, these numerical methods have a greater physical validity, but simultaneously that involves a considerable higher computational effort than the simplified models. In addition, such numerical approaches require that the exact flow-field is known and the determination of the flow-field, either by means of experiments or numerical simulations, can be very extensive. Nevertheless, the presented methods are only able to capture the physical effect of refraction while the phenomena of scattering and spectral broadening cannot be treated, because this requires a modeling of the unsteady turbulence. Concerning this matter Campos (1978a,b) has developed a procedure where the turbulent fluctuations of the shear layer are modeled by random phase shifts. As before, the application of this method requires statistical information about the unsteady flow field which has to be acquired somehow. The next step in evolution was conducted by Ewert et al. (2008, 2009). They have proposed a totally numerical approach. The flow-field of the open jet wind tunnel is firstly calculated by a numerical simulation including the turbulent field and then, in a second step, an acoustic source is placed within the flow and the sound propagation through the flow is calculated using Computational Aeroacoustics (CAA) methods. However, until today one typically prefers simplified flow models for the correction of flow effects in the beamforming process due to the better cost-benefit ratio in terms of the general computational effort and the effort to determine the exact flow field. Based on this fact in this thesis the vortex-sheet model of Amiet (1975) is applied for the correction of the flow effects: refraction, transmission and reflection. This simplified model is widely used for the microphone array processing of aeroacoustic data and in the following, it will be outlined in detail.

Refraction

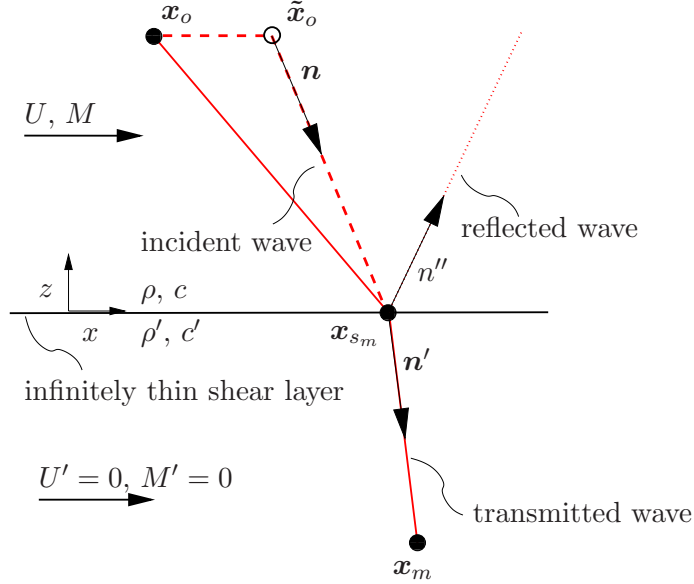


Figure 2.6: Sound refraction at an infinitely thin shear layer.

The sound source is located in the uniform parallel flow with the free jet velocity U in positive x -direction as illustrated in figure 2.6. The shear layer is modeled as a plane infinitely thin interface lying in the xy -plane at the position of the lip line at $z = 0$ implicitly assuming that the wavelength is large compared to the actual scales of the shear layer. Outside the jet the medium is at rest where the observer is located. This choice of the shear layer position facilitates the derivation, but is without loss of generality. The emitted wave fronts are convected by the flow until the shear layer is reached. While propagating through the velocity discontinuity the incoming sound waves are refracted. Being similar to the transmission of sound waves across an interface between two media the incoming wave is split into two waves caused by the velocity discontinuity giving rise to a transmitted and a reflected wave. Again, without loss of generality, the incident wave is assumed to be plane since every kind of waves can be considered as plane wave at least in a finite domain. The pressure field of an incoming plane wave can be written as:

$$p(\mathbf{x}, t) = Ae^{i(\omega t - \mathbf{k}\mathbf{x})}. \quad (2.3.8)$$

The parameter A denotes the amplitude, ω the angular frequency, \mathbf{x} the position vector and \mathbf{k} the wavenumber vector of the incident wave with the components k_x , k_y and k_z . According to [Born and Wolf \(2010\)](#) the resulting transmitted and reflected waves are also plane since the interface has no

curvature. In a similar manner one can formulate the pressure fields of the transmitted wave

$$p'(\mathbf{x}, t) = A' e^{i(\omega t - \mathbf{k}' \cdot \mathbf{x})}, \quad (2.3.9)$$

and the reflected wave

$$p''(\mathbf{x}, t) = A'' e^{i(\omega t - \mathbf{k}'' \cdot \mathbf{x})}. \quad (2.3.10)$$

The frequency is not affected by the interface so that ω is the same in all three wave fields. At the shear layer the time variation of the secondary fields will be in agreement with the primary field. Equating the arguments of the three wave functions at the boundary $z = 0$ and omitting the time dependence $e^{i\omega t}$ because it must remain valid for all times one obtains

$$k_x x + k_y y = k'_x x + k'_y y = k''_x x + k''_y y. \quad (2.3.11)$$

Since 2.3.11 must hold for all values of x and y on the infinitely thin shear layer, the components k_x , k_y are identical on both sides of the shear layer and only k_z varies. In the following the notations $(\cdot)'$ and $(\cdot)''$ denote all physical variables associated with the transmitted and with the reflected wave, respectively.

The convected wave equation describes the sound propagation in the presence of flow (see e.g. Pierce (1981))

$$\left(\frac{1}{c^2} \left(\frac{\partial}{\partial t} + \mathbf{U} \cdot \nabla \right)^2 - \nabla^2 \right) p = 0.$$

In the case of uniform flow U in x -direction it simplifies to:

$$\frac{1}{c^2} \left(\frac{\partial^2 p}{\partial t^2} + 2U \frac{\partial^2 p}{\partial t \partial x} + U^2 \frac{\partial^2 p}{\partial x^2} \right) - \Delta p = 0. \quad (2.3.12)$$

The substitution of equation (2.3.8) in equation (2.3.12) results:

$$k_z^2 = \left(1 - M k_x \frac{c}{\omega} \right)^2 \frac{\omega^2}{c^2} - (k_x^2 + k_y^2), \quad (2.3.13)$$

whereas M represents the Mach-number. The normal vector \mathbf{n} is perpendicular to wave front and has unit length. It is found by taking the gradient of equation (2.3.8) and using equation (2.3.13)

$$\mathbf{n} = \frac{\nabla(p)}{|\nabla(p)|} = \begin{pmatrix} \frac{k_x}{\frac{\omega}{c} - M k_x} \\ \frac{k_y}{\frac{\omega}{c} - M k_x} \\ \frac{k_z}{\frac{\omega}{c} - M k_x} \end{pmatrix}. \quad (2.3.14)$$

Substituting the function of the transmitted wave field (2.3.9) in the convected wave equation (2.3.12) with flow velocity U' on the other side of the shear layer one yields the solution

$$k'^2_z = \left(1 - M' k'_x \frac{c'}{\omega} \right)^2 \frac{\omega^2}{c'^2} - (k'^2_x + k'^2_y). \quad (2.3.15)$$

Herein, M' constitutes the Mach-number on the other side of the shear layer. The calculation of the unit normal vector \mathbf{n}' of the transmitted wave is performed in a uniform manner as for the unit normal vector \mathbf{n} using equation (2.3.15) resulting in

$$\mathbf{n}' = \frac{\nabla(p')}{|\nabla(p')|} = \begin{pmatrix} \frac{k'_x}{\frac{\omega}{c'} - M'k'_x} \\ \frac{k'_y}{\frac{\omega}{c'} - M'k'_x} \\ \frac{k'_z}{\frac{\omega}{c'} - M'k'_x} \end{pmatrix}. \quad (2.3.16)$$

Resolving the component n_x of \mathbf{n} to k_x and n'_x of \mathbf{n}' to k'_x yields

$$k_x = \left(\frac{n_x}{1 + n_x M} \right) \left(\frac{\omega}{c} \right) \quad (2.3.17)$$

$$k'_x = \left(\frac{n'_x}{1 + n'_x M'} \right) \left(\frac{\omega}{c'} \right). \quad (2.3.18)$$

As shown at the beginning of this paragraph it holds $k'_x = k_x$ and $k'_y = k_y$ in order that the phase of the incident and transmitted waves are equal across the shear layer. From this condition one obtains

$$\left(\frac{n'_x}{c'(1 + n'_x M')} \right) = \left(\frac{n_x}{c(1 + n_x M)} \right). \quad (2.3.19)$$

After resolving and rearranging the component n'_x of the normal vector from the transmitted wave is found to be

$$n'_x = \frac{n_x \left(\frac{c'}{c} \right)}{1 + n_x \left[M - M' \left(\frac{c'}{c} \right) \right]}. \quad (2.3.20)$$

Let us suppose that the temperature on both sides of the shear layer is equal, which is equivalent to $c = c'$, and $M' = 0$ one derives a solution for the first component of the normal vector from the transmitted wave

$$n'_x = \frac{n_x}{1 + n_x M}. \quad (2.3.21)$$

Applying the already mentioned relation $k_y = k'_y$ the normal vector components n_y and n'_y can be rearranged and equalized using the equations (2.3.14) and (2.3.16). This results in the expression

$$n_y \left(\frac{\omega}{c} - M k_x \right) = n'_y \left(\frac{\omega}{c'} - M' k'_x \right). \quad (2.3.22)$$

In this equation the variables k_x and k'_x can be substituted by the expressions in equation (2.3.17) and equation (2.3.18). The subsequent rearrangement

and resolving to n'_y leads to the determination of the second component of the normal vector from the transmitted wave:

$$n'_y = n_y \left(\frac{c'}{c} \right) \left(\frac{1 + n'_x M'}{1 + n_x M} \right). \quad (2.3.23)$$

This simplifies to

$$n'_y = n_y \left(\frac{1}{1 + n_x M} \right) \quad (2.3.24)$$

when using the fact that the temperature is the same on both sides of the shear layer and $M' = 0$. Therewith n'_x and n'_y are known and finally, the missing third component is given by

$$n'_z = \sqrt{1 - n'^2_x - n'^2_y}. \quad (2.3.25)$$

Travel time

The total travel time of the sound waves from the source at \mathbf{x}_o to the observer \mathbf{x}_m in the open test section consists of two areas as illustrated in figure 2.7. (I) denotes the domain with flow having the velocity U in posi-

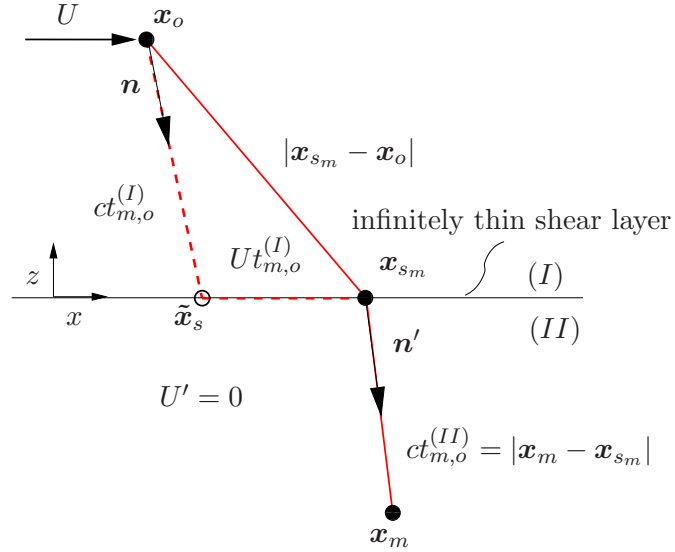


Figure 2.7: Illustration of the source-microphone scenario in the open test section.

tive x -direction. In the area (II) the flow is at rest and both domains are separated by the infinitely thin shear layer constituting the boundary surface. At first one has to find the intersection point \mathbf{x}_{s_m} where the sound waves have to pass through the shear layer and are refracted on their way to the m -th microphone at the location \mathbf{x}_m . This can be achieved by performing an iteration of the wave normal vector \mathbf{n} of the incident wave (using

equation 2.3.14 and 2.3.16) as long as the position \mathbf{x}_{sm} is found, so that the transmitted refracted wave with wave normal vector \mathbf{n}' reaches the position of \mathbf{x}_m . If \mathbf{x}_{sm} is known the travel time $t_{m,o}^{(I)}$ for the domain (I) can be computed by means of the travel time solution of the closed test section (equation 2.3.6) whereas the adopted form reads as:

$$t_{m,o}^{(I)} = \frac{1}{c\beta^2} \left[M(x_{sm} - x_o) - \sqrt{(x_{sm} - x_o)^2 + \beta^2\{(y_{sm} - y_o)^2 + (z_{sm} - z_o)^2\}} \right] \quad (2.3.26)$$

with $\beta^2 = 1 - M^2$. The travel time for domain (II) is simply given by

$$t_{m,o}^{(II)} = \frac{|\mathbf{x}_m - \mathbf{x}_{sm}|}{c}, \quad (2.3.27)$$

so that the complete solution results to $t_{m,o} = t_{m,o}^{(I)} + t_{m,o}^{(II)}$. Now, this travel time can be applied for the calculation of the phase of the steering vector for the open test section using equation 2.2.9.

Transmission

Since only a part of the incident acoustic energy is transmitted through the shear layer it is desirable to know the transmission coefficient in order to be able to correct the measured signal. This is the subject of the following considerations.

The incident, the transmitted and the reflected wave can be described by means of the velocity potential

$$\phi = A_\phi e^{i(\omega t - \mathbf{k}\mathbf{x})} \quad (2.3.28)$$

$$\phi' = A'_\phi e^{i(\omega t - \mathbf{k}'\mathbf{x})} \quad (2.3.29)$$

$$\phi'' = A''_\phi e^{i(\omega t - \mathbf{k}''\mathbf{x})}. \quad (2.3.30)$$

The pressure is given by (see e.g. Pierce (1981)):

$$p = -\rho_o \left(\frac{\partial \phi}{\partial x} + U \frac{\partial \phi}{\partial t} \right). \quad (2.3.31)$$

It consists of the temporal variation and the convective part caused by the flow in x -direction. Using equation (2.3.31) the pressures of the three waves correspond to:

$$p = -\rho_o i\omega A_\phi \left(1 - M k_x \frac{c}{\omega} \right) e^{i(\omega t - \mathbf{k}\mathbf{x})} \quad (2.3.32)$$

$$p' = -\rho'_o i\omega A'_\phi \left(1 - M' k'_x \frac{c'}{\omega} \right) e^{i(\omega t - \mathbf{k}'\mathbf{x})} \quad (2.3.33)$$

$$p'' = -\rho_o i\omega A''_\phi \left(1 - M k''_x \frac{c}{\omega} \right) e^{i(\omega t - \mathbf{k}''\mathbf{x})} \quad (2.3.34)$$

In the term

$$\left(1 - Mk_x \frac{c}{\omega}\right) \quad (2.3.35)$$

k_x can be substituted by equation 2.3.17 and one obtains

$$\eta = \frac{1}{1 + n_x M}. \quad (2.3.36)$$

The same procedure is applied to the transmitted and reflected wave. For the further derivation it is essential to consider the boundary condition in detail. Following Ribner (1956) the pressure has to be identical on both sides of the shear layer. According to that, one has

$$\rho_o A_\phi \eta e^{i(\omega t - \mathbf{k} \mathbf{x})} + \rho_o A''_\phi \eta'' e^{i(\omega t - \mathbf{k}'' \mathbf{x})} = \rho'_o A'_\phi \eta' e^{i(\omega t - \mathbf{k}' \mathbf{x})}. \quad (2.3.37)$$

Now, the question arises what is the second boundary condition: Continuity of velocity or displacement? The acoustic community was engaged in a controversy about this issue for several decades. A brief historical review was given by Campos (1986). Early references as Rayleigh (1879), Keller (1955) and Ingard and Franken (1956) base on the assumption that the normal velocity is continuous. In contrast to that, authors of later publications have arrived at the conclusion that the continuity of the normal component of displacement must be satisfied (see e.g. Ribner (1956), Ingard (1959)). These days it is generally believed that the latter boundary condition is the correct one because "from a physical point of view, an acoustic wave requires a medium to support it, i.e., the fluid particles must attached to the interface, so that the normal component of the displacement must be continuous; it follows that the normal component of the acoustic velocity is different on the two sides of the interface, e.g., for a jet in still air" (Campos (1986)). Furthermore various experimental results substantiate this boundary condition (see e.g. Amiet (1975), Campos (1978b), Schlinker and Amiet (1980), Ahuja et al. (1981)). Applying the second boundary condition the displacement of the incident wave is

$$s_z(\mathbf{x}, t) = S_z e^{i(\omega t - \mathbf{k} \mathbf{x})}. \quad (2.3.38)$$

Consequently, the particle velocity results to

$$v_z(\mathbf{x}, t) = \frac{\partial s_z(\mathbf{x}, t)}{\partial t} + U \frac{\partial s_z(\mathbf{x}, t)}{\partial x}. \quad (2.3.39)$$

Again, the particle velocity consists of the temporal variation and the convective part caused by the flow in x -direction. Employing equation (2.3.17) and equation (2.3.36) one yields for equation (2.3.39)

$$v_z(\mathbf{x}, t) = S_z i \omega \eta e^{i(\omega t - \mathbf{k} \mathbf{x})}. \quad (2.3.40)$$

The particle velocity $v_z(\mathbf{x}, t)$ can be determined by means of the velocity potential:

$$v_z(\mathbf{x}, t) = \frac{\partial(\phi)}{\partial z} = -A_\phi i k_z e^{i(\omega t - \mathbf{k}\mathbf{x})} \quad (2.3.41)$$

Using the equations (2.3.14), (2.3.17) and (2.3.36) k_z can be expressed by

$$k_z = n_z \eta \frac{\omega}{c}. \quad (2.3.42)$$

By combining the equations (2.3.40), (2.3.41) and (2.3.42) one obtains for the third component of the particle displacement:

$$S_z = \frac{-A_\phi n_z}{c}. \quad (2.3.43)$$

The determination of the particle displacement from the transmitted and reflected wave can be performed in the same way. It results for the displacement of the shear layer:

$$\frac{A_\phi n_z}{c} e^{i(\omega t - \mathbf{k}\mathbf{x})} + \frac{A''_\phi n''_z}{c} e^{i(\omega t - \mathbf{k}''\mathbf{x})} = \frac{A'_\phi n'_z}{c'} e^{i(\omega t - \mathbf{k}'\mathbf{x})}. \quad (2.3.44)$$

Resolving to A''_ϕ leads to

$$A''_\phi = \frac{\frac{A'_\phi n'_z}{c'} e^{i(\omega t - \mathbf{k}'\mathbf{x})} - \frac{A_\phi n_z}{c} e^{i(\omega t - \mathbf{k}\mathbf{x})}}{\frac{n''_z}{c} e^{i(\omega t - \mathbf{k}''\mathbf{x})}}. \quad (2.3.45)$$

Then, the solution for A''_ϕ is substituted in equation (2.3.37):

$$\begin{aligned} \rho_o A_\phi \eta e^{i(\omega t - \mathbf{k}\mathbf{x})} + \left(\frac{\frac{A'_\phi n'_z}{c'} e^{i(\omega t - \mathbf{k}'\mathbf{x})} - \frac{A_\phi n_z}{c} e^{i(\omega t - \mathbf{k}\mathbf{x})}}{\frac{n''_z}{c} e^{i(\omega t - \mathbf{k}''\mathbf{x})}} \right) \rho_o \eta'' e^{i(\omega t - \mathbf{k}''\mathbf{x})} \\ = \rho'_o A'_\phi \eta' e^{i(\omega t - \mathbf{k}'\mathbf{x})}. \end{aligned} \quad (2.3.46)$$

This simplifies to

$$\begin{aligned} \rho_o A_\phi \eta e^{i(\omega t - \mathbf{k}\mathbf{x})} + \frac{\rho_o c A'_\phi n'_z \eta'' e^{i(\omega t - \mathbf{k}'\mathbf{x})}}{c' n''_z} - \frac{\rho_o A_\phi n_z \eta'' \eta e^{i(\omega t - \mathbf{k}\mathbf{x})}}{n''_z} \\ = \rho'_o A'_\phi \eta' e^{i(\omega t - \mathbf{k}'\mathbf{x})}. \end{aligned} \quad (2.3.47)$$

The wavenumber vectors \mathbf{k} , \mathbf{k}' and \mathbf{k}'' only differ in the third component. Furthermore it is $n''_z = -n_z$ and $\eta = \eta''$. The shear layer is located at the position $z = z_s$ and subsequently, it yields by taking into account the made assumptions

$$\rho_o A_\phi n_z \eta e^{-ik_z z_s} - \frac{c}{c'} \rho_o A'_\phi n'_z \eta e^{-ik'_z z_s} + \rho_o A_\phi n_z \eta e^{-ik_z z_s} = \rho'_o A'_\phi n_z \eta' e^{-ik'_z z_s}. \quad (2.3.48)$$

Finally, the transmission factor T_ϕ associated with the velocity potential is given by

$$\frac{A'_\phi}{A_\phi} = \left(\frac{2\rho_o\eta n_z}{\rho'_o\eta' n_z + \frac{c}{c'}\rho_o n'_z \eta} \right) \left(\frac{e^{-ik_z z_s}}{e^{-ik'_z z_s}} \right). \quad (2.3.49)$$

This equation simplifies to

$$T_\phi = \left(\frac{2\eta n_z}{\eta' n_z + n'_z \eta} \right), \quad (2.3.50)$$

when using the fact that the density and the temperature are equal on both sides of the shear layer and therewith it holds $c = c'$ and that the shear layer position is at $z_s = 0$. Employing equation (2.3.32) the transmission coefficient with respect to the pressure determines to

$$T_p = \left| \frac{p'}{p} \right| = \left| \frac{\eta' \phi'}{\eta \phi} \right| = \left| \frac{\eta'}{\eta} T_\phi \right| = \frac{\eta'}{\eta} \left(\frac{2\eta n_z}{\eta' n_z + n'_z \eta} \right). \quad (2.3.51)$$

Alternatively T_p can be given in the form of

$$T_p = \frac{2n_z(1 + n_x M)}{n'_z(1 + n'_x M) + n_z(1 + n_x M)}. \quad (2.3.52)$$

The transmission factor T_p depends solely on the x and z components of the incident and transmitted wave normal vectors \mathbf{n} and \mathbf{n}' and the Mach number. This solution is valid provided that the transmitted wave exists and subsequently, it is interesting to know the limiting case when total reflection occurs which is the case in the so-called "zone of silence". No transmitted wave exists for subsonic Mach numbers in an area upstream of the source where $n'_x = -1$. Using this relation and the equation (2.3.21) one obtains

$$n_{x,0} = \cos \vartheta_0 = \frac{1}{1 + M}. \quad (2.3.53)$$

For a Mach number of 0.1 total reflection of the incoming wave at the shear layer will be present at angles of incidence of $\vartheta \leq 24.6^\circ$. The refraction and total reflection of sound waves at a plane zero thickness shear layer are exemplarily shown in figure 2.8.

Amplitude divergence

After the refraction and transmission through the shear layer the amplitude variations of the sound waves in the quiescent part of the fluid domain remain an issue. It will be shown that they do not follow the initial spherical divergence by means of the concept of rays which will be briefly introduced below, following the formulations of Pierce (1981) and Dowling

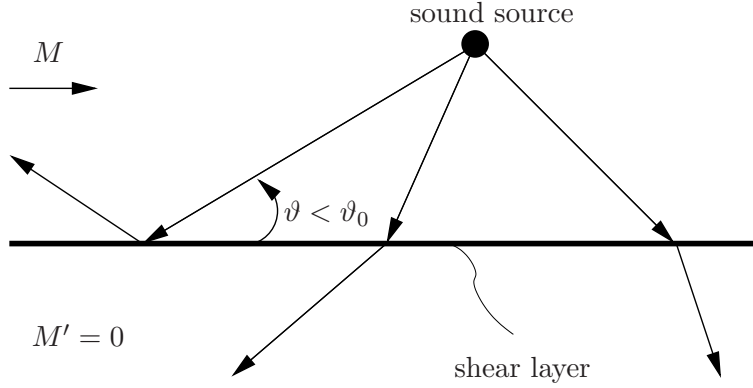


Figure 2.8: Refraction and total reflection of sound waves at a plane zero thickness shear layer.

and Ffowcs Williams (1983). Assuming that the sound waves move in a quiescent fluid with constant sound speed and constant ambient density, then they will satisfy the wave equation of the form

$$\left(\frac{1}{c^2} \frac{\partial^2}{\partial t^2} - \nabla^2 \right) p = 0 \quad (2.3.54)$$

In the current context it is beneficial to express the time harmonic solution of the wave equation as a power series in inverse powers of ω :

$$p(\mathbf{x}, t) = e^{i\omega[t - \mathcal{T}(\mathbf{x})]} \sum_{\mathcal{N}=0}^{\infty} \frac{1}{(i\omega)^{\mathcal{N}}} A_{\mathcal{N}}(\mathbf{x}, \omega). \quad (2.3.55)$$

Such a power series is a so-called ray series. When the wave arrives at \mathbf{x} at time $\mathcal{T}(\mathbf{x})$, which constitutes the so-called phase function, the set of all points satisfying $t = \mathcal{T}(\mathbf{x})$ describes the corresponding wavefront at time t . Rays are defined as curves which are everywhere normal to the wave fronts. The insertion of equation (2.3.55) into equation (2.3.54) yields

$$\begin{aligned} & \sum_{\mathcal{N}=0}^{\infty} \frac{1}{(i\omega)^{\mathcal{N}}} \left\{ (i\omega)^2 \left[(\nabla \mathcal{T})^2 - \frac{1}{c^2} \right] A_{\mathcal{N}} \right\} \\ & + \sum_{\mathcal{N}=0}^{\infty} \frac{1}{(i\omega)^{\mathcal{N}}} \left\{ -i\omega [2\nabla A_{\mathcal{N}} \cdot \nabla \mathcal{T} + A_{\mathcal{N}} \nabla^2 \mathcal{T}] \right\} \\ & + \sum_{\mathcal{N}=0}^{\infty} \frac{1}{(i\omega)^{\mathcal{N}}} \left\{ \nabla^2 A_{\mathcal{N}} \right\} = 0. \end{aligned} \quad (2.3.56)$$

If one limits our considerations to high-frequency waves, only the leading amplitude term A_0 is important, because A_1 is divided by ω , A_2 by ω^2 etc. and thus, the higher order terms are negligible as long as ω is sufficiently

high enough. By solving equation (2.3.56) in the high-frequency limit the coefficient of each power of ω must vanish identically in order that the equation is true for all values of ω . Zeroing the coefficient of the highest power of ω one obtains

$$(\nabla\mathcal{T})^2 - \frac{1}{c^2} = 0. \quad (2.3.57)$$

This is the so-called *eikonal equation* which is a nonlinear first order partial differential equation of hyperbolic type. One encounters this type of equation in many various fields in physics. Following [Rienstra and Hirschberg \(1999\)](#) it can always be reduced to an ordinary differential equation and can be solved along characteristics which correspond to ray paths in this acoustic context. Applying the condition to the coefficient of ω , since it must vanish also, this results in the *transport equation*

$$2\nabla A_0 \cdot \nabla\mathcal{T} + A_0\nabla^2\mathcal{T} = 0 \quad (2.3.58)$$

describing the *conservation of energy*. The solution can be derived in terms of *ray-tube areas* for equation (2.3.58). The concept of ray tubes is similar to the concept of stream tubes in fluid mechanics. A ray tube passing from \mathbf{x}_0 to \mathbf{x} is defined as a tube whose boundary consists of rays, as shown in figure 2.9. All rays pass through the tiny finite area $S(\mathbf{x}_0)$ centered at \mathbf{x}_0

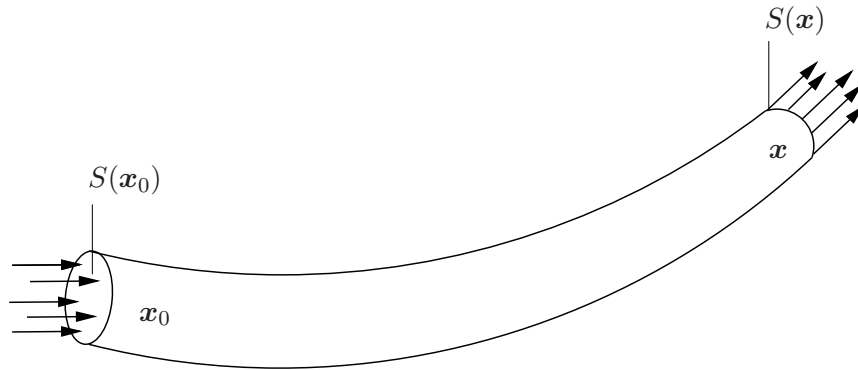


Figure 2.9: Sketch of a ray tube.

transverse to the ray path. The cross-sectional area $S(\mathbf{x})$ of the ray tube is a function of \mathbf{x} , so that the ray-tube cross-section at \mathbf{x} will be $S(\mathbf{x})$. In order to obtain a solution of equation (2.3.58) one integrates the equation over the volume of ray-tube segment connecting \mathbf{x}_0 and \mathbf{x} and applies the divergence theorem of Gauss to convert it from a volume integral into a surface integral. The surface integral over the ray-tube sides vanishes identically, since the rays propagate parallel to side boundaries of the ray tube and only the two ray-tube ends contribute to the integral. Finally, it results in an expression which directly relates the pressure amplitudes $A(\mathbf{x})$ with the cross-sectional

area $S(\mathbf{x})$ at the position \mathbf{x} of the ray tube:

$$A(\mathbf{x}) = A(\mathbf{x}_0) \left(\frac{S(\mathbf{x}_0)}{S(\mathbf{x})} \right)^{1/2}. \quad (2.3.59)$$

Consequently, the amplitude variation of diverging or converging rays tubes can be simply calculated in terms of the cross-sectional area of the ray tube (see e.g. Morfey and Joseph (2001)). Applying the concept of ray tubes to the shear layer problem the sound waves, emitted by the source inside the flow, propagate along the ray path until the infinitely thin shear layer is reached at the point $\mathbf{x}_{s_m} = [x_{s_m}, y_{s_m}, z_s = 0]^T$. The ray path changes its direction at this point due to refraction at the shear layer before reaching the m -th microphone. In practice, the ray tube can be approximated by four rays emanating from the source and intersecting the shear layer at the points $\mathbf{x}_{s_m}^{(1)} = [x_{s_m}, y_{s_m} + dy, z_s = 0]^T$, $\mathbf{x}_{s_m}^{(2)} = [x_{s_m} - dx, y_{s_m}, z_s = 0]^T$, $\mathbf{x}_{s_m}^{(3)} = [x_{s_m}, y_{s_m} - dy, z_s = 0]^T$ and $\mathbf{x}_{s_m}^{(4)} = [x_{s_m} + dx, y_{s_m}, z_s = 0]^T$ forming a quadrangle with the surface area $S_{B,m}$, whereas dx and dy are infinitesimal distances. The spreading of the ray tube depends on the individual refraction of the four rays and thus, the amplitude measured by the m -th microphone depends on the divergence or convergence of the ray tube which illustrated in figure 2.10. The four rays, constituting the ray tube, will intersect the

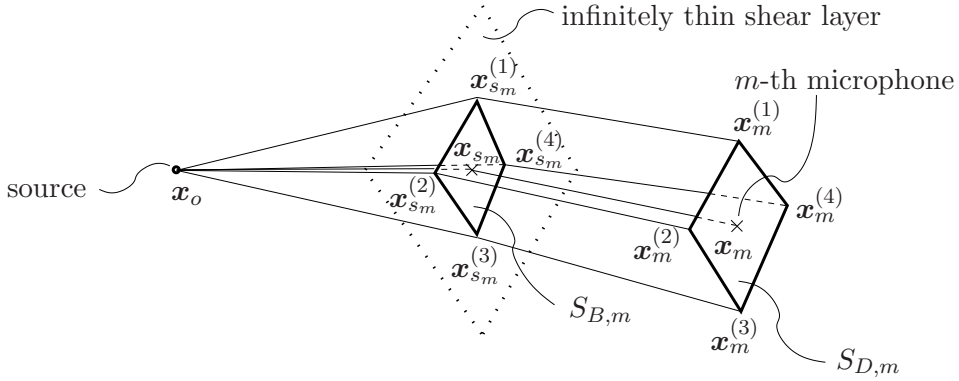


Figure 2.10: Ray tube spreading caused by the shear layer.

plane which incorporates the position of the m -th microphone and which is parallel to the plane spanned by the infinitely thin shear layer at the points $\mathbf{x}_m^{(1)}$, $\mathbf{x}_m^{(2)}$, $\mathbf{x}_m^{(3)}$ and $\mathbf{x}_m^{(4)}$ forming the quadrangle with the surface area $S_{D,m}$. Finally, the easily computable surface areas $S_{B,m}$ and $S_{D,m}$ in combination with equation (2.3.59) can be used to correct the measured amplitude for the ray-tube spreading.

Amplitude correction

The effects influencing the amplitude of a spherical sound wave traveling on their way from the source at \mathbf{x}_o to the observer \mathbf{x}_m in the open test section are summarized in the following. Within the parallel mean flow the sound wave amplitude undergoes a spherical divergence which is superimposed by the convective flow and the convective amplification. The influence of these effects on the amplitude is subject of equation 2.3.7. After reaching the plane shear layer an amount of the incident wave energy is transmitted and while the rest is reflected at the shear layer. The relation between the incident and transmitted wave amplitudes is given by equation 2.3.52. Then, the transmitted wave propagates through the quiescent medium to the observer and the amplitude is finally affected by the ray tube divergence formulated in equation 2.3.59 which arises from the differing refraction of the sound waves at the shear layer. The total amplitude changes of the sound waves have to take into account in the steering vector formulation 2.2.9 in order to compensate for these effects. Furthermore, the sound wave amplitudes will be influenced by the scattering of sound waves at the shear layer turbulence. Currently, no practical correction procedure is available in order to take into account this effect.

Comments to the shear layer model of Amiet

The Amiet shear layer model is widely used for the microphone array processing of aeroacoustic data due to its simplicity and practicability. In spite of making many confinements, and sometimes they are of conflicting kind as the requirements to the wavelengths with respect to the infinitely thin shear layer and the to the validity of the acoustic ray theory, one can obtain good results for realistic open jet wind tunnel conditions. The validity of this vortex-sheet model was verified experimentally by Amiet (1975) using a point source in an open jet and by numerical simulations (Amiet (1978)). Larger deviations occur upstream in the vicinity of the zone of silence.

2.3.3 Turbulent scattering and spectral broadening

As briefly pointed out in section 1.2.2 the phenomena of scattering and spectral broadening of sound by turbulence can effect the accuracy of aeroacoustic measurements and consequently, beamforming results may be affected. Therefore it is reasonable to look at these effects more in detail.

Lighthill (1953) was one of the first who examined intensively the scattering of plane sound waves by turbulence. He confined the problem to inhomogeneities which vary in space alone, on the basis of the assumption that the temporal variations are negligible during the time of passage of an incident wave. Thus in the case of the propagation of sound through turbulence he has assumed that the turbulence is frozen for the duration of

the interaction and he neglects the influence of mean flow. In his theoretical work he identified important parameters influencing the phenomena of scattering per unit time from unit volume of turbulence with respect to the scattered energy and the directional distribution. On the one hand, the effectiveness of a component of the turbulence in scattering the sound was found to depend on the Mach number of the mean square velocity of the turbulent disturbances, while on the other hand the ratio of the correlation length of the turbulent eddies and the wavelength of the incident sound is important. The scattered energy increases with the growing of these particular values. With the additional assumption of isotropic and homogeneous turbulence he further derived predictions about the directional distribution of the scattered sound field and obtained further information about the scattered energy. In the case of long sound waves compared with the typical length-scale of the main energy-bearing eddies (Taylor's macro scale of turbulence) the bulk of scattered energy is relatively small and its directional maximum is opposite to the direction of the incident wave. More energy is scattered when the sound wavelength is smaller than the macro-scale of turbulence. In this case the scattering angle, namely the difference between the propagation angle of incident and scattered wave, vanishes indicating a strong forward scatter so that the scattered waves are confined in a small cone around the not scattered wave path. The further evaluation of the scattering theory of [Lighthill \(1953\)](#) shows, that if sound of a wavelength less than the typical length of the energy-dissipating eddies (Taylor's micro-scale of turbulence) multiple successive scattering takes place and the scattering will become uniform (i.e. quite random) in its directional distribution. Physically the assumption of frozen turbulence having no mean flow simplifies the theory because it restricts all scattered waves to be of the same frequency as the incident wave. Therefore, [Howe \(1973\)](#) has abandoned this simplification and has extended the scattering theory of [Lighthill \(1953\)](#) in terms of temporally evolving inhomogeneities (as they occur in the atmosphere), again, without considering mean flow. He noted that the presence of temporal fluctuations actually tends to broaden the spectrum of frequencies, a phenomenon essentially distinct from spatial scattering. The spectral broadening of sound waves by turbulence was actually observed in wind tunnel experiments by [Candel et al. \(1975\)](#) conducting combined aerodynamic and aeroacoustic measurements. They found that a monochromatic test tone generated by an acoustic source inside the potential core of the jet is received outside, by using a microphone, as a broadened frequency spectrum resulting from the sound transmission through the turbulent shear layer. The tone broadening is schematically depicted in figure [2.11](#). The broadened spectrum is characterized by a reduced tone amplitude (compared with no flow case) and two lateral bands which exhibit both a local maximum. According to [McAlpine et al. \(2009\)](#) the depicted case in figure [2.11](#) is termed "weak scattering", since the proportion of scattered energy is small relative to the

energy that remains in the tone so that the tone is clearly distinguishable in the spectrum. This means that some part of the acoustic sound wave energy can propagate through the shear layer without being affected by scattering.

”Strong scattering” is existent when the original tone itself disappears in the ”haystack” and is replaced by a broadband hump. [Candel et al. \(1975\)](#) figured out that the frequency difference of the local maxima and the tone in the side bands are independent of tone frequency, but proportional to the flow velocity and inversely proportional to the shear layer thickness. In addition, he performed correlations between the turbulent velocity fluctuations in the shear layer using hotwires and the acoustic pressure fluctuations measured by microphones. He came to the conclusion that the large scale

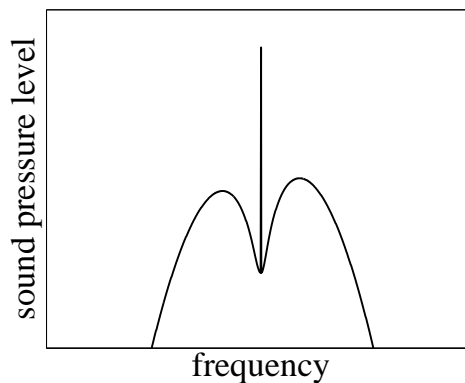


Figure 2.11: Schematic sketch of ”weak” spectral broadening of a monochromatic tone by a shear layer.

main energy-bearing eddies provide the essential contribution to the scattered acoustic field. The underlying Doppler effect caused by the convected turbulence is responsible for the frequency shift and is associated with the large eddy convection velocity. More precisely, the Doppler shift of the tone frequency is proportional to the ratio of the local eddy convection velocity and the length-scale of the large eddies. Moreover, the scattered acoustic energy increases by positioning the source and the observer more downstream which is a result of an increased shear layer thickness so that the sound wave has to propagate longer through the turbulent medium. In situations where the wavelength is small compared to the length-scale of the large eddies the scattering angle is small and the microphone receives energy mainly scattered by the turbulence volume surrounding the source-microphone line. This forward scatter phenomenon was already predicted by [Lighthill \(1953\)](#) in his theoretical study, but [Candel et al. \(1975\)](#) succeeded in verifying this prediction experimentally. The seminal work of [Candel et al. \(1975\)](#) gave the starting signal for further similar experimental studies examining the phenomenon of spectral broadening and scattering in the late 70’s and early 80’s (see e.g. [Candel et al. \(1976\)](#), [Ahuja et al. \(1978\)](#), [Schlinker and Amiet \(1979\)](#), [Schlinker and Amiet \(1980\)](#), [Ahuja et al. \(1981\)](#), [Ross \(1981\)](#), [Ross et al. \(1983\)](#)). This period of scientific Storm and Stress was followed by a break of almost two decades until the attention of the aeroacoustic community turned back to this phenomenon resulting in further experimental studies (see e.g. [Ezerskii et al. \(2000\)](#), [Sijstma \(2010\)](#), [Tibbe \(2010\)](#)). In general, these studies verified the experimental and theoretical results ob-

tained by [Candel et al. \(1975\)](#). An exception are merely the results from [Sijstma \(2010\)](#). The broadened spectra, measured in the open test section of the DNW-LLF, differ in some extent strongly from the [Candel et al. \(1975\)](#) results. The reason for that is still unclear so far. The important findings of the other publications are briefly summarized in the following. [Ahuja et al. \(1978\)](#) found in their experimental study that the scattering of discrete tones and broadband noise becomes more dominant only when the ratio of shear layer thickness and wavelength approaches a value of 10 and becomes more significant at higher free jet Mach number. [Schlinker and Amiet \(1980\)](#) pursued a more formal approach for deriving a criterion for the onset of scattering being important. From the scattering theory of [Lighthill \(1953\)](#) they deduced the dimensionless scattering parameter $M\delta_s/\lambda$ whereas δ_s denotes the shear layer thickness. By means of their experimental data they observed that the scattering becomes important for values above 0.5 for the scattering parameter. This observation could be verified by the experimental study of [Ross \(1981\)](#). [Schlinker and Amiet \(1980\)](#) also noted, that directional scattering is a prerequisite to frequency scattering which thus results in spectral broadening. The direction scattered sound which now arrives at the observer position has a different frequency compared with the original source frequency caused by the Doppler shift. As already mentioned, in some time segments there is no large-scale eddy present in the respective shear layer volume when the sound wave propagates through the shear layer. In this case the sound wave will not undergo scattering, neither directional nor frequency scattering. Solely, the sound ray path will be refracted by the mean flow velocity gradient in the shear layer. Scattering volumes of the shear layer located downstream of this just described ray path (unaffected, but refracted) cause a Doppler shift to lower frequencies. In contrast, upstream scattering volumes lead to a shift to higher frequencies.

If the scattering is sufficiently strong the resulting measured spectrum will be a broad hump with no perceptible discrete tone, since frequency and directional scattering dominate the sound transmission through the shear layer. Besides the remarkable number of mainly experimental publications, only a few theoretical studies aiming at the modeling of directional and frequency scattering are available which intend to provide a prediction and correction procedure for the scattering effects as for instance proposed by [Campos \(1978a,b\)](#), [Guedel \(1985\)](#) and [McAlpine et al. \(2009\)](#). All of these authors came back to the experimental data of [Candel et al. \(1975\)](#) and used them to evaluate their models assuming weak scattering. The model of [Campos \(1978a,b\)](#) incorporates an irregular and unsteady interface across which the properties of the flow change discontinuously. This model suffices when the wavelength greatly exceeds the mean shear-layer width, but at higher frequencies it is necessary to take account of the details of the flow in the interior of the shear layer. Therefore he combined the low frequency model with an approximation based on geometrical acoustics in order to pro-

vide also corrections for the propagation of higher frequency sound through the turbulent shear flow. [Guedel \(1985\)](#) adjusted the Born and Rytov approximation (assuming single scattering), which originates from the optical theory of scattering from inhomogeneous media (see e.g. [Born and Wolf \(2010\)](#)), to the turbulent shear flow configuration. The scattering process can also be modeled analytically using an approximate form of Lilley's equation ([Lilley \(1973\)](#)) as shown by [McAlpine et al. \(2009\)](#). The crucial point of these approaches is related to the modeling of the turbulence, since the turbulence characteristics constitute the features of the broadened spectrum. By using the measured flow quantities of the experiment of [Candel et al. \(1975\)](#) the various authors were approximately able to reproduce qualitatively the double-humped shape of the broadened spectrum employing their models. Nevertheless, there are strong quantitative differences in the simulated results compared with the measurements.

In the previously mentioned experimental and theoretical studies the main focus was rather lying on the considerations of single microphone measurements than on phased microphone array processing. Besides the amplitude changes the scattering also influences the signal phases. The scattering distorts the original spatial coherent signals (having a definite phase relation) leading to decorrelation. [Brooks and Humphreys \(1999\)](#) have examined these scattering influences on beamforming results using different array sizes in open jet wind tunnel measurements. They observed that results from larger arrays are more affected by scattering than smaller arrays. This effect depends primarily on the microphone separation. The larger the distance between the sensors the higher the degree of decorrelation. The decorrelation leads typically to a lower spatial resolution, a decrease in the SNR and reduced peak levels in the source maps, because the beamforming process makes only use of the coherent part of the signals. Furthermore, the integrated source levels are decreased. In order to reduce the influence of turbulent scattering one can apply a shading procedure as performed by [Brooks and Humphreys \(1999\)](#) and [Oerlemans et al. \(2007\)](#). This procedure aims at the reduction of the effective array size. Typically, the chosen effective array diameter is inversely proportional with frequency, so that for higher frequencies smaller arrays find use having the drawback of a reduced resolution caused by the smaller aperture.

Another interesting concept was proposed by [Ehrenfried et al. \(2005\)](#). The idea is to use a known signal, e.g. test tone, in array measurements to correct the phase fluctuations induced by the shear layer turbulence at all microphones. This approach is deduced from the "guide star" methods applied at astrophysical telescopes where an adaptive optic is used to correct the unsteady distortions of light waves in the turbulent atmosphere. It was experimentally demonstrated that the phase fluctuations of the acoustic signal could be compensated and thus, the cross-correlation coefficient could be significantly increased. [Sijstma \(2008\)](#) applied the "guide star" concept

to measurements on an A320 model in the open jet of the DNW-LLF. A tiny loudspeaker was mounted on the model emitting the tone needed for the guide star method. He obtained promising results as long as some requirements are met. The directivity of the used loudspeaker and the extreme high computational effort constitute a restriction for practical applications.

[Dougherty \(2003\)](#) has incorporated a turbulence model in the beamforming process in order to take into account the influence of turbulence scattering by introducing the transverse mutual coherence function (MCF). The MCF predicts the effect of the array diameter on the turbulence scattering depending on the choice of the turbulence model with its statistical properties (here von Kármán model) and the separation between the microphones. He evaluated his approach by means of open test section data measured by [Brooks and Humphreys \(1999\)](#) and closed test section data generated by [Storms et al. \(1998\)](#). The predicted results match some of the measurement data, but not all, so that there are still some uncertainties regarding the modeling of the turbulence and the scattering process.

At present, the obtained results from the theoretical modelings and the experimental correction procedures are not satisfactorily or even inadequate in order to provide practical corrections for measurement data in terms of directional and frequency scattering. The current situation can be summarized as follows. The measured microphone signals are potentially affected by turbulence in the shear layer leading to amplitude and phase fluctuations and changes. In the case of underlying broadband signals the effect of spectral broadening on the measured amplitude in single microphone measurements is negligible, provided that weak scattering is dominant. On the one hand each small frequency band loses energy by scattering, but on the other hand it also gets back approximately the same energy amount from the other subbands by the same scattering process. This statement does not hold for pure tones as explained above in this section so that the interpretation of broadened spectra can be very challenging. In phased microphone array application the phase distortions and the accompanied decorrelation effects are of major concern, because they can degrade the quality and quantity of the source maps and integrated spectra. Applying shading is currently the only reliable and widely used procedure to reduce the impact of scattering on the beamforming results. Besides that the scattering parameter $M\delta_s/\lambda$ can be used to predict approximately the onset when scattering becomes important.

In general, the influence of turbulent scattering will be typically assumed to be insignificant for boundary layers, because of the small thickness compared with the wavelength. For boundary layers this effect might become important for very high frequencies, but there are almost no studies available concerning this matter. In contrast to that, the great majority of the previously published studies is related to scattering by turbulent shear layers.

The bispectrum and three-wave coupling

The phenomenon of spectral broadening can be modeled in a very simple way by means of the widely used concept of three-wave coupling (see [Nikias and Petropulu \(1993\)](#)). In this concept two primary waves having the annular frequency ω_m and ω_n interact with each other and generate a third wave at their sum (or difference) annular frequency $\omega_l = \omega_m \pm \omega_n$. Assuming that a measured time series contains information about all three waves, then the Fourier transformation of this series is given by the complex-valued spectrum $X(\omega)$. Based on $X(\omega)$ the power spectrum can be easily computed using the second order moment spectrum (auto powers)

$$\mathcal{M}_2^x(\omega) = E\{X(\omega)X(\omega)^*\}, \quad (2.3.60)$$

where the asterisk denotes the complex conjugate. The real-valued power spectrum exhibits information about the spectral power distribution and in respect of the current time series, it provides information about the presence of the three waves at ω_m , ω_n and $\omega_m \pm \omega_n$. This linear spectral analysis technique is obviously of limited value when there is a nonlinear interaction between spectral components. In such a case, higher order spectral techniques are required to characterize the measured signal, since the wave-coupling results in new spectral components which are phase coherent. In the case of quadratic wave coupling the detection of such phase coherent signal contents can be carried out by means of the third order moment spectrum, the so-called complex-valued bispectrum:

$$\mathcal{M}_3^x(\omega_m, \omega_n) = E\{X(\omega_m)X(\omega_n)X^*(\omega_m \pm \omega_n)\}. \quad (2.3.61)$$

The application of an adequate normalization of the bispectrum yields the real-valued bicoherence spectrum

$$B_c(\omega_m, \omega_n) = \frac{|\mathcal{M}_3^x(\omega_m, \omega_n)|}{\sqrt{\mathcal{M}_2^x(\omega_m)\mathcal{M}_2^x(\omega_n)\mathcal{M}_2^x(\omega_m \pm \omega_n)}}. \quad (2.3.62)$$

The bicoherence spectrum is a measure of the coherence between the three waves due to quadratic wave coupling. In particular, it can be used to discriminate between nonlinearly coupled waves and spontaneously excited waves. As a result of the normalization of the bispectrum by the second order moments the bicoherence takes on values between 0, indicating a spontaneously excited wave, and 1 which refers to the presence of the wave coupling phenomenon. The bispectrum and the related bicoherence spectrum have been widely used for analysis of signals arising from various physical mechanisms. For example, [Lii et al. \(1976\)](#) examined the energy transfer and dissipation in turbulence by means of bispectral estimates. Also [Kim and Powers \(1979\)](#) and [Kim et al. \(1980\)](#) investigated the nonlinear wave-wave

interaction of coherent waves in plasma by examining the phase coherence among waves.

The application of the three wave-coupling model to the current problem of the sound propagation through turbulent shear layers would establish the following process. The incident monochromatic acoustic sound wave with frequency $\omega_m = \omega_{tone}$ is modulated by the turbulent shear layer fluctuations which are modeled as a wave packet having spectral components at ω_n . The nonlinear wave-wave interaction leads to a broadened spectrum which is measured by an out-of-flow microphone. The measured spectrum contains, besides the tone frequency, spectral components at $\omega_{tone} \pm \omega_n$ as a result of the nonlinear interaction. Now, applying higher order spectral analysis by computing the bicoherence spectrum can give information about which spectral components are related to the original tone. This fact cannot be provided by the power spectrum without having a priori information about the involved physical process or details about the source spectrum. The bicoherence spectrum is able to accomplish that as long as the sensor signal contains information about all spectral components which are involved in the three wave coupling process. This point seems to be the crux of this approach concerning the application to microphone measurements outside the open jet. It requires that the turbulent fluctuations, which modulate the incident monochromatic wave, generate sound which has to be radiated as acoustic waves so that the microphone receives the corresponding pressure fluctuations at ω_n . If this information is missed or insufficiently low in the measured microphone signal the bispectral analysis will fail. Supposing that the bicoherence analysis results in values close to zero then the following cases are conceivable. On the one hand it could mean that there is really no wave coupling phenomenon present or on the other hand wave coupling occurs, but the measured signal contains too less information about the modulation process with the spectral components at ω_n . In turn, it appears paradox that in the closed test section a flush-mounted microphone in the wind tunnel wall would acquire this required information about the pressure fluctuations of the boundary layer, but for such measurements the effect of spectral broadening is typically negligible, because of the small boundary layer thickness compared with sound wavelength. Nonetheless, in this thesis the concept of the bicoherence spectrum is applied to single microphone measurements of tonal sound in order to evaluate the possibility to identify the broadened components of tone spectra after the sound propagation through turbulent shear layers.

2.3.4 Absorption

In the previous section dealing with scattering of sound by turbulence it was implicitly assumed that the turbulence is unchanged by the passage of sound, and accordingly that all of the energy diverted from the incident wave reap-

pears as sound elsewhere in the medium. This approximation is acceptable only if the characteristic time scale of the turbulence is significantly different from that of sound. When this is not the case a substantial amount of acoustic energy may be absorbed by turbulence as examined theoretically by Howe (1984). The absorption is caused by the rotation and stretching of the turbulence vortex lines by sound, i.e. by the strain imposed by the acoustic field. The evolution of turbulence due to non-linear self-interactions during the period of strain then provides the degree of irreversibility necessary to achieve a net transfer of energy from sound to turbulence. Now the attenuation is maximal when the turbulence time scale is of the same order as that of sound. However, Ahuja et al. (1978) performed experiments to determine the extent of wave absorption by turbulence in the shear layer of an open jet wind tunnel. They found that for frequencies below 30 kHz, the effect of turbulence absorption was not important for the attenuation of sound waves. Typically, the impact of sound absorption by turbulence is considered as less important compared with the influence of scattering. At the moment, no one has developed a reliable correction procedure so that this effect is generally ignored in aeroacoustic measurements.

2.4 Source type and directivity effects

This section considers the question whether the source type and directivity effects may influence the results derived from the DSB. Particularly with regard to aeroacoustic sound generation this issue becomes important, since aeroacoustic sources of practical interest have typically dipole or quadrupole characteristics (Crighton (1990)). For example, the most dominant airframe noise sources (landing gear and high-lift devices) can often be modeled as baffled dipoles or free acoustic dipoles (Soderman et al. (2002), Dobrzynski (2010)) generating roughly a sound field with a figure-8 directivity. Therefore, the following analysis focuses on the characteristic of dipole sources and compares their properties with monopole sources.

Dipole sources can be easily modeled as superposition of a pair of closely spaced coherent monopole sources with opposite phase at distance \mathbf{d} apart (see e.g. Pierce (1981)). For the medium at rest, the inhomogeneous wave equation with the dipole source term on the right side reads as:

$$\left(\frac{1}{c^2} \frac{\partial^2}{\partial t^2} - \nabla^2 \right) p = -q(t) [\delta(\mathbf{x} - \mathbf{x}_o) - \delta(\mathbf{x} - \mathbf{x}_o - \mathbf{d})]. \quad (2.4.1)$$

The two coherent monopole sources are located at \mathbf{x}_o and $\mathbf{x}_o - \mathbf{d}$, respectively. This modeling correspond to a point dipole as long as the distance $d = |\mathbf{d}|$ is small enough to ensure that $kd \ll 1$. In this limit and provided that the observer \mathbf{x}_m is far enough away so that $|\mathbf{x}_m - \mathbf{x}_o| \gg d$ holds the dipole source strength can be approximated with a truncated Taylor series

2.4. SOURCE TYPE AND DIRECTIVITY EFFECTS

as $-\nabla \cdot [q(t)\mathbf{d}\delta(\mathbf{x} - \mathbf{x}_o)]$. Then, the free-field solution of equation 2.4.1 is given by

$$p(\mathbf{r}_m, t) = \frac{1}{4\pi} \mathbf{r}_m \left[\frac{1}{r_m^2} + \frac{1}{r_m c} \frac{\partial}{\partial t} \right] \cdot \frac{q(t - r_m/c)}{r_m} \mathbf{d}, \quad (2.4.2)$$

whereas $\mathbf{r}_m = \mathbf{x}_m - \mathbf{x}_o$ denotes the distance vector between the source and the observer having the absolute value $r_m = |\mathbf{r}_m|$. The first term in the bracket is the near-field term characterized by the $1/r_m^2$ decay. If one is only interested in the sound radiated into the far-field, this term can be discarded. Finally, the Fourier transformed far-field solution can be expressed by

$$P_{di}(\mathbf{r}_m, \omega) = \frac{Q_{di}(\omega)e^{-i\omega t_{m,o}}}{4\pi r_m} \left[\frac{i\omega}{r_m c} \mathbf{d} \cdot \mathbf{r}_m \right]. \quad (2.4.3)$$

The variable $t_{m,o} = |\mathbf{x}_m - \mathbf{x}_o|/c$ denotes signal travel time from the source to the observer. Differences between the dipole and monopole far-field become apparent by comparing equation 2.4.3 with the free-field solution of a monopole source in the frequency domain (see equation 2.2.6):

$$P_{mono}(\mathbf{r}_m, \omega) = \frac{Q_{mono}(\omega)e^{-i\omega t_{m,o}}}{4\pi r_m}.$$

The monopole solution is in total agreement with the first term of the dipole solution. This particular term is the important one with respect to the source localization via beamforming since it contains the important information about the signal travel time from the source to the receivers. The difference between both sound fields consists of the second term $[i\omega/(r_m c)]\mathbf{d} \cdot \mathbf{r}_m$ in equation 2.4.3. The dipole term is responsible for the typical figure-8 directionality. Primarily, it influences the measured amplitudes by the observer. If the vector \mathbf{d} is perpendicular to the distance vector \mathbf{r}_m then the scalar product $\mathbf{d} \cdot \mathbf{r}_m$ vanishes and the observer receives no sound. In principle, the steering vector formulation for beamforming can be extended in order to take into account the dipole term (Liu et al. (2008)), but this requires prior knowledge about the orientation of the dipole source so that this approach is only applicable for selected configurations.

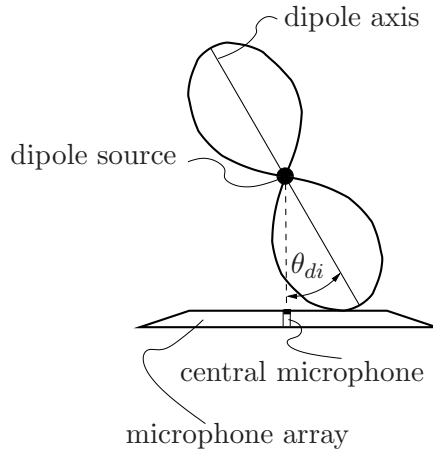


Figure 2.12: Illustration of the dipole orientation angle θ_{di} .

The influence of a dipole source on the beamforming results which base upon the monopole assumption is examined in simulations. The simulated setup consists of a microphone array as it

was employed for measurements in this thesis (see chapter 4.2) and a dipole source. The source-array arrangement corresponds to a typical experimental setup used throughout this thesis (see chapter 4.3). The origin of the coordinate system is located in the middle of the central microphone membrane of the adopted microphone array. The simulated dipole source was modeled by two closely spaced coherent monopoles. One monopole source is located at $[0 \text{ m}, 0 \text{ m}, 0.975 \text{ m}]^T$ and the other at distance $|\mathbf{d}| = 0.001 \text{ m}$ apart. The selected source frequency is exemplarily set to 5 kHz in the simulation ensuring that for the current setup the compactness and far-field condition are fulfilled. The dipole orientation angle θ_{di} is given by $\cos(\theta_{di}) = \mathbf{d} \cdot \mathbf{r} / (|\mathbf{d}| |\mathbf{r}|)$. At $\theta_{di} = 0^\circ$ the dipole main lobe points directly to the central array microphone. Simulations were performed for the three angles of 0° , 45° and 90° . For a dipole orientation angle of 90° there is no sound radiation of the dipole source in the direction of the central array microphone. The computed source maps using the DSB assuming a monopole sound source are depicted in figure 2.13. All maps are normalized with the retrieved source map maximum of the 0° case. For the dipole orientation angle of 0° and

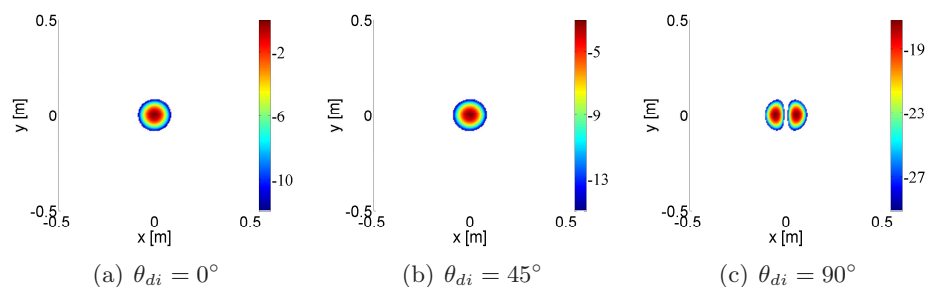


Figure 2.13: Beamforming results of a simulated dipole source at various dipole orientation angles θ_{di} . The plots have a dynamic range of 12 dB from the maximum peak level using the retrieved source map maximum of the 0° case for normalization.

45° the resulting source maps are nearly identical. In both cases the dipole source location can be clearly identified and the difference in the maximum peak level between both angles amounts to 3 dB. A different situation occurs at an angle of 90° when there is only a weak sound emission of the source in the direction of the microphone array. Then, two sources are found in the source maps whereas each source is associated with one of the sources of the monopole pair. The maximum peak level in the map is about 17 dB lower compared with the $\theta_{di} = 0^\circ$ configuration. For the current selected simulation setup one can conclude that the dipole can be correctly localized and the peak level deviations are smaller than 3 dB as long as the dipole axis is arranged within the angular range of $\pm 45^\circ$ with respect to the microphone array center.

Chapter 3

Overview of the employed sound sources

The present chapter deals with the different sound sources used for the comparison of phased microphone array measurements in open and closed wind tunnel test sections.

3.1 General sound source requirements

For the comparison of phased microphone array measurements in open and closed wind tunnel test sections an appropriate test sound source has to be available. Optimal would be an ideal point monopole source such as is typically assumed as source model in the beamforming process (see chapter 2). Further, such a source should have no disturbing influence on the flow field, the sound generation should remain unaffected by the surrounding flow and the source should be able to emit sufficiently high sound pressure levels in a broad frequency range up to 100 kHz which is required due to the use of scaled wind tunnel models (Moshier (1996), King and Underbrink (2008)). Then, it would be possible to examine the various test section dependent effects influencing the sound propagation. These specifications are hard to fulfill and therefore one has to accept a compromise. The relaxed source requirements include low directivity, robustness, reliability and repeatable sound generation with high sound pressure levels for a sufficiently high SNR in both types of test sections, together with, finally, a well-defined source location. An overview of the advantages and disadvantages of various concepts of sound sources involving the generation of sound fields by plasma, electromechanical and aeroacoustic means was given by Kröber et al. (2008).

Apart from an examination and comparison of the test section-dependent sound propagation effects, the influence of the aerodynamic properties of the different test section types on the aeroacoustic sound generation in model scale testing is also of concern. A sound source which meets the above

formulated requirements for such an investigation does not exist, since it had been mandated that sound generation remains unaffected by the surrounding flow. Subsequently, an aeroacoustic sound source is needed where the sound is generated by the wind tunnel flow.

Therefore, three different wind tunnel model concepts acting as sound sources are used in this thesis in order to examine both the propagation and boundary effects and the influence of the aerodynamic properties on the aeroacoustic sound generation in open and closed test sections. The first wind tunnel model was designed for the examination of sound propagation effects in the different wind tunnel types, which requires that the sound propagation remains unaffected by the flow. The second wind tunnel model employs aeroacoustic sound generation, where the model design takes into account that the aerodynamic model-wind tunnel interferences, as outlined in chapter 1.2, are as small as possible. This ensures that the alteration of the flow properties in the vicinity of the aeroacoustic sound generation is as low as possible. The last and third adopted model incorporates an unswept wing with a high-lift-system, representing a realistic aeroacoustic sound source with practical relevance. Typically, for such a model the model-wind tunnel interferences are of concern and the local and global flow properties around the model can vary significantly between the two wind tunnel types. In the following the concepts underlying the three used wind tunnel models are outlined. The main requirement demands that the flow field around the model and therefore the aeroacoustic sound generation should be as similar as possible.

3.2 Reference sound source

The first wind tunnel model makes use of electromechanical sound generation. In this so-called reference sound source, a ribbon loudspeaker from ELAC is employed. The complete probe is depicted in figure 3.1. A 0.006 mm thin aluminium ribbon acts as the membrane and is placed in a magnetic field. When an alternate current passes through the membrane it expands and contracts like a breathing cylinder because of the ensuing Lorentz forces. The movement of the membrane is in a direction perpendicular to both the magnetic field lines and to the direction of current. The ribbon diameter measures 90 mm and has a height of 15 mm. A metal grid protects the sensitive membrane from damage, as can be seen in figure 3.2 (a). The abutting edges are joined by a screw connection and the protection grid has a tape interface. Two guiding flanges serve as a wave guide and as an impedance adjustment. For in-flow applications the entire wind tunnel model is enclosed within symmetrical aerodynamic fairings. The loudspeaker membrane is recessed in order to avoid direct flow-membrane interactions. As a direct consequence of the design the probe has a resonant

cavity. In wind tunnel applications the flows passes over the cavity, at whose edge flow separation can occur, leading to broadband pressure instabilities which can induce cavity resonances. A metal grid, covered with silk, masks the cavity, thereby reducing the instability excitation, as depicted in 3.2 (b). As a tradeoff, one has to accept sound wave interferences and reflections from the masking, which occur predominately at higher frequencies (Kröber et al. (2008)).

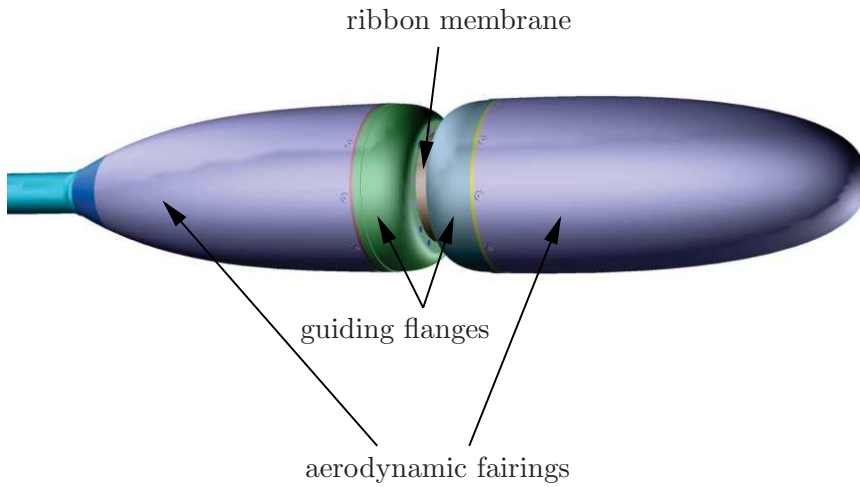
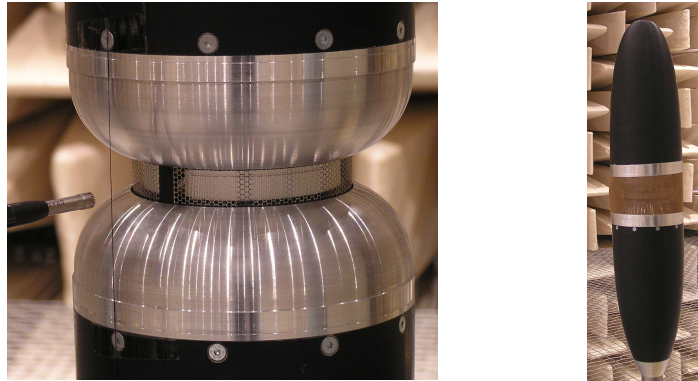


Figure 3.1: Reference sound source.



(a) Ribbon membrane with original protection grid (b) With masking

Figure 3.2: Details of the reference sound source.

The electromechanical sound generation provides great flexibility in the spectral structure of the signal (noise, pure tones, etc.). Due to sound generation method used here, this wind tunnel model is perfectly suited for the examination of flow effects on sound propagation in different wind tunnels, the sound generation here not being affected by changes of the aerodynamic

flow characteristics in the various wind tunnels. In addition, this wind tunnel model has an advantage compared with aeroacoustic sources - it can be measured without flow which is an important factor with respect to the study of flow effects on sound propagation. Furthermore the reference sound source can operate with loudspeaker turned on and off enabling the determination of the SNR of the test section under flow conditions without performing changes at the model. In terms of the amplitude and phase response, the reference sound source exhibits at least partially monopole characteristics, which has been verified by Kröber et al. (2008) in previous tests. Some important results concerning the directivity of the reference sound source are depicted in figure 3.3 and 3.4 and will be briefly summarized in the following. The experimental setup for measuring the azimuthal directivity and its

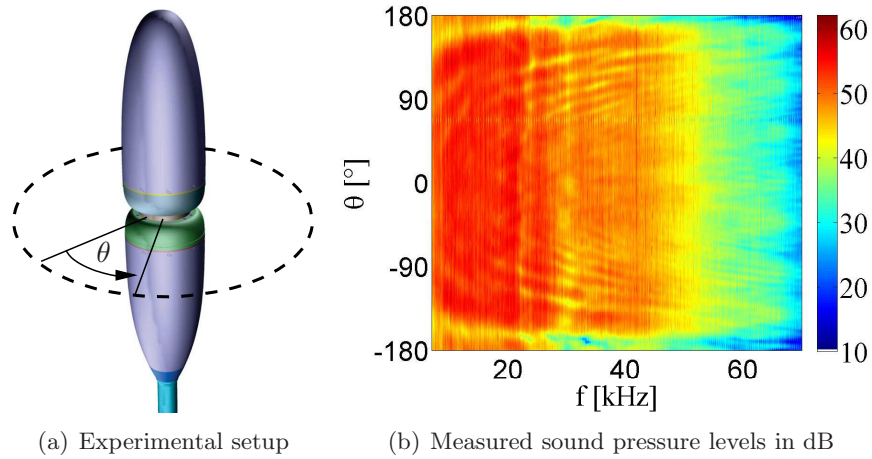


Figure 3.3: Measured azimuthal directivity of the reference sound source in an echoic chamber without flow.

results are depicted in figure 3.3. The microphone positions lie on a circle with a radius of 1.08 m in the plane which intersects the loudspeaker membrane in the center, and the abutting edges of the membrane are located at $\theta = \pm 180^\circ$. The highest levels are obtained below 20 kHz which is sufficient for audio applications. With growing frequency, the amplitude decreases and above 60 kHz the obtained amplitudes are much lower. The abutting edges with the electrodes cause a large amplitude reduction, mainly in the range of $\theta > 155^\circ$ and $\theta < -155^\circ$. Outside of this affected azimuthal range the directivity effects are very low. The symmetrical loudspeaker design leads to a symmetrical wave field with respect to the line $\theta = 0^\circ$. Starting at 25 kHz, the amplitude response of the loudspeaker has many dips due to interferences generated by the masking, but there is little influence on the azimuthal directivity.

The polar directivity analysis comprises the examination of the wave

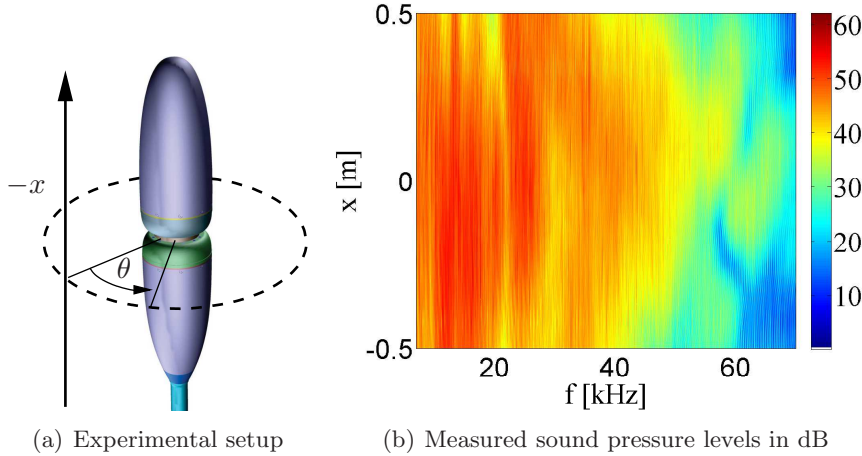


Figure 3.4: Measured polar directivity of the reference sound source in an echoic chamber without flow.

field along the vertical axis 1.08 m away from the source center line at the preferred azimuthal direction of $\theta = 0^\circ$. Figure 3.4 shows the corresponding setup and the resulting narrow band spectra. Frequency and spatially dependent amplitude decreases can be seen to be more intense than for the azimuthal directivity. In the range of $x > 0.3$ m and $x < -0.3$ m there are sound pressure level variations, especially for the frequencies above 20 kHz. More details about the reference sound source and its characteristics have been published in Kröber et al. (2008).

3.3 Plate with cavities

The second wind tunnel model used for the comparison incorporates a plate with an elliptical cross section with five different cavities and consequently constitutes an aeroacoustic sound source with known position, depicted in figure 3.5. It is widely known from numerous studies in the last 60 years that flow over cavities can generate both tonal and broadband response having intense near-field pressures which can lead to strong noise radiation into the far-field. Furthermore, the intense near-field pressure fluctuations can excite vibrations of the structure, leading to fatigue and ultimately, to possible damage of the structure. Subsequently, this phenomenon is of great significance for many practical applications involving flow over cavities at subsonic to supersonic speeds, as for example with aircraft wheel wells and weapon bays (Crighton (1990), Tam and Block (1978), Plumbee et al. (1962), Rossiter (1964)), anti-icing vent holes on the pressure side of the slat (Czech et al. (2006)), sunroofs of automobiles leading to buffeting (Islam et al. (2008)), and side-branches in pipe and duct networks for gas

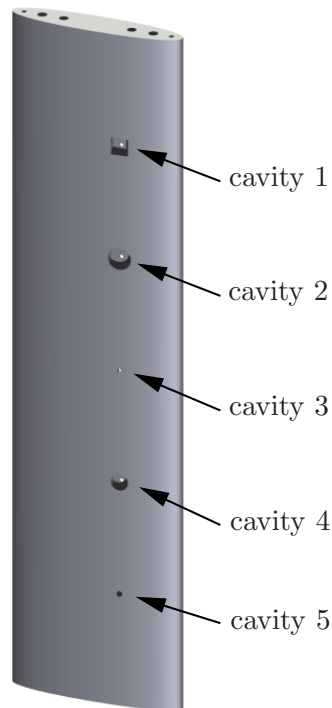


Figure 3.5: Plate with cavities.

transport systems and power plants (Bruggeman et al. (1991)). In contrast to the typical approach aiming at the suppression and reduction of flow-induced cavity oscillations, the opposite is to be achieved here. The cavities should act as tonal and broadband aeroacoustic sources which fulfill the requirements formulated at the beginning of this chapter - robust, reliable and repeatable sound generation with high sound pressure levels for a sufficient SNR in both types of test sections for the planned phased microphone array measurements at a well-known source location. In order to incorporate these requirements in an appropriate design it is essential to highlight the physical mechanisms of cavity noise.

3.3.1 Cavity noise mechanisms

A comprehensive review of flow-induced cavity noise was given by Gloerfelt (2009), Ahuja and Mendoza (1995) and Rockwell and Naudascher (1978). In this context, following the terminology of Naudascher (1967), the interaction of the fluid with the cavity can be categorized into three groups depending on the excitation phenomena of the self-sustaining oscillations: in the first group *fluid-dynamic* oscillations arise from inherent instability of the flow. In the second group the mechanism is the so-called *fluid-resonant* oscillation where the cavity oscillations are influenced by resonant wave effects within

the cavity. Thirdly, the *fluid-elastic* oscillations consider the coupling of the oscillations with the elastic cavity walls. Only the first two excitation phenomena will be important for the second wind tunnel model used for the comparisons so that details about only these two mechanisms will be outlined more in detail in the following.

Fluid-dynamic oscillations

Nowadays, the tonal cavity noise is understood to be a result of an aeroacoustic feedback loop including the amplification of shear layer instabilities leading to self-sustained oscillations in the cavity. Figure 3.6 depicts the

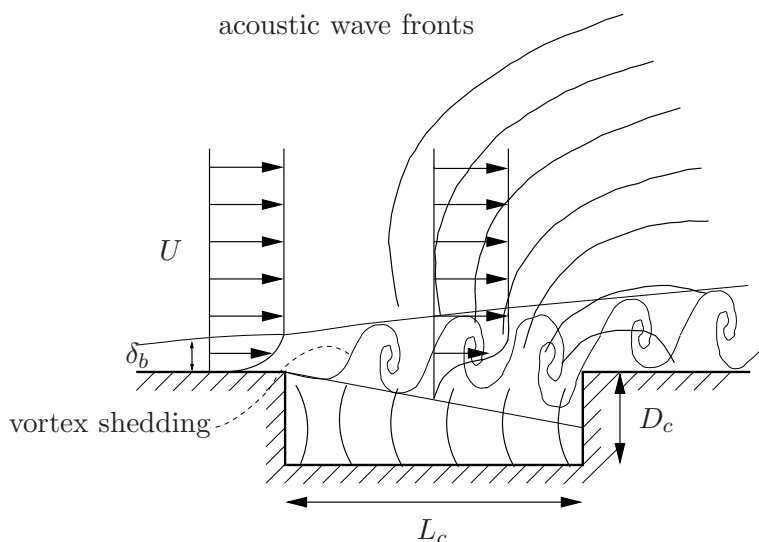


Figure 3.6: Sketch of the cavity flow with acoustic feedback (see e.g. [Gloerfelt \(2009\)](#)).

main features of the flow over a cavity. According to [Rockwell and Naudascher \(1978\)](#), the feedback process starts with the separation of the incoming boundary layer flow at the leading edge of the cavity where a shear layer develops. Then, the downstream propagating disturbances will be amplified in the shear layer and impinge on the trailing edge of the cavity. The interaction with the downstream wall leads to acoustic waves which propagate upstream inside the cavity or in the free stream and produce vorticity fluctuations near the sensitive shear layer origin. These vorticity fluctuations provide enhanced disturbances which will be further amplified in the shear layer and propagate downstream until impinging again at the trailing cavity edge, closing the loop. [Rossiter \(1964\)](#) was one of the first who suggested a feedback loop being involved in this oscillation mechanism so that today these kinds of self-sustained oscillations are termed Rossiter modes. Although numerous studies on this topic have been performed, even

today some details of the feedback mechanism are still partly poorly understood, in particular the exact process of sound generation in the vicinity of the cavity trailing edge caused by the impinging shear layer and the exact acoustic excitation of the vortex shedding process at the leading edge of the cavity. Today it is widely assumed that the involved shear layer instabilities in the feed back loop are of a Kelvin-Helmholtz type (Bilanin and Covert (1973), Tam and Block (1978), Gloerfelt (2009)). Without considering these particular and complex details, Rossiter (1964) has proposed, based on his shadow graph observations, a simple semi-empirical feedback model for the prediction of the frequencies of self-sustained oscillations in the cavity. Vortices are shed periodically at the leading edge of the cavity and grow while being convected to the trailing edge. A single vortex travels across the cavity opening in the time L_c/U_c where L_c is the length of the cavity and U_c is the convection velocity of the vortex. When the vortex impinges on the downstream cavity edge an acoustic wave is generated which propagates upstream and reaches the edge after the travel time L_c/c where the wave excites the shear layer, this in turn inducing enhanced vortex shedding. Here, c denotes the speed of sound. The timing of the various links must be synchronized so that the acoustic wave arrives at the leading edge just at the right moment to reinforce the periodical vortex shedding. Using this condition one derives the feedback equation:

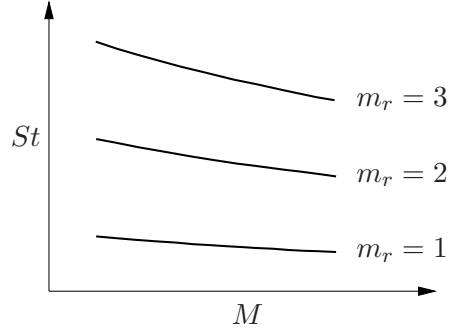
$$\frac{L_c}{U_c} + \frac{L_c}{c} = \frac{m_r}{f} \quad m_r = 1, 2, 3, \dots \quad (3.3.1)$$

where m_r denotes the mode number of the excited Rossiter mode. It also corresponds to the number of vortices being present in the cavity opening. Equation 3.3.1 was reformulated and slightly modified by Rossiter (1964) to yield an expression for the non-dimensional feedback frequencies (or Strouhal numbers)

$$St = \frac{fL_c}{U} = \frac{m_r - \gamma}{\frac{1}{K_r} + M} \quad m_r = 1, 2, 3, \dots \quad (3.3.2)$$

The modification was needed in order to obtain corresponding results between his calculated predictions and his experimental data derived from measurements at rectangular cavities. The term γ takes into account the time lag between the impingement of the vortex in the vicinity of the cavity trailing edge and the corresponding sound wave emission. The second empirical constant is K_r and it represents the ratio of the convection velocity of the vortices to the free-stream velocity. Rossiter (1964) determined the two empirical constants by a best fit to his measured data (in the Mach-number range from 0.4 to 1.2) and obtained $\gamma = 0.25$ and $K_r = 0.57$. The dependence of the non-dimensional frequency on the free stream Mach number given in equation D.1 is plotted in figure 3.7. The possible non-dimensional frequencies lie on a family of curves. At a certain Mach number only the distinct frequencies which are associated with the Rossiter modes can occur.

With the model of Rossiter (1964) it is neither possible to predict which mode number will actually be excited, nor can it provide information about the oscillation amplitudes and about which mode exhibits the highest amplitude, it thus being the predominant one. In addition, as shown by Rossiter (1964), by increasing the Mach number the predominant mode can abruptly jump from one mode to another, which also cannot be predicted by the Rossiter model. The formulation of Rossiter (1964) neglects the



flow inside the cavity and assumes implicitly a two dimensional flow over the cavity. The latter point is typically sufficient and appropriate for most flow scenarios in the case of rectangular cavities. In spite of these assumptions and simplifications the feedback frequencies can be predicted reasonably well by Rossiter's equation, as has been verified in numerous experimental studies (see e.g. Ahuja and Mendoza (1995), Czech et al. (2006), Block (1976)). This equation works best at Mach numbers between 0.4 and 1.2, which covers the Mach number range of Rossiter's own experimental data. Further, the Rossiter equation was modified by various authors in order to take into account various effects, for example, higher sound speeds inside the cavity (Heller and Bliss (1975)), deep cavities (East (1966), Block (1976)), lower Mach numbers than those in Rossiter's experiment (Block (1976), Ahuja and Mendoza (1995)) and circular cavities Czech et al. (2006).

Figure 3.7: Strouhal-Mach number relation of Rossiter modes

Fluid-resonant oscillations

In this category the self-sustaining cavity oscillations are strongly coupled with resonant wave effects within the cavity. Standing waves can be excited in length-wise, span-wise or depth-wise direction, but also Helmholtz resonator modes are possible if the cavity has a neck. The resonance frequencies of a rectangular cavity are determined with the help of equation

$$f_{\eta_x, \eta_y, \eta_z} = \frac{c}{2} \sqrt{\left(\frac{\eta_x}{L_c}\right)^2 + \left(\frac{\eta_y}{2D_c}\right)^2 + \left(\frac{\eta_z}{W_c}\right)^2}, \quad (3.3.3)$$

where η_x , η_y and η_z are the mode numbers for the length-wise, depth-wise and span-wise cavity resonance frequencies obtained by incorporating the boundary conditions of the five rigid walls and the open face of the cavity (Ahuja and Mendoza (1995)). Equation 3.3.3 gives a rough estimate since the existence of the mean flow and the shear layer has been neglected. The impedance of the cavity opening will be influenced by the

presence of shear layer and the mass exchange at the trailing edge, so that the cavity response is affected. Which mode will be the predominant one depends on the flow conditions and the shape of the cavity.

Cavities are typically classified into shallow and deep cavities (Rockwell and Naudascher (1978)). The term shallow applies to cavities with a length-to-depth ratio (L_c/D_c) larger than unity. Standing waves in length-wise direction are normally of concern for shallow cavities at higher flow velocities. This was intensively examined by Rossiter (1964) and Ahuja and Mendoza (1995). In contrast depth-wise resonances occur generally in deep cavities under the influence of low-speed grazing flow (Plumbee et al. (1962), East (1966), Block (1976)). The Strouhal-Mach number dependence is plotted schematically in figure 3.8 for depth-wise modes using equation 3.3.3 with $\eta_x = \eta_z = 0$ and the Strouhal number is given by $St = (fD_c)/U$.

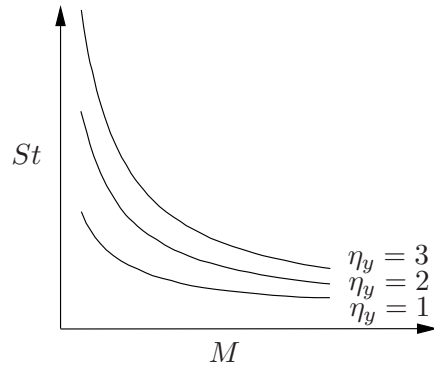


Figure 3.8: Strouhal-Mach number relation of depth-wise modes using equation 3.3.3 with $\eta_x = \eta_z = 0$.

Coincidence and mode coupling

Very strong tonal amplitudes arise when there is a coincidence between the feedback frequencies of the fluid-dynamic oscillation and the frequencies of the fluid-resonant phenomenon. For deep cavities East (1966) was one of the first who showed in his experimental study how the depth-wise mode dominates the frequency selection. An abrupt amplitude increase of the self-sustained oscillations occurs when the flow velocity is increased towards the region of coincidence, leading to an onset of the mode coupling. The same phenomenon was observed by Rossiter (1964) and Rockwell and Naudascher (1978) for length-wise modes in shallow cavities at high flow speeds. The frequencies and Mach number at which mode coupling will be present can be estimated by combining equations D.1 and 3.3.3. The intersection of the Rossiter and room mode curves designates the Mach number region of the coincidence. The mode coupling of Rossiter and cavity room modes is also termed as locked-on state.

Cavity broadband noise

Apart from the tonal self-sustained oscillations, broadband pressure fluctuations can also be generated in cavities by the flow. The experimental work

of [Rossiter \(1964\)](#) indicates that the broadband noise is related to the impingement of the shear layer on the rear cavity wall or for very long cavities, to reattachment on the cavity floor. In both these regions he found the most intense broadband pressure fluctuations inside the cavity. Further, [Rossiter \(1964\)](#) found that the random component of the pressure fluctuations predominates in the shallower cavities. In her study on the influence of cavity dimensions on the radiated noise, [Block \(1976\)](#) compared circular and square cavities of equal depth. In contrast to the square cavities, which generate a more tonal spectrum, the circular cavities produce more broad band noise. This finding can be best explained by considering the non-parallel leading and trailing edges of the circular cavities, where the lower span-wise coherence of the corner-vortex interaction at the trailing edge and the altered coherence of the excited instability waves in the shear layer at the leading edge are the possible reasons for the generation of a more broadband spectrum. Up to now, no simple model for the prediction of broadband cavity noise is available. Currently, predictions are possible using time-consuming and complex CFD and CAA methods, with which, however, it is still a challenge to predict correctly the details of the spectrum, especially the correct amplitudes ([Gloerfelt \(2009\)](#)).

Far-field directivity of cavity noise

According to the theoretical work of [Howe \(2004\)](#), the sound radiated into far-field of low Mach-number flow excited cavities can be modeled by a superposition of monopole and dipole source terms. Considering a shallow wall cavity, at very low Mach numbers the sound field is dominated by dipole radiation produced by the unsteady drag force, the radiation peaking in directions upstream and downstream of the cavity. At higher Mach numbers, however, the resonance frequency lies closer to the relevant Rossiter modes of the unstable hydrodynamic flow over the cavity and can then make a significant contribution to the radiation. The cavity resonance produces a monopole-like contribution to the sound and is governed by compressible effects in the cavity region. The monopole source strength is usually very weak at low Mach numbers. For Mach numbers exceeding about 0.05, the radiation directivity at a frequency close to the cavity resonance is governed by the correlated interference between the dipole and monopole fields. This superposition of monopole-like and dipole-like behavior regarding the radiated far-field sound of flow excited cavities was also found in experiments by [Ahuja and Mendoza \(1995\)](#). In his study they ascertained that the shallow cavities radiate sound more uniformly, whereas the deeper cavities appear to be the more directional with a peak occurring between 50° and 60° in the flow direction.

3.3.2 Design of the plate with cavities

As depicted in figure 3.5, the elliptically shaped plate has five different cavities. The model was designed with due attention paid to the acoustic and aerodynamic requirements formulated at the beginning of this chapter. The main requirement demands that the flow field around the model and consequently, the aeroacoustic sound generation, should be as similar as possible in both test sections. As described in chapter 1.2, there will be differences in the static pressure gradient along the model and variations in the velocity distribution with the open and closed test sections, caused by the different boundary conditions of these test sections. Consequently, the plate with the cavities should be as small as possible, which would reduce the test-section dependent differences of solid and wake blockage and streamline curvature. In contrast to that, the plate should be thick enough to incorporate the cavities which are responsible for the aeroacoustic sound generation. The cavities differ in shape and size to give sound emission in different frequency bands which include tonal and broadband spectral components. For tonal components the design of the cavities was carried out by using the equations for the prediction of Rossiter and room modes. Since no simple prediction methods are available for estimating the broadband pressure fluctuations of flow-excited cavities, use was made of experimental results and gathered experience of other experimenters (Rossiter (1964), East (1966), Block (1976), Ahuja and Mendoza (1995)) working with flow-excited cavities and Helmholtz-resonators. The following consideration outlines the cavity design characteristics. The geometrical details and dimensions are summarized in table 3.3.1.

cavity	shape & dimensions	D_c	L_c/D_c
1	rectangular: 15 mm \times 15 mm	5 mm	3
2	circular: \varnothing 20 mm	5 mm	4
3	circular: \varnothing 3 mm	3 mm	1
4	circular: \varnothing 15 mm	5 mm	3
5	circular: \varnothing 5 mm	10 mm	0.5

Table 3.3.1: Cavity dimension details

Cavity 1

This cavity has a rectangular shape and falls into the category of shallow cavities. In various experimental studies it was shown that the arising pressure fluctuations inside shallow cavities have broadband and tonal components (see e.g. Rossiter (1964), Block (1976) and Ahuja and Mendoza (1995)). The Rossiter modes can be estimated by using equation D.1. The results for the modes $m_r = 1$ to 4 are shown in table 3.3.2 for a flow velocity of

3.3. PLATE WITH CAVITIES

35 m/s using the two empirical values, $K_r = 0.57$ and $\gamma = 0.25$, found by [Rossiter \(1964\)](#). The flow velocity of 35 m/s is the highest available speed which can be achieved in both wind tunnels used for the comparison of the microphone array results. More details about the wind tunnels with their test sections will be presented in chapter 4. In shallow cavities mode cou-

mode number	$m_r = 1$	$m_r = 2$	$m_r = 3$	$m_r = 4$
frequency	942 Hz	2198 Hz	3454 Hz	4711 Hz

Table 3.3.2: Frequencies of Rossiter modes m_r of cavity 1

pling of Rossiter modes and standing waves across the length or width of the cavity can occur, as shown by [Rossiter \(1964\)](#) and [Rockwell and Naudascher \(1978\)](#). This can result in very strong pressure oscillations inside the cavity, but they radiate inefficiently into the far-field ([Crighton \(1990\)](#)) so that the wave coupling is essentially not of concern for the microphone array measurements.

Cavity 2

Again, this cavity was designed as a shallow cavity, but this time having a circular shape to generate of broadband noise. The dominance of broadband noise for circular cavities was demonstrated by experiments conducted by [Block \(1976\)](#).

Cavity 3

Cavity 3 has a diameter-to-depth ratio of one so that it is a limiting case. This cavity is clearly neither shallow nor deep, so it is a priori not clear whether tonal or broadband noise will dominate. The frequencies of the Rossiter modes are calculated in the same way as for cavity 1 using the diameter as the characteristic length. The results are shown in table 3.3.3. If the modes are excited they will produce sound emissions at higher frequencies than those of cavity 1, whereby the fourth Rossiter mode frequency of cavity 1 corresponds to the first mode frequency of cavity 3.

mode number	$m_r = 1$	$m_r = 2$	$m_r = 3$	$m_r = 4$
frequency	4711 Hz	10992 Hz	17274 Hz	23555 Hz

Table 3.3.3: Frequencies of Rossiter modes of cavity 3

Cavity 4

This cavity is also a shallow cavity having the same length-to-depth-ratio as cavity 1, but the shape varies. The circular shape should lead to broadband

dominated noise which is similar to cavity 2.

Cavity 5

The design of this last cavity aims at the excitation of depth modes coupled with Rossiter modes. The first four Rossiter modes and the first depth mode are shown in the Strouhal number-flow velocity plot in figure 3.9. For this length-to-depth ratio the coincidence occurs in the vicinity of 35 m/s for the first depth and second Rossiter mode. The mode coupling of the first depth and first Rossiter mode at the same flow velocity would require a length-to-depth ratio of 0.2. Theoretically, this can be easily achieved by reducing the diameter or increasing the depth of the cavity. Nonetheless, both possibilities have drawbacks. On the one hand increasing the depth would directly lead to an increased plate thickness, which in turn results in an increase of the unwanted model-wind tunnel interferences. On the other hand the diameter reduction can make the cavity "transparent" to the flow so that no oscillations are excited (Block (1976)). In this case the shear layer above the cavity spans the length of the cavity without turning in and out. This turning in and out maintains the feedback mechanism and it requires a minimum cavity length, depending on the flow velocity, for the excitation of oscillations inside the cavity. Therefore, the length-to-depth ratio of 0.5 has been kept here. For the calculation of the depth-wise mode an modified form of equation 3.3.3 was applied. This modified form takes into account that for deep cavities the ratio L_c/D_c has an influence on the frequency of the excited depth mode:

$$St = \frac{fL_c}{U} = \frac{1}{M} \frac{L_c}{D_c} \frac{0.25}{1 + 0.65 \left(\frac{L_c}{D_c} \right)^{0.75}}. \quad (3.3.4)$$

East (1966) and Block (1976) have verified the validity of this empirical equation for low Mach number flows and obtained better results than by using equation 3.3.3.

The frequencies of the Rossiter modes are calculated in the same way as for cavity 1 using the diameter as the characteristic length. The results are shown in table 3.3.4.

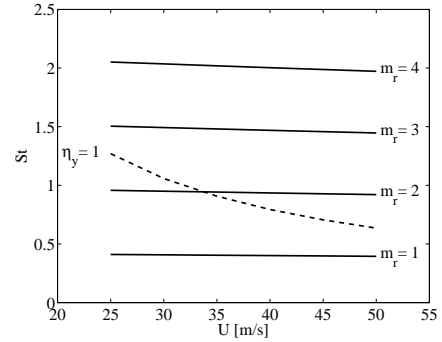


Figure 3.9: Strouhal number-velocity relation of Rossiter (m_r) and depth (η_y) modes of cavity 5

3.4. UNSWEPT WING WITH HIGH-LIFT-SYSTEM

mode number	$m_r = 1$	$m_r = 2$	$m_r = 3$	$m_r = 4$
frequency	2826 Hz	6595 Hz	10364 Hz	14133 Hz

Table 3.3.4: Frequencies of Rossiter modes of cavity 5

Plate

The elliptically shaped plate, which contains the cavities, has a length of 600 mm, a chord length of 150 mm and is 30 mm thick. Each cavity is equipped with an electret microphone, mounted at the base of the cavity, to measure the pressure fluctuations inside the cavity. The sensors provide near-field information and enable a comparison of the aeroacoustic sound generation in the different test sections. The distance between the cavities is 100 mm. This spacing ensures that the resolution of the used microphone array is sufficient in order to separate spatially the individual cavity sources over a wide frequency range (for more details see chapter 4). The cavities are arranged equidistantly along a line 50 mm from the plate leading edge. This assures that, on the one hand, the plate still has sufficient thickness in order to accommodate the cavities with their microphones and preamplifiers, but, on the other hand the cavity positions are still as close as possible to the plate tip. Above a certain ratio of the boundary layer thickness of the incoming flow to the cavity length, no tone oscillations will be excited inside the cavity. This behavior was observed by, among others, [Block \(1976\)](#) and [Ahuja and Mendoza \(1995\)](#) and it was actually used to eliminate cavity tones by increasing the boundary layer thickness through tripping. In the current case a thin boundary layer is preferable in order to ensure that tonal excitation occurs. For the plate-cavity configuration the flow-induced sound from the cavities can be simply suppressed by covering the openings with tape.

3.4 Unswept wing with high-lift-system

The third wind tunnel model employs a generic 2D unswept wing with a high-lift system consisting of slat, wing and flap, illustrated in figure [3.10](#). This wing model represents an aeroacoustic sound source with a highly complex flow field and an a priori unknown source distribution with poorly known spectral properties. The slat (red) and flap (blue) are both connected to the wing (green) by four tracks. The wing has a length in spanwise-direction of 800 mm and a clean chord length of 300 mm. Both the slat and flap deflection angles were kept constant throughout this investigation at 28° and 35°, respectively. These deflection angles correspond to a typical landing configuration of high lift systems. In order to examine its aerodynamic performance, the high-lift system was instrumented with 47 pres-

sure taps of 0.3 mm internal diameter, located at midspan. This model had been the subject of various experimental and numerical studies examining slat noise (see e.g. Ewert et al. (2010)¹). In the first instance, the generic 3-element high-lift system is used as an aeroacoustic sound source for the comparison of microphone array measurements in the open and closed test sections. For this comparison, it is not important whether the observed sound sources actually occur with real high-lift configurations or whether they result from model scaling or too low Reynolds numbers. Furthermore, the angle-of-attack of the model was not restricted to the typical ranges for landing, since the present study is focused on a comparison of microphone array measurements, so that similar aerodynamic conditions in both wind tunnels are more important than the particular angle-of-attack settings. It is already known from a number of previously performed experimental and numerical studies examining such generic model types that the slat and their tracks are the main aeroacoustic noise sources (Dobrzynski et al. (1998), Storms et al. (1998), Storms et al. (1999), Dobrzynski and Pott-Polenske (2001), Khorrami et al. (2002), Dobrzynski (2010), Ewert et al. (2010)). Details of the physical mechanisms of slat noise sources are briefly introduced in the following. The subsequent considerations are focussed on generic models, specifically on those which are similar to the employed wing model in this thesis.

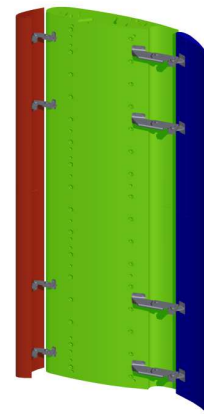


Figure 3.10: Generic 3-element high-lift model

3.4.1 Slat noise sources and physical mechanisms of sound generation

At present the physical mechanisms behind slat noise generation are not yet fully understood. The current understanding of the highly complex slat noise source mechanisms was summarized by Dobrzynski (2010), for instance. The nature of the flow in the vicinity of the slat is characterized by a multifaceted and unsteady flow field, as illustrated schematically in figure 3.11. At the slat hook, a free and therefore unstable shear layer develops as a result of the shear layer velocity profile having an inflexion point and the involved Kelvin-Helmholtz instability (König et al. (2009)). This vortex flow separates the undisturbed slot flow which is accelerated towards the slat trailing edge and the recirculation zone in the slat cove.

¹This previous study was conducted at a higher Reynolds number range and at another angle-of-attack range compared with the experimental work carried out in this thesis, so that a direct comparison is not possible.

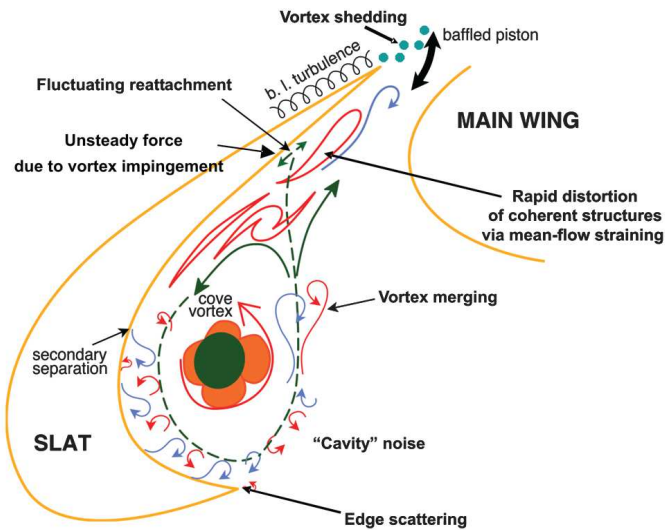


Figure 3.11: Potential sources and physical mechanisms of slat noise mechanism (taken from [Choudhari and Khorrami \(2006\)](#)).

The vortex structure in the slat cove rotates in counter-clockwise direction. The turbulent structures of the shear layer are convected from the slat hook towards the slat lower surface where the vortices impinge upon the slat surface and generate a strong unsteady force. At reattachment, vortices are entrained into the recirculation region where they diffuse, with the rest passing through the slat gap ([Jenkins et al. \(2004\)](#)). Along with the vortex passing through the slat gap, unsteady vortex shedding can occur at the slat trailing edge.

The various previously conducted slat noise studies on generic high-lift configurations revealed that the slat noise radiated into the far-field is by itself a complex aeroacoustic problem involving a combination of interdependent noise generation mechanisms in overlapping frequency bands. Based on these findings the resulting generic far-field slat noise spectrum for landing approach conditions shows high sound pressure levels in the lower frequency range followed by a gradual level decrease as the mid-frequency range is approached. At higher frequencies, the spectrum displays a broadband tonal behavior and a concurrent rise in the sound pressure levels. The peak is significantly higher than the noise for the surrounding frequencies. In addition, the slat noise spectrum can exhibit some low and high frequency tone components.

The spectral characteristics of slat noise can be attributed to particular physical sound generation mechanisms. It is assumed that the impingement of the vortical shear flow on the downstream cove surface represents one of

the slat noise sources which contributes to the low frequency noise, followed by noise that is generated when this unsteady flow is shed off the slat trailing edge. Because the wing leading edge is located in the acoustic near-field of this trailing-edge noise source, it can also be assumed that the wing leading edge reacts as a sound source. Moreover, the vortex position in the slat cove is not stationary, but is slightly oscillatory and could thus contribute to the low-frequency part of the slat noise spectrum. The observed acoustic tone phenomena can be associated with three different source mechanisms. The first one is a consequence of coherent vortex shedding off a blunt slat trailing edge leading to the high-frequency hump in the spectrum and is often observed in two-dimensional scale model experiments and simulations (Khorrami et al. (2000, 2002)). According to Dobrzynski (2010), it should be noted, however, that such tone noise phenomena are not likely to occur (and have indeed never been observed) on a real full scale slat because its relative trailing-edge thickness is smaller compared with that of most scale model slats. As an example, for a 1/10 scaled slat model a trailing-edge thickness of about 0.1 mm would be required, whereas constraints due to manufacturing and handling restrict the trailing-edge thickness of slat models typically to between 0.2 and 0.5 mm. Therefore, the occurrence of slat trailing-edge bluntness noise in scale model experiments is considered as a model artefact. The second mechanism, low-frequency tones, is related to the coherent laminar flow separation at the slat hook. This phenomenon is considered to represent a kind of cavity resonance in the slat cove in combination with the adjacent wing leading edge, so that in this case the slat noise source can be considered as baffled piston. For example, Kolb et al. (2007) and Tam and Pastouchenko (2001) interpret the slat cove as a cavity-like geometry and the observed low-frequency slat tones are then similar to Rossiter modes. However, details about this tone generating phenomenon are not clear at this time. Experiments with different tripping devices showed (see e.g. Dobrzynski et al. (2001), Fischer et al. (2006)) that low-frequency tone effects could be attenuated or even eliminated through massive tripping at the slat hook. Finally, the third tone generating process involves Tollmien-Schlichting boundary layer instabilities on the slat suction side which are responsible for high-frequency tone noise. These tones can easily be eliminated through tripping on the slat suction side to force transition to a turbulent boundary-layer and to avoid the formation of a laminar separation bubble (Dobrzynski (2010)). The last two tone phenomena are a consequence of the too low Reynolds numbers in the wind tunnel experiment as compared with flight conditions.

Based on the results from various studies, among others from Dobrzynski et al. (1998), Storms et al. (1999), Dobrzynski et al. (2001) and Guo (2010), the overall sound pressure level of slat noise sources has been found to scale with of $M^{4.5 \text{ to } 5}$ which is close to the theoretically obtained fifth power law for trailing-edge noise (compact edge dipole). Consequently, the directional

characteristic of the slat noise sources corresponds to a dipole-like source where the dipole axis is normal to the slat chord. This has been verified in different studies by various authors (see e.g. [Dobrzynski et al. \(2001\)](#), [Kolb et al. \(2007\)](#), [Ewert et al. \(2010\)](#)). Along with the slat the model slat tracks constitute another dominant aeroacoustic source for such an employed generic model. The model slat tracks are typically exposed to the unsteady slat flow field and cause additional flow separation. An experimental study by [Dobrzynski et al. \(1998\)](#) revealed that the slat tracks are broad-band noise sources. Due to the wide variety of model slat track designs and the subsequent differences between the various studies there are no further and universally valid statements possible.

CHAPTER 3. OVERVIEW OF THE EMPLOYED SOUND SOURCES

Chapter 4

Experimental setup, instruments and methods

This chapter gives a synopsis of all important facts regarding the experimental setups, apparatus and the applied measurement techniques. The wind tunnels in which the experiments were performed will be described in detail (section 4.1), together with the applied measurement techniques and employed instruments (section 4.2). The installation of the models and the measurement equipment in the various wind tunnel test sections is also illustrated. In addition, the significant influences deriving from the individual experimental setups and test section dependent boundary conditions will be estimated in advance, so long as these effects are predictable and relevant for the present measurements (section 4.5). Finally, a comprehensive overview of the conducted test program is given.

4.1 The wind tunnels

The performance and comparability of microphone array results from open and closed test sections was experimentally examined in two different wind tunnels with an open and a closed test section. In the following the two wind tunnels and their test section properties are introduced.

4.1.1 AWB

One part of the experimental investigation was conducted in the Aeroacoustic Wind Tunnel Braunschweig (AWB) of the DLR (Pott-Polenske and Delfs (2008)) which is a Göttingen type wind tunnel, depicted in figure 4.1. This closed circuit wind tunnel has an open test section (os) which is surrounded by an anechoic chamber. The sound absorbing wedges on the walls, floor and ceiling enable free field measurements above a cut-off frequency $f_c = 150$ Hz. The nozzle exit has a rectangular shape with the dimensions $1.2 \text{ m} \times 0.8 \text{ m}$

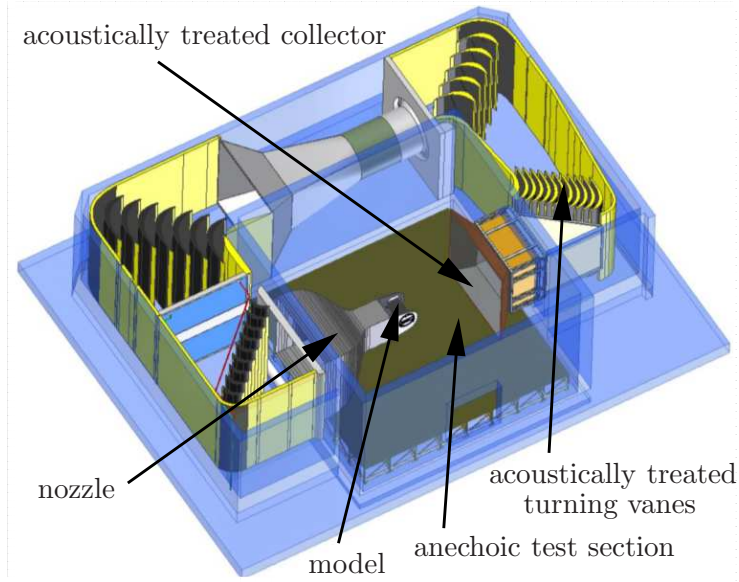


Figure 4.1: Sketch of the Aeroacoustic Wind Tunnel Braunschweig (AWB) of the DLR (Pott-Polenske and Delfs (2008)).

providing a contraction ratio of 9:1. This enables a maximum flow velocity of 65 m/s. At 60 m/s the in-flow turbulence level T_u is approximately 0.3%. Both the collector and the first set of turning vanes were acoustically treated by placing porous foam on the surfaces.

4.1.2 GroWiKa

The wind tunnel at the Institute of Fluid Mechanics and Technical Acoustics of the Technical University Berlin, schematically illustrated in figure 4.2, has a closed test section (cs) with a width of 2.0 m, a height of 1.4 m and length of 10 m. The test section is divided into four exchangeable test boxes. The single-stage axial fan is powered by a 500 kW engine. The nozzle contraction ratio is 6.25:1, thus providing a maximum flow velocity of 35 m/s. The turbulence level is less than 0.23% over the entire range of free-stream velocities (Urzyńcok (2003)). The measurements were conducted in the test section box 1.

4.2 Measurement techniques and equipment

The subsequent considerations concern the employed measurement techniques and equipment applied in the context of acoustic and aerodynamic investigations, performed in the above presented wind tunnels.

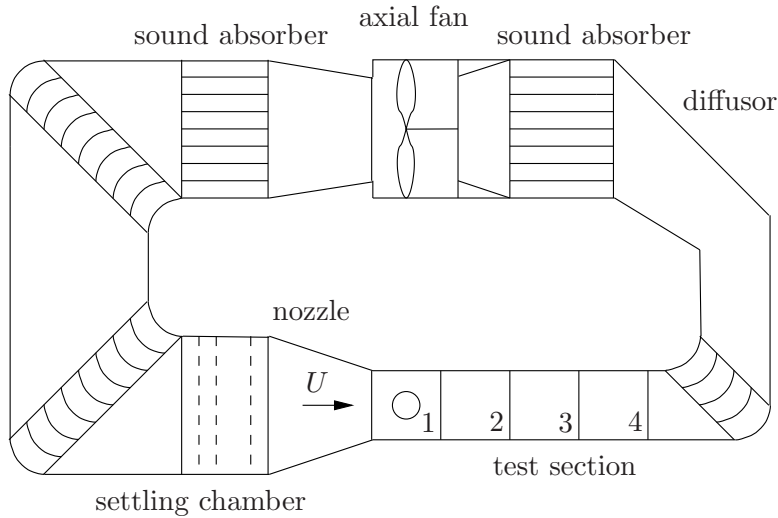


Figure 4.2: Sketch of the wind tunnel with closed test section (GroWiKa) at the Institute of Fluid Mechanics and Technical Acoustics of the Technical University Berlin.

Microphone array

The microphone array measurements were carried out using an array of 144 electret microphones, arranged in nine logarithmic spiral arms with an aperture of 1 m, as shown in figure 4.3. The fairing of the microphone array is made from aluminum, has a thickness of 25 mm and has dimensions of 1756 mm in streamwise and 1300 mm in vertical direction. The leading and trailing edges are chamfered with an angle of 6° in order to avoid disturbances due to flow separation. All microphones are recessed behind a cone in order to reduce the influence of wall pressure fluctuations caused by the turbulent boundary-layer and subsequently, to improve the SNR. As a consequence of this design the frequency response of each array microphone differs from the 6 dB pressure doubling for flush-mounted microphones compared to the free-field response. Therefore, all array microphones were calibrated in an anechoic chamber using a calibrated free-field microphone (G.R.A.S. 1/4" microphone (type 40 BF)) as a reference and a loudspeaker

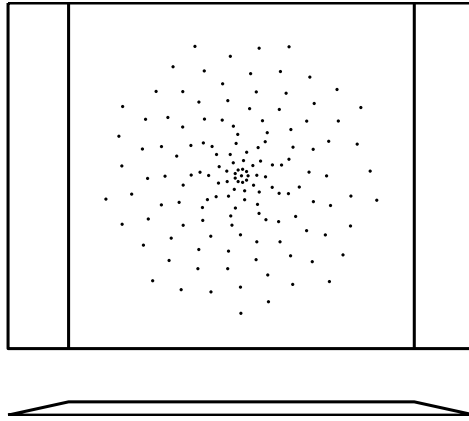


Figure 4.3: The microphone array consisting of 144 sensors.

operating in the frequency range $1 \text{ kHz} < f < 70 \text{ kHz}$. The array has already been used by [Koop and Ehrenfried \(2008\)](#) for aeroacoustic measurements in the closed wind tunnel of the Institute of Fluid Mechanics and Technical Acoustics of the Technical University Berlin. The frequency-dependent

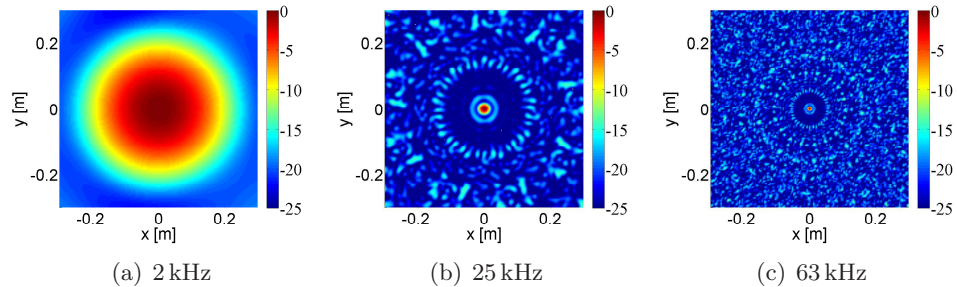


Figure 4.4: Point spread function of the microphone array

point spread function of the microphone array was simulated and is depicted in figure 4.4, where the results for the three frequencies of 2 kHz, 25 kHz and 63 kHz are shown by way of example. The monopole source is located 0.975 m above the central microphone. The simulated source lies in a plane which is parallel to the array surface and which has approximately the locations of the model sources to be used later in tests. The array resolution, as determined by the array aperture, source frequency and source-microphone arrangement, as outlined in section 2.2.2, increases with increasing frequency, meaning that at very low frequencies it is not possible to discriminate closely spaced sources. The simulation shows that in the frequency range from 1 kHz to 70 kHz the main lobe-to-side lobe ratio (MSR) is always at least -14 dB for this setup. The use of 144 microphones increases theoretically the SNR by about 21.58 dB when compared with a single microphone. In spite of great care when conducting microphone array experiments one has to expect differences between the theoretical specifications of the array and those which can be achieved in practical applications. In general, the actual SNR, MSR and resolution are lower in practice, being caused by phase and sensitivity errors introduced by the wind tunnel flow and boundaries, installation and hardware effects (microphones, data acquisition equipment).

Far-field microphone measurements

Apart from the use of phased microphone arrays, far-field measurements with single microphones are often performed in wind tunnels with anechoic open test sections, because they can provide valuable information about the source directivity and the noise radiated into the far-field. In the current study far-field measurements with a single microphone are conducted in the

open test section using a free-field G.R.A.S. 1/4" condenser microphone enabling measurements in the frequency range between 4 Hz and 100 kHz. The sensor consists of a capsule (type 40 BF) and a preamplifier (type 26TC). In the range 10 Hz and 40 kHz, the microphone exhibits a flat frequency response to within ± 1 dB. A calibration of the microphone was carried out using a pistonphone (G.R.A.S. type 42AA). The far-field microphone allows a comparison between the absolute sound pressure levels in the far-field and the integrated spectra, derived from the power integration of the sources maps of both test sections. The integration method was outlined in chapter [2.2.4](#).

Measurement of dynamic and static pressures

To assess the shear layer thickness in the open test section a Prandtl tube was traversed through the shear layer and the flow velocity was measured. The employed differential pressure transducer was from the manufacturer Setra, model 239, allowing a maximum pressure measurement of 1870 Pa and producing an output voltage within the range of ± 2.5 V.

As outlined in chapter [3.4](#), the wing is equipped with 47 static pressure taps. In the open test section a PSI 8400 pressure module measures the static pressures up to a maximum value of 34.5 kPa with an accuracy of 0.03%. All pressure ports could be measured simultaneously with this system. In the closed test section, a Scanivalve system with 48 ports was available. In combination with a differential pressure transducer this system scans successively each pressure port. The transducer used was again from Setra, model 239, but this time the maximum measurable pressure was 3700 Pa with an accuracy of 0.14%.

Data acquisition system

For this investigation, the data were acquired using the multi-channel data acquisition system VIPER-48 from GBM. The transient data recorder has an AD conversion of 16-bit at a maximum sampling frequency f_s of 250 kHz for each channel. All channels have an antialiasing filter at $f_s/2$. Furthermore, in order to reduce the influence of strong low frequency noise on the measured signals, a high-pass filter with adjustable cut-off frequencies of 1.5 Hz, 500 Hz and 6 kHz is used.

4.3 Installation of the models and measurement equipment

This thesis focusses on the performance and comparability of microphone array measurements in open and closed wind tunnels. In order to be able to assess this issue it is essential to keep the experimental setup and conditions

as identical as possible in both cases, since this then enables an examination of the test section-dependent effects.

Pictures of the each installation of the three models and the microphone array in both wind tunnels are shown in figure 4.5. The subsequent subsections contain important details on the experimental setup and the installations.

4.3.1 Reference sound source

The reference sound source is flanged at the rear end on a support consisting of several individual components, as shown in figures 4.5 (a) and (d). A curved tube connects the reference sound source and its aerodynamic fairings with an aerodynamically shaped tower. The tower again is mounted on a base plate made from aluminum. In the open test section the wind tunnel model and the entire support are installed on a lifting table so that the center line of the reference sound source is 0.0015 m above the centerline of the wind tunnel jet. The aluminum base plate of the support is located 10 cm below the lower nozzle lip line. In the closed test section the base plate with the reference sound source and the rest of the support is mounted onto the wind tunnel floor.

4.3.2 Plate with cavities

The plate with cavities is positioned between two end plates, after which follow the elliptically shaped mountings (see figures 4.5 (b) and (e)). When the model is mounted in the open test section the plate with the cavities is located in the potential core of the jet, which has flow velocity U . The elliptically shaped mountings are partially located in the potential core, partially in the turbulent shear layer and partially outside the flow. The end plates reduce the influence of the turbulent shear layer on the flow over the cavities. In the closed test section the plate and the elliptically shaped mountings are mounted vertically between the test section roof and floor. The frontal area of the plate and its mounting amounts to less than 5 % of the cross-sectional area of the nozzle exits in both wind tunnels.

4.3.3 Wing with high-lift system

The installation method of the wing with the high-lift system is very similar to the plate with cavities. The wing model is also located between two end plates, to which it is connected with elliptically shaped mountings. When the model is installed in the open test section it is located in the potential core of the jet. Again, the elliptically shaped mountings are partially located in the potential core, partially in the turbulent shear layer and partially outside the flow. Each end plate incorporates a bearing with a turnable disk allowing

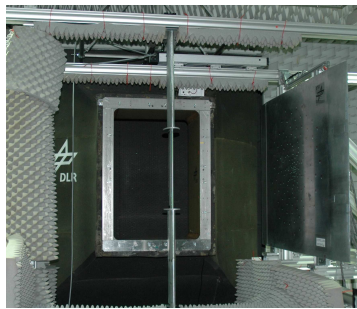
4.3. INSTALLATION OF THE MODELS AND MEASUREMENT EQUIPMENT



(a) reference sound source



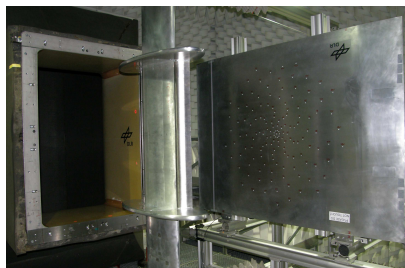
(b) reference sound source



(c) plate with cavities



(d) plate with cavities



(e) wing with high-lift system



(f) wing with high-lift system

Figure 4.5: Installation of the three models in the test section of the open (a, c, e) and the closed (b, d, f) wind tunnel, as seen looking into the nozzle, with the microphone array on the right side.

changes of the angle-of-attack of the wing model. The maximum angle-of-attack of the wing used in this thesis is 12° . Pictures of both wind tunnels with the installed model can be seen in figures 4.5 (c) and (f). The frontal area of the wing with the high-lift system, set at the maximum angle-of-attack of 12° , and its mounting amounts approximately to 5% of the cross-sectional area of the closed test section. In the open test section, the frontal area of the model installation at its highest angle-of-attack is approximately 11% of the cross-sectional area of the nozzle exit for the chosen experimental setup. According to Barlow et al. (1999) the ratio of the frontal area and the stream cross-sectional area in aeronautical wind tunnel testing is typically chosen in the range of 1% to 10% with 5% being typical. With respect to the wing model, this condition for the maximum desirable ratio could not be met with the current experimental setup.

4.3.4 Geometrical setup in the wind tunnels

With the given size of these two wind tunnels it is possible to use the same geometrical setup with the same distance between wind tunnel model sources and the microphone array. The three wind tunnel models are installed approximately in the middle of the test section. This is illustrated exemplarily for the wing model in figure 4.6. The origin of the coordinate system used here is located in the middle of the central microphone membrane of the adopted microphone array. The wind tunnel center line, which is parallel to the x -axis, is 0.975 m away from surface of the microphone array in both wind tunnel test setups and lies in the plane at $y = 0$. In the open test section the distance between the nozzle exit plane and the central array microphone is 0.8 m. According to the shear layer modeling discussed in section 2.3.2, the plane infinitely shear layer is located in the xy -plane at $z = 0.575$ m. The arrangement of the array microphones and the three models as viewed on the xy -plane is shown in figure 4.7. The chosen experimental installation ensures an identical geometrical test setup in both test sections for the individual models. Figure 4.7 (a) shows the setup for the reference sound source, which is identical for both wind tunnel measurements. The centerline of the reference sound source is positioned at $y = 0.0015$ m. The membrane is positioned 0.093 m upstream from central array microphone. In the case of the plate with cavities shown in (b), the model installation leads to a cavity midpoint position of $x = -0.093$ m. The central cavity is located in the middle of the test section height at $y = 0$ m. Finally, figure (c) depicts the arrangement of the microphones and the wing with high-lift-system. The slat cove, where one would expect the major aeroacoustic sources for this kind of configuration, is located at $x = -0.15$ m.

4.3. INSTALLATION OF THE MODELS AND MEASUREMENT EQUIPMENT

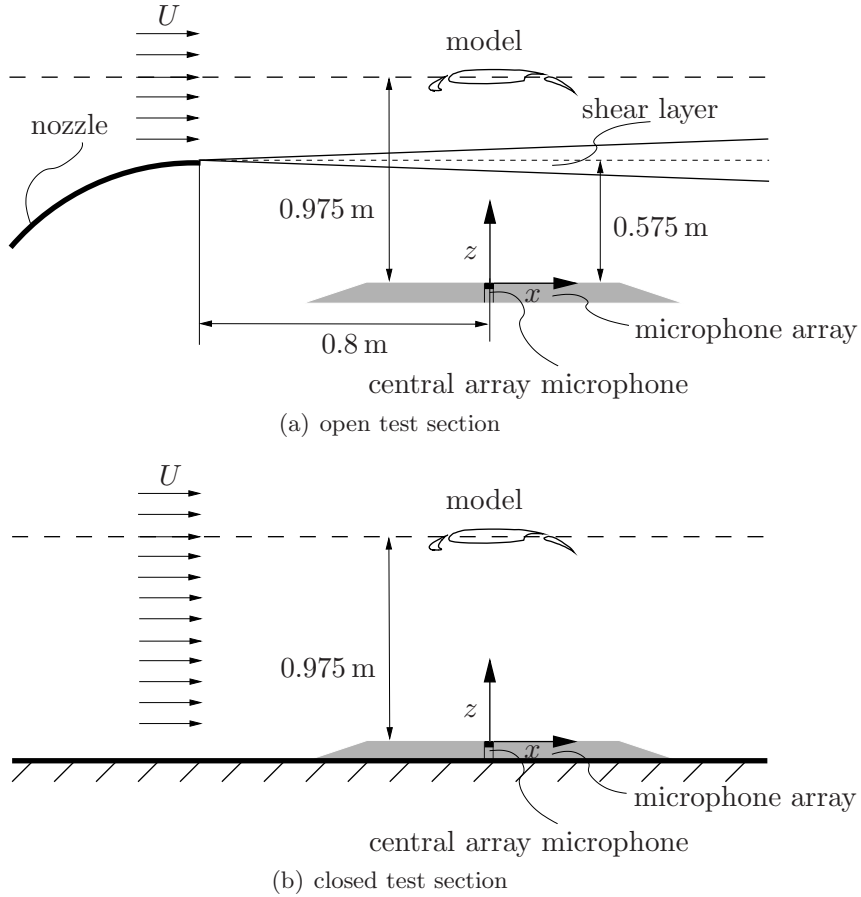


Figure 4.6: Illustration of the model and microphone array installation in both wind tunnel test sections. Flow comes from the left.

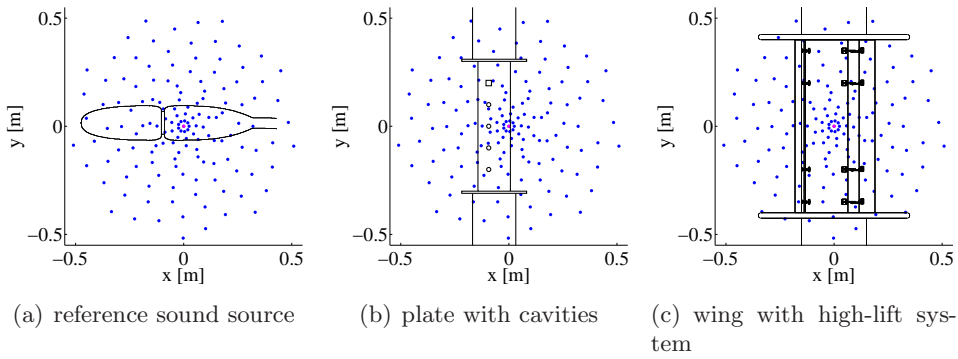


Figure 4.7: Model and microphone (blue points) arrangement in the open and closed test section. The central microphone is marked as a magenta point. Flow comes from the left.

4.3.5 Far-field measurement setup

The experimental setup for the far-field measurements is illustrated in figure 4.8. The far-field microphone is placed as far as possible from the model in

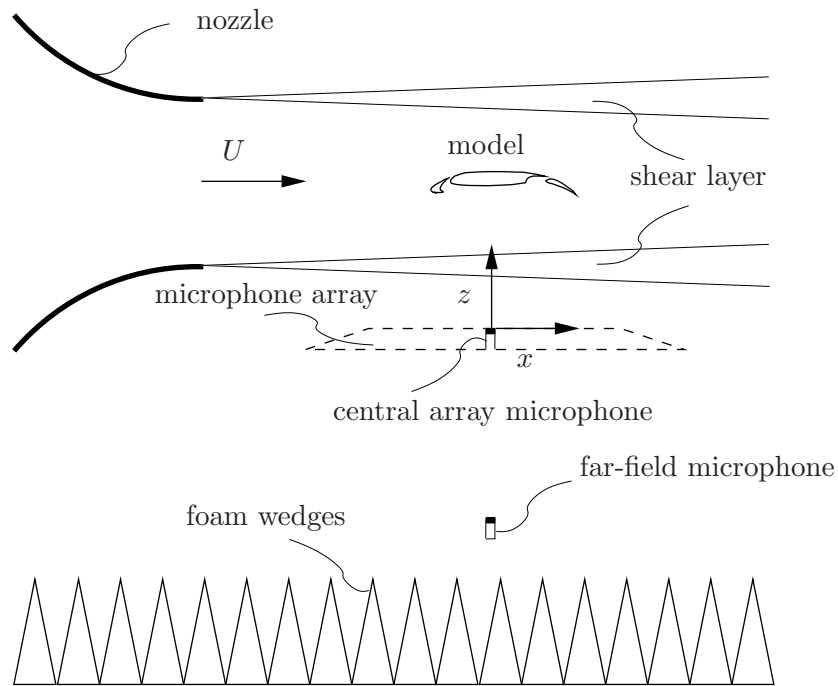


Figure 4.8: Sketch of the experimental setup for the far-field measurements using a single microphone in the open test section.

the open jet, only being restricted, of course, by the physical dimensions of the test section. The far-field observer has the same x and y -coordinate as the central array microphone in order to minimize differences between the integrated and far-field spectra resulting from directivity effects of the sources. The distance between the two microphones is 0.846 m. This means that the far-field sensor is 1.821 m away from the wind tunnel center line. The microphone is positioned in the far-field if the distance between the source region and the observer is much larger than the wave length of the emitted sound waves. It is widely accepted that the far-field condition is fulfilled when the distance is one order of magnitude higher than the wave length. With the current dimensions the single microphone can be considered to be located in the far-field for frequencies above 1.9 kHz. The microphone array was obviously removed before performing the far-field measurements.

4.4 Aeroacoustic comparability

The present thesis focuses on the comparability and the performance of microphone array measurements conducted in open and closed wind tunnel test sections and performs a systematic comparison. In this context, it is essential to ensure an aeroacoustic similarity between the measured configurations in the two different wind tunnels. Subsequently, it is important to know which dimensionless quantities describe the sound generation and propagation in flows. In general, this can be achieved by the nondimensionalization of the base equation for the underlying problem.

Lighthill's famous acoustic analogy (Lighthill (1952)) governs the aerodynamic generation and propagation of sound in fluid flows and it is based on the equations of mass and momentum conservation of a compressible fluid:

$$\left(\frac{\partial^2}{\partial t^2} - c_\infty^2 \frac{\partial^2}{\partial x_i^2} \right) \rho' = \frac{\partial^2}{\partial x_i \partial x_j} \underbrace{[\rho U_i U_j - \Upsilon_{ij} + \delta_{ij}(p' - c_\infty^2 \rho')]}_{\mathbb{T}_{ij}}. \quad (4.4.1)$$

The left side of equation 4.4.1 is the linear wave operator incorporating the density fluctuation ρ' , while the quadrupole source terms are on the right side. \mathbb{T}_{ij} is the so-called Lighthill stress tensor which includes the Reynolds stress $\rho U_i U_j$, the viscous stress Υ_{ij} and the isotropic term $\delta_{ij}(p' - c_\infty^2 \rho')$. In the underlying low-speed wind tunnel experiments ($M \leq 0.11$) the isotropic term can be typically neglected since the conduction of heat which causes deviations of p' from $c_\infty^2 \rho'$ is a very small effect (Lighthill (1952)). This source term is more important for the cases of heated jets and combustion noise (see e.g. Dowling and Ffowcs Williams (1983)).

In order to obtain a dimensionless form of Lighthill's analogy one introduces characteristic scales (marked with the subscript ∞) resulting in the following dimensionless variables (marked with a $\{\cdot\}$) for the time $t = t_\infty \hat{t}$, the position vector $\mathbf{x} = l_\infty \hat{\mathbf{x}}$, the flow velocity $U = U_\infty \hat{U}$, the density fluctuation $\rho' = \rho_\infty \hat{\rho}'$ and the density $\rho = \rho_\infty \hat{\rho}$. Inserting the dimensionless variables in the Lighthill equation 4.4.1 with removed isotropic source term leads to the following dimensionless terms: the wave operator is given by

$$\left(\frac{\partial^2}{\partial (t_\infty \hat{t})^2} - c_\infty^2 \frac{\partial^2}{\partial (l_\infty \hat{x}_i)^2} \right) (\rho_\infty \hat{\rho}') = \left(\frac{\rho_\infty}{t_\infty^2} \frac{\partial^2}{\partial \hat{t}^2} - \frac{c_\infty^2 \rho_\infty}{l_\infty^2} \frac{\partial^2}{\partial \hat{x}_i^2} \right) \hat{\rho}', \quad (4.4.2)$$

and for the Reynolds stress one obtains

$$\frac{\partial^2 (\rho_\infty \hat{\rho} U_\infty \hat{U}_i U_\infty \hat{U}_j)}{\partial l_\infty \hat{x}_i \partial l_\infty \hat{x}_j} = \frac{\rho_\infty U_\infty^2}{l_\infty^2} \frac{\partial^2 (\hat{\rho} \hat{U}_i \hat{U}_j)}{\partial \hat{x}_i \partial \hat{x}_j}. \quad (4.4.3)$$

For the viscous stress air may be taken as Newtonian fluid (see e.g. Schlichting (1968)) for all practical purposes, yielding the following equation for the

viscous stress:

$$\Upsilon_{ij} = \mu \left(\frac{\partial U_j}{\partial x_i} + \frac{\partial U_i}{\partial x_j} \right), \quad (4.4.4)$$

where μ is the dynamic viscosity. For the present experiments it is reasonable to assume that the dynamic viscosity is constant since the temperature is approximately constant everywhere in the flow field yielding $\mu = \mu_\infty$. Using the viscous stress expression in equation 4.4.4 the source term is given by

$$\frac{\partial^2 \left[\mu_\infty \left(\frac{\partial U_\infty \hat{U}_j}{\partial l_\infty \hat{x}_i} + \frac{\partial U_\infty \hat{U}_i}{\partial l_\infty \hat{x}_j} \right) \right]}{\partial l_\infty \hat{x}_i \partial l_\infty \hat{x}_j} = \frac{\mu_\infty U_\infty}{l_\infty^3} \frac{\partial^2 \hat{\Upsilon}_{ij}}{\partial \hat{x}_i \partial \hat{x}_j}, \quad (4.4.5)$$

where

$$\hat{\Upsilon}_{ij} = \left(\frac{\partial \hat{U}_j}{\partial \hat{x}_i} + \frac{\partial \hat{U}_i}{\partial \hat{x}_j} \right) \quad (4.4.6)$$

is the dimensionless viscous stress term. Finally, by combining the wave operator and the source terms one obtains:

$$\left(\frac{\rho_\infty}{t_\infty^2} \frac{\partial^2}{\partial \hat{t}^2} - \frac{\rho_\infty c_\infty^2}{l_\infty^2} \frac{\partial^2}{\partial \hat{x}_i^2} \right) \hat{\rho}' = \frac{\rho_\infty U_\infty^2}{l_\infty^2} \frac{\partial^2 (\hat{\rho} \hat{U}_i \hat{U}_j)}{\partial \hat{x}_i \partial \hat{x}_j} - \frac{\mu_\infty U_\infty}{l_\infty^3} \frac{\partial^2 \hat{\Upsilon}_{ij}}{\partial \hat{x}_i \partial \hat{x}_j}. \quad (4.4.7)$$

Dividing equation 4.4.7 by the term $(\rho_\infty c_\infty^2)/l_\infty^2$ leads to

$$\left(\frac{l_\infty^2}{c_\infty^2 t_\infty^2} \frac{\partial^2}{\partial \hat{t}^2} - \frac{\partial^2}{\partial \hat{x}_i^2} \right) \hat{\rho}' = \frac{U_\infty^2}{c_\infty^2} \frac{\partial^2 (\hat{\rho} \hat{U}_i \hat{U}_j)}{\partial \hat{x}_i \partial \hat{x}_j} - \frac{\mu_\infty U_\infty}{\rho_\infty c_\infty^2 l_\infty} \frac{\partial^2 \hat{\Upsilon}_{ij}}{\partial \hat{x}_i \partial \hat{x}_j}. \quad (4.4.8)$$

Furthermore, by replacing the time t_∞ on the left side of equation 4.4.8 by the term $1/f = \lambda/c_\infty$, where f denotes a characteristic frequency and λ the wavelength, one obtains for the term $l_\infty/(c_\infty t_\infty) = l_\infty/\lambda = He$. The Helmholtz number He is a measure of the compactness of a source (see e.g. [Dowling and Ffowcs Williams \(1983\)](#)). Additionally, the Mach number $M = U_\infty/c_\infty$ can be introduced. The term $\mu_\infty U_\infty/(\rho_\infty c_\infty^2 l_\infty)$ can also be transformed using the kinematic viscosity $\nu = \mu_\infty/\rho_\infty$ and multiplying by the term U_∞/U_∞ one obtains $[\nu/(U_\infty l_\infty)] \cdot [U_\infty^2/c_\infty^2] = (M^2/Re)$, where Re is the Reynolds number. Incorporating these identities into equation 4.4.8 the dimensionless form of Lighthill's analogy can finally be written as:

$$\left(He^2 \frac{\partial^2}{\partial \hat{t}^2} - \frac{\partial^2}{\partial \hat{x}_i^2} \right) \hat{\rho}' = M^2 \frac{\partial^2 (\hat{\rho} \hat{U}_i \hat{U}_j)}{\partial \hat{x}_i \partial \hat{x}_j} - \frac{M^2}{Re} \frac{\partial^2 \hat{\Upsilon}_{ij}}{\partial \hat{x}_i \partial \hat{x}_j}. \quad (4.4.9)$$

It is clear aeroacoustic similarity pertains when the three dimensionless quantities - Helmholtz number, Reynolds number and Mach number - are identical for two different measurement configurations.

In the present experimental study the same models were used in both wind tunnel test sections, meaning that the Helmholtz number must also be the same in both facilities. Additionally, the Reynolds and Mach number must also be identical in order to achieve aeroacoustic similarity. In the two used wind tunnels it was not possible to adjust the Reynolds and Mach numbers independent of each other. Therefore, as a compromise, the flow velocity U was kept constant in the wind tunnel tests in both test sections. This led to only very small Reynolds and Mach number differences between the conducted measurements, resulting largely from varying atmospheric conditions (ambient temperature and pressure). The maximum deviations between both wind tunnel settings are smaller than 0.33% for the Mach numbers and smaller than 0.52% for the Reynolds numbers.

4.5 Estimation of installation and wind tunnel effects

The experimental setups in conjunction with the individual test-section dependent boundary conditions can differently influence the microphone array measurements in both wind tunnels, as has been outlined in chapter 1.2 and 2. The possible consequences will be estimated in this section, given that these effects are currently predictable and possess a relevant significance for the present measurements. In particular, this section considers the array resolution and the emission angle with resulting directivity effects in both wind tunnels. The transmission coefficient is also examined for the open test section setup, whereas for the closed test section the reflections are of more major concern.

4.5.1 Array resolution

The plate model is well suited to give an insight into the microphone array resolution capabilities for the current experimental setup. If the cavities are excited by a grazing flow, then the various source positions and their distances to each other are known in advance. This statement does not apply for the reference sound source and the wing model. On the one hand, one expects only one single strong source, but on the other, the source positions are not known a priori. Therefore, the plate was selected to estimate exemplarily the array resolution. Figure 4.9 shows the narrow band source map for five simulated incoherent monopole sound sources exhibiting equal and normalized source strengths and a source frequency of 5 kHz. The simulated source positions correspond to the cavity locations. It is barely possible to

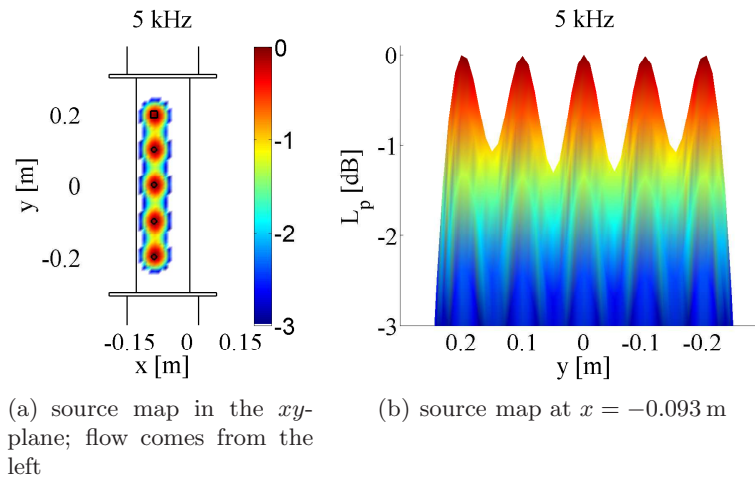


Figure 4.9: Narrow band source map of simulated incoherent monopole sources with equal and normalized source strengths, each at the individual cavity positions for various views. The monopole sources are located 0.975 m above the microphone array surface. The source frequency is 5 kHz. The normalized sound pressure level L_p is shown color-coded.

discriminate the various sources in the map due to the superposition of the individual main lobes from the monopoles. Especially in the side view in (b), it can clearly be seen that the resulting local minima between two main lobe maxima is just 1 dB below the peak level. Since in the current case the source-observer arrangement is fixed, only the source frequency will affect the main lobe width (see section 2.2.2). This means that for the current experimental setup, sources which have a distance smaller than 0.1 m cannot be separated from each other at frequencies below 5 kHz. With increasing frequency the main lobe width becomes smaller and subsequently, the array resolution increases. Due to the identical geometrical setup of the experiments in both wind tunnels the microphone array resolution is the same as long as no other disturbances are present (flow effects, reflections, etc.).

4.5.2 Emission angle and directivity effects

In the following the question whether a source directivity has an influence on the comparison of beamforming results for the current test setup will be examined. A schematic sketch of the setup in both test section types is depicted in figure 4.10. Looking at the n -th microphone of the microphone array installed in the open test section (figure (a)) the source, located in the potential core of the jet, emits a wavefront at an angle ϑ_{os} . The convection of the wave takes place due to the parallel flow until the turbulent shear layer is reached. While propagating through the shear layer the sound

4.5. ESTIMATION OF INSTALLATION AND WIND TUNNEL EFFECTS

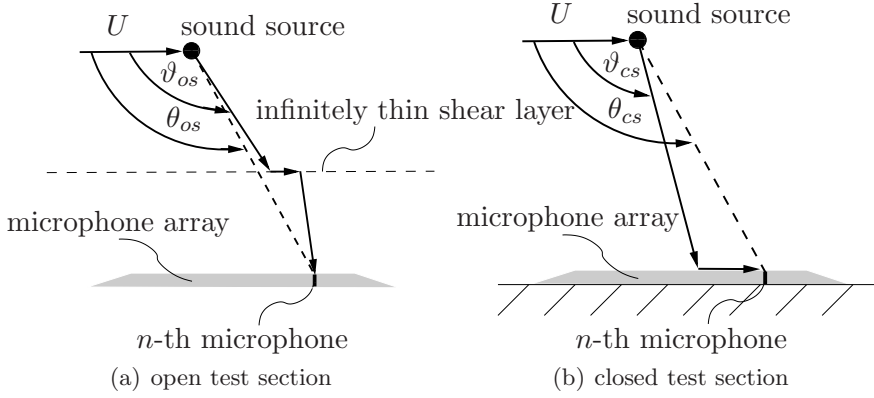


Figure 4.10: Illustration of the differing emission angles in both test sections, although an identical geometrical experimental setup has been used.

waves are refracted. Hence, with the sound propagation through the potential flow and the shear layer, ϑ_{os} is different from the geometrical angle θ_{os} . In the case of the closed wind tunnel the situation is different, as shown in figure 4.10 (b). The uniform, parallel flow carries the waves on their way to the n -th microphone. Hence, with the sound propagation through the parallel flow, ϑ_{cs} is different from the geometrical angle θ_{cs} . An influence of the thin boundary layer on the array surface on the incoming sound waves has been neglected. Although the geometrical situation in the open and closed test section is identical and hence $\theta_{os} = \theta_{cs}$ for the n -th microphone, the original emission angles ϑ_{os} and ϑ_{cs} of the impinging waves differ from each other. This has to be taken into account when examining a source with non-negligible directivity, since it may influence the beamforming results. Shifting each microphone along the x-axis to a particular position can compensate for this effect for a given flow velocity. For a microphone array this is normally not practicable, because the individual microphone shifts depend on the source location and on the location of the microphones.

Concerning the employed models in this thesis the aeroacoustic cavity sources of the plate model and the aeroacoustic slat sources of the wing model may constitute such types of source having a non-negligible directivity. As outlined in section 3.4, the slat sources are typically dipole-like sound sources, so that the emission angle difference can be exemplarily evaluated for a simulated point source (illustrated as red point in figure 4.11 (a)) in the vicinity of the slat cove of the wing model. Figure 4.11 (b) shows the individual emission angle difference $\Delta\vartheta = |\vartheta_{os} - \vartheta_{cs}|$ between the open and closed test section for each array microphone in the case of the same geometrical setup. The performed comparison is based on the assumption of uniform flow in the closed wind tunnel and in the open test section. The infinitely thin plane shear layer model from section 2.3.2 has been applied.

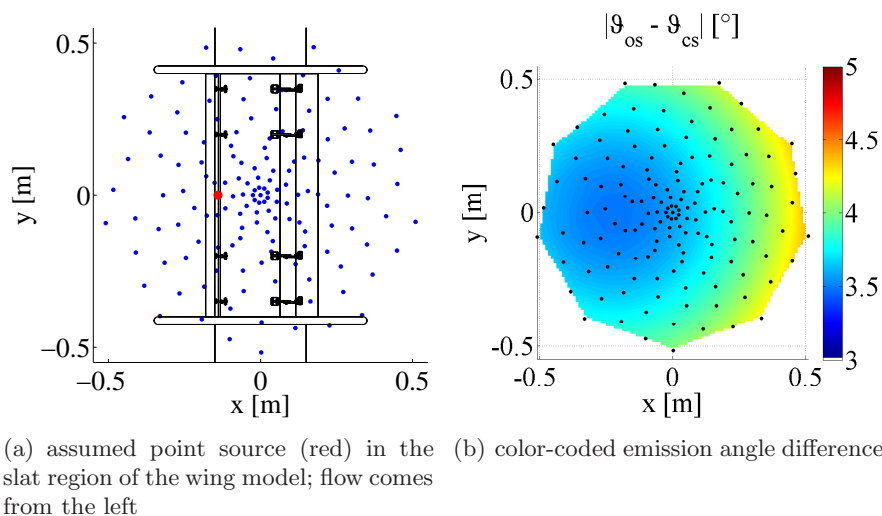


Figure 4.11: Emission angle difference $|\vartheta_{os} - \vartheta_{cs}|$ between open and closed test section for each array microphone and for an assumed point source in the vicinity of the slat cove at flow velocity $U_{\infty} = 35$ m/s.

The flow velocity is 35 m/s. For the present configuration the angle deviations are smaller than 4.5° . This value seems to be small, but the actual influence on the measured amplitudes depends on the orientation of the dipole source, which is examined next. The scenario used for the illustration of this fact is depicted in figure 4.12 (a). In the open test section the n -th array microphone would measure the root-mean-square pressure value p_{os} which results from the sound generation of a point dipole source. The orientation of the dipole main lobe compared with the microphone position is given by the angle θ_{di} . Assuming that $\theta_{di} = 0^{\circ}$, the dipole main lobe would point directly to the microphone. For the case that the orientation angle θ_{di} is 90° , the measured pressure value p_{os} would vanish, since there is no sound radiation in this direction from the dipole. As previously described, although the source-microphone array arrangement in the open and closed test section is identical, the emitted wave fronts travel along different paths to the n -th array microphone in both test sections due to the different flow conditions and, subsequently, to the received waves fronts being originally emitted under different emission angles. This corresponds to a virtual shift of the n -th microphone along the x -axis when comparing both test sections, leading to an altered orientation of the n -th microphone to the dipole axis in the closed wind tunnel. Thus, in the closed test section the n -th microphone measures the root mean square pressure value p_{cs} , which differs from p_{os} due to the dipole directivity. Figure 4.12 (b) shows the level difference between both measured root-mean-square pressures employing an emission angle difference of 4.5° . For a dipole orientation angle smaller than 34° , the

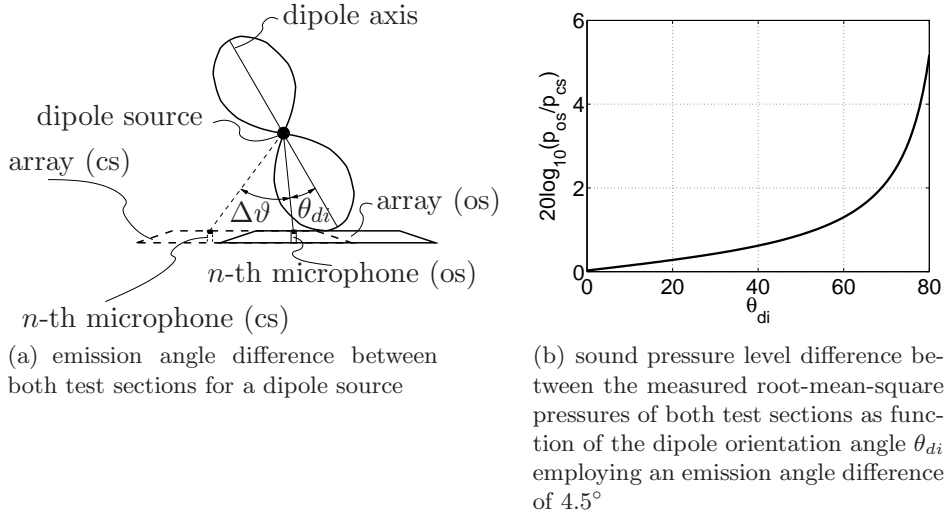


Figure 4.12: Illustration of the emission angle difference and directivity effects by means of a dipole source.

pressure difference is smaller 0.5 dB. At $\theta_{di} = 53^\circ$ deviations of the order of 1 dB will be obtained. Then, with further increasing dipole orientation, angle the level differences grow rapidly. Since there is no practicable compensation approach available at the present time one has to live with this influence.

4.5.3 Transmission coefficient

Besides the variation of the emission angle mentioned above, the shear layer in the open jet wind tunnel gives rise to a reflected and transmitted wave, as described in section 1.2.2 and 2.3.2. In the limiting case, total reflection can occur and no sound wave is transmitted through the shear layer, so that it would then not make sense to perform a comparison between the measurements in both wind tunnels. To preclude this phenomenon the transmission coefficient T_p was computed for the current experimental setup for the flow velocity of 35 m/s using equation 2.3.52 of chapter 2.3.2. The transmission coefficient depends solely on flow Mach number and the normal vector of the incident wave which carries the information about the angle of incidence of the wave fronts on the shear layer. For the current experimental setup, the transmission coefficient deviates less than 5% from unity, which is equivalent to level variations below 0.4 dB, indicating that total reflection is not of concern for the present experimental study.

4.5.4 Reflections in the closed test section

In contrast to the open jet wind tunnel reflections arise from the reverberant walls in the closed test section. As described in section 2.3.1, the reflections can influence beamforming results in a qualitative and quantitative manner, mainly the source strength and source position are affected. To avoid these effects Moshier (1996) suggests to apply a time window for the processing of the time series in beamforming which is shorter than the travel times differences between the source signals and their reflected waves. In this special case the reflections appear incoherently at the array for broadband sources. For the current experimental setup of the closed test section measurements this approach cannot be applied, because it would lead to a too low frequency resolution. In the selected time window for the FFT the sound waves can travel a distance of 9.94 m. In order to implement Moshier's method for the dimensions of the closed wind tunnel the time window has to be approximately 10 times smaller than the selected one, which in turn would reduce the frequency resolution to a non-acceptable band width. Taking into account the experimental experiences of Sijstma and Holthusen (2003) the influence of the reflecting walls on the beamforming results can be minimized by placing the model sources as far as possible away from the reverberant walls. In their experiments in a closed test section they deduced that for sources which are positioned 0.3 m away from the walls the source position found in the 1/3 octave band beamforming results are mainly affected below 2 kHz. This influence on the localized source position could be reduced by shifting the source to the middle of the wind tunnel. These results were incorporated in the current experimental setup. All models are placed in the middle of the wind tunnel test section as far this was possible. Nonetheless, one has to expect deviations in the closed test section with its reverberant walls compared with anechoic conditions of the open test section.

4.6 Data acquisition and test program

In this section all important aspects which are associated with the parameter settings of the data acquisition system and the course of the test program are addressed. Settings which were identical in the measurements with all three models are presented directly in the following. Additional settings or deviations from these overall settings will be described in the individual model subsections. In all measurements the data acquisition system VIPER-48 from GBM is located outside the test section. The microphone signals were simultaneously sampled with a sampling frequency of $f_s = 140$ kHz for all measurements on all three models. All channels had an anti-aliasing filter at $f_u = 70$ kHz. In both wind tunnels the recording time for one measurement was 30 s. The measured microphone time series were processed using an

FFT block size of 4096 samples and a Hanning window with 50 % overlap. This results in a frequency resolution $\Delta f = 34.18$ Hz and enables averaging over 2051 FFT blocks. Additionally, a high-pass filter was used for the measurements in both test sections with a cut-off frequency of 6 kHz in order to suppress low frequency wind tunnel noise. Typically, such a filter is not needed in open jet wind tunnels with an anechoic test section, but keeping in mind the issue of the comparability of microphone array measurements this adjustment was kept constant for both wind tunnel test sections. Furthermore, there is no need to correct all shown results in the chapters 5, 6 and 7 in terms of the high-pass filter response, since it is a comparable study and the identical filter was used for all performed measurements.

4.6.1 Reference sound source

The reference sound source, a loudspeaker, provides great flexibility in the spectral signal structure in that it can be operated with broadband and tonal signals. The details of the measurement parameters and settings are given below.

Measurements of broadband signals

For the reference sound source, band-pass filtered white noise served as the loudspeaker input signal. The rms-value of the input voltage was kept constant for the measurements in both tests sections. In former experiments (Kröber (2007)) it had been shown that with this procedure the amplitude can be reliably adjusted to an accuracy which is repeatable to within ± 0.55 dB in terms of 1/3 octave bands. In order to generate high amplitude oscillations with the loudspeaker and to get sufficiently large SNR, the measurements were performed in two steps. Especially in the closed test section strong low frequency wind tunnel background noise will be present. Therefore the measurements were divided into a low and high frequency part: for the low frequency measurements band-pass filtered white noise, in the range of 1 kHz to 12.5 kHz, was employed as the loudspeaker input signal. The sampling frequency of 30 kHz for the low frequency case deviates from that of the overall settings. The recording time in these measurements was extended to 40 s. The achieved frequency resolution of $\Delta f = 29.3$ Hz derives from an FFT block size of 1024 samples. With these parameter settings and a window overlap of 50 % it was possible to perform 2343 averages. For the high frequency measurement the setup parameters were set to the previously described overall settings. The computed results, which will be presented later in chapter 5, consist of these two measured parts. All shown results up to and including the 1/3 octave band of $f_m = 8$ kHz are derived from the low frequency measurements, while all above this frequency from the high frequency measurements. A flow speed of 35 m/s was used, which

is the highest velocity available in both wind tunnels. In order to examine the flow effects on sound propagation further measurements were conducted when the fluid in the tunnels was at rest.

For the computation of the source maps an equidistant grid consisting of 42411 points is used. The grid covers the region of the reference sound source and is in the observation plane which lies in the xy -plane 0.975 m above the array surface and it also corresponds to the mid-plane of the test sections. It has a resolution of $\Delta_x = 0.0047$ m and $\Delta_y = 0.01$ m.

Measurements of tonal signals

The target of the measurements using a tonal loudspeaker input signal is to evaluate the influence of spectral broadening on the measured spectra in both test sections. This requires modified signal and processing parameters which are displayed in table 4.6.1. These settings enable a very fine

tone frequency [Hz]	sampling frequency [Hz]	FFT window length in samples	number of averages
4096	16384	16384	1999
16384	65536	65536	1999
40960	131072	131072	1999

Table 4.6.1: Signal and processing parameters for tonal measurements with the reference sound source

frequency resolution of $\Delta f = 1$ Hz and, at the same time, the long recording time of 1000 s allows an averaging over 1999 FFT blocks. Further, such a long time series is essential because the quality of the bispectral estimate can be improved by increasing the number of data blocks.

Measurements of the flow velocity distribution in the shear layer

To assess the shear layer thickness δ_s , which is needed for the calculation of the dimensionless scattering parameter $M\delta_s/\lambda$, a Prandtl tube was traversed through the shear layer in the open test section and the flow velocity was measured. The probe was traversed along the z -axis at $y = 0$ and various x -positions (-0.4 m, 0.0 m and 0.4 m), with the Prandtl tube situated between 0.4 m and 1.2 m away from the nozzle and at the same height as the central microphone. The shear layer thickness was then estimated by means of the measured shear layer velocity profiles. However, the term shear layer thickness is ambiguous, since there is no universally accepted definition of the shear layer boundaries. In many publications, among others cited in this thesis, the term shear layer thickness is used and thickness values are

presented without giving details of the estimation procedure. The underlying estimation method of the shear layer thickness applied in this study is based on the approach of [Liepmann and Laufer \(1947\)](#) and was also employed by [Candel et al. \(1976\)](#), [Schlinker and Amiet \(1980\)](#) and [Brooks and Humphreys \(1999\)](#) in their experiments concerning the sound transmission through turbulent shear layers. The approach is briefly presented in the appendix [B.1](#).

4.6.2 Plate with cavities

The parameter settings for the data acquisition and the signal processing of the plate measurements coincide with the overall settings mentioned at the beginning of this section. At first, the plate with cavities was measured in the open jet wind tunnel. Due to the maximum achievable flow velocity of 65 m/s this wind tunnel is suited for conducting velocity variations in order to characterize the cavity noise mechanisms. The measurements were performed starting at a flow speed of 25 m/s and then, the flow velocity was increased successively in 5 m/s steps up to a speed of 50 m/s. In the closed wind tunnel the measurements were only performed at the highest available flow velocity of 35 m/s. In addition, the cavity openings were covered with tape in order to suppress the flow-induced sound from the cavities. In conjunction with the other measurements without this covering, a calculation of the SNR in both wind tunnels is thereby possible.

As before for the reference sound source, for the computation of the beamforming results an equidistant grid consisting of 42411 points is used, lying in the mid-plane of the test sections, 0.975 m above the array surface. This time, the grid covers a smaller region than the grid used for the reference sound source, because of the smaller model dimensions and an expected onset of sound radiation at higher frequencies compared with the reference sound source. Consequently, this leads an increased resolution of $\Delta_x = 0.0024$ m and $\Delta_y = 0.004$ m.

4.6.3 Wing with high-lift system

In the case of the wing with a high-lift system combined aerodynamic and acoustic measurements were performed in both wind tunnels. The aerodynamic measurements provide the basis for the comparison of the acoustic results measured in the open and closed test section.

Aerodynamic measurements

At first, the measurements of the generic high-lift system were conducted in the open jet wind tunnel for an angle-of-attack of 12° at the flow velocity 35 m/s. Higher angles-of-attack were not possible with the chosen setup

since the jet deflection induced by the model causes problems with wind tunnel collector flow.

A typical angle-of-attack for landing of a real civil passenger aircraft in unbounded flow is around 6° (Dobrzynski (2010)). According to the experimental and numerical work from Ewert et al. (2010), for the used wing model with high-lift system the effective angle-of-attack has to be set to 17° in the open jet wind tunnel (AWB) in order to obtain a close correspondence with the pressure distribution arising from landing conditions at free-flight (6° angle-of-attack). This means that typical landing conditions at free-flight cannot be achieved with the current experimental setup, but this fact does not deter a comparison between the open and closed test section results.

For the closed test section the measurements were carried out at angles-of-attack in the range between -1.5° and 12° in order to find the corresponding angles-of-attack for the open jet wind tunnel having a similar flow field. The similarity of the flow fields is evaluated by means of the pressure coefficient c_p and the resulting lift force derived from the integration of the measured surface-pressure distribution around the three wing elements. More details about aerodynamic measurements and the data processing can be found in the appendix B.2.

Acoustic measurements

For the data acquisition and the signal processing for the aeroacoustic measurements of the wing model the parameters were set to the overall settings, as introduced in the preparatory part of this section. The grid used for the computation of the source maps consists of 52461 grid points which are equidistantly distributed. It covers the region of interest in the observation plane and the grid is rotated together with the wing model in order to take into account the deployed angle-of-attack variations of the model. At an angle-of-attack of 0° , the employed grid has a resolution of $\Delta_x = \Delta_y = 0.005$ m.

4.7 Comments to the presentation of the results

Some brief comments are given below regarding the presentation of the results from the three models in the chapters 5 to 7.

4.7.1 Single microphone spectra

All shown narrow band and 1/3 octave band spectra are plotted as sound pressure level:

$$L_p = 20 \cdot \log_{10} \left(\frac{p_{rms}}{p_{ref}} \right) \text{ dB}, \quad (4.7.1)$$

where p_{rms} indicates the measured root-mean-square value and p_{ref} denotes the reference pressure of $2 \cdot 10^{-5}$ Pa. This reference pressure corresponds to the hearing threshold for a typical human ear in air at 1 kHz.

4.7.2 Source maps

The computation of the beamformer output for each grid point following the procedure in chapter 2 yields the so-called source maps. For each grid point an equivalent monopole source strength corresponding to the measured microphone data is calculated. In the maps these source strengths are displayed as equivalent sound pressure levels which would pertain at a distance of 1 m away from the source, using again the reference pressure of $2 \cdot 10^{-5}$ Pa. The dynamic range of the source maps is typically 12 dB. If the resulting map is associated with a physical case where flow is present, then the flow is always from left to right. For the computation of the source maps no shading (see chapter 2.3.3) was applied; this ensures the same array aperture and array characteristics in both wind tunnels for the comparison of the beamforming results. Furthermore, the obtained source maps provide the basis for the integration approach which was outlined in section 2.2.4.

4.7.3 Microphone signal coherence

Besides the computation of source maps the coherence between the measured microphone signals can give information about the existence of decorrelation processes affecting the sound propagation from the source to the receiver. The coherence $\Gamma_{n,m}$ of the signals of the array microphones m and n can be easily computed using the entries of the cross-spectral matrix \mathbf{R} :

$$\Gamma(\omega)_{n,m} = \sqrt{\frac{R(\omega)_{m,n}R(\omega)_{n,m}}{R(\omega)_{m,m}R(\omega)_{n,n}}}. \quad (4.7.2)$$

The coherence function takes values from 0 to 1 depending on whether there is no or a completely linear dependence between the signals.

4.7.4 Far-field microphone spectra

The results from the far-field microphone requires an amplitude correction so that these results and the corresponding microphone array results can be compared; this is due to the different experimental setups leading to differing distances between the models and the sensors. For the far-field spectra an Amiet flow correction (accounting for travel path and amplitude decay, transmission coefficient and amplitude divergence, see section 2.3.2) related to the point at $(-0.093 \text{ m}, 0 \text{ m}, 0.975 \text{ m})$ was conducted. This reference point coincides with the center point of the loudspeaker membrane with the position of cavity 3 of the plate model and is close to the slat cove of the

CHAPTER 4. EXPERIMENTAL SETUP, INSTRUMENTS AND METHODS

wing model. Finally, the far-field spectra are again related to a reference distance of 1 m, enabling a comparison between the integrated and far-field spectra.

Chapter 5

Experimental results of the reference sound source

This chapter discusses the experimental results of the reference sound source obtained from measurements in the open and closed wind tunnel test section. The following considerations begin with an examination of single microphone spectra (section 5.1), quasi as an introduction to the evaluation of the experimental results. Subsequently, the beamforming results from both test sections, including source maps, and the examination of the microphone signal coherence are presented and analyzed in-depth (sections 5.2 and 5.3). Finally, in section 5.4 an extensive comparison between both wind tunnel test campaigns is performed, comprising the source maps, microphone coherence, integrated and far-field spectra, the SNR and the localized source position.

5.1 Single microphone spectra measured in both wind tunnels

The analysis of the measurements of the reference sound source starts with a consideration of single microphone spectra. At first, the measured spectra of broadband signals (loudspeaker input signal: bandpass filtered white noise from 1 to 70 kHz) are evaluated and secondly, tonal signals with various frequencies are examined.

5.1.1 Broadband signals

Figure 5.1 shows the spectra of the broadband loudspeaker signals measured by the central array microphone under various conditions in both test sections. On the one hand the fluid is at rest and the loudspeaker was turned on, while on the other the loudspeaker was turned off, but the wind tunnel was operated at 35 m/s, so that the central array microphone measures also

the existing wind tunnel noise, including also that from the background, boundary and shear layer.

For the case without flow, the highest sound pressure levels are obtained below 20 kHz and with growing frequency the measured amplitude decreases. In both test sections the measured spectra possess the same trend. Especially at low and high frequencies there are sizable level deviations between both spectra caused by reflections at the reverberant walls in the closed test section.

In the closed test section the wind tunnel noise is dominated by the background noise and the turbulent pressure fluctuations of the boundary layer. Below 2.5 kHz and above 60 kHz the background noise and turbulent boundary layer noise start to overwhelm the loudspeaker signal. In contrast to that, in the open test section the background and shear layer noise are mostly far below the signal of interest for the given frequency range.

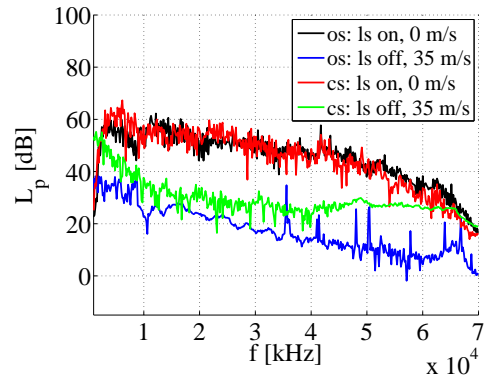


Figure 5.1: Sound pressure level of the central array microphone measured in the open (os) and closed (cs) wind tunnel under various conditions (loudspeaker on and off; with flow velocity of 35 m/s and flow at rest).

5.1.2 Tonal signals

Besides the broadband signal, tonal signals were used as loudspeaker input signal having the particular tone frequencies of 4096 Hz, 16384 Hz and 40960 Hz. The influence of the flow velocity on the measured spectra is evaluated by means of the loudspeaker tone frequency of 4096 Hz, shown in the diagrams in figure 5.2. All curves are normalized to the tone amplitude which was measured for the case with the fluid at rest. In plot (a) the results for the open jet wind tunnel are shown. The curves illustrate the effect which is known as spectral broadening. The sound propagation through the turbulent shear layer is accompanied by a transfer of acoustic energy, which was originally associated with the tone frequency, into adjacent frequency bands. The broadened spectrum is characterized by two lateral bands which both exhibit both a local maximum as a consequence of the acoustic energy transfer. As outlined in chapter 2.3.3, the depicted case in figure 5.2 falls into the category of weak scattering; i.e. the proportion of scattered energy is small relative to the energy that remains in the tone so that the tone is clearly distinguishable in the spectrum. A similar spectral shape was exper-

5.1. SINGLE MICROPHONE SPECTRA MEASURED IN BOTH WIND TUNNELS

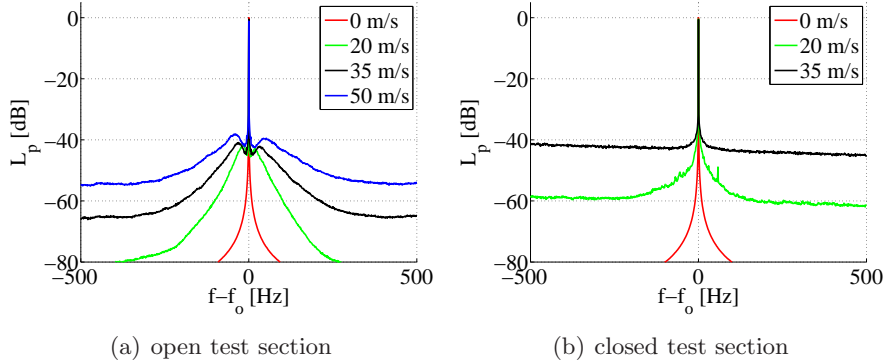


Figure 5.2: Normalized sound pressure levels of the central array microphone for a tone of $f_o = 4096$ Hz at various flow velocities. The results are centered around f_o showing a bandwidth of 1 kHz.

imentally observed by [Candel et al. \(1975\)](#). The scattered acoustic energy increases with rising flow velocity. The frequency shift Δf between the local maxima in the side bands and the tone frequency is shifted to higher values with increasing flow velocity. As shown by [Candel et al. \(1975\)](#) the large scale main energy-bearing eddies provide the essential contribution to the scattered acoustic field. The underlying Doppler effect is responsible for the frequency shift which is proportional to the ratio of the local eddy convection velocity and the length-scale of the large eddies. For example, at a flow speed of 35 m/s the frequency shift between the maximum of the lateral bands and the tone is approximately ± 30 Hz. At 50 m/s this value has increased to ± 40 Hz. The same measurements in the closed test section do not reveal a broadening effect in the tone spectra, as can be seen in figure 5.2 (b). In fact, it cannot be ruled out here that the background and boundary layer noise mask the spectral broadening effect at 35 m/s, since the background noise levels outside the tone frequency are considerably higher than in the open test section. In spite of that, at 20 m/s the noise levels are low enough in the closed test section so that spectral broadening effects could be examined; nevertheless one cannot observe such an effect in the closed test section.

To which extent the tone frequency will affect the spectral broadening is examined in the following. Figure 5.3 presents the broadened spectra for the three different tone frequencies, where in each case the results are centered around the individual tone frequency f_o and plotted for a bandwidth of 1 kHz for the flow speed of 35 m/s. Each curve is normalized to the individual measured tone amplitude. In the open test section, all three tone spectra exhibit the typical broadened shape for a weak scattering process (see figure 5.3 (a)). The local maxima of the side bands are independent of the tone frequency. Solely the scattered energy is greater for higher fre-

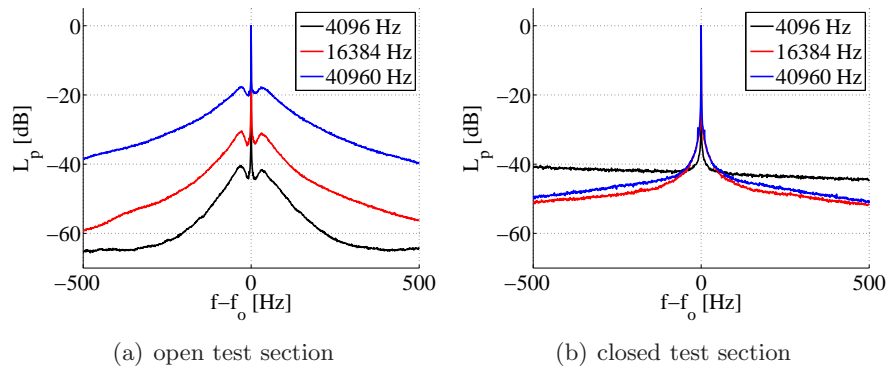


Figure 5.3: Normalized sound pressure levels of the central array microphone for various tones at a flow velocity of 35 m/s. The results are centered around f_o with a bandwidth of 1 kHz.

quencies leading to an extended broadband hump and a smaller difference between the tone peak level and the level of the local side band maxima. This is a result of an increased ratio of the shear layer thickness to the wavelength of the incident sound wave. The closed test section results in figure 5.3 (b) do not harbor any surprises. Of concern for the current experimental setup in the closed test section is not the spectral broadening, but rather the wind tunnel background and boundary layer noise.

The bicoherence spectrum was computed as described in chapter 2.3.3 in order to evaluate the possibility of identifying the broadened components of tone spectra after the sound propagation through the turbulent shear layer. The frequency f_m was set to the tone frequency f_o and kept constant in the calculation of the bicoherence spectrum and the frequency f_n was varied in the range of -500 Hz to 500 Hz in 1 Hz steps so that only a slice of the two-dimensional bicoherence spectrum was computed. The results of the 4096 Hz tone at a flow speed of 35 m/s are shown in figure 5.4. In the open test section the bicoherence spectrum has approximately the same double hump as in the power spectrum. The maxima of the local side bands of the bicoherence spectrum correspond approximately with the local side band maxima of the power spectrum and at the tone frequency one obtains the highest value of $B_c = 0.93$. Furthermore, the bicoherence spectrum matches qualitatively the different hump heights of the power spectrum. Finally, it is possible to identify the coupling of the tone and the spectral components of the side bands in the present case by means of higher order spectral analysis techniques. The same measurement was conducted in the closed test section and the obtained results are shown in figure 5.4 (b). Neither the power spectrum nor the bicoherence spectrum shows any spectral broadening. The bicoherence spectrum has zero values except at the tone frequency.

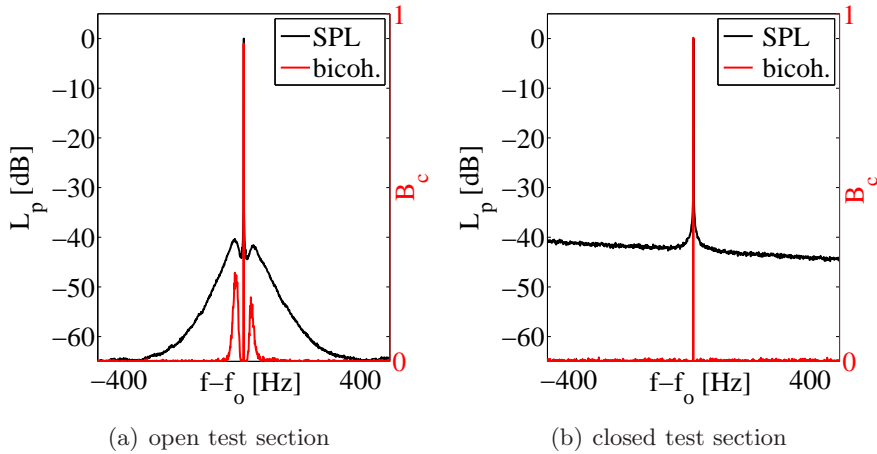


Figure 5.4: Normalized sound pressure level (SPL) of the central array microphone and the corresponding bicoherence spectrum for a tone of $f_o = 4096$ Hz at 35 m/s. The results are centered around f_o with a total bandwidth of 1 kHz.

5.1.3 Brief summary of the single microphone measurements

The evaluation of the single microphone spectra revealed that the SNR is different in both test section types. In general the SNR is higher in the open test section than in the closed test section, where, for the latter, strong wind tunnel background and boundary layer noise are present. In contrast, the turbulent shear layer in the open jet wind tunnel is responsible for the spectral broadening effect which is not of concern in the closed test section. Spectral broadening effects are predominant at higher frequencies, since more acoustic energy is redistributed into other frequency bands than at lower frequencies. As pointed out in chapter 2.3.3 directional scattering is a prerequisite of spectral broadening which means that one has to expect an influence of directional scattering on the beamforming results in the open test section, in particular for high frequencies.

5.2 Microphone array results from the open test section

Beginning with results from the open test section, the results comprise an evaluation of the source maps with and without flow correction and an analysis of the microphone signal coherence. This is conducted by way of example for 1/3 octave bands with low, middle and high frequencies.

5.2.1 Source maps

Figure 5.5 depicts 1/3 octave source maps of 2 kHz of the reference sound source, measured in the open test section for the two flow velocities 0 and 35 m/s, respectively and various beamforming parameters.

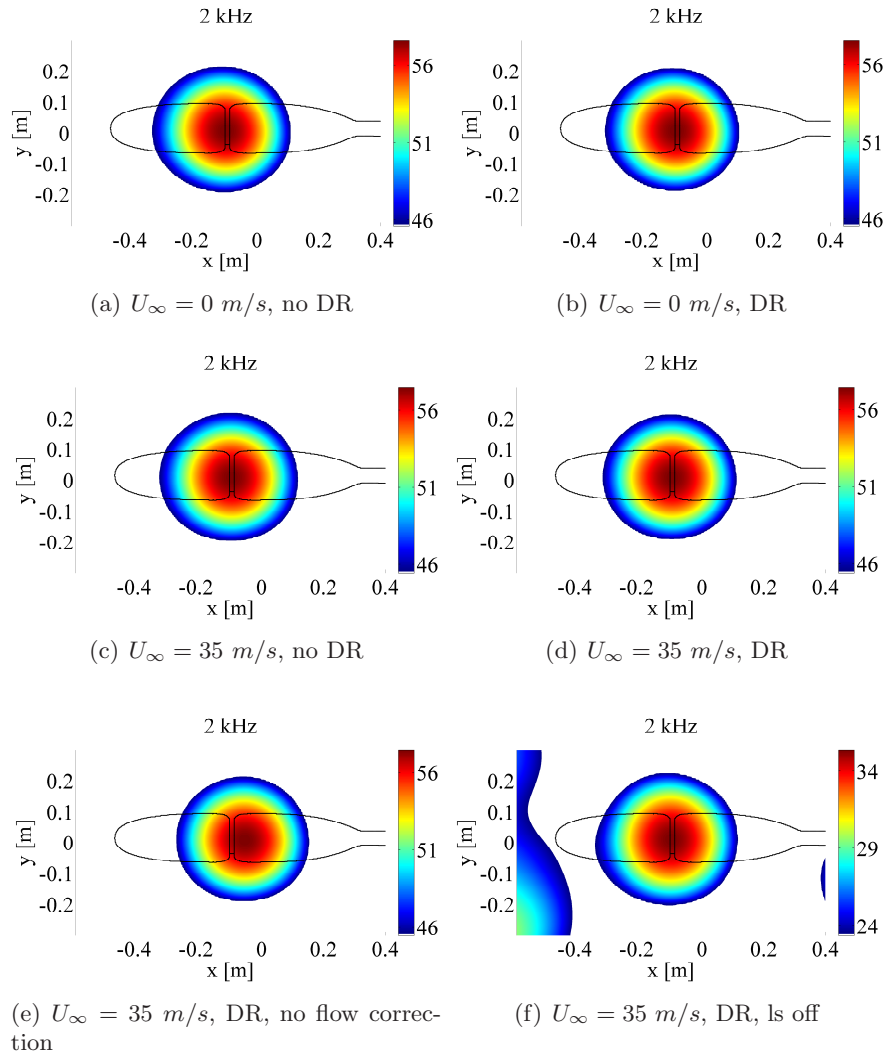


Figure 5.5: Beamforming results (in dB) of the reference sound source for the 1/3 octave band of 2 kHz for the open test section for various flow velocities, various beamforming parameters and with loudspeaker (ls) on and off. Flow comes from the left.

The source maps in (a) and (b) show that in the no flow case there is no observable influence of diagonal removal on the results indicating that the main diagonal of the cross spectral matrices are not dominated by additional

noise (wind tunnel background and shear layer noise is negligible compared with source strength of the loudspeaker) and that there is a good coherence between the microphone signals. The found source location coincides with the position of the loudspeaker membrane. In (c) and (d) the source maps with flow are plotted. Again, DR has no influence on the source maxima and on the general source appearance. Furthermore, the flow correction using the Amiet model gives almost identical results with respect to source position, appearance and maximum value compared with the source maps without flow. For all depicted cases from (a) to (d) the source is located in the vicinity of the ribbon membrane of the loudspeaker. When the flow correction is not applied, the source will be located more downstream at a wrong position, as shown in (e). It is remarkable that for such low frequencies the amplitude measured by the microphones is apparently not affected by the flow, meaning that the transmission coefficient of the shear layer is approximately one (this was actually predicted in chapter 4.5.3), the travel paths of the sound waves are only insignificantly altered by the flow and sound scattering off turbulent structures is not important in the underlying case. The final plot (f) in figure 5.5 depicts the source map when the loudspeaker is turned off. For this configuration an aeroacoustic source can be identified at the position of the cavity where the ribbon membrane is recessed, but the source strength is more than 20 dB lower than compared with the electromechanical sound generation of the loudspeaker.

Figure 5.6 shows a similar comparison, this time for the 1/3 octave band of 25 kHz and having the same beamforming and configuration parameters as before. One major difference to the 2 kHz case is the better resolution, which typically increases with rising frequency, as already pointed out in chapter 4.2 where theoretical aspects of beamforming were discussed. For the source maps in (a) and (b), the application of DR gives no additional improvement and hardly changes the source maps, which are characterized by the excellent SNR and the microphone signal coherence of the measurements. The found source position was located correctly in the vicinity of the loudspeaker membrane, as was to be expected. The same statements can be made with respect to the results with a flow velocity of 35 m/s, as plotted in (c) and (d). Nonetheless, a difference is observable concerning the maximum peak level in the maps with and without flow. The scattering of sound in the turbulent shear layer becomes more important than at the lower frequency for the open test section. The coherence loss caused by the turbulent shear layer degrades the source maximum by about 1 dB. The phenomenon of turbulent scattering is not part of the Amiet shear layer correction procedure, so that, with respect to this aspect, no improvements can be expected in the computed source maps where this flow correction has been applied. In spite of all this, the flow correction again produces good results with respect to the localized source position. Ignoring the presence of the flow in the beamforming process, the source is determined to be located

CHAPTER 5. EXPERIMENTAL RESULTS OF THE REFERENCE SOUND SOURCE

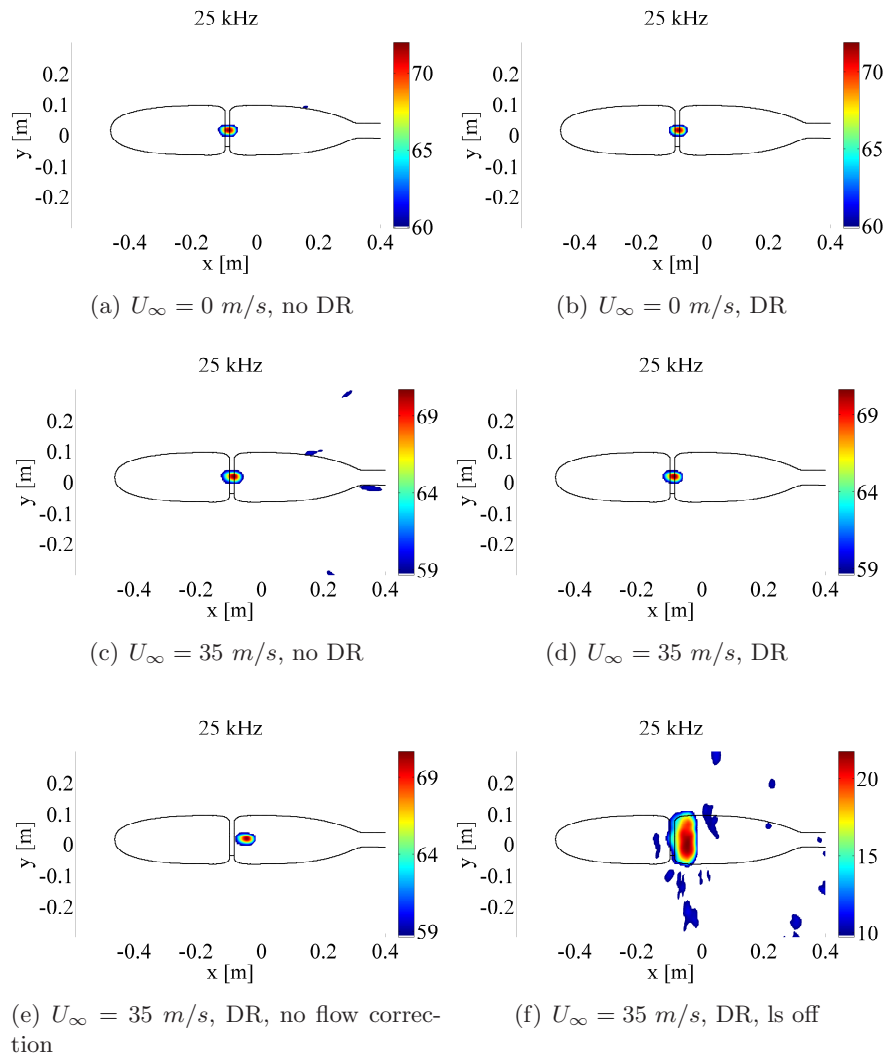


Figure 5.6: Beamforming results (in dB) of the reference sound source for the 1/3 octave band of 25 kHz for the open test section for various flow velocities, various beamforming parameters and with loudspeaker (ls) on and off. Flow comes from the left.

further downstream at a position which does not correspond to that of the membrane, as depicted in (e). Apart from that the two obtained results are very similar and confirm the influence of turbulent scattering on the peak level reduction in the source maps, provided that the transmission factors remain frequency independent in this frequency range (as suggested by other experimental results (Amiet (1975), Morfey and Tester (1977), Tester and Morfey (1976) and Ahuja et al. (1981))), so that the transmission factors are approximately unity, as had been verified in the 2 kHz case. Again, when the loudspeaker is off (see (f)), an aeroacoustic source can be seen to be located at the rear end of the cavity, with a peak level almost 50 dB lower than with the loudspeaker on. In all likelihood the aeroacoustic noise is generated by the flow separating from the front part of the cavity and then re-imping on the rear part later on.

The beamforming results for the highest measured 1/3 octave band are shown in figure 5.7 (a) and (b) for the no flow case. At 63 kHz the localized source position is again in the vicinity of the loudspeaker membrane. The lower output power of the loudspeaker (compared with its source power at lower frequencies), coupled with phase deviations and self-noise of the measurement chain, yield a lower SNR than at lower frequencies. For this reason the application of diagonal removal slightly reduces the maximum value in the source map. For the present case the presence of flow has a more distinctive impact on the results, as shown in (c) and (d). Depending on whether diagonal removal has been applied or not, the maximum peak levels in the source maps are dramatically reduced by 8 or 7 dB, respectively, which is caused by the scattering of the sound waves off turbulent structures in the shear layer. During this process the original coherent source signals are partly distorted into incoherent noise. This incoherent part of the source signal cannot contribute to the source localization via beamforming, and only leads to a reduction of the SNR in the source maps. For the 1/3 octave band of 63 kHz the acoustical wavelength λ is about 5 mm, so that λ is much smaller than the shear layer thickness ($\approx 28\lambda$, for details of the determination see B.1) in the region where the sound waves pass through the shear layer to the microphones. Other authors, such as Candel et al. (1975), Schlinker and Amiet (1980) or Ahuja et al. (1981), have also observed in their experiments that the amount of scattered acoustic energy increases dramatically if the shear layer thickness is at least 10 times the incident acoustic wavelength, whereby they had examined pure tones in single microphone measurement. Furthermore, for such high frequencies, the influence of turbulent absorption can have an effect similar to that of turbulent scattering, leading also to a reduction of the SNR and the source maximum. After applying the flow correction, the source can be seen to be localized in the vicinity of the membrane (see (d) and (e)), but for the first time the source map with flow correction shows a lower maximum source level than in the case without. The reason for that is in all likelihood the

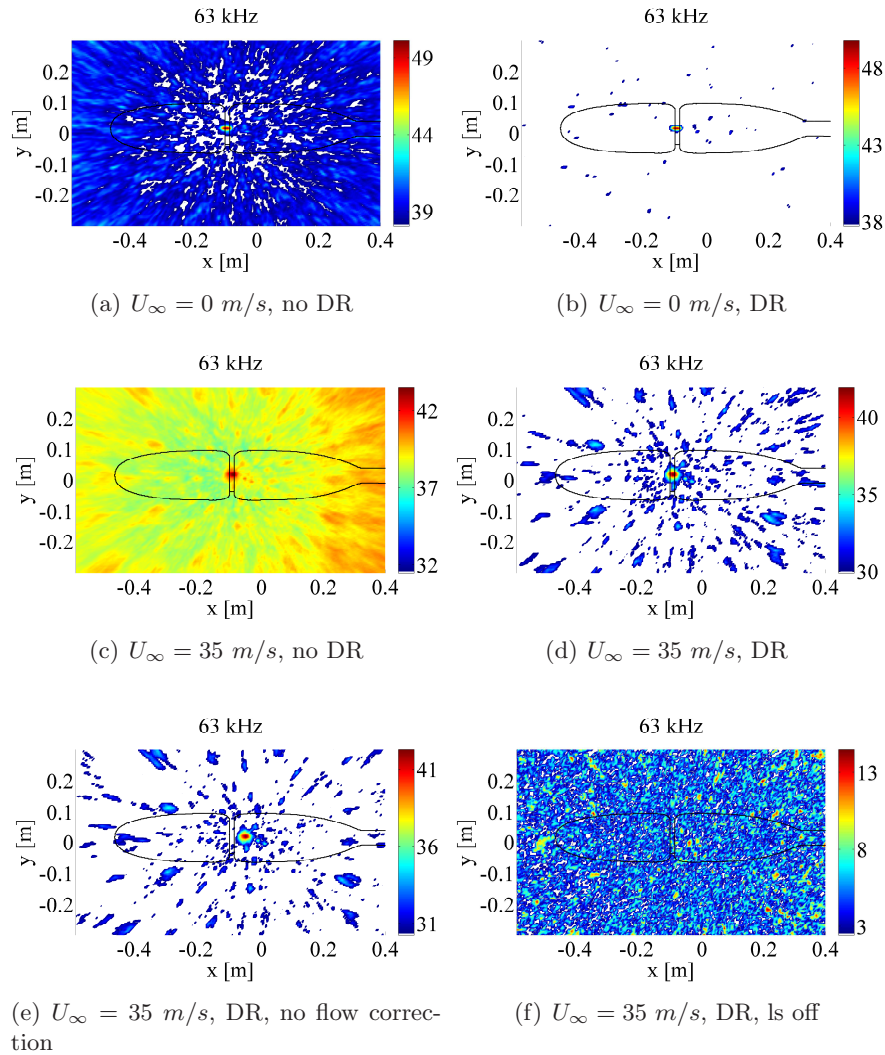


Figure 5.7: Beamforming results (in dB) of the reference sound source for the 1/3 octave band of 63 kHz for the open test section for various flow velocities, various beamforming parameters and with loudspeaker (ls) on and off. Flow comes from the left.

simplified flow model. Especially at higher frequencies the inaccuracy of the estimated signal travel time yields a much larger phase error than at lower frequencies. These phase errors can result in a reduced source maximum, a broadened main lobe of the source and additional spurious sources, so that the SNR is degraded. If the loudspeaker is turned off no aeroacoustic source can be identified, as shown in 5.7 (f).

In all considered cases of the open test section the DSB provides good results for the reference sound source for all configurations with and without flow. The Amiet model for the flow correction worked well with respect to the amplitude correction (including transmission factors and amplitude divergence) and source position, so that the found source locations coincide with the position of the loudspeaker membrane. With growing frequency the sound scattering in the turbulent shear layer becomes more important and influences the beamforming results detrimentally. As a consequence of that the source strength estimate is too low, blurring affects the source appearance and the SNR decreases. If the loudspeaker is turned off an aeroacoustic source can be identified at the position of the cavity where the ribbon membrane is recessed, but the source strength is typically much lower than compared with the electromechanical sound generation of the loudspeaker.

5.2.2 Microphone signal coherence

As pointed out in the previous paragraph, the quality and accuracy of the beamforming source maps depend on the coherence between the measured microphone signals, so that, it is therefore of utmost importance for the successful application of beamforming. In the previously shown source maps it was cited that the coherence loss of the individual microphone signals was responsible for the degradation of the source map quality and quantity. This can be substantiated by looking at the coherence between two microphone signals. The frequency-dependent coherence function between two signals is a measure of the linear degree of dependence of the two signals (see appendix 4.7.3 for details of the computation). The coherence function can take values from 0 to 1, representing either two completely independent signals or two completely dependent signals, respectively.

Figure 5.8 shows the coherence of the measured signals of the central array microphone and all other array microphones. The coherence values are averaged over the 1/3 octave bands of 2, 25 and 63 kHz for various flow velocities. If the fluid is at rest the coherence is close to one at the frequencies of 2 and 25 kHz for all microphones, indicating a very high coherence between the measured signals. The coherence at 63 kHz is close to one only for microphones which are close to the central microphone. With growing distance between the central microphone and the other sensors the signal coherence decreases quickly. It is already known from former mea-

surements (see chapter 3.2) that, as a consequence of the lower output power of the loudspeaker in this high frequency range and also of the self-noise of the measurement chain, the SNR is quite low. The combination of both these effects results in the low coherence. Nonetheless, such a low signal coherence does not constitute an obstacle with respect to the application of beamforming, since it was demonstrated in figure 5.7 that one can obtain good results in terms of source localization indicating the robustness of the applied beamforming algorithm.

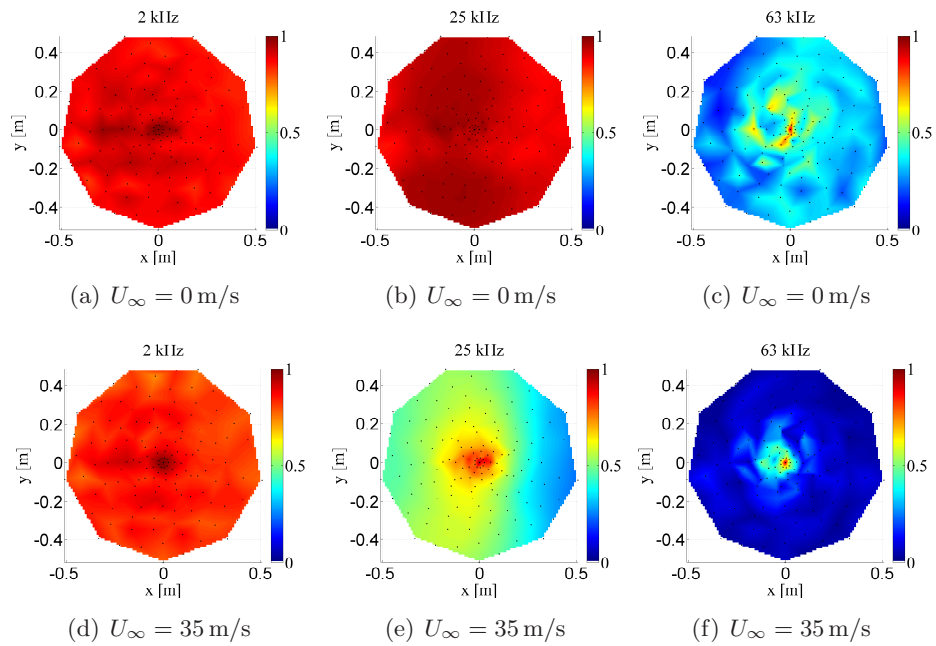


Figure 5.8: Averaged coherence between the central array microphone and all other array microphones for various 1/3 octave bands in the open test section and for various flow velocities. The loudspeaker of the reference sound source is turned on. The black dots mark the positions of the array microphones. Flow comes from the left.

In the plots (d) to (f) of figure 5.8 the flow influence and its frequency dependency become apparent. The flow goes from left to right in the pictures with a flow velocity of 35 m/s. At 2 kHz the coherence is only slightly reduced and still close to one. This means that the sound waves are not really affected by the flow and the shear layer. In this case the sound wavelengths are larger than the shear layer thickness and hence the dimension of the turbulent vortices in the shear layer are also smaller than the wavelength. With increasing frequency and thus decreasing wavelength the coherence is affected by the shear layer, as illustrated by way of example at 25 kHz, in (e). One only obtains correlation values close to one for microphones close to

the central sensor. For microphones which are located further away the correlations decrease. Moreover, a second effect arises, showing that it makes a difference whether the sensor positions are upstream or downstream with respect to the central microphone. Sound waves traveling to an observer located upstream have to pass through a thinner shear layer than sound waves which are received by downstream positioned microphones, since the shear layer thickness grows in downstream direction. Subsequently, the sound waves cover a longer distance through the shear layer and are exposed for a longer time to turbulent fluctuations in the shear layer. Consequently, the coherence of the central microphone is higher for upstream located sensors than for downstream when compared with the position of the central microphone. It can be summarized so far that the signal coherence is not only a function of the relative distances between the microphones, it is also influenced by the absolute sensor positions. Although the coherence is lowered by the shear layer turbulence, partly more than about 50 %, the corresponding source maps in figure 5.6 are only insignificantly affected compared to the case without flow.

For the 1/3 octave band of 63 kHz the decorrelation effect is even more distinct. Effectively, only the inner microphones possess a higher signal coherence and can contribute in a positive manner to the beamforming process. This time, as illustrated in the source maps in figure 5.7, the microphone pairs with a low or zero correlation are responsible for a more distinct peak level reduction and decrease of the SNR in the source maps compared to the 25 kHz case. Nonetheless, the application of diagonal removal yields improved results with a much higher SNR, but the true strength cannot be recovered. This information is lost due to turbulent scattering. Strictly speaking, for the computed results with diagonal removal, the significance of the coherence function is limited. When applying diagonal removal the beamforming process neglects the auto-correlations of the microphone signals, which however, are essential for the computation of the coherence where these values are needed for the normalization so that the coherence function takes a value from 0 to 1.

In order to approach the decorrelation problem it is common practice to apply shading with the aim of reducing of the effective array size (e.g. Brooks and Humphreys (1999); Oerlemans et al. (2007)) as outlined in chapter 2.3.3. Typically, the chosen effective array diameter is inversely proportional to frequency, so that for higher frequencies smaller arrays find use, having the drawback of reduced resolution due to the smaller aperture. Moreover this approach also has the disadvantage that on the one hand the selection of the frequency-dependent effective array aperture is usually a somehow arbitrary choice which is based on the qualitative appearance of the source maps and the experience of the researcher. On the other hand such a shading procedure does not take into account the aforementioned upstream and downstream influence on the signal coherence of microphone pairs caused

by the varying shear layer thickness. It just uses all microphones for beamforming within the chosen shading radius around the central microphone, so that this approach can possibly not give complete consideration to the existing information contents of the measured signals. Under certain conditions this may mean that microphone pairs with a low signal coherence (downstream effect) are still included in the beamforming computation and microphone pairs with relevant coherence (upstream effect) are excluded and subsequently, existing information remains unused. An approach incorporating a criterion for exclusion which is based on the microphone signal coherence could avoid these drawbacks. Apart from that it seems that the use of such a criterion would be more beneficial for a comparison of beamforming results from different wind tunnels with open test sections. Due to different shear layer characteristics (turbulence levels, thickness, etc.) the application of the same effective array aperture in combination with similar experimental setups does not have to result inevitably in similar results. In contrast to the distance-based criterion for the exclusion of microphones, the coherence appears as a more appropriate, comprehensible and quantitative discrimination property. Of course, the performance and robustness of such an approach has to be evaluated very carefully beforehand.

5.3 Microphone array results from the closed test section

In the following the microphone array results of the closed test section will be presented and evaluated in detail. This is conducted for low, middle and high frequencies, as for the presentation of the open test section results beforehand.

5.3.1 Source maps

The analysis begins with the 1/3 octave source maps of 2 kHz for the two flow velocities 0 and 35 m/s, and with various beamforming parameters. The corresponding source maps are depicted in figure 5.9. The maps (a) and (b) show that in the no flow case there is a slight improvement of the SNR in the results brought about by applying diagonal removal. The observed source location coincides with the position of the loudspeaker membrane. In (c) and (d) the source maps with flow are plotted. Strong wind tunnel background and turbulent boundary layer noise degrades the SNR significantly for the case with flow, so that a reliable source localization is not possible even when the loudspeaker is turned on. The maximum level in the map with flow (c) corrupted with background and boundary layer noise exceeds the electromechanical sound generation by 7 dB (comparison with (a)). If diagonal removal is applied a source can be identified which seems to be

5.3. MICROPHONE ARRAY RESULTS FROM THE CLOSED TEST SECTION

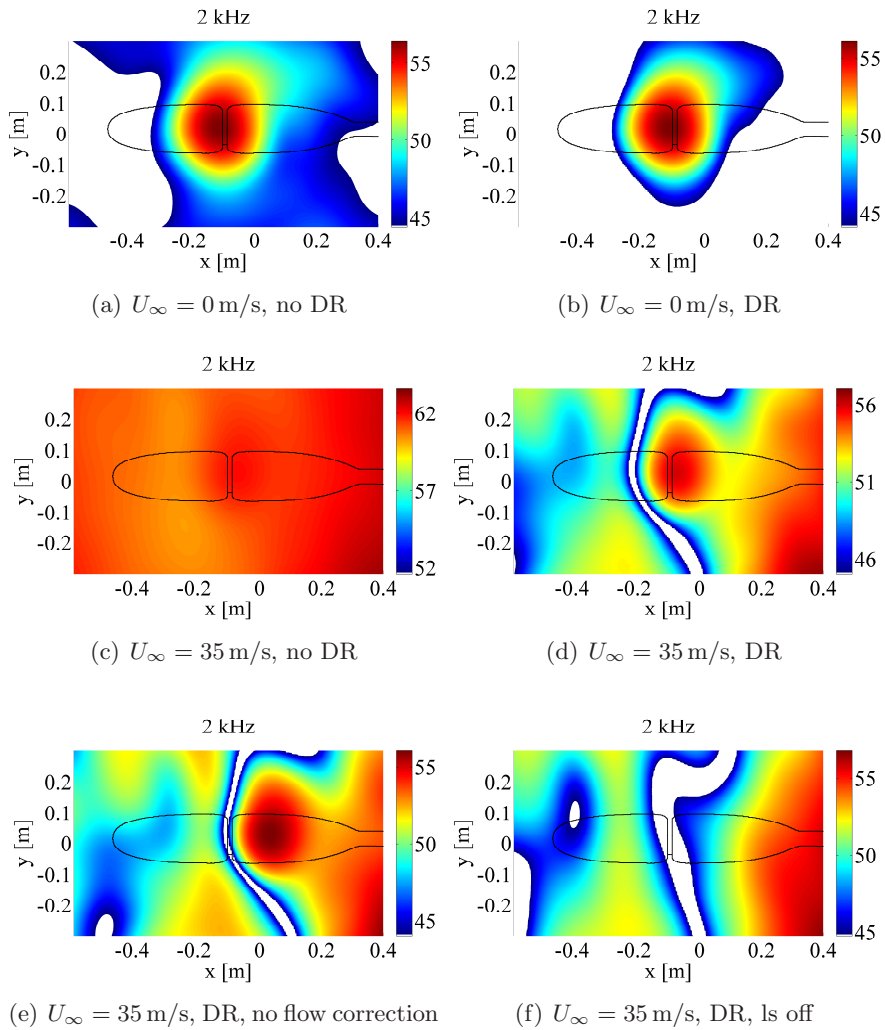


Figure 5.9: Beamforming results (in dB) of the reference sound source for the 1/3 octave band of 2 kHz for the closed test section for various flow velocities, various beamforming parameters and with loudspeaker (ls) on and off. Flow comes from the left.

associated with the ribbon membrane of the loudspeaker, but the source map is still dominated by spurious noise sources. Neglecting the flow in the beamforming process yields a source map (e) where the source is shifted downstream. Due to the strong wind tunnel background noise no aeroacoustic source in the cavity is detectable when the loudspeaker is off, as shown in figure 5.9 (f).

Figure 5.10 shows a similar comparison, but now for the 1/3 octave band of 25 kHz, and with the same beamforming and configuration parameters as before. The first major difference to the 2 kHz is again the improved

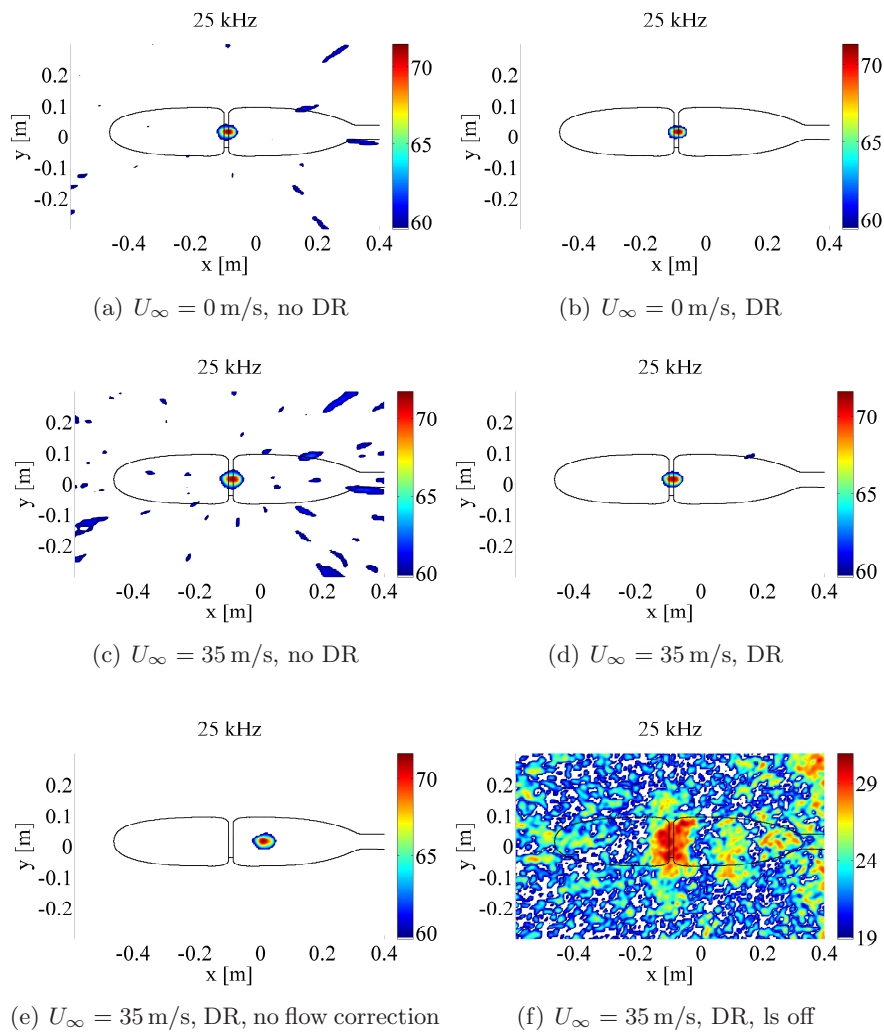


Figure 5.10: Beamforming results (in dB) of the reference sound source for the 1/3 octave band of 25 kHz for the closed test section for various flow velocities, various beamforming parameters and with loudspeaker (ls) on and off. Flow comes from the left.

5.3. MICROPHONE ARRAY RESULTS FROM THE CLOSED TEST SECTION

resolution caused by the frequency-dependent point spread function of the microphone array. The second aspect is the much better SNR; this, on the one hand, results from the minor influence of the wind tunnel background and boundary layer noise, and, on the other hand, results from the high generated sound pressure level by the loudspeaker in this frequency range. The source maps with the fluid at rest, depicted in (a) and (b), exhibit an excellent SNR so that the application of DR gives no additional improvements and hardly changes the source maps. The found source position was located correctly in the vicinity of the loudspeaker membrane, as was to be expected. The same statements can be made with respect to the results with a flow velocity of 35 m/s, as plotted in (c) and (d). Ignoring the presence of the flow in the beamforming process the source is seen to be located further downstream at a position which does not correspond to the membrane position, as depicted in (e). Furthermore, it is noteworthy that the flow has no dominant influence on the beamforming results in this frequency range, so that the source maxima are all almost the same in all maps from (a) to (e). Again, the low SNR when the loudspeaker is off (see (f)), means that an aeroacoustic source cannot be reliably localized in the vicinity of the cavity.

For still air the beamforming results for the highest measured 1/3 octave band are shown in figure 5.11 (a) and (b). At 63 kHz the localized source position is again in the vicinity of the loudspeaker membrane. The application of diagonal removal reduces the maximum value in the source map, but it also improves the SNR. In contrast to that the flow has a more distinct impact which becomes apparent in (c) and (d). Depending on whether diagonal removal has been applied or not, the maximum peak levels in the source maps are reduced by 1 or 2 dB, respectively. Nonetheless, it is actually not an option to perform the analysis without DR because the largely spatially incoherent boundary layer noise and the wind tunnel background noise in combination with the low generated sound pressure levels by the loudspeaker limits dramatically the array capabilities of source localization due to the significantly reduced SNR. Subsequently, the application of DR yields improved beamforming results with a good quality of the source maps, enabling a reliable source localization. The retrieved source position corresponds with the loudspeaker membrane, but the source map with flow correction (d) shows a lower maximum source level than in the case without (e). The used flow model assumes a uniform flow profile and subsequently, it takes into account the convection effects by the flow. Even though it corrects the source position successfully this approach degrades the SNR and broadens the main lobe of the source in the currently considered frequency range. Especially at these short wavelengths the inaccuracy in the estimated signal travel time yields much larger phase errors than at lower frequencies. These phase errors can result in the before mentioned effects. The reason for these differences could be, for example, deviations from the assumed uniform flow field in the beamforming process. If the loudspeaker is turned

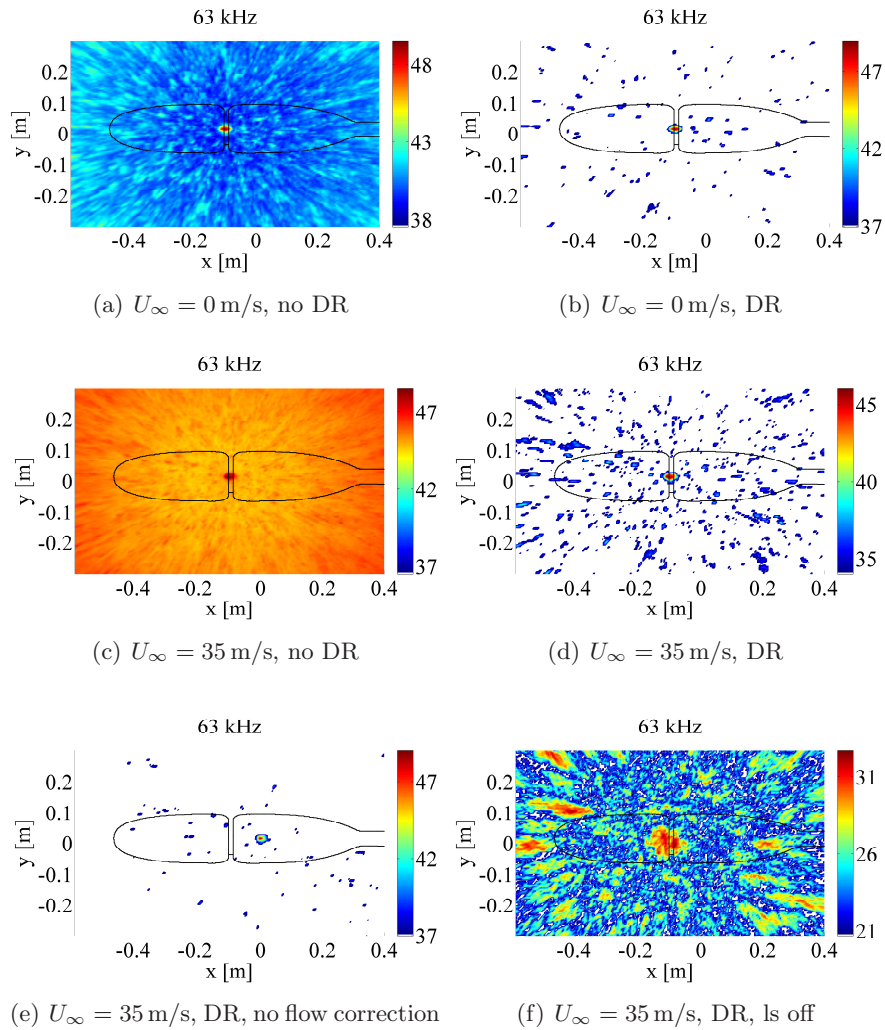


Figure 5.11: Beamforming results (in dB) of the reference sound source for the 1/3 octave band of 63 kHz for the closed test section for various flow velocities, various beamforming parameters and with loudspeaker (ls) on and off. Flow comes from the left.

off no aeroacoustic source can be retrieved and only spurious noise sources are present, as shown in 5.11 (f).

The shown cases reveal the following tendencies for the obtained source maps in the closed test section. The beamforming technique yields largely good results for the reference sound source for all configurations with and without flow, provided that the SNR is sufficiently high. Especially in the low frequency range this is not the case since wind tunnel background noise dominates the measured microphone signals. These limitations do not exist for the mid- and high-frequency range because the influence of the wind tunnel background noise is negligible and the diagonal removal technique can attenuate substantially the influence of the turbulent boundary layer noise on the beamforming results. In general, the model for the flow correction provided good results. The source was localized in the vicinity of the loudspeaker membrane, as was expected. In the mid-frequency range the flow has a negligible influence on the beamforming results leading to almost identical source maps for the case in still air and with flow in conjunction with the applied flow correction. This statement does not hold for the high-frequency range. The flow reduces the SNR significantly so that DR is required, otherwise the SNR is too low for a reliable source identification. Incorporating the flow correction into the beamforming process the retrieved source position coincides with the position of the loudspeaker membrane, but the source appears broadened and the peak level is decreased in the source map compared to the case without out flow correction. Particularly with regard to performing future phased microphone array measurements up to 100 kHz it seems to be beneficial to improve the current flow correction procedure in order to obtain a better beamforming performance at such high frequencies.

5.3.2 Microphone signal coherence

As already mentioned in the analysis of the open test section results, the quality and accuracy of the source maps depends on the coherence between the measured microphone signals. Therefore the same coherence analysis needs to be performed. Figure 5.12 shows the coherence of the measured signals of the central array microphone and all other array microphones. The coherence is computed and depicted in the same way as for the open test section data, thus they are averaged over the 1/3 octave bands of 2, 25 and 63 kHz for various flow velocities. In still air one might intuitively assume that the coherence values should be approximately one, because no flow induced disturbances are present, but this is obviously not the case as shown in the coherence maps in (a) to (c). The values in the coherence map for 2 kHz deviate clearly from one for the majority of the sensors. Since no flow is present, the reflections from the reverberant wind tunnel walls are solely responsible for the reduction in the coherence. The same effect is observable for the 1/3 octave band of 25 kHz, only in a less distinct manner.

CHAPTER 5. EXPERIMENTAL RESULTS OF THE REFERENCE
SOUND SOURCE

In the closed test section the emitted sound waves of the reference sound source are reflected at the reverberant wind tunnel walls. This results in single and multiple reflections which interfere with each other and interfere with the original emitted sound field of the loudspeaker in the closed test section. Nonetheless, the reflections off the reverberant test section

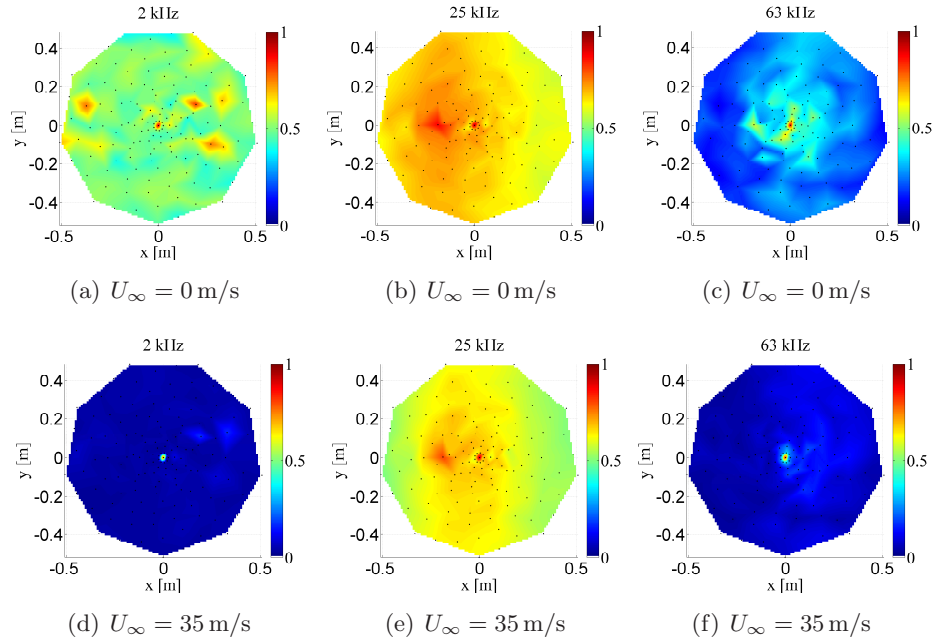


Figure 5.12: Averaged coherence between the central array microphone and all other array microphones for various 1/3 octave bands in the closed test section and for various flow velocities. The loudspeaker of the reference sound source is turned on. The black dots mark the positions of the array microphones. Flow comes from the left.

walls cannot explain the observed decorrelation of the microphone signals since the reflected sound waves remain coherent with the direct sound. The reasons for the observed phenomenon are the chosen signal processing parameter of the FFT and the characteristics of the employed loudspeaker signal (band-pass filtered white noise) of the reference sound source. For the computation of the FFT a time window with 4096 samples was used. As briefly discussed in chapter 2.3.1, there are differences in the travel time of direct sound and reflected waves due to the varying travel paths of the sound waves. This means that the reflections appear as incoherent when they are not present together with the direct sound in the same time window used for the FFT. Concerning the coherence maps in figure 5.12 the concurrence of the reflections and the selected time window length for the FFT leads to the underlying results having coherence values far below 1.

5.3. MICROPHONE ARRAY RESULTS FROM THE CLOSED TEST SECTION

In return, based on the aforementioned conclusions, a longer time window length should therefore increase the coherence in the maps since more reflections and the direct sound will be present in the same time window of the FFT processing (see 2.3.1). This predicted trend is confirmed by the computation of the coherence maps using time windows with a length of 8192 and 16384 samples. The results are given in the appendix A.1. Apart from the reflections and the signal processing parameter, also the lower loudspeaker output power and the self-noise of the measurement chain influence the appearance of the coherence maps, thereby degrading the values more than at the lower frequencies, as can be seen in the case of 63 kHz in (c).

By means of the coherence maps (d) to (f) the frequency-dependent influence of flow on the microphone signal coherence can be evaluated. As a consequence of the strong turbulent pressure fluctuations in the boundary layer the coherence is nearly zero in the map of the 2 kHz band. These low values show that at least the spatial coherence lengths of the hydrodynamic pressure fluctuations of the turbulent boundary layer are smaller than the microphone distances in the array. The impact of the turbulent pressure fluctuations on the beamforming results is clearly visible in the source maps, depicted in figure 5.9 (c) when using the auto- and cross-correlations in the beamforming process. No source localization is possible due to the strong boundary layer noise. Improvements can be achieved by applying diagonal removal because of the short spatial coherence length of the turbulent pressure fluctuations, so that after averaging the majority of the off-diagonal elements of the cross spectral matrix can be considered as noise-free, as discussed in chapter 2.2.3. As already mentioned in the analysis of the open test section, for the computed results with diagonal removal the validity of the coherence maps is restricted due to the applied normalization using the auto-correlations.

In the mid-frequency range the coherence maps are not affected in such a dramatic manner by the flow, as shown in figure 5.12 (e) where only small deviations occur compared with the corresponding results without flow. The reason for this is that the sound pressure amplitudes generated by the loudspeaker are much higher in this frequency band than the wind tunnel background and turbulent boundary layer noise, as shown by the single microphone spectra in figure 5.1. The coherence differences between the cases without and with flow can be explained by the alteration of the travel paths of the direct sound waves and reflections in conjunction with the selected time window length for processing the FFT. As discussed before, a longer time window length would increase the coherence values in the maps (as shown in the appendix A.1). Nonetheless, one obtains beamforming results (see figure 5.10) with excellent SNR and with very similar quality regardless of whether diagonal removal has been applied or whether flow is present or not. Such results cannot be achieved for the 1/3 octave band of 63 kHz. The depicted coherence map in figure 5.12 (f) is rather alike the

2 kHz case. The turbulent boundary layer and reverberations in conjunction with the low SNR due to the lower output power of the reference sound source and noise from the measurement chain itself degrade the coherence of the measured microphone signals. Effectively, only the inner microphones possess a higher coherence and can contribute in a positive manner to the beamforming process. The microphone pairs with low or zero correlations are responsible for the peak level reduction and decrease of the SNR in the source maps, shown in figure 5.11. The low microphone signal coherence requires the application of diagonal removal in order to obtain meaningful results with sufficient SNR.

5.4 Comparison of the results of the open and closed test section

The obtained results of both test section have been analyzed in great detail without so far having conducted a comparison between both wind tunnel types. Subsequently, the following analysis is dedicated to this particular concern and evaluates the comparability and performance of results obtained in both test sections. The performed comparison incorporates the previously considered source maps and microphone-coherence maps. In addition, the similarities and differences of the integrated source spectra and the SNR of both wind tunnels are discussed in detail. Finally, the localized source positions in each narrow band source map derived in both test sections are examined and compared with each other. For the comparison, the measurement without flow, conducted in the anechoic test section of the open jet wind tunnel, is regarded as the reference case, since this is the case which is least affected by disturbances.

5.4.1 Source maps and microphone signal coherence

In general, there are many differences and similarities between the source maps in the figures 5.5 to figure 5.11 computed from the measured data in the open and closed test sections. This behavior is typically frequency-dependent. Beginning with the results of the 1/3 octave band of 2 kHz in figures 5.5 and 5.9, the source maps are very different. The influence of the reverberant walls of the closed test section becomes apparent by comparing the source maps of both test sections in still air. The reflections cause a reduced peak level of about 1 dB and a more extended source area due to interferences which are not present in the open test section due to the anechoic environment. In the case with flow the results from the open test section have excellent SNR and agree very well with the results without flow. The opposite observation can be made by looking at the source maps obtained for the closed wind tunnel. Strong wind tunnel background and

5.4. COMPARISON OF THE RESULTS OF THE OPEN AND CLOSED TEST SECTION

turbulent boundary layer noise degrade the SNR significantly for the case with flow, so that a reliable source localization is not possible, even when the loudspeaker is turned on. In the low frequency range the open test section with anechoic environment is clearly superior to the closed test section.

This statement does not hold for the mid-frequency range. By comparing the results of both test sections (figure 5.6 and 5.10), it is clear that there are almost no deviations in the source maps for this frequency range, as shown by way of example for 25 kHz. In both test sections it is possible to generate almost identical and comparable results. However, here one point should be noted: the scattering of sound in the turbulent shear layer of the open jet wind tunnel becomes more important than at the lower frequencies. The coherence loss caused by the turbulent shear layer degrades the source maximum by about 1 dB in the map compared with the case without flow. In contrast to that in the closed test section the results are not affected by wind tunnel background and boundary layer noise as in the case before. The source maps for the cases with and without flow are almost identical and coincide with the open test section results without flow: here both test sections exhibit a very similar performance and provide nearly identical results.

Finally, the high-frequency range is evaluated for both test sections. The just described tendencies become more intense, as shown in figure 5.7 and 5.11. With flow, at the 1/3 octave band of 63 kHz, the source maps of both wind tunnels have lower SNR than at the mid-frequencies so that it is recommended to apply diagonal removal in order to obtain results with a better SNR and improved resolution. In the open test section the coherence loss caused by the turbulent shear layer reduces significantly the maximum peak level in the source maps by about 8 dB, whereas one observes a peak level decrease of about 3 dB in the closed test section when compared with the open test section result without flow and under anechoic conditions.

5.4.2 SNR, integrated and far-field spectra

Until now, only the source maps, obtained from both wind tunnel types, have been evaluated. Using this basis a further analysis aimed at characterizing the test-section dependent properties in a more detailed kind by means of the SNR, integrated spectra and far-field spectra can be performed. On the one hand the SNR is such a very useful numerical value, since if this value is too low one cannot expect meaningful results. On the other hand integrated spectra enable a further more detailed comparison. For example, there can be identical peak level values in different source maps, but this does not then necessarily mean that the radiated total acoustic power is then the same; this is due to differences in the source strength distribution. In this context it is helpful to compute integrated spectra as introduced in 2.2.4.

SNR Figure 5.13 gives information about the SNR in both test sections and its differences. The SNR was defined as the difference in maximum peak

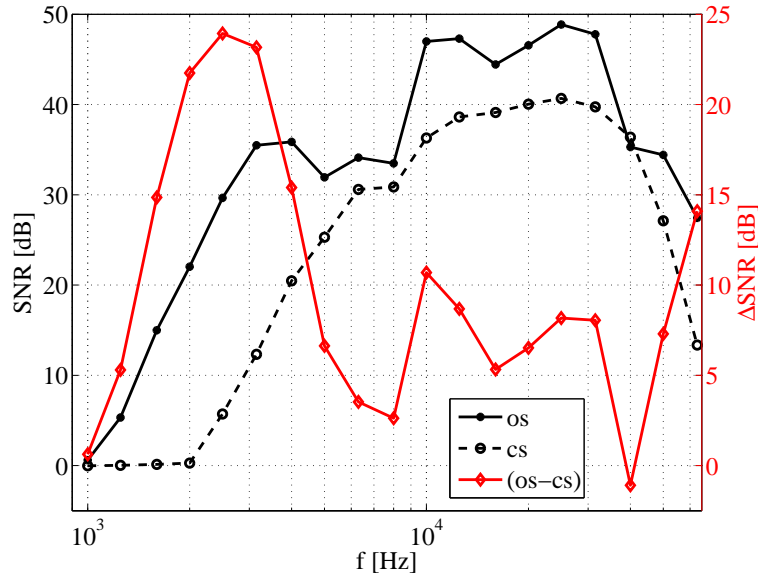


Figure 5.13: SNR of the reference sound source in the open (os) and closed (cs) test section.

level of each 1/3 octave band source map (with applied diagonal removal) with loudspeaker turned on and off and with incoming flow. In both test sections the SNR increases with growing frequency until 25 kHz is reached, at which one achieves SNR values of almost 50 dB and 40 dB in the open and closed test sections, respectively. Then, a decrease begins with further growing frequency. In general, the SNR is higher in the open test section, but the differences become smaller with increasing frequency. However, in the closed test section no usable measurements below 2 kHz were possible with the reference sound source due to the strong wind tunnel background and boundary layer noise. The individual SNR of each test section depends on the wind tunnel noise (generated by the fan, channel modes, boundary layers, shear layers, aeroacoustic noise from mountings, etc.) and the radiated sound power of the source used for the comparison. Hence, the difference in SNR for both test sections gives information about the existing wind tunnel noise in both wind tunnels. Especially in the lower frequency range the wind tunnel noise of the open jet wind tunnel is partially much lower (up to 25 dB) than that in the closed test section.

Integrated spectra By means of the aforementioned definition of the SNR it is not possible to make a statement about the influence of the test section-dependent flow properties on the sound propagation. In order to be

5.4. COMPARISON OF THE RESULTS OF THE OPEN AND CLOSED TEST SECTION

able to do this, the influence of the individual test section characteristics was analyzed using integrated source spectra, shown in figure 5.14. For this

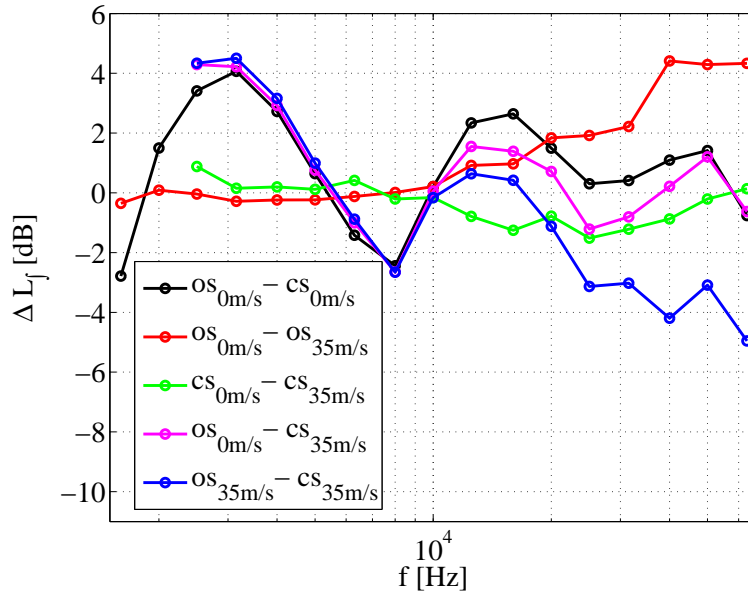


Figure 5.14: Differences of integrated spectra of the reference sound source in the open (os) and closed (cs) test section for various flow velocities.

purpose, differences of integrated source spectra of both test sections with and without flow were computed in order to quantify the deviations (the source integration scheme was discussed in chapter 2.2.4). As a consequence of the lower SNR for lower frequencies with the flow in the closed test section, the source power integration starts above the 1/3 octave band of 2 kHz. Without flow the difference in the integrated spectra in both facilities (see black curve) can only arise from the influence of the reverberant walls in the closed test section in the form of reflections and standing waves. One observes the largest deviations of 4 dB for low frequencies while with increasing frequency these differences become smaller.

The spectra from the open wind tunnel measurement for the flow at rest and at 35 m/s (red curve) reveal almost no differences up to 10 kHz. Above 10 kHz a power level reduction which grows with increasing frequency can be seen, starting at almost 0 dB and reaching up to 4.4 dB. This means that in this frequency range the estimated levels are too low as a result of the sound propagation through the shear layer which causes a coherence loss. The effect becomes significant for higher frequencies when the ratio of the shear layer thickness (for details of the determination see B.1) and acoustic wavelength is greater than 4 which is fulfilled for frequencies above 10 kHz in the current experimental setup. Ahuja et al. (1978) and Schlinker and Amiet (1980) found in their experimental study using single

microphone measurements that the scattering of discrete tones leads to an amplitude reduction and becomes more dominant when the ratio of shear layer thickness and wavelength approaches a value of 10. For the present experimental setup, a value of 10 would be achieved for 24.2 kHz, so that at this frequency for the evaluated spectra a 2 dB reduction can already be observed. According to [Lighthill \(1953\)](#) the scattered incident acoustic energy depends further on the intensity of the turbulent fluctuations which is typically proportional to the free stream Mach number in the case of free shear layers. Subsequently, it seems fitting to consider the reduction of the integrated spectra caused by turbulent scattering as a function of the scattering parameter $M\delta_s/\lambda$ as introduced in section 2.3.3. This relation is plotted in figure 5.15 for the differences in the peak level values of the integrated spectra with and without flow in the open test section.

The scattering becomes important for values of the scattering parameter above 0.5. This result agrees with observations made by [Ross \(1981\)](#) and [Schlinker and Amiet \(1980\)](#) in the context of single microphone measurements of tonal sound which was transmitted through a shear layer. To the author's knowledge, the only known publication that can provide experimental microphone array data concerning the level reduction of integrated spectra is that of [Brooks and Humphreys \(1999\)](#). One corresponding data set, obtained under similar experimental conditions to the ones used here, has been taken from the publication and also plotted in 5.15 (for more details about the measurements from this publication see appendix C.1). Both curves show the same amplitude reduction trend, and only differ at high scattering parameter values which behavior can probably be explained by the varying directivity influences of the used sound sources at high frequencies.

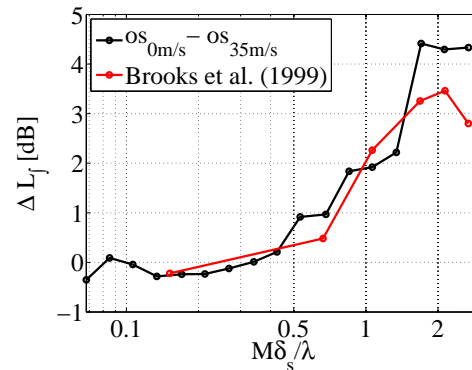


Figure 5.15: Differences of the integrated spectra as a function of the scattering parameter $M\delta_s/\lambda$.

The spectra in figure 5.14 are similar for the flow and no flow conditions in the closed test section (green curve). The deviations between no flow and flow do not exceed 1.6 dB. Nonetheless, the closed test section results in the case without flow are still corrupted by reverberation influences.

Under the anechoic conditions in the open test section the reverberations are negligible so that the measurements without flow, performed there, can be considered as a reference case with approximately free-field conditions. The integrated spectra differences (magenta curve) between the open wind

5.4. COMPARISON OF THE RESULTS OF THE OPEN AND CLOSED TEST SECTION

tunnel results without flow and with flow at 35 m/s in the closed test section show larger deviations for the lower frequencies and smaller deviations for higher frequencies. With respect to this reference case, above 16 kHz the resulting differences are smaller in the closed test section at 35 m/s (magenta curve) than in the open wind tunnel for the corresponding case (red curve) where the coherence loss has a more dominant influence than the impact of the reverberations and the wind tunnel noise in the closed test section. This effect increases with growing frequency.

The comparison of the beamforming results under flow conditions between both wind tunnels is also illustrated by the blue curve. These are deviations which result from the test section-dependent characteristics and from the application of the beamforming procedures which are at the present time widely in use. In the low- and high-frequency range the results are dominated by the reverberations on the one hand and the coherence loss on the other, leading to considerable deviations of about 4 and -5 dB, respectively. Only in the mid-frequency range does one obtain comparable results having smaller deviations.

Taking into account the two effects, reflection and coherence loss, one can interpret the differences in both wind tunnel spectra with flow as follows: In the low frequency range the major deviations are caused by the reflections in the closed test section, and with increasing frequency, the coherence loss in the open test section dominates the deviations provided that the SNR is sufficiently high.

Far-field spectra Figure 5.16 compares the integrated spectra of the microphone array with the measured far-field spectra in the anechoic open test section for a flow velocity of 35 m/s. At first, one has to ensure that the SNR of the far-field microphone measurements is sufficiently high to enable meaningful comparisons. In the current case this can be easily checked by looking at the far-field spectrum when the loudspeaker is turned off and with running wind tunnel. Then, only the wind tunnel background and shear layer noise are present, showing that the SNR is at least 19 dB and is subsequently high enough. In the low frequency range there are larger deviations between the 1/3 octave band far-field microphone spectra and the integrated spectra of the open test section. This can have various reasons. The microphone array was removed before conducting the far-field measurements so that the differences might be explained by installation effects. On the one hand reflections, diffraction and standing waves between the model and the hard-walled array surface can occur and on the other hand the altered experimental setup, used for the far-field measurements, can influence the reflection characteristics in a variety of ways so that the generated sound field might have changed. Another important fact is associated with the different distances between the source and the observers. For

low frequencies neither the array microphones nor the far-field microphone can be considered to be in the far-field; this is due to the short distances between source and receiver which is a result of the dimensions of the test section in the open wind tunnel. That is, the applicability of the near- or far-field case is a further important variable which can lead to differences in the results. The mid-frequency range exhibits smaller deviations except at the 1/3 octave band of 8 kHz. In contrast to that, for higher frequencies one observes increasing deviations. The integrated array spectra result in too low values due to the coherence loss caused by the sound transmission through the turbulent shear layer. As pointed out in chapter 2.3.3, the auto-spectrum of the far-field microphone is hardly influenced by spectral broadening and turbulent scattering for broad band noise sources.

The deviations between the integrated spectrum for the closed test section and the far-field microphone spectrum show similarities to those in the open test section results for low and middle frequencies. Again, there are considerable differences in the low frequency range which are larger compared with the open test section results. In addition to the possible near-field influences and installation effects, as mentioned before in conjunction with the open wind tunnel analysis, the reflections in the reverberant closed test section are also of concern and can be responsible for deviations from the far-field microphone results performed under anechoic conditions in the open test section. Note that the plot for the integrated spectrum starts at 2.5 kHz because of the low SNR in the closed wind tunnel. For middle frequencies one observes mostly smaller deviations. In contrast to the open test section results the far-field and integrated closed wind tunnel spectra agree quite well for high frequencies leading to smaller deviations compared with the open jet facility results, since no coherence loss is present in the closed test section due to the missing turbulent shear layer.

5.4.3 Source position

The 1/3 octave band source maps in figure 5.5 to 5.11 reveal only a small influence of the respective test section characteristics on the found source

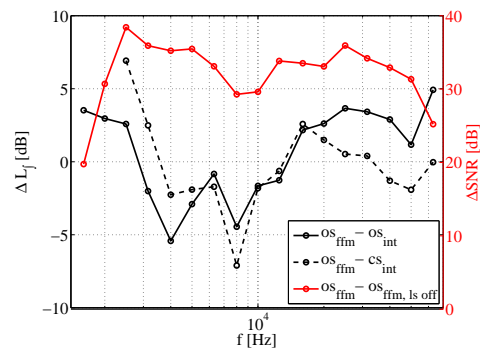


Figure 5.16: 1/3 octave band spectra differences obtained from far-field measurements (ffm) and integrated spectra (int) derived from phased array measurements in the open (os) and closed (cs) wind tunnel at 35 m/s and with loudspeaker on and off (ls off).

5.4. COMPARISON OF THE RESULTS OF THE OPEN AND CLOSED TEST SECTION

positions. At least for cases without flow in the closed test section this was expected, since former loudspeaker tests, performed by [Sijstma and Holthusen \(2003\)](#) in the DNW-LST using a similar experimental setup have revealed an influence of reflections on the localized source position only for loudspeaker locations close to the wall (0.3 m distance from the wall). In these cases the source maxima in the 1/3 octave bands beamforming maps did not coincide with the true loudspeaker positions for frequencies below 2.5 kHz.

Nevertheless, the test section influence on the accuracy of the source localization will still be examined and evaluated in detail, as shown in figure [5.17](#). Here the position of the localized source maximum of all narrow band source maps in both wind tunnels within the frequency range from 2.5 kHz to 68 kHz is shown. This frequency domain selection excludes those narrow band maps having a too poor SNR, which concerns especially the closed test section source maps. If the fluid is at rest the source is found in the vicinity of the loudspeaker membrane in the open test section results. In principle, the same statement can be made with regard to the closed test section results, but one should add two additional notes. The variation of the found position has increased and there are two outliers where the localized source maximum is outside of the loudspeaker membrane. In all likelihood the outliers result from the reflections in the hard-walled closed test section, since this is the only difference in the experimental setup compared with the open test section with its anechoic boundaries. The number of position outliers in the closed wind tunnel increases with flow, but less than 0.5 % of all narrow band source maps are affected. In contrast to this, in all narrow band source maps no outliers are observable in the open test section. By examining broadband sources these source location errors are only of small importance as long as 1/3 octave band results are considered because the multitude of narrow band source maps with correct position will dominate the results. This would be more problematical for the investigation of tonal sources in the closed test section, since completely wrong conclusions can possibly be drawn regarding the source position. By way of example for this phenomenon, the source position outlier at 8819.3 Hz will be examined more closely. Figure [5.18](#) shows the narrow band source maps for this particular (c) and the adjacent frequencies ((a) and (e)). For the adjacent frequencies the source maximum in the maps can be unambiguously assigned to the loudspeaker position. In the particular case of 8819.3 Hz some spurious sources appear in the source map. Although a source located in the vicinity of the loudspeaker membrane could be localized, the maximum in the map (c) is due to some spurious source. In order to investigate how far these spurious sources are related to the loudspeaker signal, the spatial source coherence to the source maximum in the maps is computed as described in chapter [2.2.2](#). The source maximum is designated by the white X in the maps. In the cases (b) and (f), in which the source maximum in the source

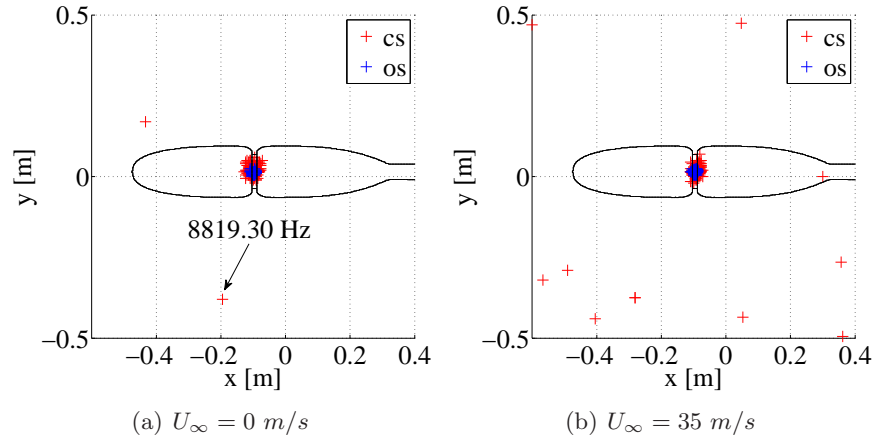


Figure 5.17: Position of the localized source maximum of all narrow band source maps for the reference sound source for the open (os) and closed (cs) test section for various flow velocities.

map belongs clearly to the loudspeaker, the spatial coherence is very low for locations removed from the loudspeaker membrane. In (c) the opposite is the case. There, the maximum source location exhibits a high spatial coherence to many other points in the source map, including also in the vicinity of the loudspeaker membrane. This indicates that the reflections which are coherent to the original source signal of the loudspeaker cause interferences at the array microphone positions, which in turn lead to the present source pattern with spurious sources.

5.4. COMPARISON OF THE RESULTS OF THE OPEN AND CLOSED TEST SECTION

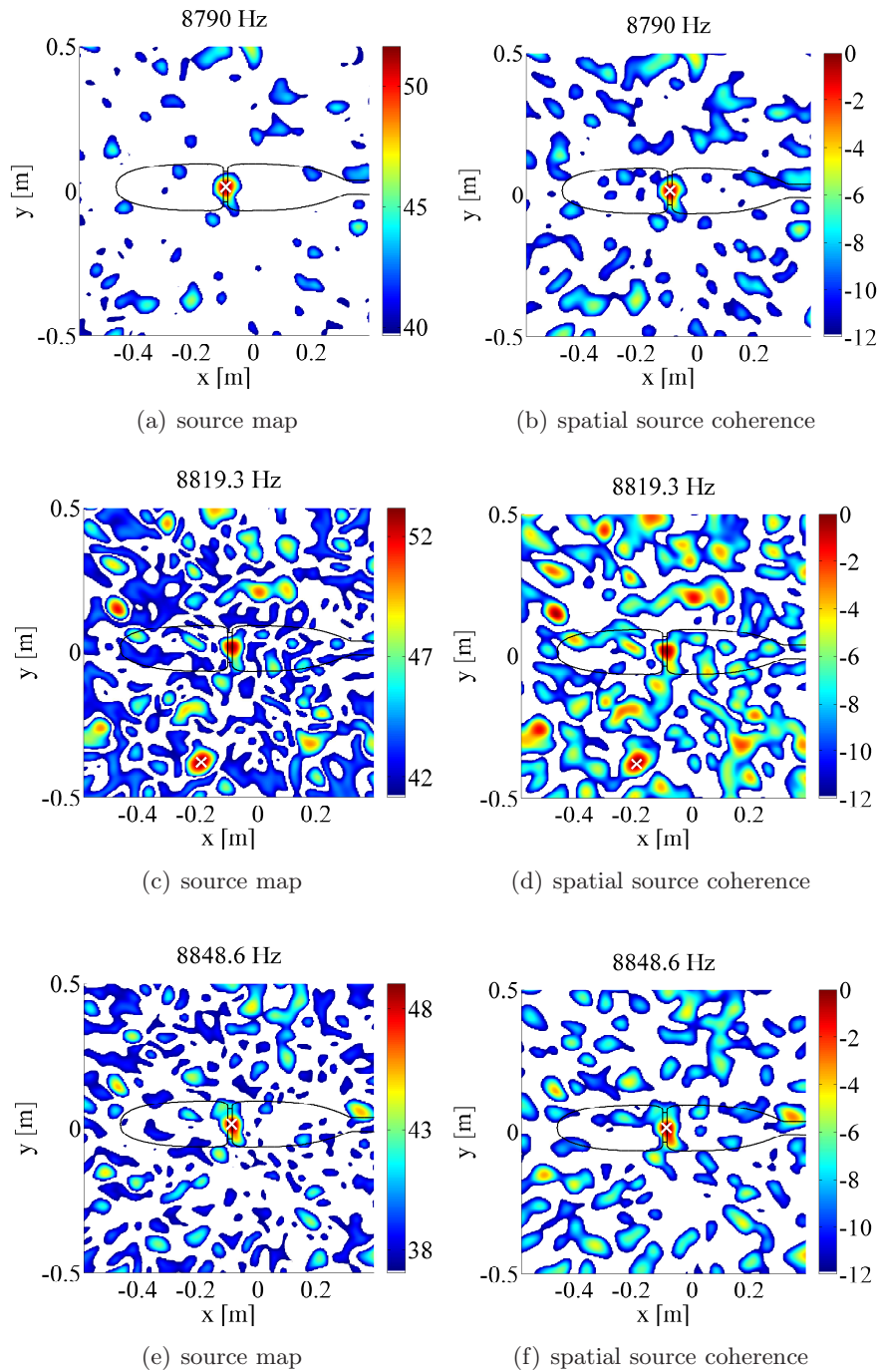


Figure 5.18: Beamforming results and spatial source coherence (in dB) of the reference sound source for various narrow bands measured in the closed test section. The fluid is at rest. The white X marks the source maximum position of each source map. In the spatial source coherence maps the white X marks the point at which the spatial source coherence is calculated.

5.5 Summary of the results of the reference sound source

The reference sound source has successfully served its purpose and has enabled the examination and the comparison of the test section-dependent sound propagation effects over a wide frequency range. The model has fulfilled the requirements imposed on such a source so that a wide range of propagation and boundary effects influencing the sound propagation could be identified, investigated and quantified. In summary it can be said, therefore, that both test section types have advantages and disadvantages with regard to aeroacoustic testing due to various effects, as illustrated in figure 5.19:

1. The wind tunnel background noise degrades significantly the SNR and thus the quality of the obtained source maps in the closed test section, especially in the low frequency regime. In contrast to that, in the open test section the wind tunnel background noise typically is not of concern.
2. Reflections at the reverberant walls of the closed test section are always present and affect the microphone array results whereby the major impact was observed for lower frequencies, becoming minor for higher frequencies. In general the possible reflections at the shear layer in the open test section are negligible for low-speed wind tunnel testing provided that the angle of incidence of the impinging sound waves on the shear layer is not too small.
3. The turbulent boundary layer in the closed test section induces strong hydrodynamic pressure fluctuations which degrades the SNR of the beamforming results. This influence is more distinct in the low frequency range due to the low source strength of the reference sound source in this frequency range. In contrast to that, the interaction of sound with turbulence in the shear layer of the open test section leads to scattering of the sound waves, which in turn results in a beamforming performance loss at the higher frequencies.

The statements 1 to 3 can be concretized in detail in terms of the SNR, source map performance and integrated and far-field spectra obtained from the performed wind tunnel measurements. The open test section stands out due to its excellent SNR, which is generally higher compared with the closed test section where the wind tunnel background and boundary layer noise degrades the SNR, these differences, however, becoming smaller with increasing frequency. In the closed test section no usable measurements below 2 kHz were possible with the reference sound source due to the strong background and boundary layer noise. In contrast to that, good results had already been obtained at 1 kHz in the open jet wind tunnel.

5.5. SUMMARY OF THE RESULTS OF THE REFERENCE SOUND SOURCE

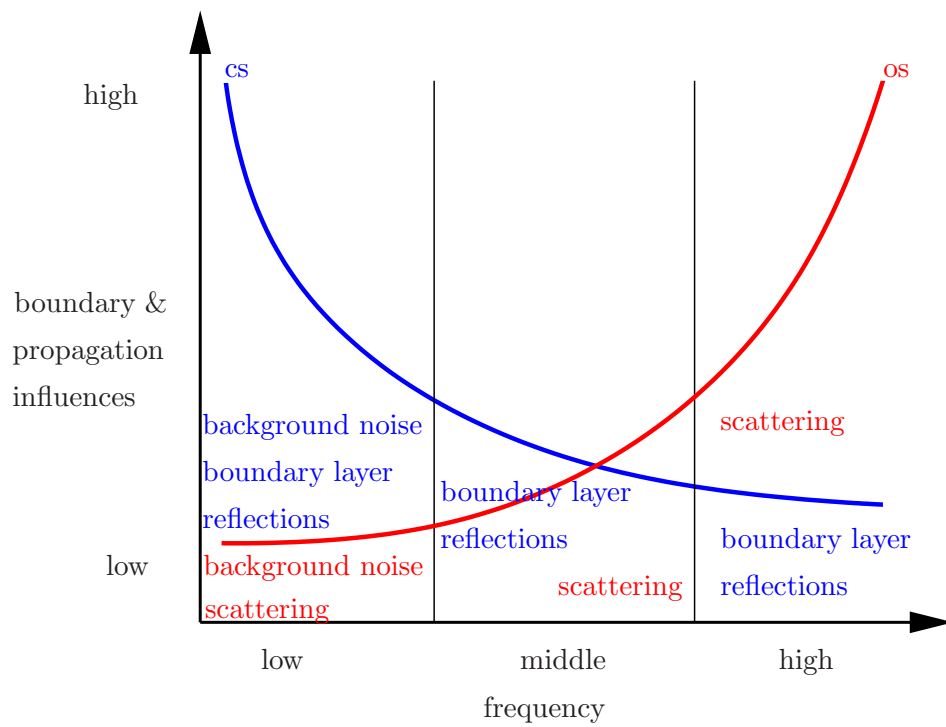


Figure 5.19: Illustration of the frequency-dependent influences on beam-forming results caused by boundary and propagation effects in the open (os) and closed test sections (cs). All aspects associated with the closed and open test sections are color-coded in blue and in red.

In principle, the 1/3 octave band source maps, derived from measurements in both wind tunnels, show a similar and comparable source topology, although frequency-dependent differences and disturbances in the source maps do manifest themselves. At low frequencies the closed test section source maps are affected by the strong wind tunnel noise which influences negatively the ability to localize the source and to determine the source strength. The open test section results are not affected in this way. Although for middle frequencies the source maps show the best agreement with both test sections, there are nevertheless still small deviations in the maximum levels in the source maps. In the high frequency range scattering effects and the accompanied coherence loss lead to a blurred source appearance and a decreased peak level in the source maps of the open jet wind tunnel measurements compared with the closed test section results. Besides the influences of wind tunnel background noise, turbulent boundary layer noise and scattering effects, reflections at the reverberant walls in the closed test section contribute also to the deviations of the beamforming results between both test section types, in particular in the low frequency range. The reflections are responsible for peak level deviations and in some cases they lead to an incorrect source position in the source maps, but less than 0.5% of all narrow band source maps are affected altogether whereas in the 1/3 octave band source maps no such phenomena have been observed. For the current experimental setup the influence of sound reflection at the shear layer on the beamforming results is negligible in the open test section.

Based upon the beamforming source maps integrated spectra were computed and evaluated. In relation to the common reference case, the integrated open wind tunnel spectrum shows almost no differences up to 10 kHz. Then, the coherence loss caused by the turbulent shear layer leads to integrated level deviations which increase with growing frequency and decrease the level by more than 4 dB at very high frequencies. The closed test section exhibits an opposite behavior: the reference case related deviations achieve values up to 4.4 dB in the vicinity of 3 kHz and they originate from the reflections at the reverberant wind tunnel walls. With increasing frequency the differences become smaller and vary mainly in the range of ± 2 dB which means that above 20 kHz the level deviations are smaller than in the open test section. The same tendencies can be observed by performing a comparison between the far-field microphone spectrum of the open test section and the integrated spectra of both wind tunnels.

Chapter 6

Experimental results of the plate with cavities

The present chapter is dedicated to an evaluation of the measurement results from the plate model obtained from the experiments in the open and closed test section. Its structure largely follows that of the previous chapter on the experimental reference sound source results. Thus, the evaluation of the results of the plate model begins with an examination of the signals from the cavity microphones (section 6.1). On the one hand this aims at a determination of the source characteristics and possible test section influences on the cavity sound generation, while on the other hand the accuracy of the predictions made by the simple semi-empirical models (see chapter 3.3) is evaluated. Then, the successive considerations encompass the beamforming results of both wind tunnel facilities (section 6.2). Finally, in section 6.3 a comprehensive comparison between the results obtained in both test sections is performed with the aid of the source maps, integrated and far-field spectra and the SNR.

6.1 Cavity microphone results

Beginning with a consideration of the cavity microphone spectra, primary interest will be concentrated on the details of the flow-induced cavity excitations and the differences between the two wind tunnel test sections. In addition, the cavity spectra will be characterized in detail in order to ascertain to what extent the design criteria have been met and to compare the predictions from chapter 3.3.2 with the measurements.

6.1.1 Noise spectra of the cavity microphones

The measured sound pressure levels of the five cavity microphones from both wind tunnel experiments are shown in figure 6.1, where they are primarily

being shown to give a global overview of how the analysis of the experimental plate results is to be carried out. A more comprehensive and cavity-wise comparison between both test section results follows later. The spectrum

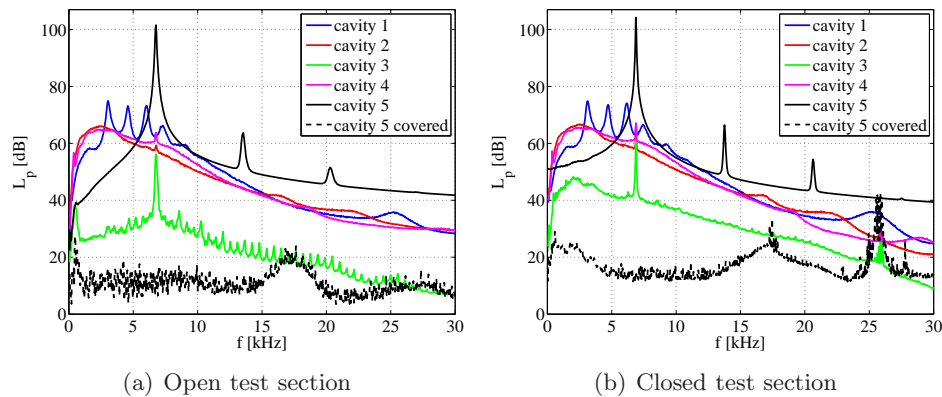


Figure 6.1: Narrow band frequency spectra of the cavity microphones at the flow velocity of 35 m/s measured in both test sections. The spectra of cavity 5 is also shown with tape covering. The measurement values are depicted as sound pressure level L_p in dB.

of cavity 1 is composed of broadband and tonal components, as had been intended in the design process. The first three tones have frequencies below 7 kHz and exhibit similar peak levels. Regarding the broadband noise part of the spectrum, the measured sound pressure levels have their highest values at the range of lower frequencies, after which the level decreases towards higher frequencies. Cavities 2 and 4 were designed as shallow cavities with a circular shape, with the aim of generating broadband noise. As shown by the measured cavity spectra, this design goal can be considered as successfully reached. The displayed broadband spectra are characterized by higher levels in the low frequency domain and decreasing values for growing frequencies. In contrast to that, the spectrum of cavity 5 is dominated by three tones, with especially the one at lowest frequency showing a very strong amplitude, whereafter an amplitude drop can be reported for increasing tone frequencies. The measured pressure fluctuations of cavity 3 are very low and the spectrum exhibits the lowest levels compared with all other measured cavity spectra, so that one would not necessarily expect strong sound radiation into the far-field. Later this statement will be shown to be substantiated on the basis of the beamforming results to be presented in section 6.2. In addition, the measured cavity spectrum reveals a comparatively strong tonal component, but the tone frequency is far away from the predicted cavity modes (see chapter 3.3.2). Unexpectedly, the tone frequency coincides exactly with the first tone of cavity 5 which has a much stronger amplitude than the tone of cavity 3. For the present case one could speculate that the measured

tone in cavity 3 is an artefact and originates from sound radiation of cavity 5. Due to these characteristics of cavity 3, all following considerations will disregard this cavity. Finally, the last plotted spectrum shows by way of example the measured spectrum of cavity 5 when it is covered with tape so that no flow excitation can take place; this shows generally low measured values, but with the exception of some occurring disturbances. The covered cavity spectra are quite similar for all the cavities 1 to 5. As far as one can evaluate by this manner of representation the measured cavity spectra in both wind tunnel test sections seem at first glance to correspond to each other quite well. As already noted above, a more detailed analysis will follow later.

6.1.2 Microphone signal coherence

Although the single narrow-band cavity spectra in figure 6.1 provide near-field information about the pressure fluctuations in the vicinity of the cavities, it still remains unclear to which extent sound will be radiated into the far-field. Assessing this issue the microphone signal coherence (see chapter 4.7.3), depicted in figure 6.2, between the cavity microphone signal and the measured signal from the central array microphone can give information about the spectral components of the radiated far-field noise. For concerning

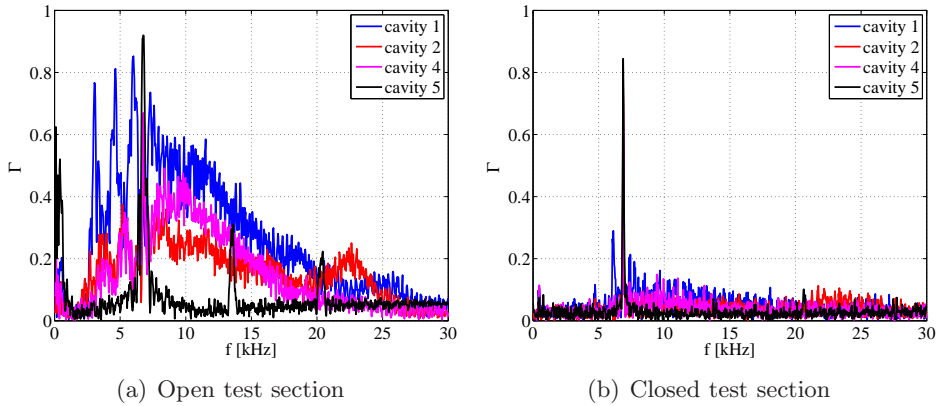


Figure 6.2: Microphone signal coherence of the cavity narrow band spectra and the spectrum of the central array microphone from both wind tunnel measurements at 35 m/s for various cavities.

the open test section results, the rectangular cavity 1 shows high correlation values with the central array microphone, both at the tone frequencies and with the broadband components, indicating that sound radiation into the far-field over a wide frequency range with emphasis on the lower and middle frequencies domain has occurred. A similar statement can be made with respect to the coherence of cavity 2 and 4. Contrary to this, for cavity 5 the

microphone signal coherence is only high at the tone frequencies, and apart from that almost zero at all other frequencies. A zero correlation coefficient does not necessarily mean that no sound is emitted into the far-field. Under certain conditions it is conceivable that the cavity microphone measures no pressure fluctuations, but nevertheless sound is radiated into the far-field. This can theoretically occur, for example, if the microphone position lies at a nodal point of a standing wave, but this phenomenon can only occur at certain frequencies and not to all frequencies in the broadband spectrum. In this case only the far-field measurements can shed light onto the actually radiated noise.

For the closed test section results the situation appears quite different, as shown in figure 6.2 (b). As already explained in chapter 5.3.2, the coherence between the sensors is negatively affected by the hydrodynamic pressure fluctuations induced by the boundary layer. Significant coherence values are obtained for only one tone of cavity 1 and 5 each. Nonetheless, such a low signal coherence does not necessarily constitute an obstacle with respect to the application of beamforming, since it was demonstrated in chapter 5.3 that one can still obtain good results, in spite of the low coherence, by neglecting the auto-spectra in the beamforming process. However, these results demonstrate quite clearly that the SNR will be much better in the open than in closed test section for measurements of the plate model.

6.1.3 Flow velocity influence on cavity microphone spectra

Within the frame work of this experimental study, velocity variations were conducted in the open rather than in the closed test section of the AWB, since the latter can provide considerably higher flow velocities. These data serve to characterize the cavities and evaluate the applied tone prediction models (Rossiter modes, depth-wise modes). The flow speed was varied in steps of 5 m/s in the range from 25 to 50 m/s. At first, cavity 1 will be examined, with the results being illustrated in figure 6.3. The shown spectra exhibit almost always four distinct tones (modes). The increase in flow velocity is accompanied by a frequency shift of the modes towards higher frequencies, whereby the frequency shift is not equal for all modes, but rather mode-dependent. Furthermore, larger amplitudes are obtained typically at higher flow velocities. The amplitude of the broadband part of the spectrum increases also with growing flow speed. This was as expected, since the sound intensity of aeroacoustic sources is proportional to the n -th power of the flow velocity (see e.g. Crighton (1990)). The value n depends on the source type (e.g. $n = 4$ for monopole source, $n = 6$ for compact dipole source, $n = 8$ for quadrupole). Figure 6.3 (b) compares the measured cavity modes with the estimated modes using the prediction formula of Rossiter (see equation D.1). This estimation agrees quite well with the experimental results, especially for higher frequencies. Depending on the flow velocity,

6.1. CAVITY MICROPHONE RESULTS

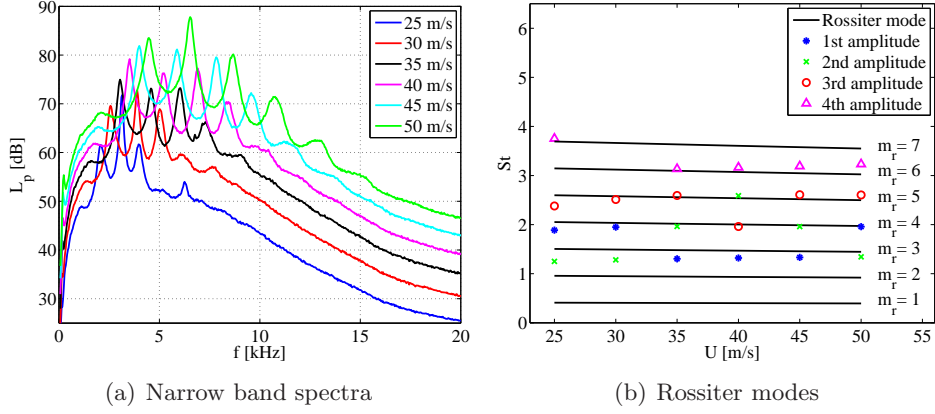


Figure 6.3: Spectra of cavity 1 for various flow velocities, shown for the open test section. The measured tones are sorted according to their amplitudes beginning with the highest one, which is labeled as "1st amplitude" (see (b)).

the excited Rossiter modes m_r lie in the range from 3 to 7. The term "predominant mode" is assigned to the mode with the highest amplitude in the spectrum. In the present case the highest amplitude is associated with the third or fourth Rossiter mode, whereas the predominance depends again on the flow velocity. The predicted and measured tone frequencies for a flow

mode number	$m_r = 3$	$m_r = 4$	$m_r = 5$	$m_r = 6$
f [Hz]: predicted	3454	4711	5967	7223
f [Hz]: measured	3042	4580	6050	7280

Table 6.1.1: Predicted and measured frequencies of Rossiter modes m_r for cavity 1 for a flow velocity of 35 m/s in the open test section.

velocity of 35 m/s are summarized in table 6.1.1. The differences become smaller for the higher modes, with the relative errors between predicted and measured tone frequencies ranging from about 13.54 % for $m_r = 3$ and 0.78 % to $m_r = 6$.

The same mode analysis has been performed for cavity 5, with the results shown in figure 6.4. At a flow speed of 25 m/s no substantial tones arise from flow induced cavity excitation. At a flow velocity of 30 m/s between two and four distinct tones become apparent in the spectrum of the cavity microphone. The number of clearly observable tones increases with increasing flow speed. Basically, up to a flow velocity of 40 m/s the same flow velocity-frequency dependence can be noticed as for cavity 1. An increase of the flow velocity is accompanied by a frequency shift of the tones towards higher frequencies, whereas again the frequency shift is not equal

for all modes, but rather mode-dependent.

In contrast to the previously observed flow velocity-tone frequency evolution, at 45 m/s, the identified tone frequency is slightly lower than in the 30 m/s case. This phenomenon can be easily explained by looking at the predicted Rossiter and depth-wise modes (using equation 3.3.4) and by plotting the measured cavity tones in figure 6.4 (b) against the Strouhal number and flow velocity. While at 40 m/s the observed tone is a consequence of the involved Rossiter modes, for the 45 m/s case the tone generating process in the vicinity of the cavity has changed and now is linked to the first depth-wise mode. The tone phenomenon at 50 m/s is also associated with the first depth-wise mode ($\eta_y = 1$) and the resulting tone frequencies and measured amplitudes are higher than for the tones in the spectrum at 45 m/s. The same behavior is present for the amplitude of the Rossiter modes at 30 and 40 m/s. Only the 35 m/s case is a special one; the coupling of the two different mode types yields higher amplitudes compared with the single Rossiter mode tones at 30 and 40 m/s. This means that the intended design goal of the excitation of depth modes coupled with Rossiter modes was also successfully reached.

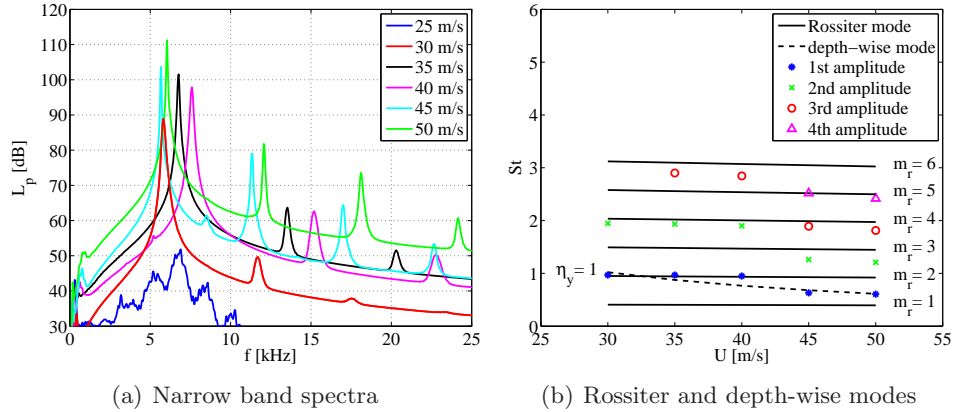


Figure 6.4: Spectra of cavity 5 for various flow velocities, shown for the open test section. The measured tones are sorted by amplitude, beginning with the highest one which is labeled as "1st amplitude" (see (b)).

Again, the predicted and measured tone frequencies for a flow speed of 35 m/s are summarized in table 6.1.2. The measurements and the prediction agree quite well for the first two tones, which correspond to the Rossiter modes $m_r = 2$ and $m_r = 4$. For these modes the relative error between the predicted and measured tone frequencies are smaller than 5%. In terms of the third tone the measured tone frequency lies between the predictions of the Rossiter modes $m_r = 5$ and $m_r = 6$, but this tone might more likely be associated with a higher depth-wise mode. The employed depth-wise mode prediction formula (equation 3.3.4) incorporates empirical coefficients which

6.1. CAVITY MICROPHONE RESULTS

were only verified for the first mode, so that it was decided not to attempt a computation of higher mode predictions with this formula.

mode number	$m_r = 2$	$m_r = 4$	$m_r = 6$
f [Hz]: predicted	6595	14133	21671
f [Hz]: measured	6768	13535	20303

Table 6.1.2: Predicted and measured frequencies of Rossiter modes m_r for cavity 5 for a flow velocity of 35 m/s in the open test section.

The influence of the flow on the broadband excitation of cavities 2 and 4 was also investigated. Figure 6.5 shows the resulting spectra. For both cavities the tendency is clear simple - the measured sound pressure levels increase for higher flow velocities. At 35 m/s a tonal component is visible in both cavity spectra, but the tone frequency corresponds exactly to the first tone frequency measured in cavity 5, indicating that this contribution arises from emitted sound from cavity 5.

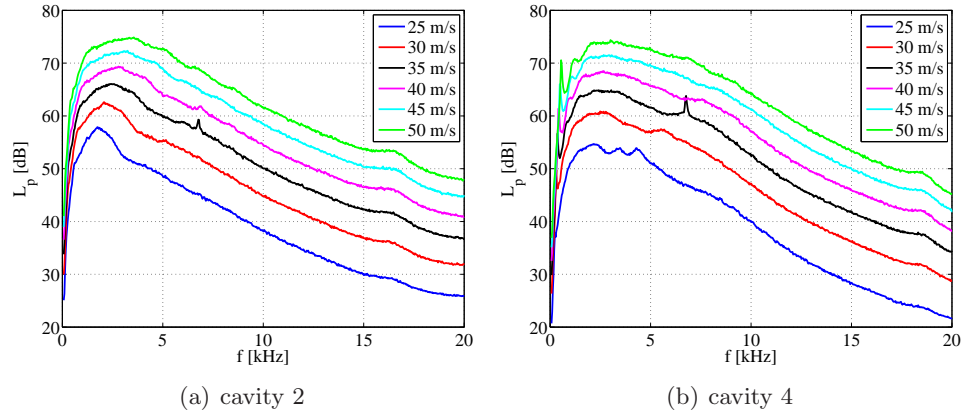


Figure 6.5: Narrow band microphone spectra of cavity 2 and 4 for various flow velocities, shown for the open test section.

6.1.4 Test section type influence on cavity microphone spectra

The next important point in the analysis of the cavity microphone spectra is a direct comparison of the measured cavity spectra in both test sections at the flow velocity of 35 m/s, which provides significant information for the interpretation of the source maps to be presented in section 6.2. The corresponding results are shown in figure 6.6. For cavity 2 the broadband excitation agrees very well in both test sections. However, below frequencies of 15 kHz the measured sound pressure levels are marginally higher in the

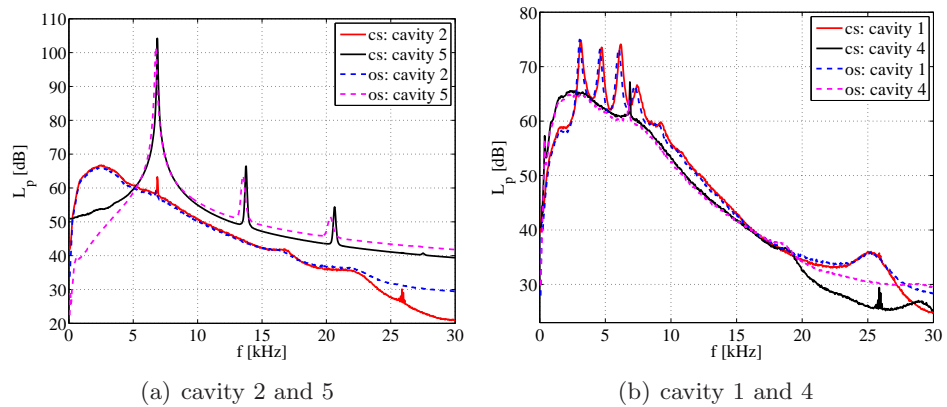


Figure 6.6: Comparison of narrow band microphone spectra of various cavities measured in both test sections at 35 m/s.

closed test section. Taking into account the observed velocity dependence in figure 6.5, one can infer that in the closed test section the local flow velocity is slightly higher in the vicinity of the cavity. Above 22 kHz both measured spectra deviate more and more.

The major differences regarding the spectra of cavity 5 are related to the measured tone frequencies and amplitudes. In the closed test section the tone frequencies are shifted towards higher frequencies and compared with the open wind tunnel results the amplitudes are larger. The frequency shift is 102 Hz for the first tone reaches a value of 340 Hz for the third tone. The level difference of each tone pair is to approximately 3 dB. Keeping in mind the influence of the velocity increase on the tone spectra it is reasonable to assume that a higher local flow velocity is responsible for this behavior. Nonetheless, there are further possible effects which may lead to the same observed influence on the cavity microphone spectra, e.g. the different turbulence levels and temperature deviations from the measurements in both test sections. As investigated by Kröber et al. (2010) in a previous study, the turbulence level differences in both test sections does not lead alone to such observed frequency shifts. In the same way, temperature deviations during the measurements in both test sections can be excluded as a cause since they are too small (a simple numerical estimation is presented in the appendix D). In contrast to that, it can be shown by a simple estimation that the solid blockage of the flow by the plate model and by other installations such as the microphone array and mountings in the closed wind tunnel increase the local flow velocity in the vicinity of the cavities. This velocity increase is sufficiently high to generate such an observed frequency shift of the cavity tones. All performed estimations concerning the frequency shift issue are discussed in the appendix D.

The direct comparison is now continued with an analysis of the results

from cavities 1 and 4, shown in figure 6.6(b). These results do not reveal any new fundamental findings. The broadband parts of the spectra exhibit marginally increased levels in the closed wind tunnel compared with the open test section results. The tonal spectral components of cavity 1 are characterized once again by a frequency shifts ranging from 68 Hz for the first tone pair to 102 Hz for the fourth tone couple. The tone level deviations are smaller than 0.9 dB.

In summary, the differences between the cavity spectra obtained in the open and closed wind tunnels can most likely be traced back to slightly increased local flow velocities, in all likelihood caused by the solid blockage of the flow by the plate model in the closed wind tunnel. This effect leads to small level deviations with respect to the broadband parts of the cavity spectra. Discernible differences were observed between the measured tone amplitudes and frequencies.

6.2 Beamforming results of the plate model

In the following, an evaluation of the source maps with and without flow correction is presented, beginning with results from the open test section. This is, as so far, conducted for selected 1/3 octave bands.

6.2.1 Open test section

Figure 6.7 depicts 1/3 octave source maps of 6.3 kHz of the plate with the five cavities measured in the open test section at a flow velocity of 35 m/s and with application of various beamforming parameters. As expected from

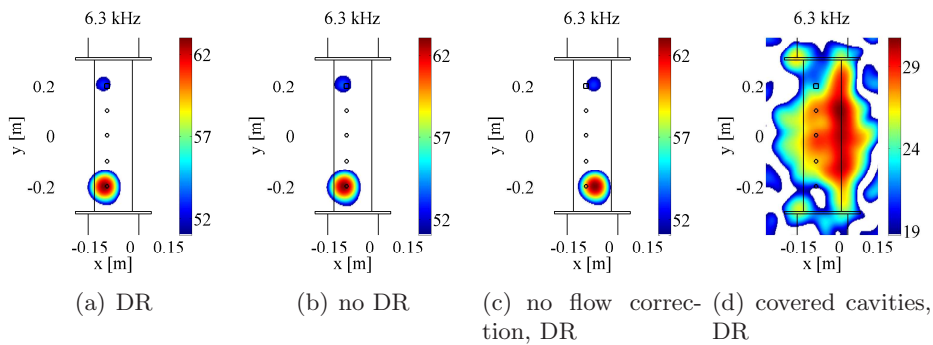


Figure 6.7: Beamforming results (in dB) of the plate with cavities for the 1/3 octave band of 6.3 kHz for the open test section for a flow velocity of 35 m/s and with various beamforming parameters. Flow comes from the left.

the measured cavity microphone spectra, cavity 5 is the predominant source

in this 1/3 octave as a consequence of the strong tone generated by mode coupling; as can be seen it can be clearly localized. A source which can be associated with cavity 1 can also be clearly seen. All other cavities radiate sound which is too low to be detected by the microphones within their used dynamic range. The SNR is excellent, as shown by the source maps in (a) and (b), from which it can be seen that diagonal removal had no impact on the shown source maps. The found source location coincides with the position of the cavities, indicating again that flow correction using the Amiet model works well. When flow correction is not applied the source will be located further downstream of the cavity position as shown in (c). Furthermore, the obtained results infer that the transmission coefficient is approximately unity, thereby confirming again the predictions performed in chapter 4.5.3. The final plot (d) in figure 6.7 depicts the source map when the cavities are covered with tape so that no cavity excitation induced by the flow can take place. For this configuration aeroacoustic sources can be identified in the vicinity of the junction between mounting, end plates and plate model. A stronger source is linked to the trailing edge of the plate model, but the source strength is more than 30 dB lower than that compared with the uncovered cavity sources.

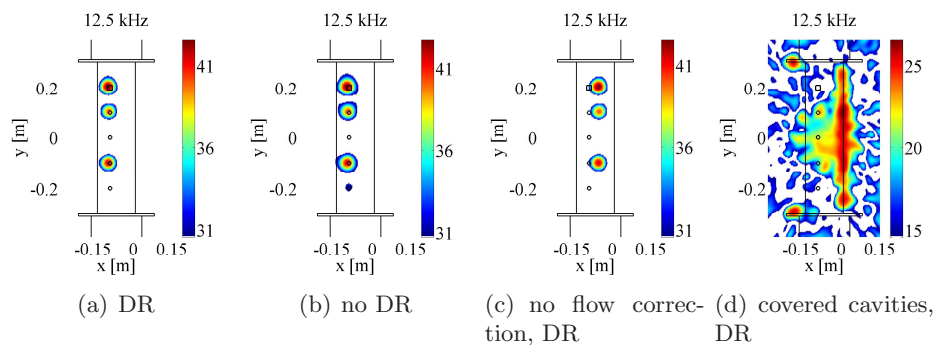


Figure 6.8: Beamforming results (in dB) of the plate with cavities for the 1/3 octave band of 12.5 kHz for the open test section for a flow velocity of 35 m/s and various beamforming parameters. Flow comes from the left.

Figure 6.8 shows a similar comparison, but this time for the 1/3 octave band of 12.5 kHz with the same beamforming and configuration parameters as before. In the vicinity of cavities 1, 2 and 4 sources have been detected, and it had already been determined from the cavity microphone spectra in figure 6.1 that the found sources in the maps arise only from broadband excitation of the cavities. Even though there is a Rossiter mode present in cavity 5 in this 1/3 octave band as shown in table 6.1.2, the sound radiation into the far-field is too weak compared with the other cavity sources, so that no source can be found (at least within the used dynamic range) in the

source map at the position of cavity 5. Source maps in (a) and (b) show that the application of DR gives no additional improvement and hardly changes the source map, which is again a direct result of the excellent SNR. When not applying the flow correction in the beamforming process, the sources appear further downstream at positions which do not correspond to the cavity locations, as shown in (c). Again, aeroacoustic sources are seen to be located at the plate trailing edge and in the vicinity of the leading edge of the end plates when the cavities are masked (see (d)); they have a peak levels about 16 dB lower than with the uncovered cavity sources.

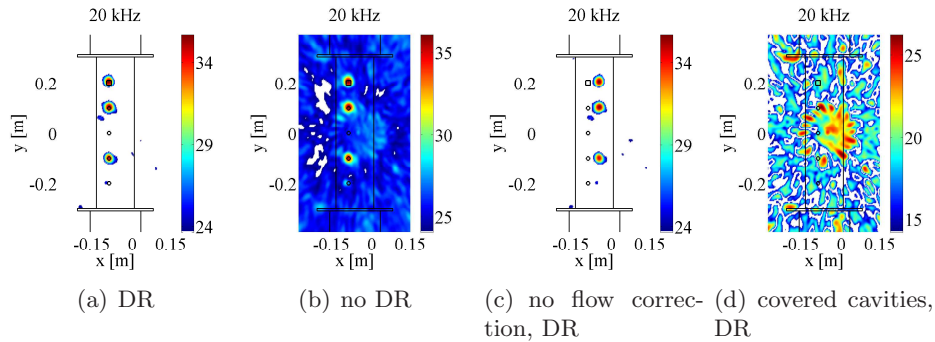


Figure 6.9: Beamforming results (in dB) of the plate with cavities for the 1/3 octave band of 20 kHz for the open test section for a flow velocity of 35 m/s and various beamforming parameters. Flow comes from left.

The beamforming results for the 1/3 octave band of 20 kHz are depicted in figure 6.9. This is the highest frequency band where a reliable source localization was possible with the beamforming maps of the plate model. However, one can see a similar source distribution as in the 12.5 kHz case. The localized sources coincide with the cavity positions of cavity 1, 2 and 4. The third tonal component of cavity 5 (as identified in the cavity microphone spectra in figure 6.1), does not radiate or radiate not enough sound into the far-field since no source can be identified in the source maps at this location. The SNR is still very good, but it is also reduced compared with the results at lower frequencies, as shown by beamforming map without DR (see map (b)). Without flow correction the map shows the sources as shifted downstream, but still having the same maximum peak level as in the case where the Amiet model has been used to account for the flow effects. If the cavities are masked, the source maps are again dominated by artifacts and noise.

6.2.2 Closed test section

This analysis begins with the 1/3 octave source maps of 6.3 kHz. The source maps are depicted in figure 6.10. The retrieved sources correspond to the

6.2. BEAMFORMING RESULTS OF THE PLATE MODEL

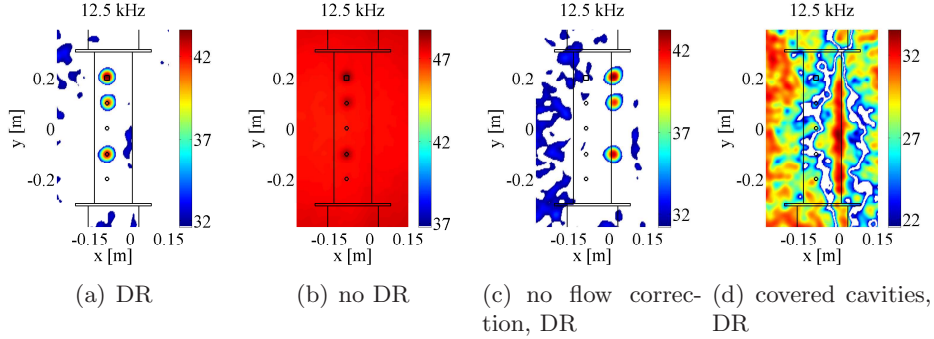


Figure 6.11: Beamforming results (in dB) of the plate with cavities for the 1/3 octave band of 12.5 kHz for the closed test section for a flow velocity of 35 m/s and with various beamforming parameters. Flow comes from the left.

quality of the source maps enabling a reliable source localization. In addition, flow correction ensures that sources are localized at the correct cavity positions. This procedure is accompanied by a reduction of the source dimensions, which yields better defined results and consequently a higher peak level of about 1 dB, as can be seen in a comparison of source maps (a) and (c). When the cavities are masked (see (d)), although there are spurious sources present in the source map caused by the wind tunnel background noise, aeroacoustic sources can be seen located at the plate trailing edge and in the vicinity of the leading edge of the end plates.

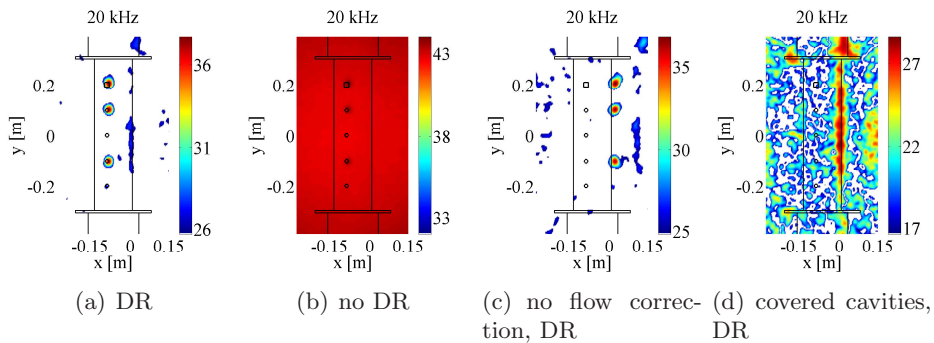


Figure 6.12: Beamforming results (in dB) of the plate with cavities for the 1/3 octave band of 20 kHz for the closed test section for a flow velocity of 35 m/s and with various beamforming parameters. Flow comes from the left.

6.3 Comparison of the results of the open and closed test section

The successive considerations aim at the comparison between the plate model measurements carried out in both wind tunnels. Similarities and differences of the obtained source maps, integrated source spectra and the SNR of both wind tunnels are discussed in detail. In this context, the differing aeroacoustic cavity excitation is taken into account, and, in this particular analysis, the comparability and performance of both test sections is evaluated.

6.3.1 Source maps

Beginning with some general remarks, the observed source topology in all considered 1/3 octave band source maps (figures 6.7 to 6.12) is identical for measurements in both types of test sections. This means the same frequency-dependent source distribution associated with the cavities and the same source strength ranking have been observed in both test sections. Furthermore the source maps reveal that the test section-dependent flow correction procedures have worked well with respect to the retrieved source positions, since the localized sources have in all cases been found to be in the vicinity of the cavities. The SNR is obviously higher in the open than in the closed test section for the examined frequency ranges. Basically, the open jet wind tunnel results with applied DR are excellent, so that DR is actually not even essential. In contrast to that, for the closed test section data without DR no source localization would have been possible for middle and higher frequencies. When the cavities were masked with tape preventing the flow-induced cavity excitation, the trailing edge of the plate model was identified as one of the major aeroacoustic sources in both wind tunnels, whereas the quality of the open test section source maps is superior to those of the closed wind tunnel, for the above stated reasons. Nonetheless, the initial requirements of robust, reliable and repeatable sound generation in both test sections have been met, although flow-induced cavity noise dominates the sound radiated from the plate model and its mountings.

Besides these general facts, individual differences between both test facilities have become apparent, depending on the frequency. In the source maps for 6.3 kHz (figure 6.7 and 6.10), deviations can be observed with respect to the maximum peak level and the source appearance at cavity 5. In all likelihood these differences can be explained by the differing aeroacoustic source generation caused by a slightly higher local flow velocity in the vicinity of cavity 5 in the closed test section, brought about by the solid blockage of the plate model (see appendix D). This 1/3 octave band is dominated by a tone resulting from the excitation of a coupled cavity mode. As pointed out in figure 6.6 (a), this cavity tone appears at different frequencies and has

6.3. COMPARISON OF THE RESULTS OF THE OPEN AND CLOSED TEST SECTION

approximately a 3 dB difference in peak level in the near-field. Nonetheless, one cannot rule out the possibility that reflections in the closed test section may be also involved in contributing to the deviations in the obtained results.

The source maps of the 1/3 octave band of 12.5 and 20 kHz show sources at the positions of cavities 1, 2 and 4. The results are similar in both test sections, only that the maximum peak level in the closed test section is approximately 1 or 2 dB higher for the two frequencies 12.5 and 20 kHz, respectively. On the one hand, this can again be explained the increased local flow velocity in the closed wind tunnel, which yields an increased sound pressure level inside the cavity, as discussed for the figures 6.3 and 6.5 so that potentially higher levels will be achieved in the far-field. On the other hand, reflections at the reverberant walls in the closed test section can also contribute to the observed differences. In addition, in the case of the reference sound source, turbulent scattering reduced the measured peak levels above 10 kHz in the open test section. Since the geometrical setup of the sources and microphones for the plate is very similar to the reference sound source setup, the turbulent scattering might influence the plate results in the same way at the higher frequencies.

6.3.2 SNR, integrated and far-field spectra

Figure 6.13 (a) and (b) show the SNR in both test sections and their differences in terms of the plate with cavities. Similar to the reference sound source in chapter 5.4.2, the SNR was defined as the difference in maximum peak level of each 1/3 octave band source map (with applied diagonal removal) with open (and therefore flow-excited) and masked cavities, where for the latter the flow-induced fluctuations have been suppressed. In general, the SNR is higher in the open test section. At frequencies below 5 kHz no measurements were possible in the closed test section due to the strong background and boundary noise in conjunction with the low source strength of the cavities. In contrast to that, the open jet wind tunnel enables measurements beginning already at above 2.5 kHz, but exhibits a SNR at lower frequencies which is more than 10 dB higher than with the closed test section. For the 1/3 octave band of 6.3 kHz the SNR is almost identical for both test sections; this is because of the strong and dominant aeroacoustic source in the vicinity of cavity 5, so that the existing wind tunnel noise in both test sections plays a non-significant role. A decrease in SNR then begins with further increasing frequency in both test facilities, whereby the SNR remains higher in the open test section. The consideration is restricted to frequencies below 20 kHz, because at higher frequencies the aeroacoustic cavity sources are too weak or non-existent, so that the maps become dominated by wind tunnel noise.

Figure 6.13 (b) compares the differences of the integrated spectra of the

microphone array and the measured far-field spectra for a flow velocity of 35 m/s in both test sections. The differences in the integrated array spectra obtained in the open and closed test facility will be considered first. At low frequencies the deviations are much more pronounced (max. deviations of about 4.2 dB) than at higher frequencies where the typical differences are smaller than 2 dB. The found deviations lie in the range of the observed differences for the case of the reference sound source (see chapter 5.4.2). Possible reasons for these deviations can be differences in the flow-induced excitation of the cavities due to varying local flow conditions brought about by wind tunnel characteristics (see chapter 1.2.1) and also due to reflections occurring in the closed test section. A dominating influence of turbulent scattering on the open wind tunnel results does not become apparent by means of a comparison of integrated spectra. This is in agreement with the observations made in the course of the open jet wind tunnel testing of the reference sound source (see chapter 5.4.2). There, the scattering effects become more important at higher frequencies (> 10 kHz).

Before comparing differences between the far-field spectra with the test-section dependent integrated spectra, one has to make sure that the SNR of the far-field microphone measurements is sufficiently high. In the current case this can be easily achieved by looking at the far-field spectra when the plate cavities have been masked with tape and when the wind tunnel is in operation. Then, only the wind tunnel background and model noise can be present, which are not associated with the cavities. For this the comparison, the SNR of the single far-field microphone is high enough up to 16 kHz, so that consequently the comparison with the integrated microphone array spectra will be limited to this upper 1/3 octave frequency band. However, as can be seen in figure 6.13 (a), the SNR of the integrated microphone array spectra is considerably higher than that for the single far-field microphone due to the large number of array microphones. In the observed frequency range there are larger deviations between the 1/3 octave band far-field microphone spectra and the integrated spectra of the open test section, reaching values up to 3 dB in the low frequency regime. In all likelihood these deviations are mainly caused by installation effects, which can occur due to the removal of the microphone array before conducting the far-field microphone measurements. A distinct influence of sound scattering by the open jet shear layer on the spectra differences can be excluded, since, as mentioned previously, scattering effects become more important at frequencies above 10 kHz, as shown by means of the reference sound source in chapter 5.4.2. The integrated spectra obtained from the closed test section measurements differ from the maximum value by about 3.6 dB when compared with the far-field microphone measurements. In addition to the possible installation effects, as mentioned before in the open wind tunnel analysis, the reflections in the reverberant closed test section are also of concern and can be responsible for differences compared with the far-field microphone results performed under

6.4. SUMMARY OF THE RESULTS WITH THE PLATE MODEL

anechoic conditions in the open test section. The highest deviations occur at low frequencies in the closed test facility and are larger compared with the open test section spectra.

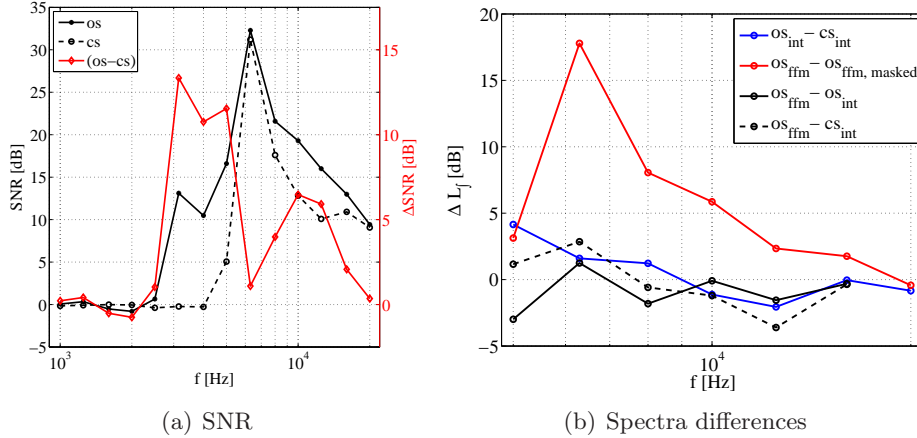


Figure 6.13: SNR and 1/3 octave band spectra differences obtained from far-field measurements (ffm) and integrated spectra (int) derived from phased array measurements in the open (os) and closed (cs) wind tunnels at 35 m/s and with open and masked cavities.

6.4 Summary of the results with the plate model

The objective of the plate model design was to employ broad band and tonal aeroacoustic sound generation which will deliver sufficiently high SNR. Furthermore, the model design should assure that the aerodynamic model-wind tunnel interferences are as small as possible, ensuring that the alteration of the flow properties in the vicinity of the aeroacoustic sound generation are as low as possible. These design criteria have been almost met with the finally chosen plate design. The aeroacoustic sound generation in both test facilities exhibits small differences caused by variations of the local flow conditions in the vicinity of the cavities due to the varying aerodynamic test section characteristics and could therefore not be kept the same. The local flow velocities are slightly higher in the closed test due most likely to the solid blockage. In terms of the aeroacoustic cavity excitation the higher flow speed results in slightly larger near-field pressure fluctuations and give rise to a frequency shift towards higher frequencies.

Nevertheless, the microphone array measurements had the same source topology for measurements in both test sections, meaning that the same frequency-dependent source distribution associated with the cavities and the same source strength ranking was obtained. Due to their various shapes

and dimensions, the cavities produced sound emission in different frequency bands made up of tonal and broad band components. An exception is the middle cavity, where no source localization was possible, caused by a too low source strength. In terms of the beamforming results the test section-dependent flow correction procedures worked well with respect to the retrieved source positions, since the localized sources are in all cases in the vicinity of the cavities and the sources could be clearly separated.

The source map peak levels, integrated spectra and far-field spectra of both wind tunnel types have frequency-dependent deviations up to a maximum value of 4.2 dB in both the test sections, which is a consequence of the major effects of different aeroacoustic sound generation and reflections at the reverberant wind tunnel walls of the closed test section. On the basis of the presently available information it is not possible to distinguish between these various effects and to quantify them separately, as had been possible in the case of the reference sound source.

Concerning the SNR of the plate measurements, as in the case of the reference sound source, the SNR for the examined frequency range is higher in the open test section than in the closed test section.

Finally, an analysis of the measurement results of the reference sound source produced advantages and disadvantages of both test sections with regard to aeroacoustic testing using the microphone array technique, this being due to various effects which have been summarized in the three main points in chapter 5.5. These findings are confirmed by the measurement results obtained from the plate model with cavities, but one should add an additional point arising from the aeroacoustic sound generation from this model:

4. Aerodynamic information about the local flow field is important when comparing beamforming results, since the flow field differences can influence the generated amplitudes and frequency characteristics of the emitted aeroacoustic sound. Furthermore, changes in the local flow speed can lead to an abrupt alteration of the aeroacoustic sound generation mechanism, where in particular tonal components can be affected.

Chapter 7

Experimental results on a wing with high-lift system

In the present chapter the experimental results of the generic wing model, obtained from measurements in the open and closed test section, are discussed and evaluated. The following considerations begin with an examination of aerodynamic results from the pressure taps (section 7.1). Then the beamforming results from both test facilities are presented and analyzed in-depth (section 7.2). Finally, in section 7.3 an extensive comparison between both wind tunnel test campaigns is performed, making use of source maps and integrated spectra. One of the main issues regarding the wing model consists in finding a common basis of comparison of the microphone array results for the different wind tunnel configurations, so that this section will subsequently focus on this particular topic.

7.1 Aerodynamic results

Figure 7.1 shows the pressure distributions c_p of the model (the definition of c_p is given in appendix B.2) for the open test section (os) for a geometrical angle-of-attack of $\alpha_{os} = 12^\circ$ and for the closed test section (cs) for various angles-of-attack α_{cs} . These results emphasize the different aerodynamic characteristics of both test section types. At higher angles-of-attack the pressure distribution in both test sections agrees quite well on the pressure side of the main element and flap, whereas the pressure distributions on the slat differ strongly. On the suction side there are larger deviations for all three elements, which mainly results from the different solid and wake blockage, streamline curvature and horizontal buoyancy in both wind tunnels. These effects lead to considerably higher flow velocities on the suction side of each model element in the closed test section, especially for higher angles-of-attack, compared with the measured pressure distribution in the open test section. Variations of the angle-of-attack reveal that the c_p -

distribution of each element (slat, main element, flap) responds in different ways to changes of the angle-of-attack. On the one hand, the pressure on the suction side of the model components shows a different behavior, while on the other hand, each single element exhibits its own unique sensitivity to changes in angle-of-attack. For example, the slat responds much more sensitively to the same angle-of-attack variation than the flap. As a consequence of the differing aerodynamic properties and boundary conditions, it was not possible for the conducted measurements to achieve a similar pressure distribution on the model in both test sections by means of adjusting only the angles-of-attack. This fact is consistent with the observation made by [Herrig et al. \(2005\)](#). In their work, they deduced that an identical pressure distribution could not be achieved by employing the same airfoil contour in both wind tunnel types. Possibly, a better agreement between the pressure distributions in both wind tunnels might be achievable by combining the adjustment of the angle-of-attack with an additional adjustment of the slat and flap deflection angles, but this was not tested in the experiments conducted here, since it would involve a very time consuming process. Another approach aiming at obtaining a good agreement of the pressure distributions in both test sections would be to use adaptive walls in the closed wind tunnel, with which pressure distributions along the model can be adapted to minimize the effect of the wall.

The total lift force can be estimated by an integration of the measured surface-pressure distributions on the three wing elements. Details about this integration procedure are described in appendix [B.2](#). [Table 7.1.1](#) summarizes the relative differences of the total lift force F_L of the high-lift model between the open test section for an angle-of-attack of $\alpha_{os} = 12^\circ$ and various angles-of-attack α_{cs} in the closed test section at a flow velocity of 35 m/s. At an identical angle-of-attack of $\alpha = 12^\circ$ in both test sections the resulting generated total lift force is almost 50 % higher in the closed facility compared with the open jet wind tunnel. The reduction of the angle-of-attack of the high-lift model in the closed test section leads to smaller relative lift force differences. Finally, the total lift of the model at an angle-of-attack of 12° in the open test section corresponds nearly to the case of -1.5° in the closed test section, whereby the contribution of each element (slat, wing, flap) is test section-dependent. For example, all three elements generate positive lift in the current open test section case, while in the corresponding closed test section configuration the slat generates negative lift, which is compensated for by larger positive lift from wing and flap, achieving the same total lift for both test section cases. Clearly, this setup would undermine the actual intention of a high-lift system, so that it rather constitutes an academic configuration from an aerodynamic point of view, but nevertheless it still fully serves its purpose of comparing microphone array measurement results in both test sections.

7.1. AERODYNAMIC RESULTS

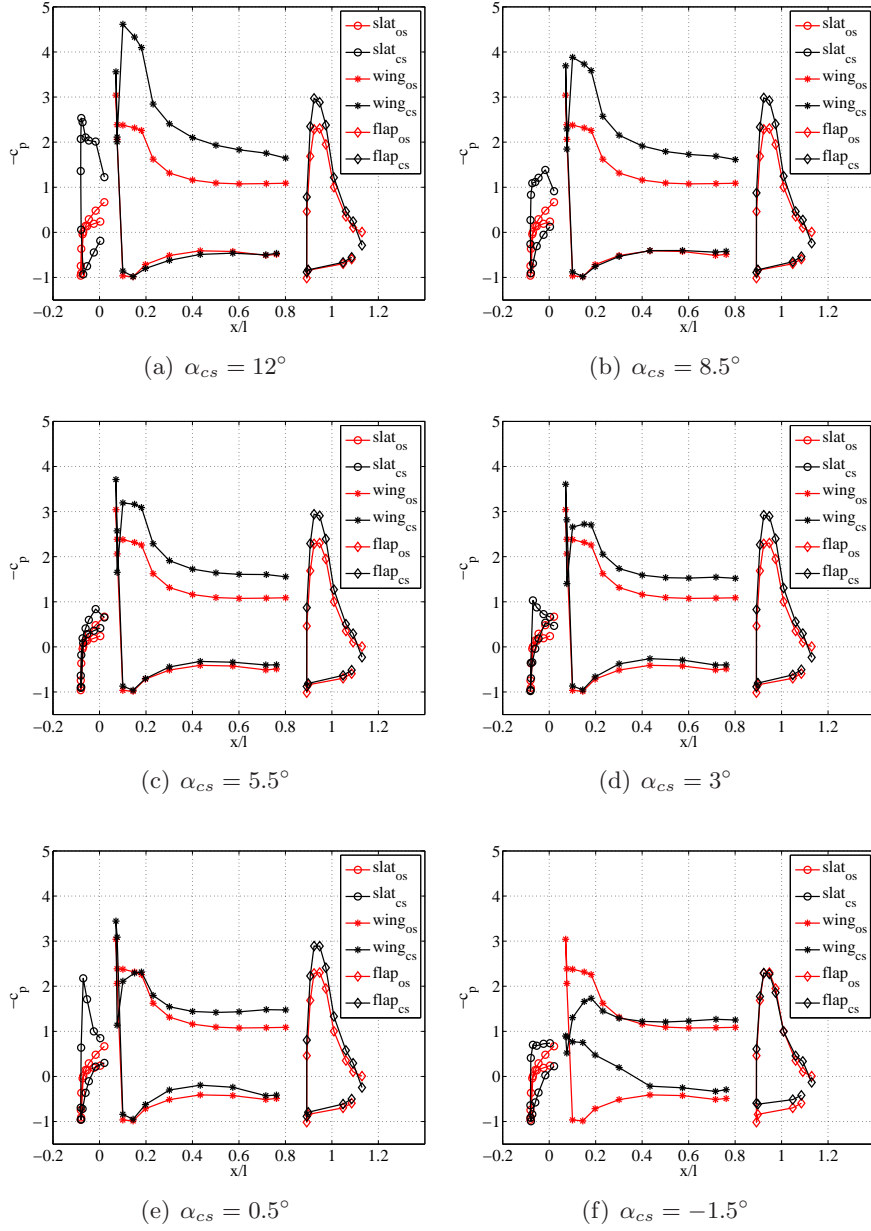


Figure 7.1: Distribution of the pressure coefficient c_p of the high-lift model in the open test section (os) for a geometrical angle-of-attack of $\alpha_{os} = 12^\circ$ (red) and in the closed test section (cs) for various angles-of-attack α_{cs} (black).

angle-of-attack α_{cs}	12°	5.5°	-1.5°
ΔF_L [%]	49.36	44.34	0.99

Table 7.1.1: Relative difference of the total lift force F_L of the high-lift model in the open test section for an angle-of-attack of $\alpha_{os} = 12^\circ$ and various angles-of-attack α_{cs} in the closed test section at a flow velocity of 35 m/s.

7.2 Beamforming results of the wing with high-lift system

The presented results comprise an evaluation of the source maps with and without flow correction for the wing model beginning with the results from the open test section. This is conducted exemplarily for 1/3 octave bands with low, middle and high frequency for an angle-of-attack of 12° in both wind tunnels.

7.2.1 Open test section

Figure 7.2 shows the 1/3 octave beamforming results of 2.5 kHz of the wing model with high-lift system, measured in the open test section for the flow velocity of 35 m/s using various beamforming parameters. The results show that the main aeroacoustic sources of the wing model are located in the vicinity of the slat, as expected (see chapter 3.4). The aeroacoustic strengths of the sources associated with the flap tracks and flap area are far less than those from the slat. The source maps in (a) and (b) show that there is almost no influence of diagonal removal (DR) on the results, indicating that the main diagonal of the cross spectral matrices is not significantly dominated by additional noise (wind tunnel background noise is negligible compared with source strength of the model) and that there is a good coherence between the microphone signals. Subsequently, a line source in the vicinity of the slat can be clearly seen in the beamforming results. When flow correction has not been applied, the sources will be located further downstream of the slat area, but nevertheless the measured amplitudes are not affected by this procedure, as shown in (c). Figure 7.3 shows a similar comparison, but this time for the 1/3 octave band of 6.3 kHz having the same beamforming and configuration parameters as before. One major difference to the 2.5 kHz case is the better resolution, which typically increases with rising frequency, as had been pointed out theoretically in chapter 4.2 and already observed in the evaluation of the reference sound source and the plate model results in chapters 5 and 6. Furthermore, with increasing frequency the slat tracks become more important as aeroacoustic sound sources. The source maps in (a) and (b) show that the application of DR gives additional improvements

7.2. BEAMFORMING RESULTS OF THE WING WITH HIGH-LIFT SYSTEM

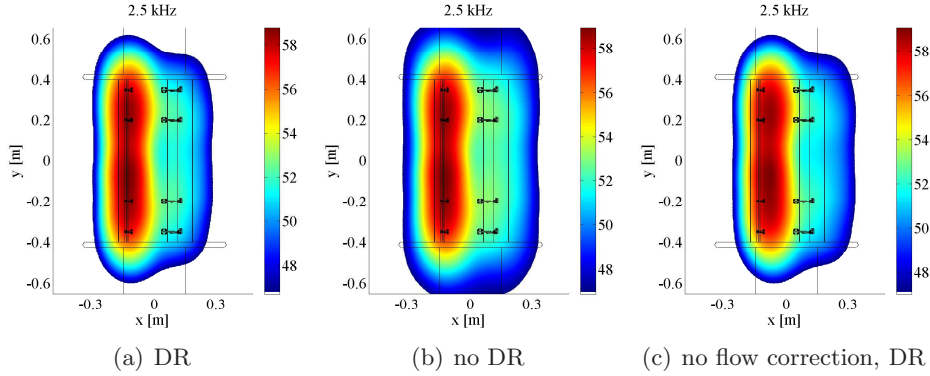


Figure 7.2: Beamforming results (in dB) of the airfoil model with high-lift system for the 1/3 octave band of 2.5 kHz for the open test section for a flow velocity of 35 m/s and with various beamforming parameters. Flow comes from the left and the angle-of-attack is 12° .

and enhances the SNR of the source map, albeit accompanied by a slight reduction of the source map peak level. Apart from the dominating slat sources in the vicinity of the slat tracks, the flap tracks also constitute source regions, but with considerably lower source strengths compared with the slat sources. The differences which arise by not applying the flow correction are manifested as downstream-shifted source positions (see (c)).

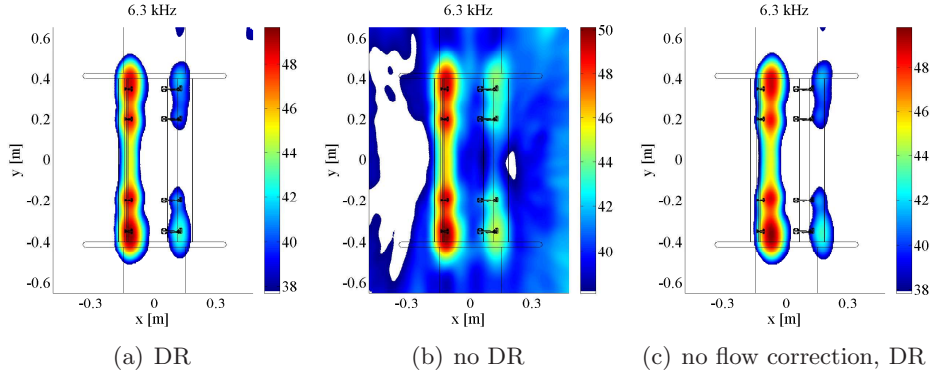


Figure 7.3: Beamforming results (in dB) of the airfoil model with high-lift system for the 1/3 octave band of 6.3 kHz for the open test section for a flow velocity of 35 m/s and with various beamforming parameters. Flow comes from the left and the angle-of-attack is 12° .

As observed previously, the slat tracks are the dominant aeroacoustic sound sources in the 1/3 octave band of 25 kHz, which is depicted in figure 7.4. The lower aeroacoustic source strength in this frequency band (with respect to the source strength at lower frequencies), in addition to the wind

tunnel background noise, yields a lower SNR as compared with the lower frequency results. For this reason the application of diagonal removal reduces the maximum value in the source map by about 2 dB, but at the same time it markedly increases the SNR. Without flow correction the map shows the sources shifted downstream, but still having the same maximum peak level as in the case using the Amiet model to take into account the flow effects (compare (a) and (c)).

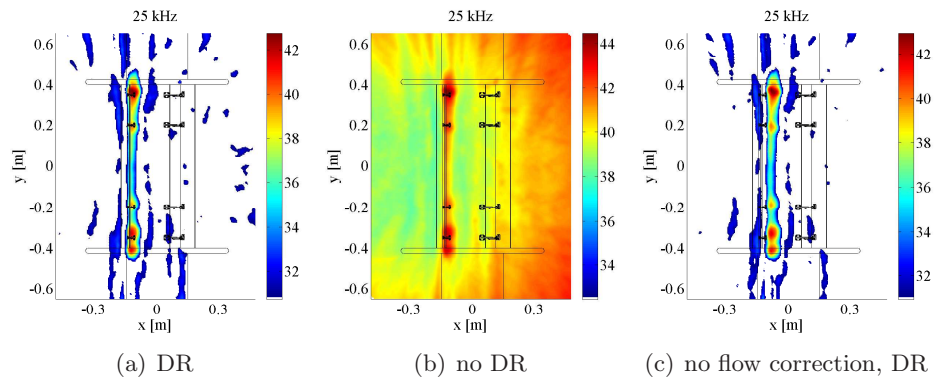


Figure 7.4: Beamforming results (in dB) of the airfoil model with high-lift system for the 1/3 octave band of 25 kHz for the open test section for a flow velocity of 35 m/s and with various beamforming parameters. Flow comes from the left and the angle-of-attack is 12° .

7.2.2 Closed test section

The closed test section results of the wing model with high-lift system are depicted in figure 7.5 for the 1/3 octave band of 2.5 kHz, measured for the flow velocity of 35 m/s using various beamforming parameters. In none of the shown cases was it possible to localize sources which are associated with the wing model, due mainly to the low aeroacoustic source strength. Only artifacts arising from the strong wind tunnel background noise are present in the source maps. At the 1/3 octave band of 6.3 kHz, the slat tracks and the junction of the high-lift system and the end plates become visible as aeroacoustic sound sources, as shown in figure 7.6. Strong background noise is still present, so that DR is absolutely necessary in order to retrieve sources (compare (a) and (b)). Ignoring the presence of the flow in the beamforming process, the sources will be located further downstream at a position which does not correspond to the slat vicinity, as depicted in (c). As observed previously, the slat tracks and the junction of the high-lift system and the end plates are the dominant aeroacoustic sound sources in the 1/3 octave band of 25 kHz, which is depicted in figure 7.7. The resolution has increased compared with the lower frequency results, leading to smaller and

7.2. BEAMFORMING RESULTS OF THE WING WITH HIGH-LIFT SYSTEM

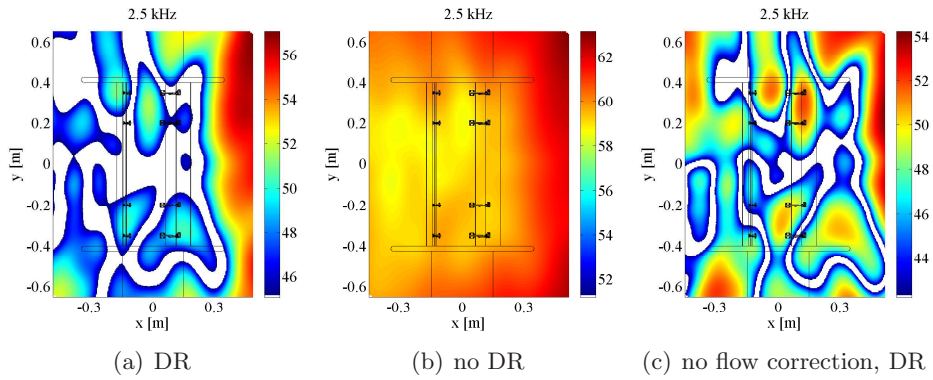


Figure 7.5: Beamforming results (in dB) of the airfoil model with high-lift system for the 1/3 octave band of 2.5 kHz for the closed test section for a flow velocity of 35 m/s and with various beamforming parameters. Flow comes from the left and the angle-of-attack is 12° .

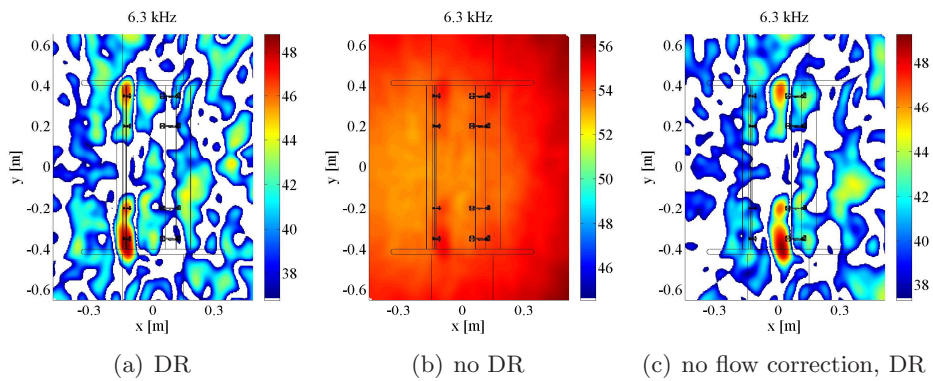


Figure 7.6: Beamforming results (in dB) of the airfoil model with high-lift system for the 1/3 octave band of 6.3 kHz for the closed test section for a flow velocity of 35 m/s and with various beamforming parameters. Flow comes from the left and the angle-of-attack is 12° .

more distinct source domains in the maps. In this frequency range the combination of relatively low acoustic source strength in the vicinity of the slat and the strong wind tunnel background noise mandates the application of DR, otherwise the source maps are again overwhelmed by the wind tunnel background noise, making a source localization impossible, as shown in map (b). The non-application of the flow correction results in downstream shifted sources, but the peak levels remain unaffected, as shown in figure 7.7 (c).

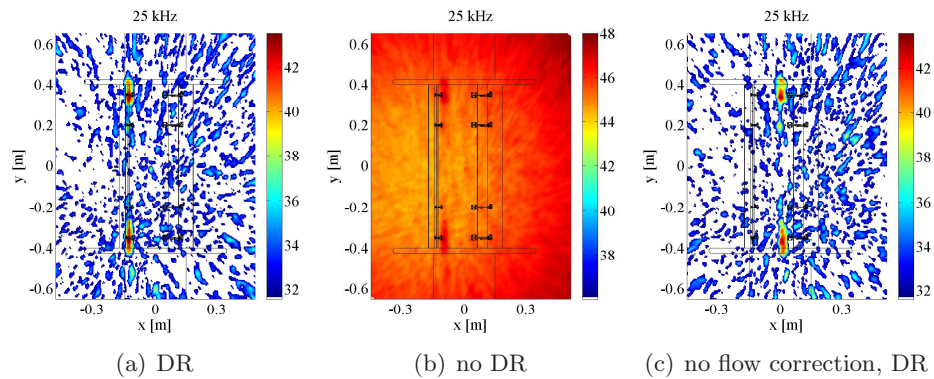


Figure 7.7: Beamforming results (in dB) of the airfoil model with high-lift system for the 1/3 octave band of 25 kHz for the closed test section for a flow velocity of 35 m/s and with various beamforming parameters. Flow comes from the left and the angle-of-attack is 12° .

7.3 Comparison of the results of the open and closed test sections

Before comparing the microphone array results it is essential to think about for which cases it is meaningful to perform the comparison. Fischer et al. (2006) have assessed the aeroacoustic performance of different high-lift devices of a half model in a wind tunnel with closed test section using a microphone array. As a basis of comparison served, amongst others, the same angle-of-attack, same lift coefficient and same lift. The obtained results vary, depending on what basis was used for performing the comparison. Finally, Fischer et al. (2006) suggest making the assessment with the same lift force, since this value would reflect the same flight operation conditions, so that a comparison would be made for those cases which correspond as closely as possible to the real flight conditions. In agreement with Fischer et al. (2006), Oerlemans et al. (2007), as described in chapter 1.3.2, have performed the comparison of microphone array results between the open and closed test sections on the basis of the same lift force. In contrast to that, Herrig et al. (2005) originally preferred an identical pressure coefficient

7.3. COMPARISON OF THE RESULTS OF THE OPEN AND CLOSED TEST SECTIONS

distribution c_p around an airfoil generating trailing edge noise, since, on the one hand, c_p is a measure for the local mean flow velocity and, on the other, the aeroacoustic source intensity is proportional to the n -th power of the flow velocity. However, this matching could not be achieved by [Herrig et al. \(2005\)](#) by employing the same airfoil contour in the open and closed wind tunnels. The relaxed requirement providing the basis for the comparison was that the boundary layer states at the trailing edge (the aeroacoustic source region) match each other reasonably well. This was achieved by ensuring that the gradient of the pressure distributions was nearly the same in both facilities, which thereby meant that the transition location was also at a similar location.

As a consequence of the garnered findings of [Fischer et al. \(2006\)](#), [Oerlemans et al. \(2007\)](#) and [Herrig et al. \(2005\)](#), the microphone array results from the open and closed test section experiments are compared to each other on the basis of the subsequent configurations. The first basis of comparison is associated with the same angle-of-attack of the model (12°) in both test facilities, because this ensures an identical geometrical setup. A further comparison is performed on the basis of the same lift force, following the suggestions of [Fischer et al. \(2006\)](#) and [Oerlemans et al. \(2007\)](#). As in the approach adopted by [Herrig et al. \(2005\)](#), the third basis of comparison used appropriate configurations of the open and closed test section where the flow field in the vicinity of the aeroacoustic sources can be considered to be nearly identical. Since it was not possible to obtain an identical pressure distribution around the model nor around the slat alone in both test facilities, as pointed out in section 7.1, those configurations were selected for performing the comparison where the lift forces on the slat were most similar. The fourth and final configuration pair comprises cases which have nothing in common with the first three quoted similarities, but are rather chosen to evaluate the differences of the emitted sound and source distribution due to varying flow fields, forces and geometrical setups.

7.3.1 Source maps

The figures 7.8, 7.9 and 7.10 show beamforming results for selected 1/3 octave bands for a flow velocity of 35 m/s, for an angle-of-attack of 12° in the open test section and different angles α_{cs} in the closed wind tunnel. The case of an angle-of-attack of 12° in both test sections reflects an identical geometrical setup (figures (a) and (b)). The total lift of the model at an angle-of-attack of 12° in the open test section corresponds to the case of -1.5° in the closed test section. Employing an angle-of-attack of 5.5° in the closed test section, the slat produces a comparable lift to that at $\alpha_{os} = 12^\circ$ in the open test section. The difference in the achieved relative slat lift force for the two configurations in the open and closed test section is about 1.63%. In the latter case, an angle-of-attack of 0.5° in the closed test section

was chosen for comparison, because this and the 12° case in the open wind tunnel have neither a similar pressure distribution, nor similar lift forces. Figure 7.8 shows a comparison of the beamforming results for the 1/3 octave

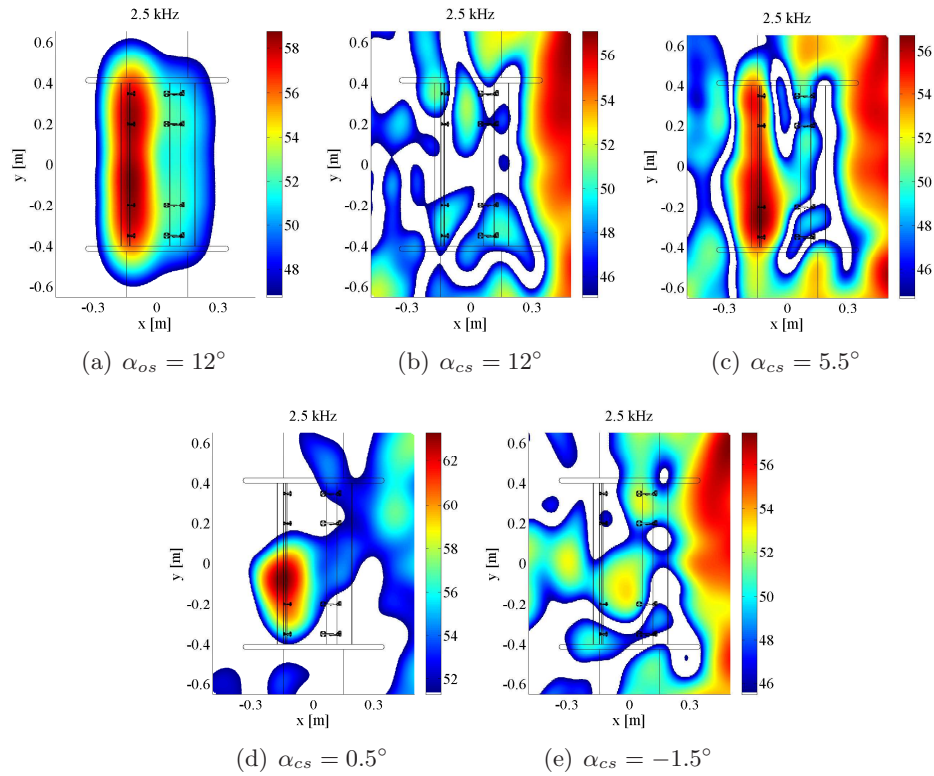


Figure 7.8: Beamforming results (in dB) of the generic high-lift model for the 1/3 octave band of 2.5 kHz for the open test section (a) and closed test section (b-e) for the flow velocity 35 m/s and for different angles-of-attack α . Flow comes from the left. In figures (a) and (b) the geometrical angle-of-attack is identical. The same total lift pertains for figures (a) and (e). The figures (a) and (c) have an identical slat lift. The cases (a) and (d) have nothing in common.

band of 2.5 kHz. In the open wind tunnel at an angle-of-attack of 12° (see (a)), a line source in the slat area can clearly be located with beamforming. Such a source is not present for the 12° and -1.5° cases in the closed test section. This is in all likelihood a result of the different flow fields in the slat area, resulting in differing aeroacoustic sound generation. In the closed wind tunnel, a line source in slat area occurs at an angle-of-attack of 5.5° , as shown in figure 7.8 (c). With this angle alignment, the slat produces nearly the same lift as the considered open test section case. For the open test section, strong wind tunnel background noise degrades the appearance of

7.3. COMPARISON OF THE RESULTS OF THE OPEN AND CLOSED TEST SECTIONS

the source map of the closed test section result. Furthermore, differences in the source distribution are observed and a peak level decrease occurs. In the previously discussed case for the closed test section (d), a tone phenomenon dominates the results, induced by the coherent laminar flow separation at the slat hook, leading to a significant higher peak level in the source map compared with the beamforming results of the other configurations. This phenomena could be suppressed by tripping, as discussed in chapter 3.4, but it is not explicitly shown here. Regardless of which angle-of-attack is considered in the closed test section, the SNR is always higher in the open test section.

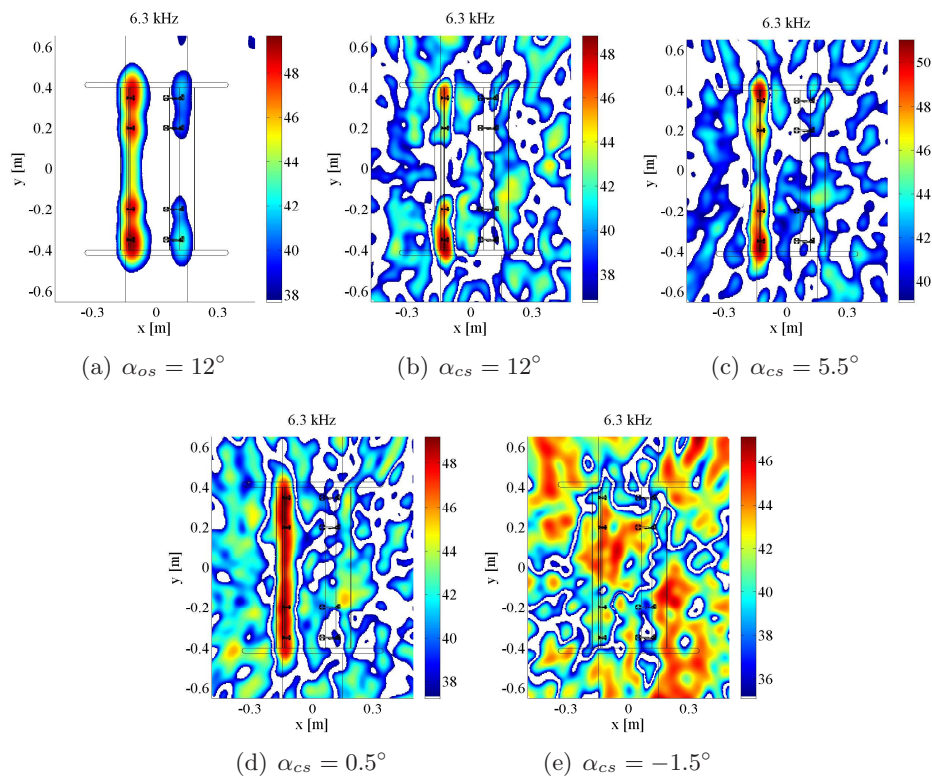


Figure 7.9: Beamforming results (in dB) of the generic high-lift model for the 1/3 octave band of 6.3 kHz for the open test section (a) and closed test section (b-e) for the flow velocity 35 m/s and for different angles-of-attack α . Flow comes from the left. In figures (a) and (b) the geometrical angle-of-attack is identical. The same total lift pertains for the figures (a) and (e). The figures (a) and (c) have an identical slat lift. The cases (a) and (d) have nothing in common.

With growing frequency the slat tracks and the junction of the high-lift system and the end plates become more important as aeroacoustic sound

sources, as shown in figure 7.9. For the 12° -configuration in the closed test section (b), the tracks are the main sources, but their appearance differs from the open test section case (a). Again, adjusting the angle-of-attack in the closed test section so that the resulting total lift amounts to the same value as obtained for the open test section, no source could be localized in (e). In contrast to this the results are similar when the slat lift is equal (see (a) and (c)), only with a difference being the higher peak levels in the closed test section and a more broadened source distribution in the open jet wind tunnel. The noise source mechanism seems to be different in the open test section at $\alpha_{os} = 12^\circ$, compared to the closed test section with an angle-of-attack of 0.5° , since here the dominant source is a line source in the slat area and not from the slat tracks. From the static pressure measurements around the model (see section 7.1) it is known that the flow field in the vicinity of the slat differs considerably between both configurations. Especially on the suction side of the slat, higher local flow velocities occur in the closed compared with the open test section configurations. Similar to the previously evaluated 1/3 octave band results, the slat tracks, and the junction of the high-lift system and the end plates are also the dominant aeroacoustic sound sources in the 1/3 octave band of 25 kHz, which is depicted in figure 7.10. With respect to the SNR, better results are again obtained in the open jet wind tunnel. The results in this frequency band illustrate the effect of the coherence loss caused by the turbulent shear layer. The sources in the map of the open test section (a) appear broadened and have a decreased peak level compared to the closed test section case with the same slat lift (c). Although the angles-of-attack in the closed test section cases differ strongly from each other, the beamforming results are quite similar ((b) and (d)). An exception is the configuration of $\alpha_{cs} = -1.5^\circ$, where again no sources related to the slat can be identified.

7.3.2 Integrated spectra

Finally, a comparison of the integrated spectra will be conducted for the measurements in the open and closed test section. The spectra in figure 7.11 were computed by integration of the slat area in the source maps. Figure 7.11 depicts the spectra deviations from the measurements in the open and closed test section for an identical geometrical angle-of-attack of 12° and for a nearly identical lift of the slat. The case of -1.5° in the closed test section, which corresponds to 12° configuration in the open test facility in terms of the same lift, was not considered, since no sources were identified with beamforming for this configuration. By comparing the open test section case with an angle-of-attack of 12° in the closed test section, it becomes apparent that a larger spectra difference (up to 7.4 dB) occurs in the lower frequency range where the slat is the main aeroacoustic source. This is not surprising since neither the flow fields in the vicinity of the

7.3. COMPARISON OF THE RESULTS OF THE OPEN AND CLOSED TEST SECTIONS

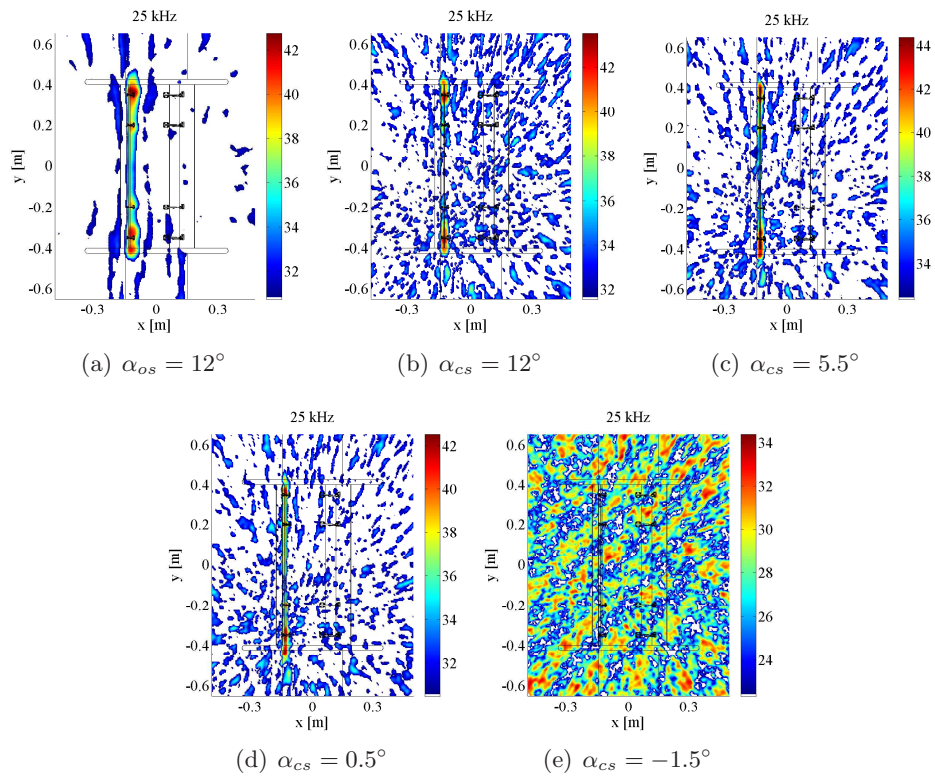


Figure 7.10: Beamforming results (in dB) of the generic high-lift model for the 1/3 octave band of 25 kHz for the open test section (a) and closed test section (b-e) for the flow velocity 35 m/s and for different angles-of-attack α . Flow comes from the left. In figures (a) and (b) the geometrical angle-of-attack is identical. The same total lift pertains to figures (a) and (e). The figures (a) and (c) have an identical slat lift. The cases (a) and (d) have nothing in common.

pressure side of the slat nor of the suction side have aerodynamic similarities, as shown in section 7.1 with the help of the pressure distribution. Further considering the 12° case, aeroacoustic sources which are clearly associated with the slat area can be retrieved with beamforming in the closed test section, beginning from the 1/3 octave band of 4 kHz (see e.g. figures 7.8 (b) and 7.9 (b)). With increasing frequency, the deviations become smaller, and it has already been determined from the source maps that the aeroacoustic source dominance has shifted from the slat to the slat tracks in this frequency range. Employing an angle-of-attack of 5.5° in the closed test section and 12° in the open test section yields integrated spectra with the same tendencies. Especially in the mid-frequency range the integrated spectra are almost identical, even though the source maps differ slightly in peak level and source dimension (figure 7.9 (a) and (c)). Nevertheless one obtains frequency-dependent deviations up to 4.6 dB, the larger ones being found in the low-frequency range. On the basis of the existing information it is not completely clear which effect is the major contributor to these deviations. To the possible influencing effects belong: (i) reflections at the reverberant walls of the closed test section; (ii) aeroacoustic source strength deviations arising from differences of the local flow field in the vicinity of the slat; (iii) directivity effects of the aeroacoustic sources resulting from different angles-of-attack; (iv) varying emission angles due to differences of the general flow conditions in open and closed test sections, as outlined in chapter 4.5.2; (v) especially for higher frequencies, coherence loss caused by turbulent scattering in the shear layer in the open test section. All mentioned effects will have an influence on the beamforming results, being potentially responsible for the observed spectra deviations.

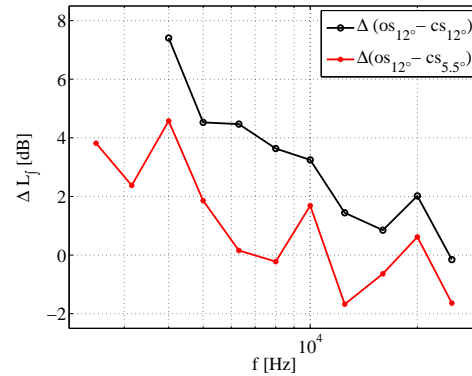


Figure 7.11: Differences of the integrated spectra of the high-lift model in the open (os) and closed (cs) test section for various angles-of-attack at $U = 35$ m/s.

7.4 Summary of the results of the wing with high-lift system

The intention of the investigation of the generic wing model with high-lift system was to examine a realistic complex aeroacoustic sound source with practical relevance in both wind tunnel types. As expected for such a model,

7.4. SUMMARY OF THE RESULTS OF THE WING WITH HIGH-LIFT SYSTEM

the model-wind tunnel interferences are of concern and the local and global flow properties around the model can vary significantly between the two wind tunnel types, and can then subsequently affect the aeroacoustic sound generation. These issues were the main objective of the examination of the third model. For that purpose aerodynamic and aeroacoustic measurements were conducted in order to compare the obtained results and to assess the comparability of microphone array measurements for such complex models. One of the main issues regarding this model consists in finding a common basis of comparison of the microphone array results for the different wind tunnel configurations. Various approaches concerning the basis of comparison were evaluated. On the one hand, geometrical similarity (same angle-of-attack) was employed for performing the comparison of the microphone array results, and, on the other, fluid mechanical similarity in terms of equal lift forces (total model and slat only) and similar pressure distributions were examined.

The aerodynamic measurements using pressure taps gave an insight into the mean flow field around the model and the differences in both wind tunnel types. As a consequence of the differing aerodynamic wind tunnel properties and boundary conditions, it was not possible to achieve an identical pressure distribution on the entire model in both test sections for the conducted measurements by means of adjusting only the angles-of-attack. Nonetheless, on the one hand, it was possible to achieve a similar lift force generated by the entire model, and on the other, a similar lift force of the slat in both test sections could be obtained by adjusting the angle-of-attack. In the present thesis, the comparative aerodynamic parameter of choice was the slat lift for the aeroacoustic sound sources in the vicinity of the slat. Furthermore, it became apparent that the total lift generated by the model was not an appropriate parameter for the comparison. Using the slat lift as a basis of comparison, the microphone array measurements revealed an identical source topology for both wind tunnel measurements, meaning that one observes the same frequency-dependent source distribution associated with the slat cove and slat tracks.

The source map peak levels and integrated spectra of both wind tunnel types possess frequency-dependent deviations reaching a maximum difference value of 4.6 dB between both test sections arising from: (i) different aeroacoustic sound generation due to deviations of the local flow field in the vicinity of the slat; (ii) reflections at the reverberant walls of the closed test section; (iii) directivity effects of the aeroacoustic sources resulting from different angles-of-attack; (iv) varying emission angles due to differences of the general flow conditions in open and closed test section; (v) especially for higher frequencies, coherence loss caused by turbulent scattering in the shear layer of the open test section. On the basis of the available information it is not possible to distinguish between these various effects and to quantify them separately.

CHAPTER 7. EXPERIMENTAL RESULTS ON A WING WITH HIGH-LIFT SYSTEM

Concerning the SNR of the aeroacoustic measurements of the generic wing model, as before in the cases of the reference sound source and the plate model, the SNR is higher in the open test section for the examined frequency range compared with the closed test section results.

Finally, based upon the measurement results from the generic wing model, the aeroacoustic advantages and disadvantages of both test section types can again be confirmed, as revealed by an analysis of the measurement results of the reference sound source in chapter 5.5. In addition, the generic wing model results emphasize the need for information about the local flow field in the vicinity of the aeroacoustic sources in order to perform a meaningful comparison of aeroacoustic measurements obtained in different test sections. Furthermore, on the one hand, the difficulty consists of finding an appropriate aerodynamic comparative parameter which sufficiently reflects the aeroacoustic sound generation process, and on the other, to ensure a similarity of the local flow fields in the different wind tunnels. These findings indeed constitute an extension of the observations made in the experimental study using the plate model concerning the influence of the flow field on aeroacoustic sound generation and the issue of comparability (see chapter 6.4).

Chapter 8

Comparison of the experimental results

The three employed models - the inflow-loudspeaker source, the plate model and the generic wing model with high-lift system - have all met the originally placed requirements (see chapter 3) on such sources, so that a wide range of propagation and boundary effects on the sound propagation and flow induced effects on the aeroacoustic sound generation could be identified, investigated and quantified.

In general, and independent of the installed model, the open test section exhibits a higher SNR than the closed test section, especially for lower frequencies where the wind tunnel background noise (generated by the fan, aeroacoustic noise from mountings, etc.), reflections and turbulent boundary layer noise predominate in the closed test section. In contrast to this, the SNR of open test section is typically decreased by shear layer induced coherence loss at higher frequencies, similar observations had already been made in previous studies (Herrig et al. (2005), Oerlemans et al. (2007), Li et al. (2011)).

Due to the source characteristics of the reference sound source, it was possible to investigate and quantify the influence of the flow and the wind tunnel-dependent boundary conditions on the beamforming results by conducting measurements with and without flow in both test sections over a broad frequency range up to 70 kHz. For the open jet wind tunnel the shear layer influence on sound propagation is of particular concern. With respect to the employed experimental setup in the open test section in this thesis, the transmission and refraction effects could be successfully allowed for using the Amiet procedure. Solely the coherence loss caused by turbulent scattering in the shear layer had a considerable influence on the microphone array results, since no reliable correction procedure is currently available. The coherence loss in the open jet wind tunnel leads to integrated levels decreased by more than 4 dB. This effect becomes significant for higher frequencies when the

scattering parameter takes values above 0.5. This result coincides with observations made by [Schlinker and Amiet \(1980\)](#), [Ross \(1981\)](#) and [Brooks and Humphreys \(1999\)](#). In contrast to this, the measurements in the closed test section are typically subjected to strong hydrodynamic pressure fluctuations induced by the turbulent boundary layer decreasing the SNR mainly in the low frequency range. Additionally, reverberations in the closed test section are also of major concern. The results for the closed wind tunnel have level drops of up to 4.4 dB compared with the corresponding free-field configuration without flow, having the same order of magnitude as those in open test section, the difference being that these drops occur principally in the lower frequency range, where they are induced by reflections.

The influence of reflection is not only restricted to the measured amplitudes; it was further found that the localized source positions were also affected. By means of the reference sound source it was revealed that the variations of the found source position is higher in the closed wind tunnel than in the open test section. Furthermore, the reflections induced by the reverberant walls in the closed test section are responsible for a small number of narrow band source maps where the found source position was not correct, even for high frequencies. To the author's knowledge, such a behavior has not yet been reported in an experimental study. In former experimental studies (see e.g. [Sijstma and Holthusen \(2003\)](#)) it was observed that the retrieved source positions in the closed test section can deviate from the true source locations due to reflections, especially in low-frequency 1/3 octave bands. For all conducted tests with the three different models such an influence could not be found and in all 1/3 octave band source maps the sources appeared at the a priori expected positions, indicating on the one hand that the flow correction procedures for the open and closed wind tunnel worked well and independent of the employed models, and on the other hand, that the reflection influence is not predominant with respect to the obtained source locations.

As partly mentioned above, for the plate and the generic wing model one obtains the same tendencies as for the reference sound source with respect to the SNR, shear and boundary layer effects, reflection influence and source positions, only with the difference that for both models the frequency range of the experiments was constrained to a maximum of 25 kHz due to the SNR and the low source strength of the aeroacoustic sources. In addition, aeroacoustic sound generation induced by the flow attains additional importance, since it responds very sensitively to changes in the flow field. Subsequently, the difficulty of a comparison between beamforming results measured in open and closed wind tunnels resides in ensuring the same flow conditions and of finding the cases with corresponding flow field in the vicinity of the aeroacoustic sources. In the present study, the comparative aerodynamic parameter for the generic wing model was the slat lift for the aeroacoustic sound sources in the vicinity of the slat. Furthermore, it has emerged that

the total lift generated by the model, as had been used by [Oerlemans et al. \(2007\)](#) in their experimental study, was not an appropriate parameter for the comparison. Concerning the generic wing model, directivity effects become more important than the other tested models as a consequence of different angles-of-attack and varying emission angles in both wind tunnels. In the high frequency range scattering effects and the accompanied coherence loss lead to a broadened source distribution and a decreased peak level in the source maps of the open jet wind tunnel measurements compared with the closed test section results. This phenomenon was also observed in a comparison of beamforming results of a scaled aircraft model performed by [Oerlemans et al. \(2007\)](#). On the basis of the available information from the experiments it was not possible to distinguish the various effects influencing the measurements of the plate and wing model in both test facilities and to quantify them separately, as had also been the case in the studies of [Herrig et al. \(2005\)](#), [Oerlemans et al. \(2007\)](#) and [Li et al. \(2011\)](#).

In principle, the 1/3 octave band source maps for all three different models, derived from measurements in both wind tunnels, show a similar and comparable source topology, provided that the flow conditions were comparable in both test facilities, whereas frequency-dependent differences and disturbances in the source maps appear due to the different test section-dependent boundary conditions and propagation effects. The maximum deviation between the absolute levels of the integrated spectra is similar for all three models and does not exceed 4.6 dB.

CHAPTER 8. COMPARISON OF THE EXPERIMENTAL RESULTS

Chapter 9

Summary and outlook

The present work focuses on the issue of the comparability and the performance of microphone array measurements in open and closed test sections.

In the last two decades, the phased microphone array has become a widely used tool in aeroacoustic testing for the localization and quantification of sound sources. Especially in aviation, this measurement technique has often been employed in various wind tunnels having open or closed test sections and has provided valuable aeroacoustic information for the improvement and design of aircraft and their components. In spite of the wide use of microphone arrays, there is still the need for examining the test-section dependent influences on and the uncertainties in the obtained aeroacoustic results arising from the differing properties of open and closed test sections. On the one hand the issue of comparability is significant for the comparison of measurement results obtained in different wind tunnels and on the other hand it plays an important role in the context of the greater group of topics concerning the comparability and transferability of aeroacoustic results derived from wind tunnel measurements to the real aircraft in free-flight.

The various effects influencing the aeroacoustic results of testing in different wind tunnel can be summarized in three main groups:

1. Model differences caused by different scaling and geometry simplifications can result in different aeroacoustic sound generation.
2. Differences in the experimental setup, which includes the influence of the use of different microphone arrays and differing source and microphone positions, might influence the measurement results. Moreover varying parameter settings and installation effects can lead to varying flow velocities and subsequently, to differing Reynolds and Mach numbers, which can also influence the aeroacoustic sound generation.
3. Finally, the third group consists of the varying test section boundary conditions and propagation effects.

In the framework of the assessment of the comparability of microphone array measurements in open and closed test sections, this thesis focuses on the third group - the influence of test section boundary conditions and propagation effects on microphone array results. Nonetheless, the first two points are also of concern and are discussed in this thesis. With respect to the third group, the aerodynamic and acoustic properties of wind tunnels with open or closed test section are a consequence of the test-section dependent boundary conditions and the typical flow field characteristics.

Concerning the open test section, the open jet wind tunnel is characterized by an unbounded test section. Beginning at the wind tunnel nozzle, a free shear layer develops which separates the potential core of the jet and the fluid at rest in the test section. Typically, the model is positioned inside the potential core of the jet and the microphone locations are outside the flow. Hence, the sound waves emitted from aeroacoustic sources on the model are convected by the potential flow in the jet core and have to pass through the turbulent wind tunnel shear layer before reaching the microphones. This sound propagation through the flow is accompanied by several effects which may influence the accuracy of aeroacoustic measurements and make it more difficult to interpret these results correctly; these effects are convection, refraction, transmission, scattering, absorption and spectral broadening of the incident sound waves. In the closed test section the flow is typically bounded by the hard walls of the test section. Along the wind tunnel surface a boundary layer develops with increasing thickness in stream wise direction. The flow outside of the boundary layers and the model wake can be practically considered as potential flow. By performing aeroacoustic measurements in closed test sections the model is normally placed inside the potential core of the flow and the microphones are typically flush mounted or recessed in the wind tunnel wall or an in-flow microphone with nose cone finds use. Hence, the sound waves emitted from aeroacoustic sources of the model are convected by the potential flow and have to pass through the typically turbulent boundary layer before reaching the microphone. In general, the sound propagation through the boundary layer has no significant effect on the measured signal in terms of transmission, reflection, refraction, scattering and absorption as long the boundary layer thickness is not too large compared with the wavelength of the examined acoustic signal.

Nonetheless, another effect which is associated with the turbulent boundary layer is important in the closed test section and has to be considered. The microphones are subjected to strong hydrodynamic pressure fluctuations induced by the turbulent boundary layer. This so-called pseudo sound is associated with the convection of turbulent eddy structures in the boundary layer. The reverberant walls of the closed test section are also of concern, since they cause reflections and the measured signal accuracy may be affected by interferences and multipath arrivals.

All mentioned effects of both wind tunnel types lead to a performance

loss of the acoustic measurements; they must be taken into account by applying appropriate corrections which enable one to quantify, localize and examine the sound source characteristics in aeroacoustic experiments. At the present time, the problem is that such appropriate correction procedures are only available for certain effects (convection, refraction, transmission), so that one has to accept discrepancies. Currently, reliable and practical correction methods do not exist for the scattering of sound at turbulent flow structures. In particular the open test section measurements are affected and the closed test section measurements are mainly plagued by uncorrected reflections.

In the past, these single effects, as they arise in the two different wind tunnel types, have been examined by many researchers, but the overall impact of all combined effects together on the comparability and the performance of microphone array results was only rarely considered. Besides a few related publications (see e.g. [Herrig et al. \(2005\)](#), [Li et al. \(2011\)](#)), to the author's knowledge there is basically only one fundamental published study (see [Oerlemans et al. \(2007\)](#)) in which microphone array measurements have been performed and compared using the same model in an open and closed test section. They found partially good agreement with the results from both test sections, but the possibilities of comparison were limited due to various reasons. Based on the publications from [Herrig et al. \(2005\)](#), [Oerlemans et al. \(2007\)](#) and [Li et al. \(2011\)](#)) the various reasons for discrepancies between the aeroacoustic results measured in different wind tunnel types can be classified into three different main groups. The first group is associated with the employed models which were the source of aeroacoustic sound generation:

- All examined models were highly complex with respect to the flow field around the models and the generated aeroacoustic sound field so that detailed noise characteristics are unknown a priori.
- The results presented in these publications further reveal that it is difficult, and sometimes impossible, to maintain the same flow conditions in both test sections, which in turn could be a source for these deviations in the aeroacoustic measurements.
- In some experiments the employed models exhibit geometrical differences. On the one hand the scaling was different which resulted in different Reynolds and Helmholtz numbers when performing the comparison of the measurement results. On the other hand the absence of some geometrical details between the used models might lead to changes in the aeroacoustic sound generation and subsequently, it might result in different results from the different measurement campaigns.

CHAPTER 9. SUMMARY AND OUTLOOK

A second type of effect responsible for possible deviations is linked to the experimental setup and test parameters:

- At least partly, different measurement techniques were used, thereby introducing uncertainties when comparing these results.
- Furthermore, different geometrical arrangements and test parameter settings were employed. On the one hand the different arrangements in conjunction with the aeroacoustic sources directivity can result in deviations between the test results. On the other hand, for example, the tests were performed employing different flow velocities which leads to differences in the Reynolds and Mach numbers and will affect the aeroacoustic sound generation. These differences require assumptions about the sources in order to convert the measured data so that a comparison is possible, thus it constituting a source for possible deviations.

The third group comprises effects which arise from the different test section-dependent boundary and flow conditions and subsequently, this can affect the sound propagation and the resulting sound field:

- In the open test section the shear layer will influence the sound propagation.
- In the closed test section the acoustic measurements will be affected by the wall boundary layer and the reverberant walls of the test section.
- The wind tunnel background noise is test section specific and will influence the measurement results in a variety of ways.

Due to the chosen models, the test setups and the parameters used in the experiments from [Herrig et al. \(2005\)](#), [Oerlemans et al. \(2007\)](#) and [Li et al. \(2011\)](#), it was clearly neither possible to distinguish between these possible sources of deviation nor to quantify their contributions.

Addressing the issues arising from the above mentioned publications, in this thesis these possible deviation sources must be kept in mind in the design of the experiment. The aim is to keep the experimental setup and test conditions as similar as possible in both cases and select appropriate models in order to avoid or at least to attenuate the influences of the aforementioned issues. This will enable the examination of these test section-dependent effects and a distinction between them.

The present study focuses on the beamforming accuracy and reliability in both wind tunnel types with respect to source position, source topology, relative and absolute levels of beamforming results, signal-to-noise ratio and integrated spectra. Therefore, three different wind tunnel model concepts acting as sound sources with varying complexity are used in this thesis in

order to examine on the one hand the propagation and boundary effects and on the other hand, the influence of the aerodynamic properties on the aeroacoustic sound generation in open and closed test sections.

The first wind tunnel model was designed for the examination of sound propagation effects in the different wind tunnel types, which requires that the sound propagation remains unaffected by the flow. The so-called reference sound source makes use of electromechanical sound generation. The other two wind tunnel models utilize aeroacoustic sound generation. In contrast to the first wind tunnel model, for these kinds of models the model-wind tunnel interferences are of concern and the local and global flow properties around the model can vary significantly in the two wind tunnel types. The finite size of the wind tunnel and the wind tunnel boundaries dominate mainly the test section-dependent aerodynamic properties and their differences to free-flight conditions in unbounded flow. The various effects (solid and wake blockage, streamline curvature, horizontal buoyancy, downwash) influence the flow field around the installed models in the wind tunnels. These result in different streamline curvature and static and dynamic pressures in the various wind tunnels. As a result of this, the forces and moments on the model are altered, whereby these effects demonstrate different and partially contrary characteristics in open and closed test sections, respectively.

The second wind tunnel model, a generic model, employs aeroacoustic sound generation in the form of a plate with cavities. The cavities differ in shape and size to give sound emission in different frequency bands including tonal and broadband spectral components. The model design should ensure that the aerodynamic model-wind tunnel interferences are as small as possible. This ensures that the difference in the flow properties in the vicinity of the aeroacoustic sound generation is as small as possible. Each cavity is equipped with an electret microphone, mounted in the base of the cavity, to measure the pressure fluctuations inside the cavity. These sensors provide near-field information and enable a comparison of the aeroacoustic sound generation and its differences in the various test sections. For the plate-cavity configuration the flow-induced sound from the cavities can be simply suppressed by covering the openings with tape.

The last and third adopted model incorporates an unswept wing with high-lift-system representing a realistic aeroacoustic sound source with practical relevance. In order to examine the aerodynamic performance, the high-lift system was instrumented with pressure taps located at midspan position. Regarding the comparison of microphone array results, the main requirement demands that the flow field around the model and therefore the aeroacoustic sound generation should be as similar as possible for performing the comparison of the results.

The three models were installed in both test sections using an identical geometrical setup with the same distance between the model sources and the microphone array. Despite the identical geometrical setup, the emission

angle of the emitted sound waves which are received by the array microphones differs in both wind tunnels due to the differing influences of sound wave convection and refraction. This effect becomes important for acoustic sources which do not have uniform sound emission. Concerning the employed models in this thesis the aeroacoustic cavity sources of the plate model and the aeroacoustic slat sources of the wing model may constitute such type of sources having a non-negligible directivity (dipole-like sources). Since there is no practicable compensation approach available at the present time one has to live with this influence.

The measurements were mostly conducted at a flow speed of 35 m/s, which is the highest velocity available in both wind tunnels. On the one hand acoustic measurements were performed using a microphone array and far-field microphones, while on the other hand aerodynamic measurements were carried out. The velocity distribution in the shear layer was measured by means of a Prandtl tube. This enables a measurement of the shear layer thickness, which is a required property for determination of the dimensionless scattering parameter (see chapter 2.3.3). In terms of the high-lift model, the similarity of the flow fields around the model in both test sections is checked by a comparison of the measurements of the pressure coefficient and the resulting lift force derived from the integration of the measured surface-pressure distribution around the three wing elements.

By means of the three employed models, by name the reference sound source, the plate model and the generic wing model with high-lift system, a systematic comparison between phased microphone array measurements in open and closed test sections has been performed in a never before published in-depth manner. Furthermore, regarding the reference sound source, the application of electro-mechanical sound generation enables a detailed examination of the test section-dependent influences on the sound propagation in different wind tunnel types without having the uncertainty of the reproducibility of flow-induced aeroacoustic sound generation.

All three used models have fulfilled the primary defined requirements on such sources so that a wide range of flow and boundary effects influencing the aeroacoustic sound generation and propagation have been identified, investigated and quantified in the conducted experiments. The successive analysis of the measurement results obtained from the three different models comprises the following items and influences:

- The SNR in both test sections is examined.
- The influence of the background noise on the beamforming results is investigated.
- In the closed test section the acoustic measurements will be affected by the turbulent wall boundary layer and reflections at the reverberant walls of the test section. The impact of these effects is also examined.

-
- In the open test section the shear layer will influence the sound propagation in the form of transmission, refraction and scattering of sound so that these effects are also a subject of the investigation.
 - The analysis further comprises source maps, relative and absolute levels of beamforming results, integrated spectra, an examination of the test section influences on the retrieved sound source positions and the source topology.
 - In the case of aeroacoustic sound generation the influence of the aerodynamic test section properties on the aeroacoustic sound generation and the resulting source topology is investigated. Moreover, various approaches concerning the finding of an appropriate basis for the comparison of microphone array results in both test section types are evaluated.
 - Finally, a ranking of the influences caused by the varying test section boundary conditions and propagation effects is given.

In general, being independent of the installed model, the open test section exhibits a higher SNR than the closed test section, especially for lower frequencies where wind tunnel background noise (generated by the fan, channel modes, aeroacoustic noise from mountings, etc.) and turbulent boundary layer noise predominate in the closed test section. In contrast to that, the SNR of the open test section is typically decreased by the shear layer induced coherence loss at higher frequencies. Similar observations have already been made in previous studies (Herrig et al. (2005), Oerlemans et al. (2007), Li et al. (2011)).

Due to the source characteristics of the reference sound source, it was possible to investigate and quantify the influence of the flow and the wind tunnel-dependent boundary conditions on beamforming results by conducting measurements with and without flow in both test sections over a broad frequency range up to 70 kHz. Considering the open jet wind tunnel the shear layer influence on the sound propagation is of particular concern. With respect to the employed experimental setup in the open test section in this thesis the refraction effects could be well corrected using the Amiet procedure and the transmission effects were negligible for the employed experimental setup and parameters. In contrast to that, the coherence loss caused by turbulent scattering in the shear layer had a considerable influence on the microphone array results, since no reliable and practicable correction procedure is currently available. The coherence loss in the open jet wind tunnel leads to integrated levels decreased by more than 4 dB. This effect becomes significant for higher frequencies when the scattering parameter takes values above 0.5. This result is consistent with observations made by Schlinker and Amiet (1980), Ross (1981) and Brooks and Humphreys (1999). As opposed

to this, the measurements in the closed test section are typically subjected to strong wind tunnel background noise and strong hydrodynamic pressure fluctuations induced by the turbulent boundary layer, which decrease the SNR mainly in the low frequency range. Additionally, reverberations in the closed test section are also of major concern. The results for the closed wind tunnel have integrated level deviations of up to 4.4 dB, having the same order of magnitude as the deviations in open test section, only with the difference that these deviations occur principally in the lower frequency range, induced by reflections in conjunction with the chosen signal processing parameters (see chapter 5.3.2).

The influence of reflection is not only restricted to the measured amplitudes; it was further found that the localized source positions were also affected. By means of the reference sound source it was revealed that the variations of the found source position is higher in the closed wind tunnel compared with open test section. Furthermore, the reflections induced by the reverberant walls in the closed test section are responsible for a small number of narrow band source maps where the found source position was not correct, even for high frequencies. The number of position outliers in the closed test section increases with flow, but less than 0.5 % of all narrow band source maps are affected altogether, whereas in the 1/3 octave band source maps no such phenomenon has been observed. In former experimental studies (see e.g. [Sijstma and Holthusen \(2003\)](#)) it was observed that the retrieved source positions in the closed test section can deviate from the true source locations due to reflections, especially in low-frequency 1/3 octave bands (in this study the source was located 0.3 m away from the wall). For all conducted tests with the three different models such an influence was not found and in all 1/3 octave band source maps the sources appeared at the a priori expected positions, indicating on the one hand that the flow correction procedures for the open and closed wind tunnels have worked well and independently of the employed models, and, on the other hand, that the reflection influence is not predominant with respect to the obtained source locations.

As partly mentioned above, for the plate and the generic wing model one obtains the same tendencies as for the reference sound source with respect to the SNR, shear and boundary layer effects, reflection influence and source positions, with the difference that for both models the frequency range of the experiments was limited to a maximum frequency of 25 kHz due to the SNR and the low source strength of the aeroacoustic sources.

The aeroacoustic sound generated by the flow is of particular importance, since it responds very sensitively to changes in the flow field. For example, in the case of the plate model with cavities the local flow velocities are slightly higher in the closed test compared with the open test section due to the solid blockage in all likelihood. In terms of the aeroacoustic cavity excitation the higher flow speed results in slightly larger near-field pressure

fluctuations and give rise to a frequency shift of the cavity tones towards higher frequencies. Subsequently, the difficulty of a comparison between beamforming results measured in open and closed test sections resides in ensuring the same flow conditions and finding the cases with corresponding flow field in the vicinity of the aeroacoustic sources. Regarding the wing with high-lift-system various approaches concerning the basis of comparison were evaluated. On the one hand, geometrical similarity (same angle-of-attack) was employed for comparing the microphone array results, while on the other hand fluid mechanical similarity in terms of equal lift forces (total model and slat only) and similar pressure distributions were examined. The aerodynamic measurements using pressure taps gave an insight into the mean flow field around the model and the differences in both wind tunnel types. As a consequence of the differing aerodynamic wind tunnel properties and boundary conditions, it was not possible to achieve an identical pressure distribution around the entire model in both test sections for the conducted measurements by means of adjusting only the angles-of-attack. Nonetheless, it was possible to achieve a similar total lift force generated by the entire model and a similar lift force of the slat in both test sections by adjusting the angles-of-attack. It had become apparent that neither the same geometrical angle-of-attack nor the total lift generated by the model were appropriate parameters for the comparison, as had been used by [Oerlemans et al. \(2007\)](#) in their experimental study. Instead of that, in the present study, the comparative aerodynamic parameter for the generic wing model was the slat lift for the aeroacoustic sound sources in the vicinity of the slat.

Concerning the generic wing model, directivity effects become more important compared with the other models as a consequence of different angles-of-attack and varying emission angles in both wind tunnels. In the high frequency range scattering effects and the accompanied coherence loss lead to a broadened source distribution and a decreased peak level in the source maps of the open jet wind tunnel measurements compared with the closed test section results. This phenomenon was also observed in the comparison of beamforming results of a scaled aircraft model performed by [Oerlemans et al. \(2007\)](#).

In principle, the 1/3 octave band source maps for all three different models, derived from measurements in both wind tunnels, show a similar and comparable source topology as long as the flow conditions were similar in both test facilities, whereby, however, frequency-dependent differences in the source maps appear. The differences can be traced back to the different test section-dependent boundary and flow conditions and different propagation effects. The maximum deviation between the absolute levels of the integrated spectra is similar for all three models and does not exceed 4.6 dB.

The answer to the question posed at the beginning of this thesis regarding the comparability of microphone array measurements in open and closed test

sections can be given in two different ways. The answer in a nutshell is:

”In principle, yes!”.

The more extensive answer turns out to be multifaceted. As shown in this thesis by means of the experiments, it is possible to obtain a similar and comparable source topology in aeroacoustic experiments measured in wind tunnels with open and closed test sections provided that several criteria are fulfilled. One principal point is the SNR, since it has to be sufficiently high in both test sections, otherwise a comparison is impossible. In addition, one has to make sure that the flow-field in the vicinity of the potential aeroacoustic sources is similar so that similar aeroacoustic sound generation can be ensured. This sounds easy, but the aeroacoustic sound generation depends to a great extent on the complexity of the model and the number of different involved sound generation mechanisms, making this, in fact, a very difficult task.

Concerning the multitude of boundary and propagation phenomena influencing the traveling of sound waves in both test facility types, there are two effects for which no appropriate and practical correction methods are currently available. On the one hand the reflections caused by the reverberant walls of the closed test section can significantly alter the measured absolute sound pressure levels compared with the open anechoic test section results where almost no reflections are present. The reflections affect strongly the results in the low frequency domain if 1/3 octave band are evaluated. Besides that, the retrieved source positions can also be influenced, even at high frequencies, but then, the impact is confined to a very small number of narrow-band source maps. On the other hand the scattering of sound waves off turbulent flow structures in the shear layer of the open test section degrades the quality and quantity of the beamforming results due to coherence loss of the measured signals. This effect becomes more dominant in the high-frequency regime. The present work can only be considered as a starting point for further investigations of the complex and extensive topic of the comparability of aeroacoustic measurements with microphone array measurements since there are further influencing parameters which can potentially affect the source topology and the absolute levels of beamforming results in wind tunnel measurements; these effects were not, however, the subject of this thesis. To this group belong influences caused by model differences in terms of geometry and scaling, model installation effects and different parameter settings leading to differences of the Helmholtz-, Mach- and Reynolds numbers. These effects are of interest for future examinations.

Besides the performed analysis and the stated facts concerning the comparability, the question should be considered as to how far it is possible to apply the employed approaches and achieved results of this thesis to other measurement campaigns and then to ascertain what would be the possible

benefits. In particular, based on the performed measurements and the corresponding analysis, one can derive the following guidelines for performing microphone array measurements in open and closed test section. Figure 9.1 illustrates the advantages and disadvantages of both test section types with regard to aeroacoustic testing and provides a rough overview of the frequency dependent boundary and propagation effects. The acoustic and

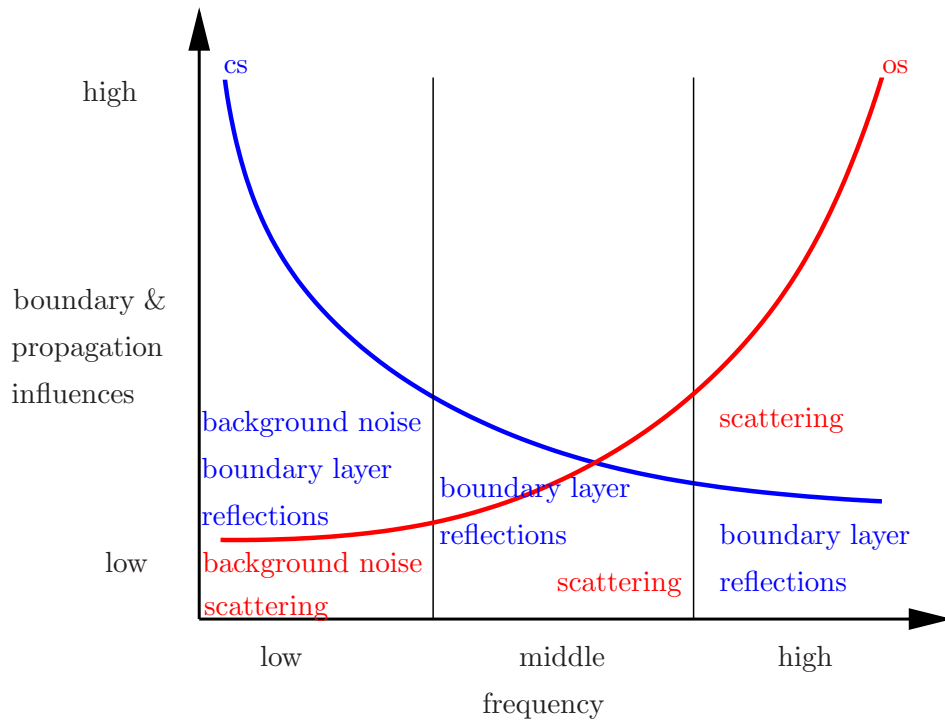


Figure 9.1: Illustration of the frequency-dependent influences on beamforming results caused by boundary and propagation effects in the open (os) and closed test sections (cs). All aspects associated with the closed test section are color-coded with blue and all aspects associated with the open test section are color-coded with red.

aerodynamic test requirements determine the selection of the test section type for performing the measurements. For example, if one is interested in examining a model emitting low frequency noise with a low source strength, then it would be recommended to conduct the testing in an open test section due to the higher SNR compared with the closed test section. In the closed test there is the danger that the wind tunnel background noise, the turbulent boundary layer and the reflections will dominate the beamforming results. Concerning the opposite case for investigating high-frequency noise-sources, one should choose a closed test section since in the open test section the coherence loss caused by the sound scattering off turbulent structures in the shear layer will significantly degrade the beamforming results. In the

mid-frequency range both test section types offer a comparable acoustic performance. In addition, there are further requirements which will restrict the possible choice of the test section. Currently, if one is interested in far-field microphone measurements then this can only be achieved by performing the testing in an open test section. Assuming that the measurement campaign is to focus on the aerodynamic performance of the model, with the aeroacoustic testing being conducted in piggyback fashion, then the closed test section is to be preferred.

Besides the brief guidelines for microphone array measurements there is a further benefit resulting from the performed measurements and analysis. The reference sound source can provide useful information because this wind tunnel model is perfectly suited to an acoustic characterization of wind tunnels under flow conditions. The applied method for the determination of the SNR in the wind tunnel can provide useful information about what can be expected from models undergoing testing, especially if predictions regarding the aeroacoustic source strength of the models are available. Furthermore, the reference sound source can also provide estimations about the level reduction caused by turbulent scattering in the shear layer of the open test section. It might be possible to develop a simple and practicable correction procedure for the reduction of integrated spectra due to the coherence loss on the basis of the reference sound source measurements and the scattering parameter. Such a simple model could correct the integrated spectra for each narrow or 1/3 octave band value, but in fact it would not be capable of improving the quality of the source maps. This would require an adaptive correction procedure for the unsteady phase and amplitude fluctuation (see e.g. the "guide star" method proposed by [Ehrenfried et al. \(2005\)](#)) or the integration of a turbulence model in the beamforming process (see e.g. [Dougherty \(2003\)](#)). At present, the obtained results from both mentioned correction procedures are not good enough to provide practical corrections for measurement data in terms of the coherence loss caused by scattering effects.

In the context of this thesis, an extensive and unique database consisting of microphone array data using three different complex models measured in an open and closed test sections was created. This database constitutes a valuable basis for future development of beamforming algorithms and flow and boundary correction procedures. In addition, the data base can be further used for modeling the various effects influencing aeroacoustic measurements in different wind tunnels (shear and boundary layer influence, background noise, reflections.). On the one hand this model of the wind tunnel disturbances can be employed for the estimation of the influence of wind tunnel effects on the beamforming results for certain measurement configurations and thus, it can be beneficial by the planning and realization of microphone array measurement campaigns. On the other hand this model of the wind tunnel disturbances should be helpful in the design and optimized

performance of future microphone arrays.

The modeling of the closed test section effects could be carried out as follows:

- The wind tunnel background noise is a superposition of various acoustic noise sources (generated by the fan, channel modes, aeroacoustic noise from mountings, etc.). Based on microphone array measurements, it is possible to assign the sound waves to certain source positions or propagation directions by means of beamforming and the computation of the wavenumber-frequency spectrum (see e.g. [Ehrenfried et al. \(2006\)](#)). Applying this extracted information one can simulate the wind tunnel background noise by a superposition of a number of plane waves and monopole sources. Finally, one obtains frequency-dependent cross-spectral matrices which contain the information about the disturbing sources.
- The influence of the turbulent boundary layer can be modeled in a similar way. The characteristics of the hydrodynamic pressure fluctuations can be extracted from the wavenumber-frequency spectrum and used for the modeling. Alternatively, the measured microphone signals can be employed for adjusting empirical wall-pressure fluctuation models like the Corcos model (see e.g. [Corcos \(1964\)](#), [Shin et al. \(2007\)](#)). Again, the modeling results in frequency-dependent cross-spectral matrices.
- The reflections can be modeled by following the approach proposed by [Sijstma and Holthusen \(2003\)](#) using mirror sources leading to modified cross-spectral matrices.

Finally, one obtains a set of cross-spectral matrices representing the various effects which influence the aeroacoustic measurements in a certain wind tunnel having a closed test section. Regarding the open test section, the influence of the coherence loss caused by turbulent scattering is of major concern:

- Based on the performed measurements with the reference sound source in the open test section with and without flow one can generate a so-called decorrelation matrix which is frequency-dependent and reflects the coherence loss influence on the beamforming results.

As mentioned above, this information about influencing effects in both test section types can be applied for the design and optimization of microphone arrays or for the planning and realization of microphone array measurement campaigns.

With a view to future developments in the microphone array technique, it is desirable to perform the aeroacoustic measurements at the same time

as the aerodynamic measurements in the closed test section, since this saves time and costs. Preference is given to the closed test section, because the aerodynamic uncertainties are reduced compared with the open section (Dobrzynski (2010)). This would require further development in the correction procedures for the disturbing effects, improvements of the SNR and improved microphone array hardware and beamforming software for the closed test facility. On the one hand, this implies a correction method for the reflections, while on the other a reliable approach has to be available which would allow the determination of quantitatively accurate far-field noise levels and directivities on the basis of microphone array data measured in the closed test section. At the moment, this latter point can only be addressed in an anechoic open test section. Currently, it is not foreseeable that these required measurement techniques and improvements will all be available in the near future.

Independent of the above mentioned long-term goal, there is still the desire to tackle the existing problems which are associated with microphone array measurements in open and closed test sections. In general, this can be normally achieved in two different ways. On the one hand the wind tunnel and/or its test section can be structurally modified in order to enhance the aeroacoustic properties. On the other hand improvements can be accomplished by modifying the microphone array hard- and software. In the following, the main thrust will concentrate on future array developments.

The improvement of the SNR is one of the main objectives for future array design. It is widely known that this can be easily achieved by increasing the number of microphones in the array. At the present time and to the author's best knowledge, the numerically largest microphone array is composed of 1020 sensors (Weinstein et al. (2007)). However, taking this path of development has some underlying restrictions. The combined costs of the microphones and the corresponding channels of the data acquisition system are one important limitation of such large microphone arrays. Moreover, the available space for the installation of the microphones is typically constrained and at a certain distance between two sensors the signal coherence will be too low due to the influence of the boundary and shear layers of the wind tunnels so that in this case more microphones do not lead to better results. Nowadays, Microelectromechanical System (MEMS) microphones afford a good performance and thus they can to some extent counteract these previously mentioned limitations due to their compact design and lower costs compared with traditional precision condenser microphones, as shown for example by Humphreys et al. (2005) and King and Underbrink (2008). Nevertheless, some challenges remain for performing a calibration of the MEMS microphones which can match the accuracy of the electrostatic calibration of condenser microphones and the dynamic range of the sensor is an issue.

In the field of communication systems (Elko (2000)), speaker localiza-

tion is often performed by applying differential microphone arrays. Due to certain signal processing techniques and microphone arrangements, the sensors exhibit more dipole, cardioid or hypercardioid characteristics rather than being omnidirectional. In this way it is possible to suppress noise, reverberation and echoes. To the author's best knowledge, until now there is no published study available concerning the application of differential microphone arrays under the harsh conditions in aeroacoustic wind tunnel testing, where especially the closed test sections will be the real challenge. In addition, the calibration and determination of absolute levels using differential microphone arrays remains an issue in this context.

Another very interesting way concerning the localization and quantification of sound sources are acousto-optic beamformer methods which use the interaction between sound and light. Recent experimental studies, performed among others by [Dittmar and Behrendt \(2008\)](#) and [Torras-Rosell et al. \(2012\)](#), applying a Laser Doppler Vibrometer and a Scanning Laser Doppler Vibrometer as a "microphone array" have shown promising results. However, this beamforming technique is in the early stages of its development and was tested so far only in laboratories and not in wind tunnels. Subsequently, it is not known when this beamforming technique will reach maturity and be able to replace the traditional microphone arrays consisting of microphones.

Apart from improvements of the SNR of microphone array measurements, there is also the need for improvement and refinement of the flow correction methods for both wind tunnel types, in particular with regard to performing phased microphone array measurements up to 100 kHz, in order to obtain better beamforming performance for such high frequencies.

CHAPTER 9. SUMMARY AND OUTLOOK

Appendix A

Results from microphone array measurements

A.1 Microphone signal coherence obtained from measurements in the closed test section

The figures [A.1](#) and [A.2](#) show the coherence of the measured signals of the central array microphone and all other array microphones derived from wind tunnel testing in the closed test section. The coherence maps were computed as explained in chapter [4.7.3](#). In addition, the coherence values are averaged over the 1/3 octave bands of 2, 25 and 63 kHz for various flow velocities. The underlying data sets have already been used for the computation of the coherence maps in figure [5.12](#) in chapter [5.3.2](#). This time longer time windows consisting of 8192 and 16384 samples are employed in order to examine the influence of the time window length on the microphone signal coherence.

APPENDIX A. RESULTS FROM MICROPHONE ARRAY MEASUREMENTS

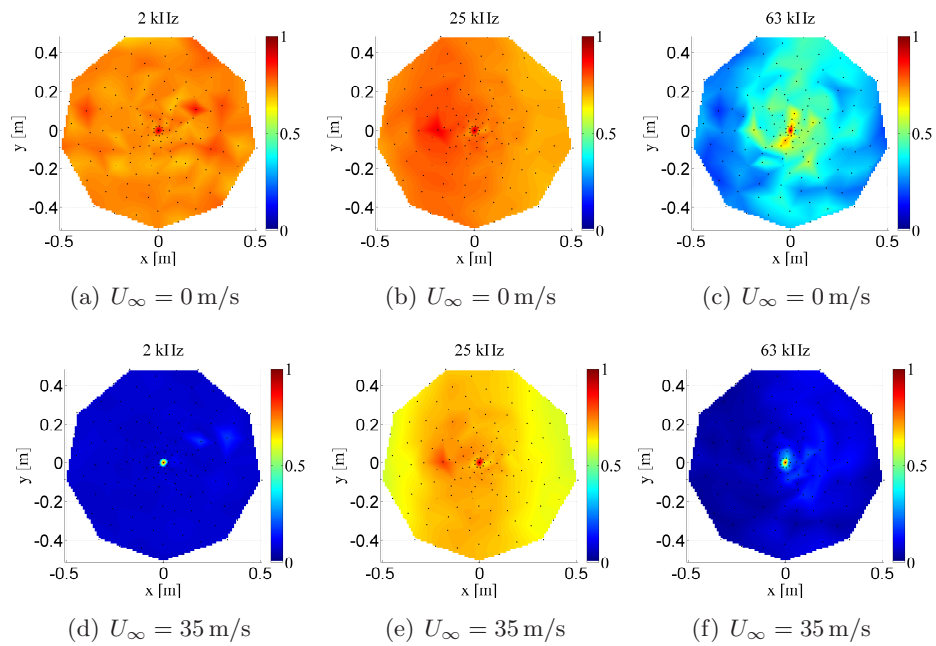


Figure A.1: Averaged coherence between the central array microphone and all other array microphones for various 1/3 octave bands in the closed test section and for various flow velocities using a time window with 8192 samples for the signal processing. The loudspeaker of the reference sound source is turned on. The black dots mark the positions of the array microphones. Flow comes from the left.

A.1. MICROPHONE SIGNAL COHERENCE OBTAINED FROM MEASUREMENTS IN THE CLOSED TEST SECTION

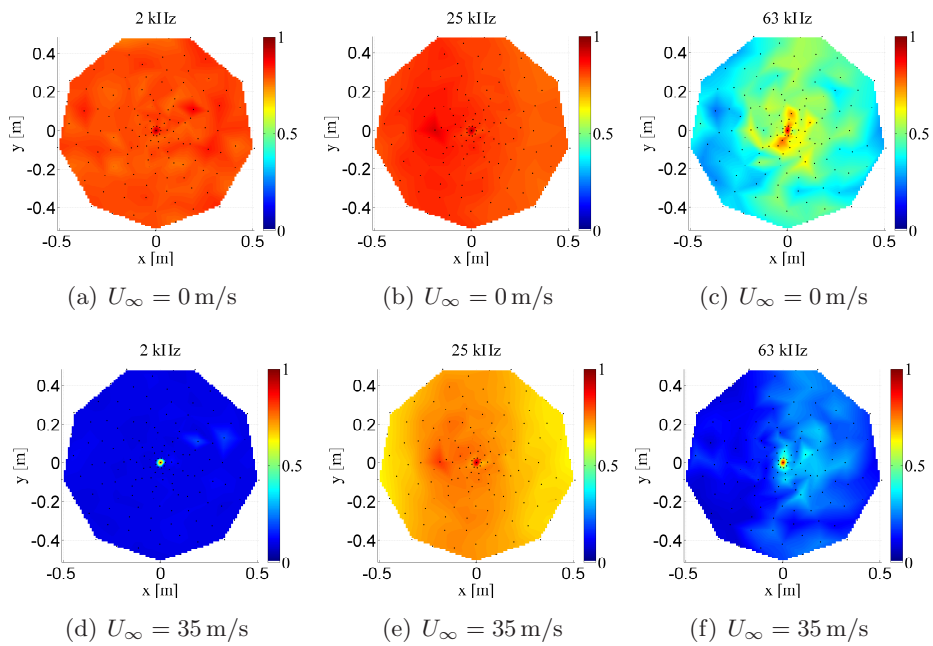


Figure A.2: Averaged coherence between the central array microphone and all other array microphones for various 1/3 octave bands in the closed test section and for various flow velocities using a time window with 16384 samples for the signal processing. The loudspeaker of the reference sound source is turned on. The black dots mark the positions of the array microphones. Flow comes from the left.

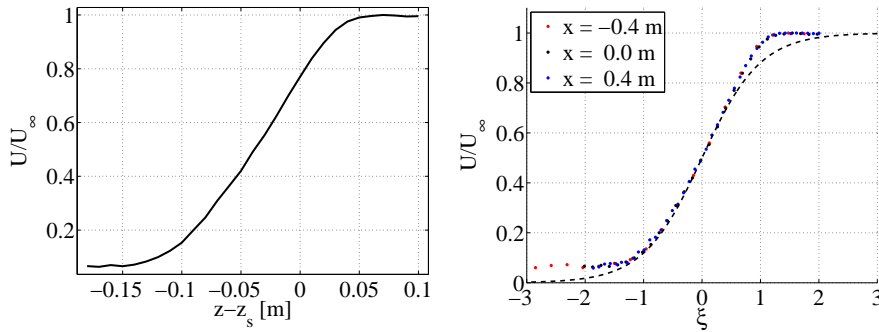
APPENDIX A. RESULTS FROM MICROPHONE ARRAY
MEASUREMENTS

Appendix B

Aerodynamic measurements

B.1 Characteristics of the shear layer in the open test section of the AWB

The shear layer profile, shown in figure B.1 (a), is normalized with the free stream velocity U_∞ . It was measured at a free stream velocity of 35 m/s



(a) normalized shear layer profile measured at $x = y = 0$ m

(b) reduced velocity profiles of the shear layer at various locations away from the nozzle (colored points) in comparison with the analytical approximation (dashed curve) using equation B.1.2.

Figure B.1: Shear layer velocity profiles, measured for a free stream velocity of $U_\infty = 35$ m/s in the open jet wind tunnel.

at $x = 0$ m. The Prandtl tube was traversed along the z -axis with step sizes of 0.005 m. The value $z_s = 0.4$ m denotes the position of the nozzle lip line. By considering the normalized velocity profile one can discern three different subdomains. Within the potential core the normalized velocity equals unity. Then a transition region begins where the velocity decreases and changes over to the domain which is characterized by a linear velocity decrease. This domain is followed by second transition region which desig-

nates the changeover to the domain where the fluid is at rest. However, the Prandtl tube in conjunction with the measurement chain does not measure an exact velocity of zero, but one can observe a small and constant offset. The half-mean velocity $U/U_\infty = 0.5$ does not correspond to the lip line position, it is displaced more outwards. In the context of the determination of the shear layer thickness the measured data were linearly interpolated in order to increase the accuracy of the computed results. The shear layer thickness δ_s was defined as the difference of the z -coordinates where the velocity achieves 10 % and 90 % of the free stream velocity U_∞ , respectively. This estimation method of the shear layer thickness was applied by [Candel et al. \(1976\)](#), [Schlinker and Amiet \(1980\)](#) and [Brooks and Humphreys \(1999\)](#) in their experiments concerning the sound transmission through turbulent shear layers. The shear layer thickness δ_s at $x = y = 0$ m yields 0.1405 m.

If the measured shear layer profiles possess self-similarity then the velocity distribution in the shear layer will be overall similar along the x -axis. This means that all velocity profiles can be mapped on one characteristic curve by the reduction with a typical length scale and a characteristic velocity. According to [Liepmann and Laufer \(1947\)](#), this can be achieved by introducing the reduced coordinate

$$\xi = \frac{2(z - z_{50\%})}{\delta_s}. \quad (\text{B.1.1})$$

The reduced coordinate is centered around the z -position where the normalized velocity U/U_∞ corresponds to 0.5 and as characteristic length scale the shear layer thickness δ_s is applied. The characteristic curve can be approximated using the analytical expression

$$\frac{U}{U_\infty} = 0.5[1 - \tanh(\xi)]. \quad (\text{B.1.2})$$

The obtained analytical characteristic curve and the reduced measured velocity profiles for various x -positions are plotted in figure [B.1 \(b\)](#) showing mostly a good agreement with the theoretical approximation. An exception is the transition region around $\xi = 1$ where one observes a discernable deviation. This is probably caused by the solid blockage of the reference sound source which affects the shear layer development.

B.2 Static pressure measurements

According to [Schlichting and Truckenbrodt \(1979\)](#) the pressure coefficient is defined as

$$c_p = \frac{p - p_\infty}{\frac{1}{2}\rho U_\infty^2} = 1 - \left(\frac{U}{U_\infty}\right)^2, \quad (\text{B.2.1})$$

whereas p denotes the static pressure at the point at which the pressure coefficient is being evaluated, p_∞ is the static pressure in the undisturbed

B.2. STATIC PRESSURE MEASUREMENTS

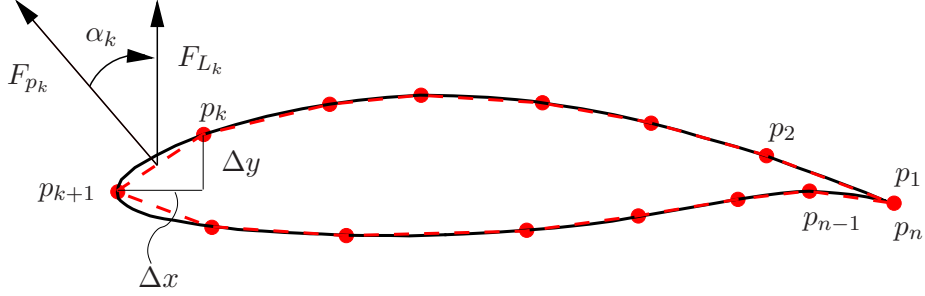


Figure B.2: Illustration of the determination of the lift force by integrating the surface-pressure distribution.

flow, ρ is the free stream fluid density, U is the local flow velocity and U_∞ labels the free stream velocity of the fluid.

The lift force F_L can be estimated by integrating the measured surface-pressure distribution of a wing. In this thesis, the trapezoidal rule was applied in order to integrate the discrete pressure values measured along the wing. This is illustrated in figure B.2. The total pressure force acting on an element between the two pressure taps k and $k + 1$ is composed by the drag and lift force. The lift force F_L can be approximated by

$$F_L \approx \sum_{k=1}^n F_{L_k} = \sum_{k=1}^n \cos \alpha_k F_{p_k} = l_w \sum_{k=1}^n \frac{p_k + p_{k+1}}{2} (x_{k+1} - x_k). \quad (\text{B.2.2})$$

In this way, the resulting lift force of each wing element (slat, main wing, flap) can be separately estimated.

APPENDIX B. AERODYNAMIC MEASUREMENTS

Appendix C

Turbulent scattering

C.1 Measurements from Brooks and Humphreys (1999)

Brooks and Humphreys (1999) conducted an experimental study aiming amongst others at the examination of the influence of turbulent scattering on microphone array results. In their measurements in an open jet wind tunnel with anechoic test section they employed a calibration point source which was capable to emit sufficiently high sound pressure up to 50 kHz. The used point source consists of a tube with one or more acoustic drivers mounted on the back end which were operated with white noise. The open end of the tube is intended to provide an omnidirectional sound source. Nonetheless, they observed mild to moderate directivity changes especially at high frequencies. The employed microphone array consisted of 35 microphones arranged in five logarithmic spirals having a maximum diameter of 0.8636 m. Figure C.1 depicts the differences of the integrated 1/3 octave band beamforming results obtained for measurements with and without flow using the calibration source. They varied the Mach number and the effective microphone array diameter (which is here labeled by the solid collection

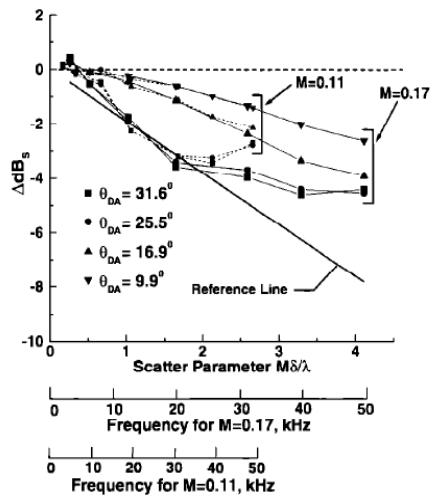


Figure C.1: Differences of the integrated spectra as a function of the scattering parameter for various array sizes and flow Mach numbers (taken from Brooks and Humphreys (1999)).

APPENDIX C. TURBULENT SCATTERING

angle θ_{DA} in terms of the radius). The experimental setup resulted in an opening angle of $2\theta_{DA}$ between array and source position. The data set for a mach number of 0.11 and an opening angle of $2\theta_{DA} = 63.2^\circ$ was reproduced from the publication and plotted in figure 5.15 in chapter 5.4.2.

Appendix D

Estimation of various effects influencing the cavity microphone spectra of the plate model

The underlying aim of this chapter is the estimation of possible effects altering the measured tone frequency of the flow-induced cavity oscillations of the plate model as discussed in chapter 6.1.4. On the one hand, temperature deviations in both wind tunnel test sections can lead to the observed shift of the tone frequency. On the other hand, variations of the local flow velocity in the vicinity of the cavities caused by test section dependent flow effects like solid blockage, streamline curvature, wake blockage and horizontal buoyancy (see chapter 1.2.1) can be a reason for tone frequency changes. In the following the influence of solid blockage on the cavity tone frequency differences is estimated. But first of all, the empirical parameters of the Rossiter model are adjusted to the obtained measurement results in order to achieve more accurate predictions of the cavity behavior. The conducted estimations are performed exemplarily for cavity 5.

D.1 Adjustment of the parameters of the Rossiter model to the measurements in the open test sections

By means of the empirical model from Rossiter (1964) the cavity tones were predicted using equation 3.3.1 as discussed in chapter 3.3.1:

$$St = \frac{fL_c}{U} = \frac{m_r - \gamma}{\frac{1}{K_r} + M} \quad m_r = 1, 2, 3, \dots$$

APPENDIX D. ESTIMATION OF VARIOUS EFFECTS
 INFLUENCING THE CAVITY MICROPHONE SPECTRA OF THE
 PLATE MODEL

Rossiter (1964) determined the two empirical constants by a best fit to his measured data and obtained $\gamma = 0.25$ and $K_r = 0.57$. As shown in table D.1.1 the predicted frequencies of the Rossiter modes using the Rossiter model with the above mentioned empirical constants and the measured frequencies in the open test section possess larger deviations. Therefore, a least square fit was performed in order to adjust the empirical parameters leading to more accurate predictions. Based on the microphone signal of cavity 5 measured in the open test section the parameters were determined to $\gamma = 0.0$ and $K_r = 0.5091$. By means of this two adjusted parameters the deviations between the measurements and the predictions based on the Rossiter model are much smaller than using the classical Rossiter model as shown in table D.1.1. The succeeding estimations are carried out by employing this adjusted Rossiter model examining the influence of temperature deviations in both test sections and solid blockage in the closed test section.

mode number	$m_r = 2$	$m_r = 4$	$m_r = 6$
f [Hz]: predicted	6595	14133	21671
f [Hz]: measured (in os)	6768	13535	20303
f [Hz]: predicted (adjusted parameters)	6773	13546	20319

Table D.1.1: Frequencies of Rossiter modes of cavity 5 at a flow velocity of 35 m/s. The frequencies were predicted employing the classical Rossiter model, measured in the open test section and predicted by using the Rossiter model with adjusted parameters.

D.2 Estimation of the temperature influence on the cavity microphone spectra

According to the Rossiter model, the frequency of the Rossiter modes will be influenced by temperature variations. A change of temperature will cause an alteration of the speed of sound c which in turn influences the Mach number M . The change of state in sound waves can be considered as isentropic (see e.g. Pierce (1981)) so that the sound speed of air is given by the equation

$$c = \sqrt{\kappa RT} \tag{D.2.1}$$

whereas κ denotes the heat capacity ratio (for dry air: $\kappa = 1.402$), R is the specific gas constant (for dry air: $R = 287 \text{ J}/(\text{Kg} \cdot \text{K})$) and the variable T denotes the temperature. Based on the respective temperature conditions in both test sections during the measurements the speed of sound was calculated employing equation D.2.1 and the resulting sound speeds are summarized in table D.2.1. Based on the preliminary considerations the

D.3. ESTIMATION OF THE INFLUENCE OF SOLID BLOCKAGE ON THE CAVITY MICROPHONE SPECTRA

temperature	sound speed
$T_{os} = 15.1\text{ }^{\circ}\text{C}$	$c_{os} = 340.56\text{ m/s}$
$T_{cs} = 17\text{ }^{\circ}\text{C}$	$c_{cs} = 341.69\text{ m/s}$

Table D.2.1: Measured temperatures in the open (os) and closed (cs) test section and the corresponding sound speeds using equation D.2.1.

temperature deviation influence on the Rossiter mode frequencies can be estimated by means of the Rossiter model employing the adjusted parameters and the different sound speeds resulting from the different temperature conditions in both test sections. The frequency shift caused by the different temperatures at a flow speed of 35 m/s are shown in table D.2.2. The slightly higher speed of sound in the closed test section leads to a maximum increase of the Rossiter mode frequencies of about 3 Hz. Subsequently, it seems to be implausible that the observed frequency shift of the Rossiter modes between the measurements in the open and closed test section in chapter 6.1.4 are only caused by temperature variations.

mode number	$m_r = 2$	$m_r = 4$	$m_r = 6$
f [Hz]: predicted with c_{os}	6773	13546	20319
f [Hz]: predicted with c_{cs}	6774	13548	20322

Table D.2.2: Predicted frequencies of Rossiter modes of cavity 5 at a flow velocity of 35 m/s using the classical Rossiter model with adjusted parameters and the corresponding sound speeds of each test section ($c_{os} = 340.56\text{ m/s}$ and $c_{cs} = 341.69\text{ m/s}$).

D.3 Estimation of the influence of solid blockage on the cavity microphone spectra

The possible influence of solid blockage on the flow velocity in the vicinity of the cavities can be approximately estimated applying the one-dimensional stream-tube theory (see e.g. Schlichting and Truckenbrodt (1979)). It assumes that viscosity and compressibility effects can be neglected and along a stream tube the mass flow must be constant yielding the equation for the conservation of mass for the steady one-dimensional motion of a incompressible fluid:

$$US = const, \quad (\text{D.3.1})$$

whereas U denotes the flow velocity and the variable S constitutes the cross-sectional area of the stream tube. In the closed test section, the cross-sectional area of the test section in the vicinity of the cavities is reduced by all model and measurement equipment related installations compared

APPENDIX D. ESTIMATION OF VARIOUS EFFECTS
 INFLUENCING THE CAVITY MICROPHONE SPECTRA OF THE
 PLATE MODEL

with the cross-sectional area at the nozzle exit where no installations are present. In the current case the microphone array and the plate model with mountings, illustrated in figure D.1, lead to a solid blockage of 3.2% of the cross-sectional area of the test section in the vicinity of the cavities. Thereby one can estimate the local flow velocity U_b in the vicinity of the cavities caused by solid blockage when the nozzle exit velocity is U :

$$U_b = \frac{U}{1 - 0.032}. \quad (\text{D.3.2})$$

The measurements using the plate model with cavities were performed at a flow speed of $U = 35$ m/s at the nozzle exit plane so that U_b is 36.16 m/s. In a second step, the flow velocity U_r in the vicinity of the cavities is es-

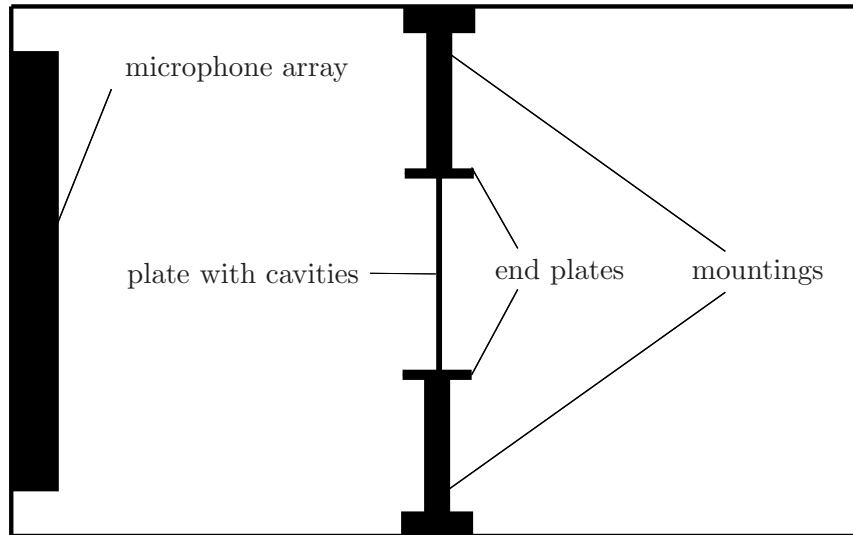


Figure D.1: Schematic sketch of the solid blockage of the installed plate with cavities and the installed microphone array in the closed test section.

timated employing the Rossiter model with the adjusted parameters and using the measured Rossiter mode frequencies in the closed test section. Table D.3.1 depicts the obtained results implying that a velocity increase induced by solid blockage is rather responsible for the observed higher mode frequencies in the closed test than the temperature difference. Nonetheless, there are discernable deviations between the velocity estimations based on the Rossiter model and the solid blockage estimation. The reasons for that are probably two-sided. On the one hand both models are very simplified and cannot capture the complexity of the flow and the sound generating process in detail. On the other hand further possible effects as horizontal buoyancy, wake blockage and the streamline curvature changes in the closed test section might also influence the measured results.

D.3. ESTIMATION OF THE INFLUENCE OF SOLID BLOCKAGE ON
THE CAVITY MICROPHONE SPECTRA

mode number	$m_r = 2$	$m_r = 4$	$m_r = 6$
f [Hz]: measured in c_{os}	6870	13775	20645
U_r [m/s]	35.53	35.59	35.61

Table D.3.1: Predicted flow velocity U_r using the Rossiter model with adjusted parameters and the measured Rossiter mode frequencies of cavity 5 from the closed test section ($c_{cs} = 341.69$ m/s and $T = 17^\circ C$).

APPENDIX D. ESTIMATION OF VARIOUS EFFECTS
INFLUENCING THE CAVITY MICROPHONE SPECTRA OF THE
PLATE MODEL

List of Figures

1.1	Overview showing the various sources providing input data for designing new aircraft and general improvements of the aeroacoustic performance. Uncertainties and effects influencing the selected method or the testing are framed by the boxes with dashed lines. The red numbers are footnote links to the bibliographical references.	2
1.2	Schematic setup of the aerodynamic testing in the closed test section of a wind tunnel.	5
1.3	Schematic setup of the aerodynamic testing in the open test section of a wind tunnel.	6
1.4	Schematic setup of aeroacoustic testing in the open test section of a wind tunnel.	7
1.5	Schematic setup of the aeroacoustic testing in the closed test section of a wind tunnel.	9
2.1	Schematic sketch of an elliptic mirror microphone.	18
2.2	Illustration of the Delay-and-Sum Beamformer (extended illustration based on a sketch from Oerlemans (2009)).	19
2.3	schematic example of the point-spread-function	23
2.4	Source map of a single monopole source as a superposition of source maps which are related to matrices \mathbf{R}_I and \mathbf{R}_{off} . The matrix \mathbf{R}_I is a diagonal matrix containing the real-valued elements of the original cross-spectral matrix \mathbf{R} on its main diagonal. The other matrix \mathbf{R}_{off} contains the complex-valued off-diagonal elements and has zeros on the main diagonal.	24
2.5	Source-observer scenario in the closed test section.	29
2.6	Sound refraction at an infinitely thin shear layer.	37
2.7	Illustration of the source-microphone scenario in the open test section.	40
2.8	Refraction and total reflection of sound waves at a plane zero thickness shear layer.	45
2.9	Sketch of a ray tube.	46
2.10	Ray tube spreading caused by the shear layer.	47

LIST OF FIGURES

2.11	Schematic sketch of "weak" spectral broadening of a monochromatic tone by a shear layer.	50
2.12	Illustration of the dipole orientation angle θ_{di}	57
2.13	Beamforming results of a simulated dipole source at various dipole orientation angles θ_{di} . The plots have a dynamic range of 12 dB from the maximum peak level using the retrieved source map maximum of the 0° case for normalization.	58
3.1	Reference sound source.	61
3.2	Details of the reference sound source.	61
3.3	Measured azimuthal directivity of the reference sound source in an echoic chamber without flow.	62
3.4	Measured polar directivity of the reference sound source in an echoic chamber without flow.	63
3.5	Plate with cavities.	64
3.6	Sketch of the cavity flow with acoustic feedback (see e.g. Gloorfelt (2009)).	65
3.7	Strouhal-Mach number relation of Rossiter modes	67
3.8	Strouhal-Mach number relation of depth-wise modes using equation 3.3.3 with $\eta_x = \eta_z = 0$	68
3.9	Strouhal number-velocity relation of Rossiter (m_r) and depth (η_y) modes of cavity 5	72
3.10	Generic 3-element high-lift model	74
3.11	Potential sources and physical mechanisms of slat noise mechanism (taken from Choudhari and Khorrami (2006)).	75
4.1	Sketch of the Aeroacoustic Wind Tunnel Braunschweig (AWB) of the DLR (Pott-Polenske and Delfs (2008)).	80
4.2	Sketch of the wind tunnel with closed test section (GroWiKa) at the Institute of Fluid Mechanics and Technical Acoustics of the Technical University Berlin.	81
4.3	The microphone array consisting of 144 sensors.	81
4.4	Point spread function of the microphone array	82
4.5	Installation of the three models in the test section of the open (a, c, e) and the closed (b, d, f) wind tunnel, as seen looking into the nozzle, with the microphone array on the right side.	85
4.6	Illustration of the model and microphone array installation in both wind tunnel test sections. Flow comes from the left.	87
4.7	Model and microphone (blue points) arrangement in the open and closed test section. The central microphone is marked as a magenta point. Flow comes from the left.	87
4.8	Sketch of the experimental setup for the far-field measurements using a single microphone in the open test section.	88

4.9	Narrow band source map of simulated incoherent monopole sources with equal and normalized source strengths, each at the individual cavity positions for various views. The monopole sources are located 0.975 m above the microphone array surface. The source frequency is 5 kHz. The normalized sound pressure level L_p is shown color-coded.	92
4.10	Illustration of the differing emission angles in both test sections, although an identical geometrical experimental setup has been used.	93
4.11	Emission angle difference $ \vartheta_{os} - \vartheta_{cs} $ between open and closed test section for each array microphone and for an assumed point source in the vicinity of the slat cove at flow velocity $U_\infty = 35$ m/s.	94
4.12	Illustration of the emission angle difference and directivity effects by means of a dipole source.	95
5.1	Sound pressure level of the central array microphone measured in the open (os) and closed (cs) wind tunnel under various conditions (loudspeaker on and off; with flow velocity of 35 m/s and flow at rest).	104
5.2	Normalized sound pressure levels of the central array microphone for a tone of $f_o = 4096$ Hz at various flow velocities. The results are centered around f_o showing a bandwidth of 1 kHz.	105
5.3	Normalized sound pressure levels of the central array microphone for various tones at a flow velocity of 35 m/s. The results are centered around f_o with a bandwidth of 1 kHz.	106
5.4	Normalized sound pressure level (SPL) of the central array microphone and the corresponding bicoherence spectrum for a tone of $f_o = 4096$ Hz at 35 m/s. The results are centered around f_o with a total bandwidth of 1 kHz.	107
5.5	Beamforming results (in dB) of the reference sound source for the 1/3 octave band of 2 kHz for the open test section for various flow velocities, various beamforming parameters and with loudspeaker (ls) on and off. Flow comes from the left.	108
5.6	Beamforming results (in dB) of the reference sound source for the 1/3 octave band of 25 kHz for the open test section for various flow velocities, various beamforming parameters and with loudspeaker (ls) on and off. Flow comes from the left.	110
5.7	Beamforming results (in dB) of the reference sound source for the 1/3 octave band of 63 kHz for the open test section for various flow velocities, various beamforming parameters and with loudspeaker (ls) on and off. Flow comes from the left.	112

LIST OF FIGURES

5.8	Averaged coherence between the central array microphone and all other array microphones for various 1/3 octave bands in the open test section and for various flow velocities. The loudspeaker of the reference sound source is turned on. The black dots mark the positions of the array microphones. Flow comes from the left.	114
5.9	Beamforming results (in dB) of the reference sound source for the 1/3 octave band of 2 kHz for the closed test section for various flow velocities, various beamforming parameters and with loudspeaker (ls) on and off. Flow comes from the left.	117
5.10	Beamforming results (in dB) of the reference sound source for the 1/3 octave band of 25 kHz for the closed test section for various flow velocities, various beamforming parameters and with loudspeaker (ls) on and off. Flow comes from the left.	118
5.11	Beamforming results (in dB) of the reference sound source for the 1/3 octave band of 63 kHz for the closed test section for various flow velocities, various beamforming parameters and with loudspeaker (ls) on and off. Flow comes from the left.	120
5.12	Averaged coherence between the central array microphone and all other array microphones for various 1/3 octave bands in the closed test section and for various flow velocities. The loudspeaker of the reference sound source is turned on. The black dots mark the positions of the array microphones. Flow comes from the left.	122
5.13	SNR of the reference sound source in the open (os) and closed (cs) test section.	126
5.14	Differences of integrated spectra of the reference sound source in the open (os) and closed (cs) test section for various flow velocities.	127
5.15	Differences of the integrated spectra as a function of the scattering parameter $M\delta_s/\lambda$	128
5.16	1/3 octave band spectra differences obtained from far-field measurements (ffm) and integrated spectra (int) derived from phased array measurements in the open (os) and closed (cs) wind tunnel at 35 m/s and with loudspeaker on and off (ls off).	130
5.17	Position of the localized source maximum of all narrow band source maps for the reference sound source for the open (os) and closed (cs) test section for various flow velocities.	132
5.18	Beamforming results and spatial source coherence (in dB) of the reference sound source for various narrow bands measured in the closed test section. The fluid is at rest. The white X marks the source maximum position of each source map. In the spatial source coherence maps the white X marks the point at which the spatial source coherence is calculated.	133

5.19	Illustration of the frequency-dependent influences on beamforming results caused by boundary and propagation effects in the open (os) and closed test sections (cs). All aspects associated with the closed and open test sections are color-coded in blue and in red.	135
6.1	Narrow band frequency spectra of the cavity microphones at the flow velocity of 35 m/s measured in both test sections. The spectra of cavity 5 is also shown with tape covering. The measurement values are depicted as sound pressure level L_p in dB.	138
6.2	Microphone signal coherence of the cavity narrow band spectra and the spectrum of the central array microphone from both wind tunnel measurements at 35 m/s for various cavities.	139
6.3	Spectra of cavity 1 for various flow velocities, shown for the open test section. The measured tones are sorted according to their amplitudes beginning with the highest one, which is labeled as "1st amplitude" (see (b)).	141
6.4	Spectra of cavity 5 for various flow velocities, shown for the open test section. The measured tones are sorted by amplitude, beginning with the highest one which is labeled as "1st amplitude" (see (b)).	142
6.5	Narrow band microphone spectra of cavity 2 and 4 for various flow velocities, shown for the open test section.	143
6.6	Comparison of narrow band microphone spectra of various cavities measured in both test sections at 35 m/s.	144
6.7	Beamforming results (in dB) of the plate with cavities for the 1/3 octave band of 6.3 kHz for the open test section for a flow velocity of 35 m/s and with various beamforming parameters. Flow comes from the left.	145
6.8	Beamforming results (in dB) of the plate with cavities for the 1/3 octave band of 12.5 kHz for the open test section for a flow velocity of 35 m/s and various beamforming parameters. Flow comes from the left.	146
6.9	Beamforming results (in dB) of the plate with cavities for the 1/3 octave band of 20 kHz for the open test section for a flow velocity of 35 m/s and various beamforming parameters. Flow comes from left.	147
6.10	Beamforming results (in dB) of the plate with cavities for the 1/3 octave band of 6.3 kHz for the closed test section for a flow velocity of 35 m/s and with various beamforming parameters. Flow comes from the left.	148

LIST OF FIGURES

6.11 Beamforming results (in dB) of the plate with cavities for the 1/3 octave band of 12.5 kHz for the closed test section for a flow velocity of 35 m/s and with various beamforming parameters. Flow comes from the left. 149

6.12 Beamforming results (in dB) of the plate with cavities for the 1/3 octave band of 20 kHz for the closed test section for a flow velocity of 35 m/s and with various beamforming parameters. Flow comes from the left. 149

6.13 SNR and 1/3 octave band spectra differences obtained from far-field measurements (ffm) and integrated spectra (int) derived from phased array measurements in the open (os) and closed (cs) wind tunnels at 35 m/s and with open and masked cavities. 153

7.1 Distribution of the pressure coefficient c_p of the high-lift model in the open test section (os) for a geometrical angle-of-attack of $\alpha_{os} = 12^\circ$ (red) and in the closed test section (cs) for various angles-of-attack α_{cs} (black). 157

7.2 Beamforming results (in dB) of the airfoil model with high-lift system for the 1/3 octave band of 2.5 kHz for the open test section for a flow velocity of 35 m/s and with various beamforming parameters. Flow comes from the left and the angle-of-attack is 12° 159

7.3 Beamforming results (in dB) of the airfoil model with high-lift system for the 1/3 octave band of 6.3 kHz for the open test section for a flow velocity of 35 m/s and with various beamforming parameters. Flow comes from the left and the angle-of-attack is 12° 159

7.4 Beamforming results (in dB) of the airfoil model with high-lift system for the 1/3 octave band of 25 kHz for the open test section for a flow velocity of 35 m/s and with various beamforming parameters. Flow comes from the left and the angle-of-attack is 12° 160

7.5 Beamforming results (in dB) of the airfoil model with high-lift system for the 1/3 octave band of 2.5 kHz for the closed test section for a flow velocity of 35 m/s and with various beamforming parameters. Flow comes from the left and the angle-of-attack is 12° 161

7.6 Beamforming results (in dB) of the airfoil model with high-lift system for the 1/3 octave band of 6.3 kHz for the closed test section for a flow velocity of 35 m/s and with various beamforming parameters. Flow comes from the left and the angle-of-attack is 12° 161

7.7 Beamforming results (in dB) of the airfoil model with high-lift system for the 1/3 octave band of 25 kHz for the closed test section for a flow velocity of 35 m/s and with various beamforming parameters. Flow comes from the left and the angle-of-attack is 12°. 162

7.8 Beamforming results (in dB) of the generic high-lift model for the 1/3 octave band of 2.5 kHz for the open test section (a) and closed test section (b-e) for the flow velocity 35 m/s and for different angles-of-attack α . Flow comes from the left. In figures (a) and (b) the geometrical angle-of-attack is identical. The same total lift pertains for figures (a) and (e). The figures (a) and (c) have an identical slat lift. The cases (a) and (d) have nothing in common. 164

7.9 Beamforming results (in dB) of the generic high-lift model for the 1/3 octave band of 6.3 kHz for the open test section (a) and closed test section (b-e) for the flow velocity 35 m/s and for different angles-of-attack α . Flow comes from the left. In figures (a) and (b) the geometrical angle-of-attack is identical. The same total lift pertains for the figures (a) and (e). The figures (a) and (c) have an identical slat lift. The cases (a) and (d) have nothing in common. 165

7.10 Beamforming results (in dB) of the generic high-lift model for the 1/3 octave band of 25 kHz for the open test section (a) and closed test section (b-e) for the flow velocity 35 m/s and for different angles-of-attack α . Flow comes from the left. In figures (a) and (b) the geometrical angle-of-attack is identical. The same total lift pertains to figures (a) and (e). The figures (a) and (c) have an identical slat lift. The cases (a) and (d) have nothing in common. 167

7.11 Differences of the integrated spectra of the high-lift model in the open (os) and closed (cs) test section for various angles-of-attack at $U = 35$ m/s. 168

9.1 Illustration of the frequency-dependent influences on beamforming results caused by boundary and propagation effects in the open (os) and closed test sections (cs). All aspects associated with the closed test section are color-coded with blue and all aspects associated with the open test section are color-coded with red. 185

LIST OF FIGURES

A.1	Averaged coherence between the central array microphone and all other array microphones for various 1/3 octave bands in the closed test section and for various flow velocities using a time window with 8192 samples for the signal processing. The loudspeaker of the reference sound source is turned on. The black dots mark the positions of the array microphones. Flow comes from the left.	192
A.2	Averaged coherence between the central array microphone and all other array microphones for various 1/3 octave bands in the closed test section and for various flow velocities using a time window with 16384 samples for the signal processing. The loudspeaker of the reference sound source is turned on. The black dots mark the positions of the array microphones. Flow comes from the left.	193
B.1	Shear layer velocity profiles, measured for a free stream velocity of $U_\infty = 35$ m/s in the open jet wind tunnel.	195
B.2	Illustration of the determination of the lift force by integrating the surface-pressure distribution.	197
C.1	Differences of the integrated spectra as a function of the scattering parameter for various array sizes and flow Mach numbers (taken from Brooks and Humphreys (1999)).	199
D.1	Schematic sketch of the solid blockage of the installed plate with cavities and the installed microphone array in the closed test section.	204

List of Tables

3.3.1 Cavity dimension details	70
3.3.2 Frequencies of Rossiter modes m_r of cavity 1	71
3.3.3 Frequencies of Rossiter modes of cavity 3	71
3.3.4 Frequencies of Rossiter modes of cavity 5	73
4.6.1 Signal and processing parameters for tonal measurements with the reference sound source	98
6.1.1 Predicted and measured frequencies of Rossiter modes m_r for cavity 1 for a flow velocity of 35 m/s in the open test section.	141
6.1.2 Predicted and measured frequencies of Rossiter modes m_r for cavity 5 for a flow velocity of 35 m/s in the open test section.	143
7.1.1 Relative difference of the total lift force F_L of the high-lift model in the open test section for an angle-of-attack of $\alpha_{os} =$ 12° and various angles-of-attack α_{cs} in the closed test section at a flow velocity of 35 m/s.	158
D.1.1 Frequencies of Rossiter modes of cavity 5 at a flow velocity of 35 m/s. The frequencies were predicted employing the clas- sical Rossiter model, measured in the open test section and predicted by using the Rossiter model with adjusted param- eters.	202
D.2.1 Measured temperatures in the open (os) and closed (cs) test section and the corresponding sound speeds using equation D.2.1.	203
D.2.2 Predicted frequencies of Rossiter modes of cavity 5 at a flow velocity of 35 m/s using the classical Rossiter model with ad- justed parameters and the corresponding sound speeds of each test section ($c_{os} = 340.56$ m/s and $c_{cs} = 341.69$ m/s).	203
D.3.1 Predicted flow velocity U_r using the Rossiter model with ad- justed parameters and the measured Rossiter mode frequen- cies of cavity 5 from the closed test section ($c_{cs} = 341.69$ m/s and $T = 17^\circ C$).	205

LIST OF TABLES

Bibliography

- T. Ahlefeldt, A. Lauterbach, and L. Koop. Aeroacoustic measurements of a scaled half model at high Reynolds numbers. In *16th AIAA/CEAS Aeroacoustics Conference, AIAA-Paper 2010-3748, Stockholm, Sweden*, 2010.
- K. K. Ahuja and J. M. Mendoza. Effects of cavity dimensions, boundary layer and temperature on cavity noise with emphasis on benchmark data to validate computational aeroacoustic codes. Technical report, NASA CR-4653, 1995.
- K. K. Ahuja, H. K. Tanna, and B. J. Tester. The free jet as a simulator of forward velocity effects on jet noise. Technical report, NASA Contractor Report 3056, 1978.
- K. K. Ahuja, H. K. Tanna, and B. J. Tester. An experimental study of transmission, reflection and scattering of sound in a free jet flight simulation facility and comparison with theory. *Journal of Sound and Vibration*, 75(1):51 – 85, 1981.
- R. K. Amiet. Correction of open jet wind tunnel measurement for shear layer refraction. In *2nd AIAA Aeroacoustics Conference, AIAA-Paper 75-532, Hampton, USA*, 1975.
- R. K. Amiet. Refraction of sound by a shear layer. *Journal of Sound and Vibration*, 58(4):467 – 482, 1978.
- J. Barlow, W. Rae, and A. Pope. *Low-Speed Wind Tunnel Testing*. John Wiley & Sons, Inc., Third Edition, 1999.
- B. Barsikow, W. F. King III, and E. Pfizenmaier. Wheel/rail noise generated by a high-speed train investigated with a line array of microphones. *Journal of Sound and Vibration*, 118(1):99 – 122, 1987.
- A. J. Bilanin and E. E. Covert. Estimation of possible excitation frequencies for shallow rectangular cavities. *AIAA Journal*, 11:347 – 351, 1973.
- J. Billingsley and R. Kinns. The acoustic telescope. *Journal of Sound and Vibration*, 48(4):485 – 510, 1976.

BIBLIOGRAPHY

- P. J. W. Block. Noise response of cavities of varying dimensions at subsonic speeds. Technical report, NASA TN D-8351, 1976.
- M. Born and E. Wolf. *Principles of Optics*. Cambridge University Press, 6th printing edition, 2010.
- T. F. Brooks and W. M. Humphreys. Effect of directional array size on the measurement of airframe noise components. In *5th AIAA/CEAS Aeroacoustics Conference, AIAA-Paper 99-1958, Bellevue, USA*, 1999.
- T. F. Brooks and W. M. Humphreys. A deconvolution approach for the mapping of acoustic sources (DAMAS) determined from phased microphone arrays. In *10th AIAA/CEAS Aeroacoustics Conference, AIAA-Paper 2004-2954, Manchester, United Kingdom*, 2004.
- T. F. Brooks and W. M. Humphreys. Extension of DAMAS phased array processing for spatial coherence determination (DAMAS-C). In *12th AIAA/CEAS Aeroacoustics Conference, AIAA-Paper 2006-2654, Cambridge, USA*, 2006.
- J. C. Bruggeman, A. Hirschberg, M. E. H. van Dongen, A. P. J. Wijnands, and J. Gorter. Self-sustained aeroacoustic pulsations in gas transport systems: Experimental study of the influence of closed side branches. *Journal of Sound and Vibration*, 150 (3):371 – 393, 1991.
- L. Brusniak. DAMAS2 validation for flight test airframe noise measurements. In *Second Berlin Beamforming Conference (BeBeC), Berlin, Germany*, 2008.
- N. J. Burnside, S. M. Jaeger, B. R. Reiner, W. C. Horne, and P. T. Soderman. Array design and performance for a large scale airframe noise study. In *8th AIAA/CEAS Aeroacoustics Conference & Exhibit, AIAA-Paper 2002-2576, Breckenridge, USA*, 2002.
- L. M. B. C. Campos. The spectral broadening of sound by turbulent shear layers. part 1. the transmission of sound through turbulent shear layers. *Journal of Fluid Mechanics*, 89 (4):723 – 749, 1978a.
- L. M. B. C. Campos. The spectral broadening of sound by turbulent shear layers. part 2. the spectral broadening of sound and aircraft noise. *Journal of Fluid Mechanics*, 89 (4):751 – 783, 1978b.
- L. M. B. C. Campos. On waves in gases. part I: Acoustics of jets, turbulence and ducts. *Reviews of Modern Physics*, 58 (1):117 – 183, 1986.
- S. M Candel. Numerical solution of conservation equations arising in linear wave theory: Application to aeroacoustics. *Journal of Fluid Mechanics*, 83:465 – 493, 1977.

- S. M. Candel, A. Guedel, and A. Julienne. Refraction and scattering of sound in an open wind tunnel. In *ICIASF '75, International Congress on Instrumentation in Aerospace Simulation Facilities, 6th, Ottawa, Canada, 1975*.
- S. M. Candel, A. Guedel, and A. Julienne. Radiation, refraction and scattering of acoustic waves in a free shear flow. In *3rd AIAA Aeroacoustics Conference, AIAA-Paper 76-544, Palo Alto, USA, 1976*.
- C. J. Chapman. Similarity variables for sound radiation in a uniform flow. *Journal of Sound and Vibration*, 233 (1):157 – 165, 2000.
- M. Choudhari and M. Khorrami. Slat cove unsteadiness: Effect of 3d flow structures. In *44th AIAA Aerospace Sciences Meeting and Exhibit, AIAA-Paper 2006-0211, Reno, USA, 2006*.
- G. M. Corcos. The structure of the turbulent pressure field in boundary-layer flows. *Journal of Fluid Mechanics*, 18 (3):353 – 378, 1964.
- D. G. Crighton. Aeroacoustics of flight vehicles: Theory and practice. Technical report, NASA Technical Report 90-3052, 1990.
- M. J. Czech, J. D. Crouch, R. W. Stoker, M. K. Strelets, and A. Gabaruk. Cavity noise generation for circular and rectangular vent holes. In *12th AIAA/CEAS Aeroacoustics Conference, AIAA-Paper 2006-2508, Cambridge, USA, 2006*.
- A. Dittmar and R. Behrendt. Measuring the 3d propagation of sound waves using scanning laser vibrometry. In *Second Berlin Beamforming Conference (BeBeC), Berlin, Germany, 2008*.
- W. Dobrzynski. Almost 40 years of airframe noise research: What did we achieve? *Journal of Aircraft*, 47 - 2:353 – 367, 2010.
- W. Dobrzynski and H. Buchholz. Full-scale noise testing on Airbus landing gears in the German Dutch wind tunnel. In *3rd AIAA/CEAS Aeroacoustics Conference, AIAA-Paper 97-1597, USA, 1997*.
- W. Dobrzynski, B. Gehlhar, and H. Buchholz. Model and full scale high-lift wing wind tunnel experiments dedicated to airframe noise reduction. *Aerospace Science and Technology*, 5(1):27 – 33, 2001.
- W. Dobrzynski, K. Nagakura, B. Gehlhar, and A. Buschbaum. Airframe noise studies on wings with deployed high-lift devices. In *4th AIAA/CEAS Aeroacoustics Conference, AIAA-Paper 98-2337, Toulouse, France, 1998*.
- W. Dobrzynski and M. Pott-Polenske. Slat noise source studies for farfield noise prediction. In *7th AIAA/CEAS Aeroacoustics Conference, AIAA-Paper 2001-2158, Maastricht, The Netherlands, 2001*.

BIBLIOGRAPHY

- R. P. Dougherty. Source location with sparse acoustic arrays; interference cancellation. In *1st CEAS-ASC Workshop: Wind Tunnel Testing in Aeroacoustics*, DNW, 1997.
- R. P. Dougherty. *Aeroacoustic Measurements*, chapter Beamforming in Acoustic Testing, pages 62 – 97. Springer Verlag, First Edition, 2002.
- R. P. Dougherty. Turbulent decorrelation of aeroacoustic phased arrays: Lessons from atmospheric science and astronomy. In *9th AIAA/CEAS Aeroacoustics Conference, AIAA-Paper 2003-3200, Hilton Head, USA*, 2003.
- R. P. Dougherty. Extensions of DAMAS and benefits and limitations of deconvolution in beamforming. In *11th AIAA/CEAS Aeroacoustics Conference, AIAA-Paper 2005-2961, Monterey, USA*, 2005.
- A. P. Dowling and J. E. Ffowcs Williams. *Sound and Sources of Sound*. Ellis Horwood Ltd, 1983.
- L. F. East. Aerodynamically induced resonance in rectangular cavities. *Journal of Sound and Vibration*, 3 (3):277 – 287, 1966.
- K. Ehrenfried and L. Koop. A comparison of iterative deconvolution algorithms for the mapping of acoustic sources. In *12th AIAA/CEAS Aeroacoustics Conference, AIAA-Paper 2006-2711, Cambridge, USA*, 2006.
- K. Ehrenfried, L. Koop, A. Henning, and K. Käpernick. Effects of wind tunnel noise on array measurements in closed test sections. In *First Berlin Beamforming Conference (BeBeC)*, 2006.
- K. Ehrenfried, L. Koop, and S. Kröber. Investigation of the systematic phase mismatch in microphone-array analysis. In *11th AIAA/CEAS Aeroacoustics Conference, AIAA-Paper 2005-2969, Monterey, USA*, 2005.
- G. W. Elko. *Acoustic Signal Processing for Telecommunications*, chapter Superdirectional Microphone Arrays, pages 181 – 235. Springer, first edition, 2000.
- R. Ewert, J. Dierke, M. Pott-Polenske, C. Appel, R. Emunds, and M. Sutcliffe. CAA-RPM prediction and validation of slat setting influence on broadband high-lift noise generation. In *16th AIAA/CEAS Aeroacoustics Conference, AIAA-Paper 2010-3833, Stockholm, Sweden*, 2010.
- R. Ewert, O. Kornow, B. J. Tester, C. J. Powles, J.W. Delfs, and M. Rose. Spectral broadening of jet engine turbine tones. In *14th AIAA/CEAS Aeroacoustics Conference, AIAA 2008-2940, Vancouver, Canada*, 2008.

-
- R. Ewert, O. Kornow, J. W. Yin, J. Delfs, T. Röber, and M. Rose. A CAA based approach to tone haystacking. In *15th AIAA/CEAS Aeroacoustics Conference, AIAA-Paper 2009-3217, Miami, USA, 2009*.
- A. B. Ezerskii, P. L. Soustov, and Chernov V. V. Sound scattering by a Karman street consisting of large-scale vortices. *Acoustical Physics*, 6: 670 – 675, 2000.
- B. A. Fenech and K. Takeda. Towards more accurate beamforming levels in closed-section wind tunnels via de-reverberation. In *13th AIAA/CEAS Aeroacoustics Conference, AIAA-Paper 2007-3431, Rome, Italy, 2007*.
- B. A. Fenech and K. Takeda. Beamforming accuracy in closed-section wind tunnels. In *14th AIAA/CEAS Aeroacoustics Conference, AIAA-Paper 2008-2908, Vancouver, Canada, 2008*.
- M. Fischer, H. Friedel, H. Holthusen, B. Gölling, and R. Edmunds. Low noise design trends derived from wind tunnel testing on advanced high-lift devices. In *12th AIAA/CEAS Aeroacoustics Conference, AIAA-Paper 2006-2562, Cambridge, USA, 2006*.
- X. Gloerfelt. *Aerodynamic Noise from Wall-Bounded Flows*. VKI LS 2009-03, 2009.
- F. R. Grosche. Distributions of sound source intensities in subsonic and supersonic jets. In *AGARD Conference Proceedings CP-131, 1973*.
- A. Guedel. Scattering of an acoustic field by a free jet shear layer. *Journal of Sound and Vibration*, 100 (2):285-304, 1985.
- S. Guidati, C. Brauer, and S. Wagner. The reflection canceller - phased array measurements in a reverberating environment. In *8th AIAA/CEAS Aeroacoustics Conference, AIAA-Paper 2002-2462, Breckenridge, USA, 2002*.
- Y. Guo. Aircraft slat noise modeling and prediction. In *16th AIAA/CEAS Aeroacoustics Conference, AIAA-Paper 2010-3837, Stockholm, Sweden, 2010*.
- H. H. Heller and D. B. Bliss. The physical mechanism of flow-induced pressure fluctuations in cavities and concepts for their suppression. In *2nd AIAA Aeroacoustics Conference, AIAA-Paper 75-491, Hampton, USA, 1975*.
- A. Herrig, W. Würz, T. Lutz, K. Braun, E. Krämer, and S. Oerlemans. Trailing-edge noise measurements of wind turbine airfoils in open and closed test section wind tunnels. In *Proceedings of the First International Meeting on Wind Turbine Noise: Perspectives for Control, Berlin, 2005*.

BIBLIOGRAPHY

- W. C. Horne, J. A. Hayes, S. M. Jaeger, and S. Jovic. Effects of distributed source coherence on the response of phased acoustic arrays. In *6th AIAA/CEAS Aeroacoustics Conference, AIAA-Paper 2000-1935, Lahaina, USA, 2000*.
- W. C. Horne and K. D. James. Concepts for reducing the self-noise of in-flow acoustic sensor and arrays. In *5th AIAA/CEAS Aeroacoustics Conference, AIAA-Paper 99-1815, Bellevue, USA, 1999*.
- M. S. Howe. Multiple scattering of sound by turbulence and other inhomogeneities. *Journal of Sound and Vibration*, 27 (4):455–476, 1973.
- M. S. Howe. On the absorption of sound by turbulence and other hydrodynamic flows. *IMA Journal of Applied Mathematics*, 32:181–209, 1984.
- M. S. Howe. Mechanism of sound generation by low Mach number flow over a wall cavity. *Journal of Sound and Vibration*, 273:103 – 123, 2004.
- W. M. Humphreys, Q. A. Shams, S. S. Graves, B. S. Sealey, S. M. Bartman, and T. Comeaux. Application of MEMS microphone array technology to airframe noise measurements. In *11th AIAA/CEAS Aeroacoustics Conference, AIAA-Paper 2005-3004 Monterey, USA, 2005*.
- K. U. Ingard. Influence of fluid motion past a plane boundary on sound reflection, absorption and transmission. *Journal of Acoustical Society of America*, 31:1035–1036, 1959.
- K.U. Ingard and P.A Franken. Sound propagation into a moving medium. *Journal of Acoustical Society of America*, 28:126 –127, 1956.
- M. Islam, F. Decker, M. Hartmann, A. Jäger, T. Lemke, J. Ocker, V. Schwarz, F. Ullrich, A. Schröder, and A. Heider. Investigations of sunroof buffeting in an idealised generic vehicle model - part I: Experimental results. In *14th AIAA/CEAS Aeroacoustics Conference, AIAA-Paper 2008-2900, Vancouver, Canada, 2008*.
- T. Ito, H. Ura, K. Nakakita, Y. Yokokawa, W. F. Ng, R. A. Burdisso, A. Iwasaki, T. Fujita, N. Ando, N. Shimada, and K. Yamamoto. Aerodynamic/aeroacoustic testing in anechoic closed test sections of low-speed wind tunnels. In *16th AIAA/CEAS Aeroacoustics Conference, AIAA-Paper 2010-3750, Stockholm, Sweden, 2010*.
- S. M. Jaeger, W. C. Horne, and C. S. Allen. Effect of surface treatment on array microphone self-noise. In *6th AIAA/CEAS Aeroacoustics Conference, AIAA-Paper 2000-1937, Lahaina, USA, 2000*.
- L. N. Jenkins, M. R. Khorrami, and M. Choudhari. Characterization of unsteady flow structures near leading-edge slat: Part I. PIV measurements.

-
- In *10th AIAA/CEAS Aeroacoustics Conference, AIAA-Paper 2004-2801, Manchester, United Kingdom, 2004.*
- D. H. Johnson and D. E. Dudgeon. *Array Signal Processing*. Prentice Hall, 1993.
- J. B. Keller. Reflection and transmission of sound by a moving medium. *Journal of Acoustical Society of America*, 27:1044 – 1047, 1955.
- A. I. Khinchin and A. Gamov. *Mathematical Foundations of Statistical Mechanics*. Dover Publications, 1949.
- M. R. Khorrami, M. E. Berkman, and M. Choudhari. Unsteady flow computations of a slat with a blunt trailing edge. *AIAA Journal*, 38 (11):2050 – 2058, 2000.
- M. R. Khorrami, B. A. Singer, and D. P. Lockard. Time-accurate simulations and acoustic analysis of slat free-shear-layer: Part II. In *8th AIAA/CEAS Aeroacoustics Conference, AIAA-Paper 2002-2579, Breckenridge, USA, 2002.*
- Y. C. Kim, J. M. Beall, and E. J. Powers. Bispectrum and nonlinear wave coupling. *Phys. Fluids*, 23(2):258 – 263, 1980.
- Y. C. Kim and E. J. Powers. Digital bispectral analysis and its applications to nonlinear wave interactions. *IEEE Transactions on Plasma Science*, PS-7 (2):120 – 131, 1979.
- J. P. King and J. R. Underbrink. Characterization of a microelectromechanical systems (MEMS) microphone. In *14th AIAA/CEAS Aeroacoustics Conference, AIAA-Paper 2008-2912, Vancouver, Canada, 2008.*
- W. F. King III and D. Bechert. On the sources of wayside noise generated by high-speed trains. *Journal of Sound and Vibration*, 66(3):311–322, 1979.
- D. König, S. R. Koh, W. Schröder, and M. Meinke. Slat noise source identification. In *15th AIAA/CEAS Aeroacoustics Conference, AIAA-Paper 2009-3100, Miami, USA, 2009.*
- A. Kolb, P. Faulhaber, R. Drobietz, and M. Grünwald. Aeroacoustic wind tunnel measurements on a 2d high-lift configuration. In *13th AIAA/CEAS Aeroacoustics Conference, AIAA-Paper 2007-3447, Rome, Italy, 2007.*
- L. Koop and K. Ehrenfried. Microphone-array processing for wind-tunnel measurements with strong background noise. In *14th AIAA/CEAS Aeroacoustics Conference, AIAA-Paper 2008-2907, Vancouver, Canada, 2008.*

BIBLIOGRAPHY

- S. Kröber. Entwicklung und Test von Referenzschallquellen für aeroakustische Windkanalexperimente. Master's thesis, Technical University of Berlin, 2007.
- S. Kröber, K. Ehrenfried, and L. Koop. Design and testing of sound sources for phased microphone array calibration. In *Second Berlin Beamforming Conference (BeBeC), Berlin, Germany*, 2008.
- S. Kröber, K. Ehrenfried, L. Koop, A. Lauterbach, and A. Henning. Systematic comparison of microphone array measurements in open and closed wind tunnels. In *16th AIAA/CEAS Aeroacoustics Conference, AIAA-Paper 2010-2803, Stockholm, Sweden*, 2010.
- Y. Li, M. Smith, and X. Zhang. Measurement and control of aircraft landing gear broadband noise. *Aerospace Science and Technology*, 7 (9):1 – 11, 2011.
- H. W. Liepmann and J. Laufer. Investigation of free turbulent mixing. Technical report, NACA, Technical Note No. 1257, 1947.
- M. J. Lighthill. On sound generated aerodynamically. I. general theory. *Proceedings of the Royal Society of London. Series A, Mathematical and Physical Sciences*, 211 (1107):564–587, 1952.
- M. J. Lighthill. On the energy scattered from the interaction of turbulence with sound or shock waves. *Proceedings of the Cambridge Philosophical Society*, 49:531–551, 1953.
- K. S. Lii, M. Rosenblatt, and C. van Atta. Bispectral measurements in turbulence. *Journal of Fluid Mechanics*, 77 (1):44 – 62, 1976.
- G. M. Lilley. On the noise from jets. Technical report, AGARD-CP-131 13.1, 1973.
- Y. Liu, A. R. Quayle, A. P. Dowling, and P. Sijstma. Beamforming correction for dipole measurement using two-dimensional microphone arrays. *Journal of Acoustical Society of America*, 124 (1):182 – 191, 2008.
- D. F. Long. Acoustic source localization in wind tunnel tests via subspace beamforming. In *41st Aerospace Sciences Meeting and Exhibit, AIAA-Paper 2003-369, Reno, USA*, 2003.
- A. McAlpine, C. J. Powles, and B. J. Tester. A weak scattering model for tone haystacking. In *15th AIAA/CEAS Aeroacoustics Conference, AIAA-Paper 2009-3216, Miami, USA*, 2009.
- U. Michel, B. Barsikow, J. Helbig, M. Hellmig, and M. Schüttpelz. Flyover noise measurements on a landing aircraft with a microphone array. In *4th*

-
- AIAA/CEAS Aeroacoustics Conference, AIAA-Paper 98-2224, Toulouse, France, 1998.*
- C. L. Morfey and P. F. Joseph. Shear layer refraction corrections for off-axis sources in a jet flow. *Journal of Sound and Vibration*, 239(4):819–848, 2001.
- C. L. Morfey and B. J. Tester. Noise measurements in a free jet flight simulation facility: Shear layer refraction and facility-to-flight corrections. *Journal of Sound and Vibration*, 54(1):83–106, 1977.
- P. M. Morse and K. U. Ingard. *Theoretical Acoustics*. Princeton University Press, 1968.
- M. Mosher. Phased arrays for aeroacoustic testing: Theoretical development. In *2th AIAA/CEAS Aeroacoustics Conference, AIAA-Paper 96-1713, State College, USA, 1996.*
- T. J. Mueller. *Aeroacoustic Measurements*. Springer Verlag, First Edition, 2002.
- E. Naudascher. From flow stability to flow-induced excitation. *Proc. of the Amer. Soc. of Civ. Eng. J. of Hydraulics Div.*, 93, No. HY4:15 – 40, 1967.
- C. Nikias and A. Petropulu. *Higher-Order Spectra Analysis - A Nonlinear Signal Processing Framework*. Prentice Hall, 1993.
- S. Oerlemans. *Detection of Aeroacoustic Sound Sources on Aircraft and Wind Turbines*. PhD thesis, University of Twente, Enschede, Netherlands, 2009.
- S. Oerlemans, L. Broersma, and P. Sijtsma. Quantification of airframe noise using microphone arrays in open and closed wind tunnels. *International Journal of Aeroacoustics*, 6 (4):309 – 333, 2007.
- S. Oerlemans and P. Sijtsma. Effects of wind tunnel side-plates on airframe noise measurements with phased arrays. In *6th AIAA/CEAS Aeroacoustics Conference, AIAA-Paper 2000-1938, Lahaina, USA, 2000.*
- S. Oerlemans and P. Sijtsma. Acoustic array measurements of a 1:10.6 scaled Airbus A340 model. In *10th AIAA/CEAS Aeroacoustics Conference, AIAA-Paper 2004-2924, Manchester, United Kingdom, 2004.*
- S. Oerlemans and P. Sijtsma. Determination of absolute levels from phased array measurements using spatial source coherence. In *8th AIAA/CEAS Aeroacoustics Conference, AIAA-Paper 2002-2464, Breckenridge, USA, 2002.*

BIBLIOGRAPHY

- A. D. Pierce. *Acoustics: An Introduction to its Physical Principles and Applications*. McGraw-Hill, 1981.
- J. F. Piet and G. Elias. Airframe noise source localization using a microphone array. In *3th AIAA/CEAS Aeroacoustics Conference, AIAA-Paper 97-1643, Atlanta, USA, 1997*.
- H. E. Plumbee, J. S. Gibson, and L. W. Lassiter. A theoretical and experimental investigation of the acoustic response of cavities in an aerodynamic flow. Technical report, U.S. Air Force Rep., WADD-TR-61-75, 1962.
- M. Pott-Polenske and J. Delfs. Enhanced capabilities of the Aeroacoustic Wind Tunnel Braunschweig. In *14th AIAA/CEAS Aeroacoustics Conference, AIAA-Paper 2008-2910, Vancouver, Canada, 2008*.
- P. A. Ravetta, R. A. Burdisso, and W. F. Ng. Wind tunnel aeroacoustic measurements of a 26%-scale 777 main landing gear model. In *10th AIAA/CEAS Aeroacoustics Conference, AIAA-Paper 2004-2924, Manchester, United Kingdom, 2004*.
- P. A. Ravetta, R. A. Burdisso, and W. F. Ng. Noise source localization and optimization of phased array results (LORE). In *12th AIAA/CEAS Aeroacoustics Conference, AIAA-Paper 2006-2713, Cambridge, USA, 2006*.
- J. W. S. Rayleigh. *The Theory of Sound*. Dover Publications, reprinted 1945, two volumes, 1879.
- M. C. Remillieux, E. D. Crede, H. E. Camargo, R. A. Burdisso, W. J. Devenport, M. Rasnick, P. Van Seeters, and A. Chou. Calibration and demonstration of the new Virginia Tech anechoic wind tunnel. In *14th AIAA/CEAS Aeroacoustics Conference, AIAA-Paper 2008-2911, Vancouver, Canada, 2008*.
- H. S. Ribner. Reflection, transmission and amplification of sound by a moving medium. *Journal of the Acoustical Society of America*, 29 (4): 435 – 441, 1956.
- S. W. Rienstra and A. Hirschberg. Introduction to acoustics. Technical report, Eindhoven University of Technology, Report IWDE 99-02, 1999.
- D. Rockwell and E. Naudascher. Review - self-sustaining oscillations of flow past cavities. *ASME Journal of Fluids Engineering*, 100:152 – 165, 1978.
- R. Ross. Spectral broadening effects in open wind tunnels in relation to noise assessment. *AIAA Journal*, 19 (5):567 – 572, 1981.

- R. Ross, K. J. Young, R. M. Allen, and J. C. A van Ditshuizen. Acoustic wave propagation through the shear layer of the DNW large open jet wind tunnel. In *8th AIAA Aeroacoustics Conference, AIAA-Paper 83-0699, Atlanta, USA*, 1983.
- J. E. Rossiter. Wind-tunnel experiments on the flow over rectangular cavities at subsonic and transonic speeds. Technical report, Aero. Res. Counc. R. & M. No. 3488, 1964.
- H. Schlichting. *Boundary-Layer Theory*. McGraw Hill Series in Mechanical Engineering, 6th Edition, 1968.
- H. Schlichting and E. Truckenbrodt. *Aerodynamics of the Airplane*. McGraw Hill Higher Education, 2nd edition, 1979.
- R. H. Schlinker and R. K. Amiet. Refraction of sound by a shear layer - experimental assessment. In *5th AIAA Aeroacoustics Conference, AIAA-Paper 79-0628, Seattle, USA*, 1979.
- R. H. Schlinker and R. K. Amiet. Refraction and scattering of sound by a shear layer. Technical report, NASA Report 3371, 1980.
- H. C. Shin, W. R. Graham, P. Sijstma, C. Andreou, and A. C. Faszer. Implementation of a phased microphone array in a closed-section wind tunnel. *AIAA Journal*, 45 (12):2897–2909, 2007.
- P. Sijstma. CLEAN based on spatial source coherence. In *13th AIAA/CEAS Aeroacoustics Conference, AIAA-Paper 2007-3436, Rome, Italy*, 2007.
- P. Sijstma. Acoustic array corrections for coherence loss due to the wind tunnel shear layer. In *Second Berlin Beamforming Conference (BeBeC), Berlin, Germany*, 2008.
- P. Sijstma. On spectral broadening in the open jet of the large low-speed facility of the DNW. Technical report, NLR-TR-2010-038, 2010.
- P. Sijstma and H. Holthusen. Source location by phased array measurements in closed wind tunnel test sections. In *5th AIAA/CEAS Aeroacoustics Conference, AIAA-Paper 99-1814, Bellevue, USA*, 1999.
- P. Sijstma and H. Holthusen. Corrections for mirror sources in phased array processing techniques. In *9th AIAA/CEAS Aeroacoustics Conference, AIAA-Paper 2003-3308, Hilton Head, USA*, 2003.
- P. Sijtsma. Experimental techniques for identification and characterization of noise sources. Technical report, NLR-TP-2004-165, 2004.

BIBLIOGRAPHY

- H. Siller, U. Michel, C. Zwiener, and G. Saueressig. Reduction of approach noise of the MD-11. In *12th AIAA/CEAS Aeroacoustics Conference, AIAA-Paper 2006-2464, Cambridge, USA, 2006*.
- B. Smith, H. Camargo, R. Burdisso, and W. Devenport. Design and testing of a novel acoustic wind tunnel concept. In *11th AIAA/CEAS Aeroacoustics Conference, AIAA-Paper 2005-3053, Monterey, USA, 2005*.
- P. T. Soderman, F. Kafyeke, N. J. Burnside, R. Chandrasekharan, S. M. Jaeger, and J. Boudreau. Airframe noise study of a CRJ-700 aircraft model in the NASA Ames 7- by 10- foot wind tunnel no. 1. In *8th AIAA/CEAS Aeroacoustics Conference & Exhibit, AIAA-Paper 2002-2406, Breckenridge, USA, 2002*.
- P. Stoica and R. Moses. *Spectral Analysis of Signals*. Pearson Prentice Hall, 2005.
- B. L. Storms, J. A. Hayes, P. J. Moriaty, and J. C. Ross. Aeroacoustic measurements of slat noise on a three-dimensional high-lift system. In *5th AIAA/CEAS Aeroacoustics Conference, AIAA-Paper 99-1957, Bellevue, USA, 1999*.
- B. L. Storms, J. C. Ross, W. C. Horne, J. A. Hayes, R. P. Dougherty, J. R. Underbrink, D. F. Scharpf, and P. J. Moriaty. An aeroacoustic study of an unswept wing with a three-dimensional high-lift system. Technical report, NASA TM-1998-112222, 1998.
- T. Suzuki. Generalized inverse beam-forming algorithm resolving coherent/incoherent, distributed and multipole source. In *14th AIAA/CEAS Aeroacoustics Conference, AIAA-Paper 2008-2954, Vancouver, Canada, 2008*.
- C. K. W. Tam and N. Pastouchenko. Gap tones. *AIAA Journal*, 39 (8): 1442 – 1448, 2001.
- K. W. Tam and P. J. W. Block. On the tones and pressure oscillations induced by flow over rectangular cavities. *Journal of Fluid Mechanics*, 89 (2):373 – 399, 1978.
- B. J. Tester and C. L. Morfey. Development in jet noise modelling - theoretical predictions and comparisons with measured data. *Journal of Sound and Vibration*, 46(1):79 – 103, 1976.
- T. G. Tibbe. Effect of open-jet shear layers on aeroacoustic wind tunnel measurements. Technical report, NLR-TR-2010-138, 2010.
- A. Torras-Rosell, F. Jacobsen, and S. Barrera-Figueroa. A beamforming system based on the acousto-optic effect. In *Euronoise, Prague, 2012*.

- J. R. Underbrink. *Aeroacoustic Measurements*, chapter Aeroacoustic Phased Array Testing in Low Speed Wind Tunnels, pages 98 – 217. Springer Verlag, First Edition, 2002.
- J. R. Underbrink and R. P. Dougherty. Array design for non-intrusive measurement of noise sources. In *Noise-Con 96, Seattle*, 1996.
- F. Urzunicok. *Separation Control by Flow-Induced Oscillations of a Resonator*. PhD thesis, Technical University of Berlin, 2003.
- E. Weinstein, K. Steele, A. Agarwal, and J. Glass. Loud: A 1020-node microphone array and acoustic beamformer. In *14th International Congress on Sound and Vibration, Cairns, Australia*, 2007.

Acknowledgments

I would like to thank all people who have directly or indirectly contributed to the success of this thesis. Especially, I would particularly like to thank:

- Prof. Dr.-Ing. Wolfgang Nitsche and Prof. Dr. rer. nat. Dr.-Ing. habil. Andreas Dillmann for supervising my dissertation and the confidence they have placed in me.
- Dr. rer. nat. Jürgen Kompenhans and Dr.-Ing. Lars Koop for the continuous supported and interest and for making it possible to perform my experiments.
- Dr.-Ing. Lars Koop, Dr. rer. nat. Klaus Ehrenfried and Dr.-Ing. Carsten Spehr for enlightening discussions and their technical expertise which have contributed to the success of this dissertation.
- Prof. Dr.-Ing. Dieter Peitsch for being the chairman of the PhD Examination Committee.
- Dr.phil. Walter Beck for reading and correcting the manuscript carefully and giving countless helpful comments.
- Birgit Müller for her moral support, her immense patience and always being there when I need her.
- My daughter Finia for getting distraction from the scientific work and who slept quietly so many nights enabling me to make progress with my dissertation.
- My parents and my family for making possible my education.